CP-Violation in Partially Reconstructed $B^{\pm} \to D^{*}h^{\pm}$ Decays at LHCb

Seophine Stanislaus
Keble College
University of Oxford

A thesis submitted for the degree of
Doctor of Philosophy
in
Particle Physics

Hilary 2024

To my parents and my brother, Beojan.

Abstract

This thesis presents a measurement of *CP*-violation in partially reconstructed $B^{\pm} \to D^{*}K^{\pm}$ and $B^{\pm} \to D^{*}\pi^{\pm}$ decays, where the neutral pion and photon from the $D^{*} \to D\pi^{0}$ and $D^{*} \to D\gamma$ decays are not reconstructed. The D meson is subsequently reconstructed in the $D \to K^{0}_{S}\pi^{+}\pi^{-}$ or $D \to K^{0}_{S}K^{+}K^{-}$ final state. The measurement of *CP*-violation is performed by analysing the distribution of the signal yields over the D-decay phase space, without relying on a D-decay amplitude model. Instead, inputs for strong phase-related parameters measured at CLEO and BESIII are used. The measurement is performed using proton-proton collision data collected by the LHCb experiment at centre-of-mass energies of 7, 8, and 13 TeV, with a total integrated luminosity of approximately $9\,\text{fb}^{-1}$. The work in this thesis measures *CP*-violating observables using partially reconstructed $B^{\pm} \to D^{*}K^{\pm}$ and $B^{\pm} \to D^{*}\pi^{\pm}$ decays at LHCb. These observables are interpreted in terms of physical parameters, including the Cabibbo-Kobayashi-Maskawa angle, γ, a fundamental Standard Model parameter. This is found to be $\gamma = (92^{+21}_{-17})^{\circ}$, where the total uncertainty includes the statistical and all systematic uncertainties.

Acknowledgements

First of all, I would like to thank my supervisor, Sneha Malde, whose attention to detail and supportive feedback have helped me produce work I am proud of. It has been a privilege to learn from such a dedicated supervisor and I look forward to continue working with her as a post-doc.

I would also like to thank Sue Geddes and Kim Proudfoot for all their support and patience.

Thanks are also owed to the Science and Technology Facilities Council and the Oxford Physics Endowment for Graduates for their generous funding of my graduate studies.

My time at Oxford and CERN have been especially enjoyable because of the friends I have made along the way. In particular, I would like to thank the Oxford LHCb students, both past and present, for all their support and good humour.

Finally, I would like to thank my parents who instilled in me a love of learning and my brother, Beojan, who first introduced me to particle physics. Without their encouragement I would not be where I am today.

Preface

Experimental particle physics is an incredibly collaborative field. The work presented in this thesis is my own, except where clearly referenced, and is built on the vital contributions of the more than 1000 members of the LHCb collaboration. This is particularly regarding data quality, but also numerous measurements similar to my own. For the present work, I devised and executed the analysis, and performed the interpretation of the final measurements. This has subsequently been published in the Journal of High Energy Physics **02** (2024) 118 [1].

In addition to this, I have also made contributions towards data quality for Run 3. I have developed and tested over 100 trigger lines for the B2OC working group, and have also played a crucial role in data calibration for reliable particle identification. This is a key component of many LHCb analyses and my work spans two aspects. Firstly, I developed a new trigger selection and preliminary calibration for electron particle identification. Secondly, and more broadly, I have been responsible for the software development and upgrade of the overarching calibration framework for Run 3. I have collaborated with other Oxford students to optimise the software package given the higher data collection rate in Run 3 compared to previous years.

Contents

1

Introduction

The universe emerged from the Big Bang 14 billion years ago consisting of matter and antimatter. They interacted in different ways resulting in a very small imbalance between them; a single extra matter particle for every 10 billion antimatter particles. This imbalance was sufficient that when they annihilated, matter survived, enabling the evolution of the early universe into the matter-dominated one we see today.

In 1967, Andrei Sakharov proposed three conditions necessary for this matter-antimatter asymmetry [2]. First, baryon number violation to allow a net imbalance of matter and antimatter. Second, a departure from thermal equilibrium to prevent the reversal of any baryon-number-violating process. Finally, the topic of this thesis, C and CP-violation where the charge-conjugation operator (C) converts particles to their antiparticles, and the parity operator (P) inverts spatial coordinates.

The Standard Model provides a mechanism for CP-violation in weak interactions. This, as of yet, has only been measured in the quark sector. There are two types of CP-violation: indirect, which occurs via mixing, and direct, which

occurs in the decay itself. Indirect *CP*-violation was first observed in 1964 by Christenson, Cronin, Fitch, and Turlay in the decay of neutral kaons after mixing [3]. Direct *CP*-violation was also observed in the kaon system in the 1990s by the NA48 experiment [4]. Since then, it has also been measured in the B system by the BaBar [5], Belle [6], and LHCb collaborations [7], the latter also observing *CP*-violation in the charm sector [8]. In the B system, one of the ways that *CP*-violation is studied is using precise measurements of the *CP*-violating phase, γ; a fundamental Standard Model parameter. Direct measurements of this phase can be achieved using tree-level decays, where new physics contributions can be neglected [9]. These are compared to indirect measurements of γ which are sensitive to new physics, thereby testing the Standard Model [10]. This test is especially important in the study of *CP*-violation where measurements show that the Standard Model description, discussed in Ch. 2, insufficiently describes the observed matter-antimatter asymmetry in the universe. Precise measurements of *CP*-violation, described in Ch. 3, are therefore essential to facilitate searches for new physics which could account for these differences.

One such measurement is presented here using data collected by the LHCb experiment. This is a dedicated heavy flavour physics experiment which is uniquely optimised to measure *CP*-violation, as will be discussed in Ch. 4. In the present work, the *CP*-violating phase γ is measured using $B^\pm \to D^* K^\pm$ and $B^\pm \to D^* \pi^\pm$ decays, where decays of the D^* meson to $D\pi^0$ and $D\gamma$ are partially reconstructed, and the resulting D meson is reconstructed in the $K^0_S\pi^+\pi^-$ or $K^0_S K^+ K^-$ final state. The strategy for this is described in Ch. 5. Of note is the use of partial reconstruction which means candidates are reconstructed as $B^\pm \to DK^\pm$ or $B^\pm \to D\pi^\pm$. This is described in Ch. 6. Partial reconstruction leads to greater signal yields but

also requires a careful consideration of backgrounds, which is explained in Ch. 7. The measurement of γ is detailed in Ch. 8, with a discussion of the systematic uncertainties in Ch. 9. This is followed by an interpretation of the results, as well as a discussion of their implications in Ch. 10. Finally, the thesis is concluded in Ch. 11 with a look to the future of *CP*-violation measurements.

2

Theoretical Background

2.1 | The Standard Model of Particle Physics

The Standard Model (SM) is our current understanding of particle physics. It describes the known fundamental particles and interactions between them, which are also exchanges of particles. This is depicted in Fig. 2.1. In black are the fermions, spin-$\frac{1}{2}$ particles, named as such since they obey Fermi-Dirac statistics. The first two rows are the quarks, consisting of up-type quarks (first row) with electric charge $+\frac{2}{3}e$ and down-type quarks (second row) with electric charge $-\frac{1}{3}e$. The third and fourth rows of fermions are the leptons, the electron (e), muon (μ), and tau lepton (τ) each with electric charge $-e$, followed by the electrically neutral neutrinos (ν_e, ν_μ, and ν_τ). There are three generations of fermions, indicated by the three columns. For the quarks and charged leptons, these generations depict the mass hierarchies within each sector. In comparison, the neutrino states in Fig. 2.1 are superpositions of separate states with well-defined, and almost negligible, masses. In addition to the fermions shown in Fig. 2.1, there are also anti-fermions, for example $\bar{u}$. These are anti-particles which have the same mass

and spin but opposite additive quantum numbers, such as electric charge.

In Fig. 2.1, the coloured letters depict the bosons, integer-spin particles which obey Bose-Einstein statistics. In blue is the photon, a massless spin-1 particle which mediates the electromagnetic force between the quarks and charged leptons. These are, therefore, enclosed within the blue line in Fig. 2.1. In red is the gluon, also a massless spin-1 particle, but this mediates the strong force between the quarks. Only quarks (and antiquarks) can participate in the strong interaction because they carry colour charge, denoted red, green, and blue. Quarks form bound states called hadrons (in quark-antiquark pairs as mesons or three-quark systems as baryons) which are observable and overall colour-neutral. In Fig. 2.1, the $W^{\pm}$ and Z bosons are shown in green. These are massive spin-1 bosons which mediate the weak force between all fermions.

Finally, in Fig. 2.1, in orange is the Higgs boson, a massive spin-0 particle, which provides the mechanism by which all fundamental particles acquire their mass. Therefore, in Fig. 2.1, it is shown to interact with all massive particles. The Higgs boson is an excitation of the Higgs field, which has a non-zero vacuum expectation value. As a result, when an initially massless particle interacts with the non-zero Higgs field, it acquires mass [11].

The SM is one of the most well-tested theories in physics. Despite this, there are a number of phenomena which are not described; gravity, dark matter and dark energy, the masses of neutrinos, and the matter-antimatter asymmetry of the universe. There are new physics searches for Beyond the Standard Model (BSM) particles to describe these phenomena. To facilitate these searches, precise measurements of SM parameters are needed. Of particular interest for this thesis is the search for BSM physics to describe the matter-antimatter asymmetry of the

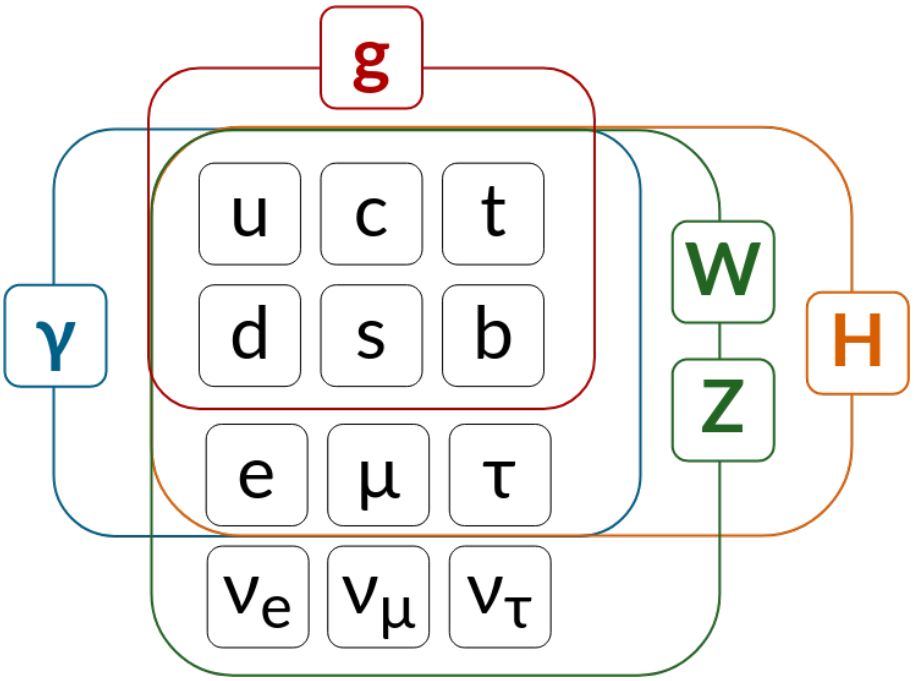

Figure 2.1: Elementary SM particles with fermions in black and bosons in blue, red, green, and orange where they interact with particles enclosed within their coloured lines.

universe. To aid this, measurements of *CP*-violation in the SM are necessary.

2.2 | *CP*-Violation in the Quark Sector

Symmetries are a vital component of physics. Noether's theorem states that for every continuous symmetry there is a corresponding conserved quantity [12]. For example, symmetry under translations in time results in the conservation of total energy. This concept underpins the SM where interactions between particles are derived by requiring invariance under local $U(1) \times SU(2) \times SU(3)$ gauge transformations [13].

Discrete symmetries are of particular importance for the work in this thesis,

specifically charge conjugation (C), parity (P), and time reversal (T). Charge conjugation replaces particles with their antiparticles, and vice versa, for example transforming an u quark into an $\bar{u}$ quark. Parity inverts spatial coordinates about the origin, for example, transforming a spatial vector from $\vec{x}$ to $-\vec{x}$. Finally, time reversal inverts time coordinates from t to $-t$. The combination of these three transformations, CPT, is believed to be an exact symmetry of the universe, and this is known as the CPT theorem [14]. However, any one, or a combination of two of these discrete symmetries, can be broken. Specific to this thesis is the combination of C and P, known as CP, which is not conserved in the SM in weak interactions. This non-conservation of CP is known as CP-violation and is one of Sakharov's conditions necessary for the matter-antimatter asymmetry of the universe to arise, as discussed in Ch. 1.

This thesis presents a SM measurement of CP-violation. In the SM, CP-violation occurs at a much smaller level than that required by Sakharov's conditions. Therefore, such measurements cannot explain the matter-antimatter asymmetry of the universe, but they can facilitate BSM searches. Standard Model-only measurements are compared to measurements which can be altered by new physics contributions, thereby guiding BSM searches. Then, if a BSM mechanism is found which exhibits much larger CP-violation than the SM and was also prevalent in the early universe, this could reconcile our understanding of particle physics and the matter-antimatter asymmetry of the universe.

In the SM, CP-violation is present in weak interactions. As yet, this has only been observed in the quark sector, and is the focus of this thesis, but evidence has also been found in the neutrino sector [15]. In the quark sector, there are three classifications of CP-violation. First, CP-violation in decay, where a decay rate

and its *CP*-conjugate are not equal, $\Gamma(M \to f) \neq \Gamma(\overline{M} \to \bar{f})$, for initial states, M, with *CP*-conjugates $\overline{M}$, and final states, f, with *CP*-conjugates $\bar{f}$. Second, there is *CP*-violation in mixing, where the rate of mixing for a neutral meson differs under *CP*-conjugation, $\Gamma(M \to \overline{M}) \neq \Gamma(\overline{M} \to M)$. Finally, interference can occur between an initial state, M, reaching a final state, f, directly through decay without mixing, $M \to f$, and decaying after mixing, $M \to \overline{M} \to f$. This will only occur in decays where f is common to both M and $\overline{M}$. For a charged initial state, as is the case in this thesis, only *CP*-violation in decay is possible, and this is the mechanism by which *CP*-violation is measured here.

The theoretical description of *CP*-violation in the quark sector is encoded in the Cabibbo-Kobayashi-Maskawa (CKM) matrix [16,17]. This matrix relates mass eigenstates, which constitute observed hadrons, with weak eigenstates, which interact with the $W^{\pm}$ boson,

$$\begin{pmatrix} d' \\ s' \\ b' \end{pmatrix} = V_{CKM} \begin{pmatrix} d \\ s \\ b \end{pmatrix} = \begin{pmatrix} V_{ud} & V_{us} & V_{ub} \\ V_{cd} & V_{cs} & V_{cb} \\ V_{td} & V_{ts} & V_{tb} \end{pmatrix} \begin{pmatrix} d \\ s \\ b \end{pmatrix}, \tag{2.1}$$

where the primes indicate the weak eigenstates. This enables quark mixing, for example, V_{ud} describes mixing between an up and down quark. The weak interaction vertex between an up quark and down quark is shown in Fig. 2.2 and the corresponding term in the Lagrangian is [18],

$$\mathcal{L} = -\frac{g_W}{\sqrt{2}} \left[\overline{u} \gamma^{\mu} W_{\mu}^{+} V_{ud}^{*} d \right], \tag{2.2}$$

where g_W is the weak coupling constant, γ^{μ} are the Gamma matrices [19], and W_{μ}^{+} represents the W^{+} boson.

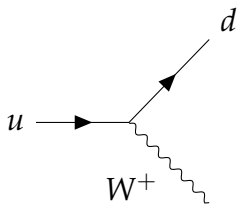

Figure 2.2: Example of a weak interaction vertex between an up and down quark.

The construction of the CKM matrix can be understood as follows. To relate the weak and mass eigenstates for three generations of quarks, a 3×3 matrix is needed. Regardless of the representation (weak or mass eigenstate), the same physics results are observed. This means that, if $|\psi\rangle$ is the mass eigenstate and $|\psi'\rangle$ is the weak eigenstate,

$$\langle\psi|\psi\rangle = \langle\psi'|\psi'\rangle = \langle\psi|V_{CKM}^{\dagger}V_{CKM}|\psi\rangle, \tag{2.3}$$

hence, $V_{CKM}^{\dagger}V_{CKM} = \mathbb{1}$, *i.e.* the CKM matrix is unitary. This can also be written as

$$\sum_k |V_{ik}|^2 = 1 \qquad \text{and} \qquad \sum_k V_{ik}V_{jk}^{*} = 0, \tag{2.4}$$

where the i, j, and k indices run over the three generations of quarks. This results in three independent constraints from the first condition and six from the second. As a result, the 3×3 matrix with 18 parameters (from 9 complex elements) is reduced to 9 independent parameters.

Furthermore, as the CKM matrix is unitary, and not real, there can be six complex phases, one associated with each quark in either its mass or weak eigenstate. Of these six phases, five are unphysical. This is because the term in the

Lagrangian, Eq. 2.2, is unchanged by the transformations,

$$\overline{u} \rightarrow \overline{u}e^{-i\theta_u} \tag{2.5a}$$

$$d \rightarrow de^{i\theta_d} \tag{2.5b}$$

$$V_{ud} \rightarrow V_{ud}e^{i(\theta_u - \theta_d)} \tag{2.5c}$$

and therefore complex phases in the CKM matrix can be absorbed into the definitions of the eigenstates. An overall phase applied to all CKM elements has no physical effect, *i.e.* $V_{CKM} \rightarrow V_{CKM}e^{i\theta}$. Using this, a common phase can be factorised out of all CKM elements. For example, $\theta = \theta_u$ and the phases for the five other quarks can be written as $\theta_d = \theta_u + \theta'_d$. This absorbs five of the six phases into the quark definitions since $\theta'_u = 0$ and the transformations are

$$\overline{u} \rightarrow \overline{u}e^{-i\theta_u} \tag{2.6a}$$

$$d \rightarrow de^{i\theta_d} \tag{2.6b}$$

$$V_{ud} \rightarrow V_{ud}e^{i(\theta_u - \theta_d)} = V_{ud}e^{-i\theta_d} \tag{2.6c}$$

where the equality in Eq. 2.6c arises from physics results being invariant under $V_{CKM} \rightarrow V_{CKM}e^{i\theta}$, and therefore also $V_{ud} \rightarrow V_{ud}e^{i\theta_u}$. As a result, these transformations do change the Lagrangian. Hence, only one complex phase has a physical effect.

This means that the CKM matrix can be described by four parameters: three quark–mixing angles, θ_{12}, θ_{23}, and θ_{13}, and one complex phase, δ_{CP}. Due to this complex phase, the CKM matrix is not identical to its complex conjugate and this allows for *CP*-violation. For ease of notation, the cosine and sine of the quark-mixing angles can be written as $c_{ij} = \cos(\theta_{ij})$ and $s_{ij} = \sin(\theta_{ij})$. The CKM matrix

is thus written as

$$V_{CKM} = \begin{pmatrix} c_{12}c_{13} & s_{12}c_{13} & s_{13}e^{-i\delta_{CP}} \\ -s_{12}c_{23} - c_{12}s_{23}s_{13}e^{i\delta_{CP}} & c_{12}c_{23} - s_{12}s_{23}s_{13}e^{i\delta_{CP}} & s_{23}c_{13} \\ s_{12}c_{23} - c_{12}c_{23}s_{13}e^{i\delta_{CP}} & -c_{12}s_{23} - s_{12}c_{23}s_{13}e^{i\delta_{CP}} & c_{23}c_{13} \end{pmatrix}. \quad (2.7)$$

This is the standard parameterisation [20], where terms along the diagonal are largest. Experimentally, it has been determined that $s_{13} \ll s_{23} \ll s_{12} \ll 1$, and using this hierarchy, an alternative parameterisation [21] can be defined using,

$$s_{12} \equiv \lambda \quad (2.8a)$$

$$s_{23} \equiv A\lambda^2 \quad (2.8b)$$

$$s_{13}e^{i\delta_{CP}} \equiv A\lambda^3(\overline{\rho} + i\overline{\eta}). \quad (2.8c)$$

This is called the Wolfenstein parameterisation [21],

$$V_{CKM} = \begin{pmatrix} 1 - \lambda^2/2 & \lambda & A\lambda^3(\overline{\rho} - i\overline{\eta}) \\ -\lambda & 1 - \lambda^2/2 & A\lambda^2 \\ A\lambda^3(1 - \overline{\rho} - i\overline{\eta}) & -A\lambda^2 & 1 \end{pmatrix} + \mathcal{O}(\lambda^4), \quad (2.9)$$

where *CP*-violation is parameterised using the complex plane in $\overline{\rho}$ and $\overline{\eta}$. Since only the V_{ub} and V_{td} matrix elements are complex, *CP*-violation in kaons and D mesons is negligible up to $\mathcal{O}(\lambda^4)$. A visual representation of the Wolfenstein parameterisation can be derived using the six vanishing constraints given by the second condition in Eq. 2.4. Each term represents the side of a triangle and thus a unitarity triangle can be drawn. The most common form arises from,

$$V_{ub}{}^* V_{ud} + V_{cb}{}^* V_{cd} + V_{tb}{}^* V_{td} = 0, \quad (2.10)$$

which can be normalised and rearranged as,

$$1 + \frac{V_{tb}{}^* V_{td}}{V_{cb}{}^* V_{cd}} + \frac{V_{ub}{}^* V_{ud}}{V_{cb}{}^* V_{cd}} = 0. \quad (2.11)$$

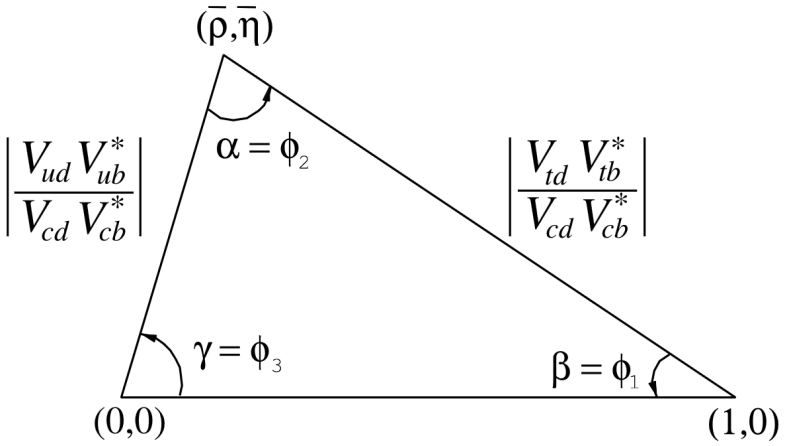

Figure 2.3: The unitarity triangle as given in Ref. [18].

This form is particularly useful as each term in Eq. 2.11 can be represented by a vector in the $\overline{\rho} - \overline{\eta}$ plane and drawn to form the unitarity triangle shown in Fig. 2.3. The three angles can be determined using the vectors, leading to

$$\alpha \equiv \arg\left[-\frac{V_{tb}{}^*V_{td}}{V_{ub}{}^*V_{ud}}\right] \qquad \beta \equiv \arg\left[-\frac{V_{cb}{}^*V_{cd}}{V_{tb}{}^*V_{td}}\right] \qquad \gamma \equiv \arg\left[-\frac{V_{ub}{}^*V_{ud}}{V_{cb}{}^*V_{cd}}\right]. \quad (2.12)$$

The final angle is the CKM angle γ; the subject of this thesis[1].

From the definitions in Eq. 2.12, it is clear that γ is the only angle which does not involve top-quark couplings. As a result, only γ can be measured using solely tree-level processes, as BSM physics can enter via top loops in the form of new, heavy particles and exhibit *CP*-violation. Therefore, under the assumption that tree-level processes do not include BSM physics [22, 23], direct measurements of γ provide a SM benchmark.

[1]There is also a formulation that exists in literature where the CKM angles α, β, and γ are denoted ϕ_1, ϕ_2, and ϕ_3 respectively.

2.3 | Testing Standard Model *CP*-Violation

The SM description of *CP*-violation is tested by comparing direct and indirect determinations of γ. From Fig. 2.3, it is evident that indirect determinations of γ can be ascertained using measurements of the other angles and sides and imposing unitarity. Figure 2.4 demonstrates how this is possible by combining measurements of Δm_d, Δm_s, ϵ_K, and $\sin(2\beta)$. The $\Delta m_{d(s)}$ parameters are related to $B^0_{(s)} - \bar{B}^0_{(s)}$ mixing, and ϵ_K is a measure of kaon-mixing. By combining these the length of the side opposite γ can be determined. Then, measurements of $\sin(2\beta)$ can be obtained from time-dependent *CP*-violation in, for example, $B^0_s \to J/\psi K^0_S$ decays. The CKMFitter group reports a combination of these indirect determinations, $\gamma = (65.29^{+0.72}_{-1.86})^\circ$, and a combination of direct measurements using tree-level processes, $\gamma = (65.9^{+3.3}_{-3.5})^\circ$ [24]. The comparison of these determinations, and therefore the test of the SM, is currently limited by the experimental uncertainty on direct γ measurements. Here, precision is driven by studies of charged and neutral $B \to D^{(*)}K^{(*)}$ decays. Therefore, further precision measurements of *CP*-violation in these decays are needed to enable closer tests of the SM.

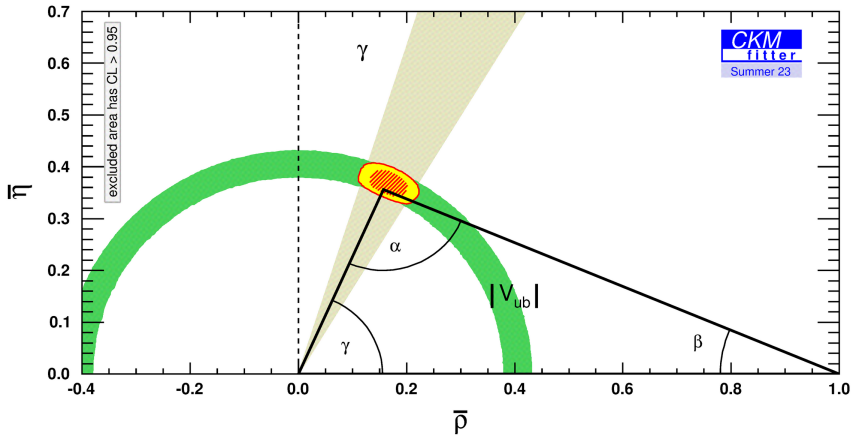

(a) Combinations of tree-level measurements for γ.

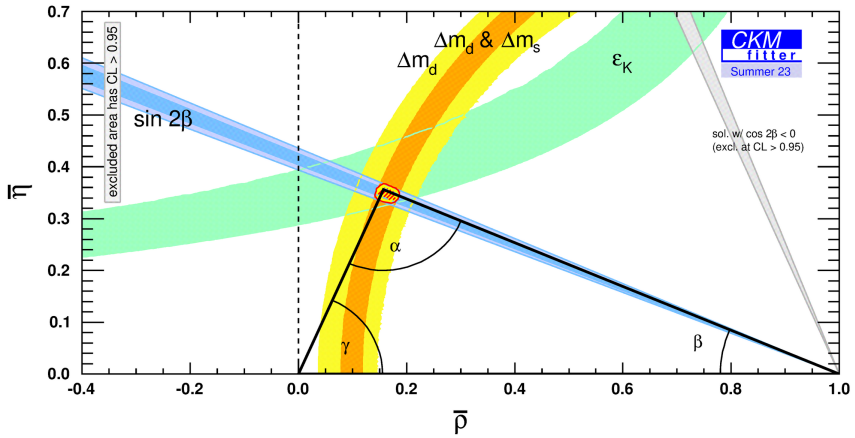

(b) Combinations of loop-level measurements for γ.

Figure 2.4: Figures from the CKMFitter group as of Summer 2023 [24] demonstrating how various measurements are combined to determine γ (a) directly from tree-level processes and (b) indirectly from loop-level processes.

2.4 | Measuring γ in Tree-Level Decays

This thesis presents a study of charged B decays which only exhibit direct *CP*-violation where $\Gamma(M \to f) \neq \Gamma(\overline{M} \to \bar{f})$. Since the decay rate, Γ, is proportional to the modulus-squared of the amplitude, $|\mathcal{A}|^2$, to measure a *CP*-violating phase, there must be interference between two or more contributing amplitudes to a decay. For a decay, $M \to f$, with *CP*-conjugate, $\overline{M} \to \bar{f}$, if each decay has two contributing amplitudes which interfere, this interference can be depicted as shown in Fig. 2.5, where the amplitudes are labelled.

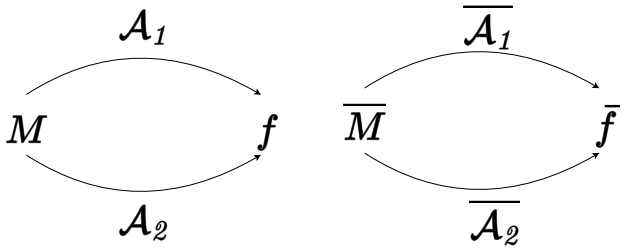

Figure 2.5: Interference diagrams for (left) a generic $M \to f$ decay, and (right) its *CP*-conjugate, $\overline{M} \to \bar{f}$ decay, with interfering amplitudes labelled.

Each amplitude can be written in terms of the magnitude of the amplitude, a *CP*-conserving phase (or strong phase), δ, due to strong and electromagnetic interactions, and a *CP*-violating phase (or weak phase), ϕ, due to weak interactions. For example,

$$\mathcal{A}_1 = |\mathcal{A}_1| e^{i(\phi_1 + \delta_1)}. \tag{2.13}$$

Since the $\overline{M} \to \bar{f}$ decay is the *CP*-conjugate of the $M \to f$ decay, the following

relations are true,

$$|\overline{\mathcal{A}}_{1,2}| = |\mathcal{A}_{1,2}|, \tag{2.14a}$$

$$\overline{\delta_{1,2}} = \delta_{1,2}, \tag{2.14b}$$

$$\overline{\phi_{1,2}} = -\phi_{1,2}. \tag{2.14c}$$

Using these relations, the total amplitudes for the $M \to f$ and $\overline{M} \to \bar{f}$ decays can be written as,

$$\mathcal{A}(M \to f) \equiv \mathcal{A} = |\mathcal{A}_1| e^{i(\ \phi_1 + \delta_1)} + |\mathcal{A}_2| e^{i(\ \phi_2 + \delta_2)}, \tag{2.15a}$$

$$\mathcal{A}(\overline{M} \to \bar{f}) \equiv \overline{\mathcal{A}} = |\mathcal{A}_1| e^{i(-\phi_1 + \delta_1)} + |\mathcal{A}_2| e^{i(-\phi_2 + \delta_2)}. \tag{2.15b}$$

Then, since these decays exhibit direct *CP*-violation and $\Gamma(M \to f) \neq \Gamma(\overline{M} \to \bar{f})$, it can be deduced that $|\mathcal{A}|^2 \neq |\overline{\mathcal{A}}|^2$. Therefore, the difference between the modulus-squared of these amplitudes can be determined,

$$\begin{aligned} |\mathcal{A}|^2 - |\overline{\mathcal{A}}|^2 = &\left| \left[|\mathcal{A}_1| e^{i(\ \phi_1 + \delta_1)} + |\mathcal{A}_2| e^{i(\ \phi_2 + \delta_2)} \right] \right|^2 - \\ &\left| \left[|\mathcal{A}_1| e^{i(-\phi_1 + \delta_1)} + |\mathcal{A}_2| e^{i(-\phi_2 + \delta_2)} \right] \right|^2 \\ = &-4 |\mathcal{A}_1| |\mathcal{A}_2| \sin(\delta_1 - \delta_2) \sin(\phi_1 - \phi_2). \end{aligned} \tag{2.16}$$

This means that for direct *CP*-violation to occur, $\delta_1 \neq \delta_2$ and $\phi_1 \neq \phi_2$; the interfering amplitudes must have different strong and weak phases. This is the case for $B^\pm \to DK^\pm$ decays, which are similar to the $B^\pm \to D^* K^\pm$ decays studied in this thesis, and are used as an example for the theoretical formalism here. The impact of the D^* decay is established later in Ch. 3.4.

In $B^\pm \to DK^\pm$ decays, the D meson is a superposition of the D^0 and $\overline{D}^0$ states, both of which decay to the same final state. Thus, there are two interfering amplitudes, as shown in Fig. 2.6, with strong and weak phase differences, δ_B

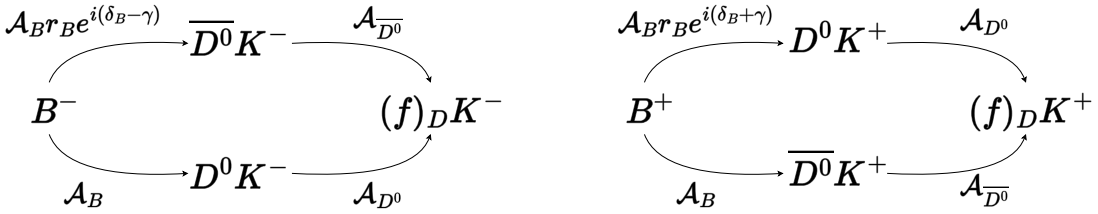

Figure 2.6: Interference diagrams for (left) $B^- \to DK^-$ decays, and (right) its *CP*-conjugate, $B^+ \to DK^+$ decays, where $(f)_D$ is the D-decay final state and amplitudes are labelled.

and γ. The weak phase difference is found to be γ because using the Feynman diagrams for the $B^- \to D^0 K^-$ and $B^- \to \overline{D}^0 K^-$ decays in Fig. 2.7, the weak phase difference is $\Delta\phi = \arg\left[\frac{V_{cb}V_{us}^*}{V_{ub}V_{cs}^*}\right]$. As shown in Eq. 2.9, up to $\mathcal{O}(\lambda^4)$,

$$V_{ud} \approx V_{cs}, \tag{2.17a}$$

$$V_{cd} \approx -V_{us}. \tag{2.17b}$$

Therefore, the weak phase difference,

$$\Delta\phi \approx \arg\left[-\frac{V_{cb}{V_{cd}}^*}{V_{ub}{V_{ud}}^*}\right] \tag{2.18}$$

$$= \arg\left[-\frac{{V_{ub}}^* V_{ud}}{{V_{cb}}^* V_{cd}}\right] \tag{2.19}$$

$$= \gamma, \tag{2.20}$$

can be equated to the CKM angle γ [25].

Figure 2.6 also shows the ratio of the magnitude of the amplitudes using a parameter, r_B. For $B^\pm \to DK^\pm$ decays, this is defined as

$$\begin{aligned} r_B &\equiv \left|\frac{\mathcal{A}(B^- \to \overline{D}^0 K^-)}{\mathcal{A}(B^- \to D^0 K^-)}\right| \\ &\equiv \left|\frac{\mathcal{A}(B^+ \to D^0 K^+)}{\mathcal{A}(B^+ \to \overline{D}^0 K^+)}\right|, \end{aligned} \tag{2.21}$$

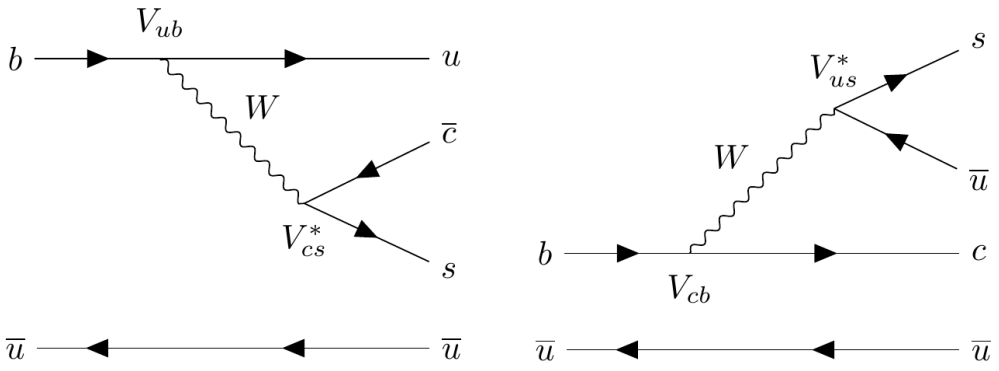

Figure 2.7: Feynman diagrams showing (left) the $B^- \to \overline{D}^0 K^-$ decay, and (right) the $B^- \to D^0 K^-$ decay, where vertices are labelled with the appropriate CKM matrix elements.

and accounts for the difference in magnitude of the strong, electromagnetic, and weak interactions between the two B^-, or B^+, decays.

Using Fig. 2.6, the total amplitudes for each of the B^- and B^+ decays can be written as

$$\mathcal{A}(B^- \to DK^-) = \mathcal{A}_B(\mathcal{A}_{D^0} + r_B e^{i(\delta_B - \gamma)}\mathcal{A}_{\overline{D}^0}), \tag{2.22a}$$

$$\mathcal{A}(B^+ \to DK^+) = \mathcal{A}_B(\mathcal{A}_{\overline{D}^0} + r_B e^{i(\delta_B + \gamma)}\mathcal{A}_{D^0}). \tag{2.22b}$$

The amplitude of the $\overline{D}^0$ decay can be written in terms $\mathcal{A}_{D^0}$ and a ratio of the magnitude of the D-decay amplitudes and the strong phase difference between them,

$$\mathcal{A}_{D^0} = \mathcal{A}_D, \tag{2.23a}$$

$$\mathcal{A}_{\overline{D}^0} = \mathcal{A}_D r_D e^{-i\delta_D}, \tag{2.23b}$$

where there is no weak phase difference since CP-violation in D decays can be ignored up to $\mathcal{O}(\lambda^4)$ [26]. This is safe to do given current experimental precision

on γ. Using this, the decay rates for the B^- and B^+ decays can be written as,

$$\Gamma(B^- \to DK^-) \propto \ 1 + r_D^2 r_B^2 + 2 r_D r_B [\cos(\delta_D)\cos(\delta_B - \gamma) + \sin(\delta_D)\sin(\delta_B - \gamma)], \tag{2.24a}$$

$$\Gamma(B^+ \to DK^+) \propto r_D^2 + \ \ r_B^2 + 2 r_D r_B [\cos(\delta_D)\cos(\delta_B + \gamma) - \sin(\delta_D)\sin(\delta_B + \gamma)]. \tag{2.24b}$$

These are general equations for any D-decay final state. If a specific D final state is studied, this will alter the sizes of the r_D and δ_D parameters and, therefore, impact the methods by which CP-violation is measured.

3

Methodology

There are many different D-decay final states that can be considered, leading to different methods for measuring CP-violation. This chapter outlines some important examples, then details the D-decay final state studied in this thesis and how it is used to measure γ.

3.1 | Types of D-decay Final States

The most intuitive final states to consider are CP-eigenstates, such as $D \to K^+K^-$, $D \to \pi^+\pi^-$, or $D \to K^0_S\pi^0$. A CP-eigenstate is an eigenvector of the $\hat{CP}$ operator with eigenvalues ± 1. In this thesis, the convention chosen for this is

$$\hat{CP}|\psi\rangle = \pm|\psi\rangle. \tag{3.1}$$

If the CP eigenvalue is $+1$, then the final state is known as CP-even. If the eigenvalue is -1, the final state is CP-odd. This means that for a D-decay final state which is a CP-eigenstate, $r_D = 1$ and $\delta_D = 0$ if it is CP-even, and $\delta_D = \pi$ if it is CP-odd. For CP-even (CP_+) and CP-odd (CP_-) final states, the decay rates in

Eq. 2.24 become

$$\Gamma_{CP_\pm}(B^- \to DK^-) \propto \; 1 + r_B^2 \pm 2r_B \cos(\delta_B - \gamma), \tag{3.2a}$$

$$\Gamma_{CP_\pm}(B^+ \to DK^+) \propto \; 1 + r_B^2 \pm 2r_B \cos(\delta_B + \gamma). \tag{3.2b}$$

Experimentally, these final states are measured using the GLW method [27, 28] developed by Gronau, London, and Wyler, where the measured observables are *CP* asymmetries and ratios. The *CP* asymmetries are defined as

$$A_{CP_\pm} \equiv \frac{\Gamma_{CP_\pm}(B^- \to DK^-) - \Gamma_{CP_\pm}(B^+ \to DK^+)}{\Gamma_{CP_\pm}(B^- \to DK^-) + \Gamma_{CP_\pm}(B^+ \to DK^+)}, \tag{3.3}$$

and using Eq. 3.2, they can be related to the physical parameters as,

$$A_{CP_\pm} = \frac{\pm 2r_B \sin\delta_B \sin\gamma}{1 + r_B^2 \pm 2r_B \cos\delta_B \cos\gamma}. \tag{3.4}$$

The *CP* ratios are defined as

$$R_{CP_\pm} \equiv 2\frac{\Gamma_{CP_\pm}(B^- \to DK^-) + \Gamma_{CP_\pm}(B^+ \to DK^+)}{\Gamma(B^- \to D^0K^-) + \Gamma(B^+ \to \overline{D}^0K^+)}, \tag{3.5}$$

where $\Gamma(B^- \to D^0K^-)$ and $\Gamma(B^+ \to \overline{D}^0K^+)$ are the decay rates to flavour-specific D mesons. The relations to the physical parameters are

$$R_{CP_\pm} = 1 + r_B^2 \pm 2r_B \cos\delta_B \cos\gamma. \tag{3.6}$$

Final states which are *CP*-eigenstates are the simplest scenario, but do not necessarily lead to large asymmetries, and therefore high sensitivity to γ. To achieve this, decays with approximately equal magnitudes for r_D and r_B are needed to maximise the interference term in the $B^\pm$ decay rates shown in Eq. 2.24. These are Cabibbo-favoured decays, $D^0 \to f$, and doubly-Cabibbo-suppressed decays, $\overline{D}^0 \to f$. The canonical examples are favoured $D^0 \to K^-\pi^+$ decays and suppressed $\overline{D}^0 \to K^-\pi^+$ decays. The interference diagrams for such a final state

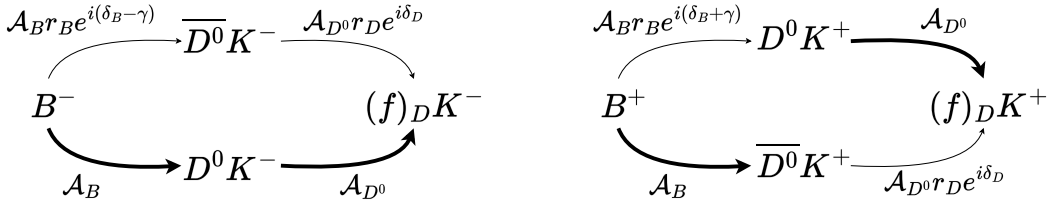

Figure 3.1: Interference diagrams for (left) $B^- \to DK^-$ decays, and (right) $B^+ \to DK^+$ decays with labelled amplitudes for the final state, $f = K^-\pi^+$. Bold arrows represent favoured amplitudes and the thin arrows represent suppressed amplitudes.

are shown in Fig. 3.1, where the bold arrows represent favoured amplitudes and the thin arrows represent suppressed amplitudes. In the B^- diagram, there is a path to the final state where the favoured $B^- \to D^0 K^-$ decay is followed by the favoured $D^0 \to K^-\pi^+$ decay, and overall this decay chain has a large amplitude. This interferes with the decay chain where the suppressed $B^- \to \overline{D}^0 K^-$ decay is followed by the suppressed $\overline{D}^0 \to K^-\pi^+$ decay, which together have a very small amplitude. The total decay rate for this can be written as

$$\Gamma_{fav}(B^- \to DK^-) \propto \ 1 + r_B^2 r_D^2 + 2 r_B r_D \cos(\delta_B + \delta_D - \gamma). \tag{3.7}$$

In the B^+ diagram, the favoured $B^+ \to \overline{D}^0 K^+$ decay is followed by the suppressed $\overline{D}^0 \to K^-\pi^+$ decay, and interferes with the suppressed $B^+ \to D^0 K^+$ decay followed by the favoured $D^0 \to K^-\pi^+$ decay. These decay chains have similar magnitudes, leading to maximal interference. The total decay rate is

$$\Gamma_{sup}(B^+ \to DK^+) \propto r_B^2 + r_D^2 + 2 r_B r_D \cos(\delta_B - \delta_D + \gamma). \tag{3.8}$$

Additionally, favoured $\overline{D}^0 \to K^+\pi^-$ and suppressed $D^0 \to K^+\pi^-$ decays can be studied. Here, the total decay rate for the B^- decay is

$$\Gamma_{sup}(B^- \to DK^-) \propto r_B^2 + r_D^2 + 2 r_B r_D \cos(\delta_B - \delta_D - \gamma), \tag{3.9}$$

and for the B^+ decay it is

$$\Gamma_{fav}(B^+ \to DK^+) \propto \ 1 + r_B^2 r_D^2 + 2 r_B r_D \cos(\delta_B + \delta_D + \gamma). \tag{3.10}$$

Experimentally, these final states are measured using the ADS method [29, 30] developed by Atwood, Dunietz, and Soni, where the measured observables are a *CP* asymmetry and the ratio of the suppressed to favoured decay rates. The *CP* asymmetry is defined as

$$A_{\text{ADS}} \equiv \frac{\Gamma_{sup}(B^- \to DK^-) - \Gamma_{sup}(B^+ \to DK^+)}{\Gamma_{sup}(B^- \to DK^-) + \Gamma_{sup}(B^+ \to DK^+)}, \tag{3.11}$$

and related to the physical parameters as,

$$A_{\text{ADS}} = \frac{2 r_B r_D \sin(\delta_B - \delta_D) \sin\gamma}{r_B^2 + r_D^2 + 2 r_B r_D \cos(\delta_B - \delta_D) \cos\gamma}. \tag{3.12}$$

The ratio of the suppressed to favoured decay rates is defined as

$$R_{\text{ADS}} \equiv \frac{\Gamma_{sup}(B^- \to DK^-) + \Gamma_{sup}(B^+ \to DK^+)}{\Gamma_{fav}(B^- \to DK^-) + \Gamma_{fav}(B^+ \to DK^+)}, \tag{3.13}$$

and related to the physical parameters as,

$$R_{\text{ADS}} = \frac{r_B^2 + r_D^2 + 2 r_B r_D \cos(\delta_B - \delta_D) \cos\gamma}{1 + r_B^2 r_D^2 + 2 r_B r_D \cos(\delta_B + \delta_D) \cos\gamma}. \tag{3.14}$$

Unlike the GLW method, where the *CP*-eigenstates set the values of the D-decay hadronic parameters (r_D and δ_D), it is evident that the ADS method requires additional inputs for these [31, 32]. In both methods, the trigonometric relations between the measured *CP* observables and the physical parameters result in a four-fold symmetry, where (δ_B, γ) could be replaced by $(-\delta_B, \gamma)$, $(\delta_B, -\gamma)$, or $(-\delta_B, -\gamma)$ and give the same *CP* observables. Alternatively, self-conjugate final states can be measured which do not have this degeneracy. For example,

$D \to K^0_S\pi^+\pi^-$ and $D \to K^0_S K^+K^-$ decays which are the topic of this thesis. The K^0_S meson is a mass eigenstate and can be written in terms of the *CP*-eigenstates,

$$|K^0_S\rangle = \frac{1}{\sqrt{1+|\epsilon|^2}}(|K_1\rangle + \epsilon|K_2\rangle), \tag{3.15}$$

where, $K_{1(2)}$ are the *CP*-even(odd) eigenstates, and ϵ denotes indirect *CP*-violation in the kaon-sector which is approximately 2×10^{-3}. Therefore, the K^0_S meson is predominantly *CP*-even. In the final states, $D \to K^0_S\pi^+\pi^-$ and $D \to K^0_S K^+K^-$, under *CP*-conjugation, the momenta of the charged hadrons are exchanged, thus the $K^0_S\pi^+\pi^-$ and $K^0_S K^+K^-$ states are self-conjugate states.

They are also multi-body final states, and unlike the 2-body D decays, there are extra degrees of freedom in the decay. This leads to decay rates which can vary over the D-decay phase-space and means that in some regions of the phase space the *CP* asymmetry can be larger than in the global phase-space. Therefore, this provides greater sensitivity to γ, albeit with additional complexity to the analysis.

3.2 | Self-Conjugate Multi-Body D Final States

When studying multi-body D-decay final states, the phase space is parameterised depending on the degrees of freedom available in the decay. For $D \to K^0_S\pi^+\pi^-$ and $D \to K^0_S K^+K^-$ decays, commonly referred to together as $D \to K^0_S h^+h^-$ where $h = \{\pi, K\}$, the number of degrees of freedom is determined as follows. Given that each decay product has a corresponding four-momentum, there are 12 degrees of freedom. Conservation of four-momentum removes 4 degrees of freedom. Furthermore, since the D meson is a pseudoscalar meson ($J = 0$), the D

decay is isotropic, removing another 3 degrees of freedom. Finally, each decay product is required to have on-shell masses, and this removes another 3 degrees of freedom. These constraints result in 2 degrees of freedom, which in the case of $D \to K^0_S h^+ h^-$ decays are described using the squared invariant masses of the $K^0_S h^+$ and $K^0_S h^-$ systems, denoted $m^2(K^0_S h^+)$ and $m^2(K^0_S h^-)$, or m^2_+ and m^2_- for brevity.

These degrees of freedom can be visualised using Dalitz plots [33], as shown in Fig. 3.2, where the x and y axes are $m^2(K^0_S \pi^-)$ and $m^2(K^0_S \pi^+)$ respectively, and each point on the Dalitz plot represents a different kinematic final state. The boundary of the Dalitz plot is determined using the kinematic limits of the D decay. The vertical, horizontal, and diagonal bands across the Dalitz plot are caused by resonances, where the structure of these bands is dependent on the spin of an intermediary resonance. For example, in Fig. 3.2, the vertical band at $m^2(K^0_S \pi^-) \approx 0.8\,\text{GeV}^2/c^4$ is caused by the $K^*(892)^- \to K^0_S \pi^-$ resonance. The spin-1 nature of this resonance gives rise to the lobe-gap-lobe structure in the band, the gap being caused by the forbidden kinematic regions.

The decay rates for the B^+ and B^- decays at specific phase-space points can be written as

$$\begin{aligned}\Gamma(B^- \to DK^-) \propto\ & 1 + r_D^2(m^2_-, m^2_+) r_B^2 \\ & + 2 r_D(m^2_-, m^2_+) r_B [\cos(\delta_D(m^2_-, m^2_+)) \cos(\delta_B - \gamma) \\ & + \sin(\delta_D(m^2_-, m^2_+)) \sin(\delta_B - \gamma)],\end{aligned} \tag{3.16}$$

$$\begin{aligned}\Gamma(B^+ \to DK^+) \propto\ & r_D^2(m^2_-, m^2_+) + r_B^2 \\ & + 2 r_D(m^2_-, m^2_+) r_B [\cos(\delta_D(m^2_-, m^2_+)) \cos(\delta_B + \gamma) \\ & - \sin(\delta_D(m^2_-, m^2_+)) \sin(\delta_B + \gamma)],\end{aligned} \tag{3.17}$$

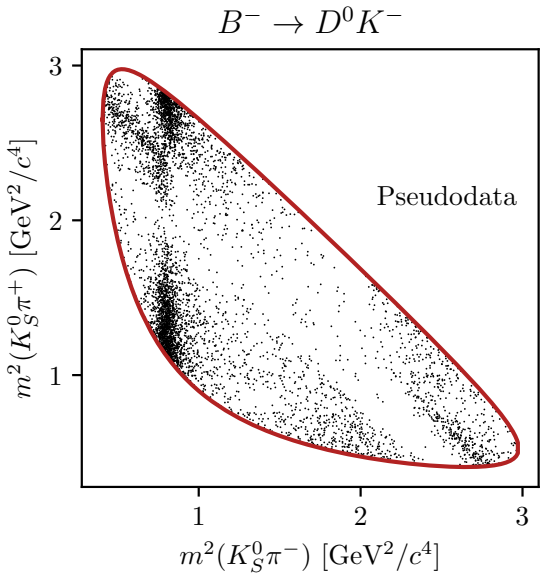

Figure 3.2: Dalitz plot for $B^- \to DK^-$ decays with $D \to K^0_S\pi^+\pi^-$ using pseudo-data.

where r_D and δ_D are written explicitly with dependence on m^2_- and m^2_+ as they vary over the Dalitz plot. The *CP*-conjugate of $B^- \to D^0K^-$ decays is $B^+ \to \overline{D}^0K^+$ decays, and the *CP*-conjugate of $D^0 \to K^0_S\pi^+\pi^-$ decays is $\overline{D}^0 \to K^0_S\pi^+\pi^-$ where the momenta of the charged pions are now swapped due to parity transformation. This means that the *CP*-conjugate for a decay at phase-space point (m^2_-, m^2_+) is found at (m^2_+, m^2_-). Therefore, *CP*-violation results in different decay rates, and hence different yields, between B^- and B^+ decays at opposite phase-space points on either side of the diagonal in the Dalitz plot where $m^2_- = m^2_+$. This is illustrated in Fig. 3.3, where it should be noted that the axes are swapped between the B^- and B^+ Dalitz plots.

In this thesis, $D \to K^0_S\pi^+\pi^-$ and $D \to K^0_SK^+K^-$ final states are studied using the BPGGSZ method [34–37], developed by Bondar, Poluektov, Giri, Grossman, Soffer, and Zupan.

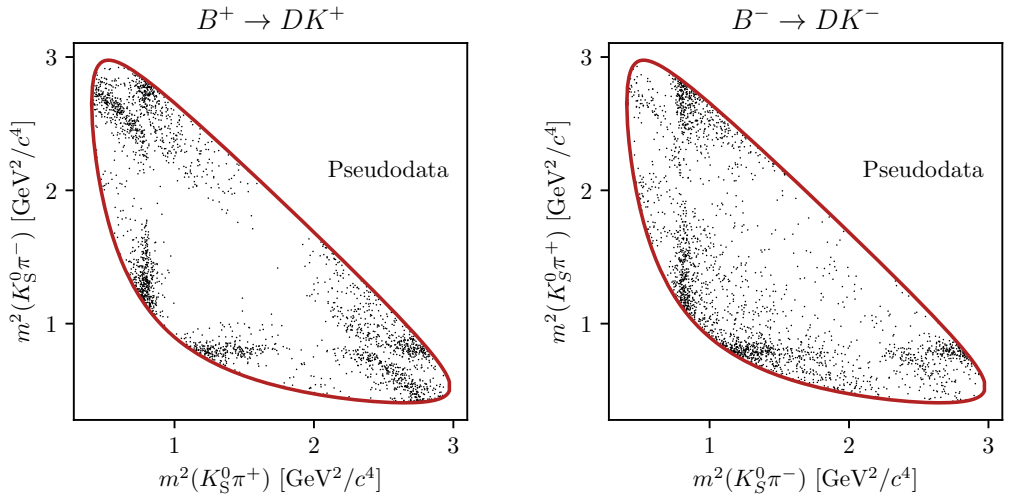

Figure 3.3: Dalitz plot for (left) $B^+ \to DK^+$ and (right) $B^- \to DK^-$ decays with $D \to K^0_S\pi^+\pi^-$ decays from pseudodata. Note the change of axes between the two plots.

3.3 | The BPGGSZ Method

To use the BPGGSZ method, the values of r_D and δ_D can be determined from an amplitude model for the D-decay or measured using coefficients related to the D-decay. In this thesis, the latter, the model-independent approach, is favoured.

First, this is because an amplitude model is determined through a fit to flavour-tagged $D^{*\pm}$ data. These data provide an intensity distribution, which is proportional to the modulus-squared of the amplitude, meaning phase information is absorbed. Therefore, there is no direct access to strong-phase information. The data are fitted using an isobar model where the amplitude model is approximated as a sum of resonant contributions and a non-resonant contribution. This means that the intensity distribution can be modelled well by altering the amplitude model. Components can be added or removed, or alternative methods, such as the K-matrix method [38], can be used until good agreement is achieved with

data. The phase information in data, however, cannot be checked in this way since it is not accessible.

In addition, because the amplitude model can be altered in different ways, the uncertainty on γ due to the model can be assessed in different ways as well. Alternative components can be considered in the isobar model, or an alternative methods, such as the K-matrix method [38], can be used. The choice in variation significantly changes the associated systematic uncertainty, and is a choice made by the analyst, but not one based on the phase agreement.

The model-independent approach avoids these problems. As will be detailed below, parameters related to the D-decay (denoted c_i and s_i) are measured by separate experiments and input to a γ measurement. To be able to use these measurements, the Dalitz plot must be divided into bins, which reduces the statistical precision on γ by 10% compared to the unbinned model-dependent approach [36]. This is an acceptable compromise given the more reliable inputs and estimate of systematic uncertainty. It should be noted that it is also possible to employ an unbinned model-independent approach [39], though the viability of this method on real data is yet to be proven.

To divide the Dalitz plots into bins, one of the simplest binning schemes is shown in Fig. 3.4 from Ref. [35]. These bins are labelled using indices, i, such that bins where $m^2_- > m^2_+$ are referred to as the $+i^{\text{th}}$ bins and those where $m^2_+ > m^2_-$ are referred to as the $-i^{\text{th}}$ bins. Thus, under CP-transformation a $B^- \to D^0 K^-$ decay in bin i becomes a $B^+ \to \overline{D}^0 K^+$ decay in bin $-i$.

The B^+ and B^- decay rates, from Eqs. 3.16 and 3.17, can be integrated over a

Dalitz plot bin, i, yielding

$$\Gamma_i(B^- \to DK^-) \propto K_i + r_B^2 K_{-i} + 2r_B\sqrt{K_i K_{-i}}[c_i \cos(\delta_B + \gamma) + s_i \sin(\delta_B + \gamma)], \tag{3.18a}$$

$$\Gamma_i(B^+ \to DK^+) \propto K_{-i} + r_B^2 K_i + 2r_B\sqrt{K_i K_{-i}}[c_i \cos(\delta_B - \gamma) - s_i \sin(\delta_B - \gamma)], \tag{3.18b}$$

where K_i is the fractional yield of a flavour-tagged D^0 decay in bin i and is defined as

$$K_i \equiv \frac{\int_i \mathrm{d}s^2 \left|\mathcal{A}_D\right|^2}{\int \mathrm{d}s^2 \left|\mathcal{A}_D\right|^2}, \tag{3.19}$$

where $\int_i \mathrm{d}s^2$ denotes integration over the phase space of the i^{th} Dalitz plot bin. Since *CP*-violation in the D decay is ignored, the fractional yield for a flavour-tagged D^0 decay in bin i is identical to that of a flavour-tagged $\overline{D}^0$ decay in bin $-i$.

The c_i and s_i values are strong-phase input parameters defined as

$$c_i \equiv \frac{\int_i \mathrm{d}s^2 \left|\mathcal{A}_D\right| \left|\mathcal{A}_{\overline{D}}\right| \cos(\delta_D)}{\sqrt{\int_i \mathrm{d}s^2 \left|\mathcal{A}_D\right|^2 \int_i \mathrm{d}s^2 \left|\mathcal{A}_{\overline{D}}\right|^2}}, \tag{3.20a}$$

$$s_i \equiv \frac{\int_i \mathrm{d}s^2 \left|\mathcal{A}_D\right| \left|\mathcal{A}_{\overline{D}}\right| \sin(\delta_D)}{\sqrt{\int_i \mathrm{d}s^2 \left|\mathcal{A}_D\right|^2 \int_i \mathrm{d}s^2 \left|\mathcal{A}_{\overline{D}}\right|^2}}. \tag{3.20b}$$

These are the amplitude-weighted averages of the cosine and sine of δ_D. To *CP*-transform the D decay, $\mathcal{A}_D$ is replaced by $\mathcal{A}_{\overline{D}}$, and vice versa, and δ_D is replaced by $-\delta_D$. As *CP*-violation in the D decay is ignored, this means that $c_{+i} = c_{-i}$ and $s_{+i} = -s_{-i}$.

The Dalitz plot binning scheme shown in Fig. 3.4 was initially proposed due to its simplicity, but it can be optimised for sensitivity to γ, as detailed in Ref. [40]. The resulting binning scheme with $\mathcal{N} = 8$ Dalitz plot bins for $i = -\mathcal{N}$ to $i = \mathcal{N}$,

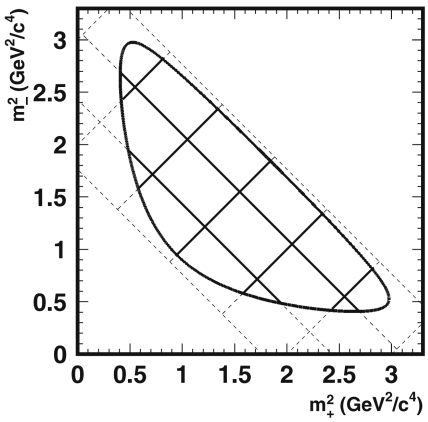

Figure 3.4: The binning of the Dalitz plot for $D \to K^0_S\pi^+\pi^-$ decays, as found in Ref. [35].

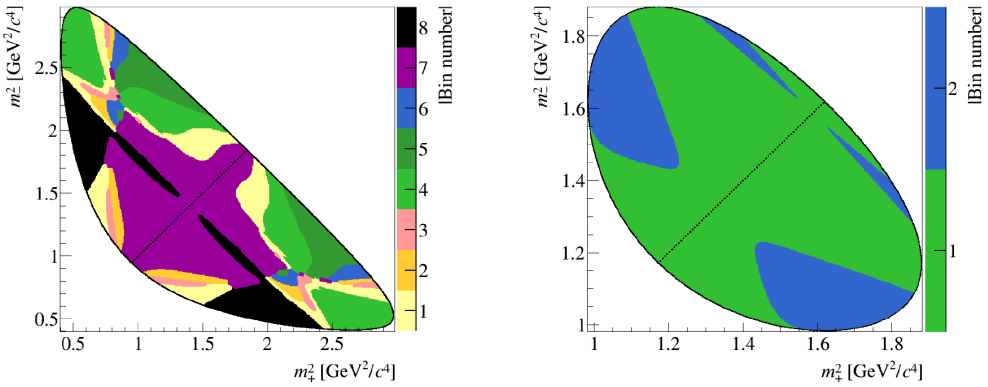

Figure 3.5: The Dalitz plot binning schemes for $D \to K^0_S\pi^+\pi^-$ (left) and $D \to K^0_S K^+K^-$ (right) decays, as determined in Ref. [40].

excluding $i = 0$, for the $D \to K^0_S\pi^+\pi^-$ mode is shown on the left of Fig. 3.5 and is called the 'optimal' binning scheme. For the $D \to K^0_S K^+K^-$ mode, the optimisation procedure results in the '2-bins' binning scheme, shown on the right of Fig. 3.5.

For each of these Dalitz plot bins, the c_i and s_i input values are needed and are taken from a combination of measurements by CLEO [41] and BESIII [42,43] as found in Refs. [42,43] and shown in Tab. 3.1. The CLEO and BESIII collabora-

tions make these measurements using e^+e^- collisions at the $\psi(3770)$ resonance, which is the threshold for $c\bar{c}$ production and has $C = -1$. At this resonance, the predominant decay is to $D\overline{D}$ pairs via the strong interaction. As this is a strong interaction, the quantum number C is conserved and the $D\overline{D}$ pair is quantum-correlated. Since there are no other decay products, the C value of the $D\overline{D}$ pair can be known. This is, therefore, an entangled state which has direct access to phase information.

Using $D\overline{D}$ pairs produced at CLEO and BESIII, by tagging the flavour or *CP* eigenstate of one of the D mesons, the flavour or *CP* eigenstate of the other D meson collapses. This other D meson is subsequently reconstructed in the desired $D \to K^0_S\pi^+\pi^-$ or $D \to K^0_S K^+K^-$ final state and enables measurements of the strong-phase inputs as follows.

1. By tagging the flavour of one of the D mesons using, for instance, Cabibbo-favoured $D^0 \to K^-\pi^+$ decays, the other D meson can be reconstructed as $\overline{D}^0 \to K^0_S\pi^+\pi^-$, where its yield is proportional to K_i [41].

2. By tagging the *CP*-eigenstate of one of the D mesons using, for instance, $D_{CP+} \to K^+K^-$, the other D meson is reconstructed as $D_{CP-} \to K^0_S\pi^+\pi^-$, and the yield per Dalitz plot bin is [41]

$$M_i \propto K_i + K_{-i} + 2\sqrt{K_i K_{-i}}c_i. \tag{3.21}$$

3. Finally, both D mesons can be reconstructed as $D \to K^0_S\pi^+\pi^-$, where each D meson is a superposition of the D^0 and $\overline{D}^0$ states, leading to interference. The event rate for one D meson decaying in bin i and the other in bin j is

given as [41],

$$M_{ij} \propto K_i K_{-j} + K_j K_{-i} - 2\sqrt{K_i K_{-i} K_j K_{-j}}(c_i c_j + s_i s_j). \tag{3.22}$$

Following this procedure, by studying a variety of flavour and *CP* tags, the c_i and s_i values can be measured.

Thus far, the BPGGSZ formalism has been described using $B^{\pm} \to DK^{\pm}$ decays. The topic of this thesis is a measurement of *CP*-violation in $B^{\pm} \to D^* K^{\pm}$ decays. Therefore, extra considerations regarding the presence of the D^* decay are necessary.

Table 3.1: Combination of measured c_i and s_i values from CLEO and BESIII, from Refs. [42, 43], for $D \to K^0_S\pi^+\pi^-$ decays in the 'optimal' binning scheme and for $D \to K^0_S K^+K^-$ decays in the '2-bins' binning scheme. Note that there is a change of sign convention between LHCb measurements and the s_i values as presented in Refs. [42, 43].

Dalitz plot bin	c_i	s_i
$D \to K^0_S\pi^+\pi^-$		
1	–0.037 ± 0.049	0.829 ± 0.097
2	0.837 ± 0.067	0.286 ± 0.152
3	0.147 ± 0.066	0.786 ± 0.154
4	–0.905 ± 0.021	0.79 ± 0.059
5	–0.291 ± 0.041	–1.022 ± 0.064
6	0.272 ± 0.082	–0.977 ± 0.176
7	0.918 ± 0.017	–0.184 ± 0.065
8	0.773 ± 0.033	0.277 ± 0.118
$D \to K^0_S K^+K^-$		
1	0.713 ± 0.032	–0.107 ± 0.132
2	–0.758 ± 0.037	–0.394 ± 0.173

3.4 | Measuring γ with $B^\pm \to D^*K^\pm$ Decays

This thesis measures *CP*-violation in $B^\pm \to D^*K^\pm$ decays followed by subsequent $D^* \to D\pi^0$ and $D^* \to D\gamma$ decays. Therefore, instead of two decay rate equations as in Eq. 3.18, there are four equations. To deduce these, the interference diagrams for the $B^\pm \to D^*K^\pm$ decays with intermediate $D^* \to D\pi^0$ and $D^* \to D\gamma$ decays are shown in Fig. 3.6. In this figure, the r_B parameter is defined as,

$$r_B \equiv \frac{|\mathcal{A}(B^- \to \overline{D}^{*0}K^-)|}{|\mathcal{A}(B^- \to D^{*0}K^-)|} \equiv \frac{|\mathcal{A}(B^+ \to D^{*0}K^+)|}{|\mathcal{A}(B^+ \to \overline{D}^{*0}K^+)|}, \tag{3.23}$$

and δ_B is the strong-phase difference between the two B^-, or B^+, decays. These values are different compared to those for $B^\pm \to DK^\pm$ decays since they param-

eterise a different B decay.

In Fig. 3.6, there is a factor of -1 between the B decay amplitudes when there are intermediate $D^* \to D\gamma$ decays. This derives from the CP eigenvalues of the D^* meson and its decay products, as detailed in Ref. [44], and is summarised here. Using the convention where $\hat{CP}|D^{*0}\rangle = |\overline{D}^{*0}\rangle$ and $\hat{CP}|\overline{D}^{*0}\rangle = |D^{*0}\rangle$, the CP-eigenstates of the D^* mesons can be written as

$$\mathcal{A}_{D^*{}_{CP_+}} = \frac{\mathcal{A}_{D^{*0}} + \mathcal{A}_{\overline{D}^{*0}}}{\sqrt{2}}, \tag{3.24a}$$

$$\mathcal{A}_{D^*{}_{CP_-}} = \frac{\mathcal{A}_{D^{*0}} - \mathcal{A}_{\overline{D}^{*0}}}{\sqrt{2}}. \tag{3.24b}$$

Therefore, taking for example B^- decays, the amplitude,

$$\mathcal{A}(B^- \to D^*K^-) = \mathcal{A}_B(\mathcal{A}_{D^{*0}} + r_B e^{i(\delta_B - \gamma)}\mathcal{A}_{\overline{D}^{*0}}), \tag{3.25a}$$

can be written as

$$\mathcal{A}(B^- \to D^*K^-) = \mathcal{A}_B\left(\frac{\mathcal{A}_{D^*{}_{CP+}} + \mathcal{A}_{D^*{}_{CP-}}}{\sqrt{2}} + r_B e^{i(\delta_B-\gamma)}\frac{\mathcal{A}_{D^*{}_{CP+}} - \mathcal{A}_{D^*{}_{CP-}}}{\sqrt{2}}\right). \tag{3.26a}$$

For $D^* \to D\pi^0$ decays, the CP-eigenvalue of the D^* meson is

$$\eta_{D^*} = \eta_D \times \eta_{\pi^0} \times (-1)^L, \tag{3.27}$$

where $\eta_{\pi^0} = -1$, thus $L = 1$ due to angular momentum conservation, and $D^*{}_{CP\pm} \to D_{CP\pm}\pi^0$. For $D^* \to D\gamma$ decays,

$$\eta_{D^*} = \eta_D \times \eta_\gamma \times (-1)^L, \tag{3.28}$$

where $\eta_\gamma = +1$, thus $L = 1$ due to parity conservation, and $D^*{}_{CP\pm} \to D_{CP\mp}\gamma$.

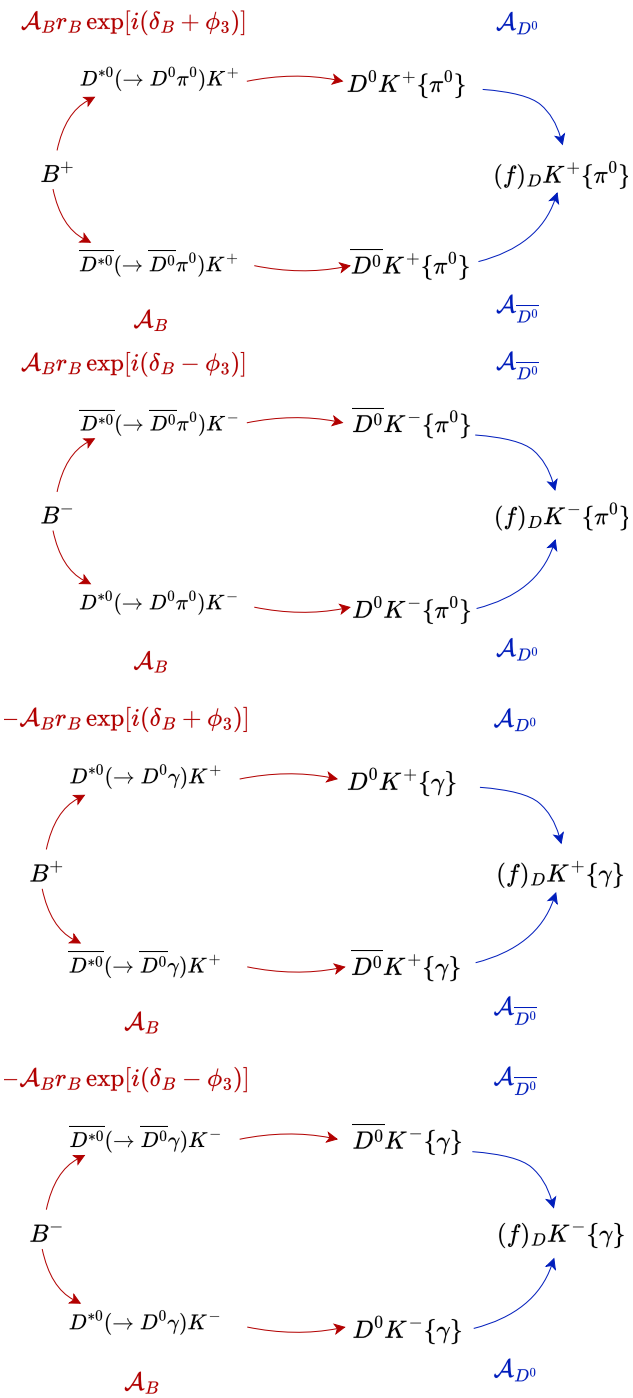

Figure 3.6: Interference diagrams (from top to bottom) for B^+ and B^- decays with intermediate $D^* \to D\pi^0$ decays, and B^+ and B^- decays with intermediate $D^* \to D\gamma$ decays. Amplitudes labelled in red correspond to the decay path shown by the red arrows, and amplitudes labelled in blue correspond to the blue arrows. For clarity, CKM angle γ is denoted ϕ_3, and photons are denoted γ.

Therefore, for an intermediate $D^* \to D\pi^0$ decay, the B^- amplitude can be written in terms of the D meson amplitudes as,

$$\mathcal{A}(B^- \to D^*K^-) \propto \mathcal{A}_B \left(\frac{\mathcal{A}_{D_{CP+}} + \mathcal{A}_{D_{CP-}}}{\sqrt{2}} + r_B e^{i(\delta_B - \gamma)} \frac{\mathcal{A}_{D_{CP+}} - \mathcal{A}_{D_{CP-}}}{\sqrt{2}} \right) \tag{3.29a}$$

$$= \mathcal{A}_B(\mathcal{A}_{D^0} + r_B e^{i(\delta_B - \gamma)} \mathcal{A}_{\overline{D}^0}). \tag{3.29b}$$

For an intermediate $D^* \to D\gamma$ decay, the B^- amplitude can be written as,

$$\mathcal{A}(B^- \to D^*K^-) \propto \mathcal{A}_B \left(\frac{\mathcal{A}_{D_{CP-}} + \mathcal{A}_{D_{CP+}}}{\sqrt{2}} + r_B e^{i(\delta_B - \gamma)} \frac{\mathcal{A}_{D_{CP-}} - \mathcal{A}_{D_{CP+}}}{\sqrt{2}} \right) \tag{3.30a}$$

$$= \mathcal{A}_B(\mathcal{A}_{D^0} - r_B e^{i(\delta_B - \gamma)} \mathcal{A}_{\overline{D}^0}). \tag{3.30b}$$

This results in a change of sign, highlighted in red, between Eqs. 3.29b and 3.30b, due to the intermediate D^* decay.

Propagating this to the B^+ and B^- decay rates in Eq. 3.18, for intermediate $D^* \to D\pi^0$ decays this leads to

$$\Gamma_i^+ = K_{-i} + r_B^2 K_{+i} + 2r_B \sqrt{K_{-i}K_{+i}}[c_i \cos(\delta_B + \gamma) - s_i \sin(\delta_B + \gamma)], \tag{3.31a}$$

$$\Gamma_i^- = K_{+i} + r_B^2 K_{-i} + 2r_B \sqrt{K_{+i}K_{-i}}[c_i \cos(\delta_B - \gamma) + s_i \sin(\delta_B - \gamma)], \tag{3.31b}$$

and for intermediate $D^* \to D\gamma$ decays, this is

$$\Gamma_i^+ = K_{-i} + r_B^2 K_{+i} - 2r_B \sqrt{K_{-i}K_{+i}}[c_i \cos(\delta_B + \gamma) - s_i \sin(\delta_B + \gamma)], \tag{3.32a}$$

$$\Gamma_i^- = K_{+i} + r_B^2 K_{-i} - 2r_B \sqrt{K_{+i}K_{-i}}[c_i \cos(\delta_B - \gamma) + s_i \sin(\delta_B - \gamma)]. \tag{3.32b}$$

Yield equations are then extracted by integrating over the decay time, therefore for intermediate $D^* \to D\pi^0$ decays this results in

$$N_i^+ = h_B^+(K_{-i} + r_B^2 K_{+i} + 2r_B \sqrt{K_{-i}K_{+i}}[c_i \cos(\delta_B + \gamma) - s_i \sin(\delta_B + \gamma)]), \tag{3.33a}$$

$$N_i^- = h_B^-(K_{+i} + r_B^2 K_{-i} + 2r_B \sqrt{K_{+i}K_{-i}}[c_i \cos(\delta_B - \gamma) + s_i \sin(\delta_B - \gamma)]), \tag{3.33b}$$

and for intermediate $D^* \to D\gamma$ decays, this is

$$N_i^+ = h_B^+ (K_{-i} + r_B^2 K_{+i} - 2r_B \sqrt{K_{-i}K_{+i}}[c_i \cos(\delta_B + \gamma) - s_i \sin(\delta_B + \gamma)]), \quad (3.34a)$$

$$N_i^- = h_B^- (K_{+i} + r_B^2 K_{-i} - 2r_B \sqrt{K_{+i}K_{-i}}[c_i \cos(\delta_B - \gamma) + s_i \sin(\delta_B - \gamma)]), \quad (3.34b)$$

where $h_B^\pm$ are normalisation constants for the B^+ and B^- decays. These normalisation constants include sensitivity to γ via the phase-space integrated B^+ and B^- yields, similarly to the global asymmetries for the 2-body D-decay final states.

3.5 | Previous γ Measurements

The current world average for γ from direct measurements is $\gamma = (65.9^{+3.3}_{-3.5})^\circ$, as determined by CKMFitter [24]. There are a range of decay modes which contribute to this, for example $B \to D^{(*)}K^{(*)}$ decays from both charged and neutral B mesons, to name a few. However, the sensitivity to γ is overwhelmingly dominated by $B^\pm \to DK^\pm$ decays, which alone have a sensitivity of 4° [45,46].

The measurement of CP-violation in $B^\pm \to DK^\pm$ decays is dominated by two LHCb measurements [45,46]. Reference [45] studied the $D \to K^0_S h^+ h^-$ final states and Ref. [46] studied the 2-body D-decay final states. The sensitivity of the $B^\pm \to DK^\pm$ mode to γ is driven by its r_B^{DK} value. This hadronic parameter controls the level of interference in the decays through which γ is measured. At a value of 0.1 [47], r_B^{DK} is relatively large, and paired with its relatively high branching ratio compared to other B decays, 3.64×10^{-4} [18], leads to a golden decay mode to measure γ.

The $B^\pm \to D^*K^\pm$ mode is expected to be equally as sensitive to γ, since its $r_B^{D^*K}$ value is expected to also be approximately 0.1 [47], and its branching ratio is

15% larger [18]. At the start of the work for this thesis, the $B^{\pm} \to D^{*}K^{\pm}$ mode had not been fully exploited. The following sections present an overview of measurements of γ made using the $B^{\pm} \to D^{*}K^{\pm}$ mode, and motivate the measurement presented in this thesis.

3.5.1 | Belle and BaBar

Measurements of *CP*-violation in $B^{\pm} \to D^{*}K^{\pm}$ decays have been performed by the Belle [48] and BaBar [49] collaborations, which analysed data from $e^{+}e^{-}$ collisions at the $\Upsilon(4S)$ resonance, the threshold for $b\bar{b}$ production. These studied the $D \to K^{0}_{S}\pi^{+}\pi^{-}$ final state, and in the case of BaBar also the $D \to K^{0}_{S}K^{+}K^{-}$ final state. In conjunction with measurements of $B^{\pm} \to D^{*}K^{\pm}$ decays, they also considered $B^{\pm} \to DK^{\pm}$, and also $B^{\pm} \to DK^{*\pm}$ decays at BaBar. This resulted in determinations of γ shown in Tab. 3.2. In this table, the uncertainties on γ are divided into statistical, experimental systematic and model-related systematic components. The latter is due to the use of the model-dependent approach, where amplitude models for $D \to K^{0}_{S}\pi^{+}\pi^{-}$ [48] and $D \to K^{0}_{S}K^{+}K^{-}$ [50] are used to determine values of r_D and δ_D. The subjectivity in the use of this approach is evidenced by the disparity between these uncertainties in the Belle and BaBar measurements, as shown in Tab. 3.2, with a conservative estimate from Belle at 9°, and a much smaller estimate from BaBar at 3°. In both measurements, the amplitude models were determined using similarly sized datasets, and therefore the statistical uncertainties on the models were similar. It is the subjectivity of the model-dependent method which led to very different model-related uncertainties on γ.

Table 3.2: Results for the CKM angle γ from Belle [48] and BaBar [49] analyses of $B^{\pm} \to D^{(*)}K^{(*)\pm}$ decays. The first uncertainty is statistical, the second is the experimental systematic uncertainty, and the third is the model-related uncertainty.

	$\gamma(^\circ)$
Belle	$78\ ^{+11}_{-12} \pm 4 \pm 9$
BaBar	$68 \pm 14 \pm 4 \pm 3$

3.5.2 | LHCb: $B^{\pm} \to D^{*}K^{\pm}$ and 2-body D final states

At the start of the work for this thesis, there was only one *CP*-violation measurement by the LHCb collaboration studying $B^{\pm} \to D^{*}K^{\pm}$ decays, and this considered 2-body D-decay final states [46]. The ADS and GLW methods discussed in Sec. 3.1 were used to measure *CP*-violation, where the observables are *CP* asymmetries and ratios. The trigonometric relation between these measured observables and the physical parameters ($r_B^{D^*K}$, $\delta_B^{D^*K}$, and γ) lead to a four-fold symmetry, as shown in Fig. 3.7. To break this degeneracy and, most importantly, to fully exploit $B^{\pm} \to D^{*}K^{\pm}$ mode, a study with self-conjugate $D \to K^0_S h^+ h^-$ final states was necessary.

3.5.3 | LHCb: $B^{\pm} \to D^{*}K^{\pm}$ and $D \to K^0_S h^+ h^-$ final states

Considering the status of measurements at the time of starting the work for this thesis, a study of $B^{\pm} \to D^{*}K^{\pm}$ decays with the $D \to K^0_S h^+ h^-$ final states by the LHCb collaboration was imminent. To tackle this, two studies began work on this mode concurrently, differing in analysis strategy based on the reconstruction of the D^* decay. One of these is Ref. [51], where the neutral pion and photon from the D^* decays are reconstructed. The second does not reconstruct these light neutral particles, and is the work presented in this thesis.

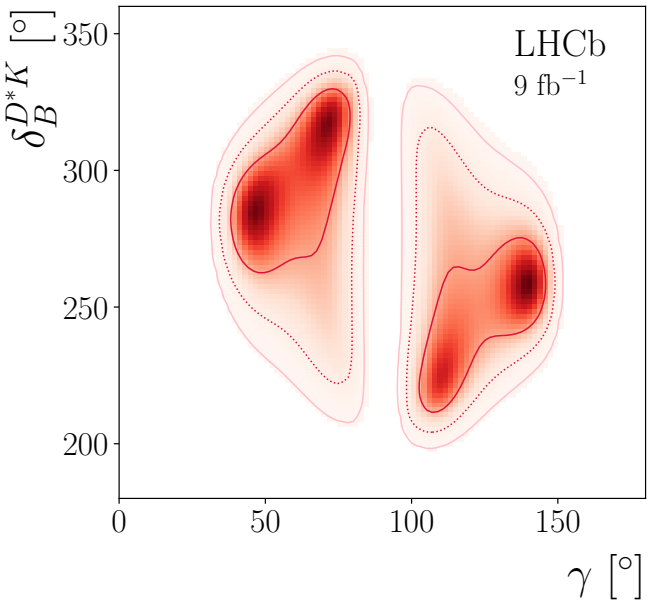

Figure 3.7: Results from Ref. [46], which studied $B^{\pm} \to D^* K^{\pm}$ decays with 2-body D-decay final states, showing the 68.3%, 95.5%, and 99.7% confidence regions for $\delta_B^{D^*K}$ vs. γ and indicating the four-fold symmetry in the solutions.

4

The LHCb experiment

The Large Hadron Collider beauty (LHCb) experiment is designed as a heavy flavour physics experiment at the Large Hadron Collider (LHC) at CERN [52]. The CERN accelerator complex is depicted in Fig. 4.1. Hydrogen atoms are ionised to produce protons which are accelerated from rest to 50 MeV by LINAC 2 (Linear Accelerator 2), and then further accelerated to 1.4 GeV by the BOOSTER (Proton Synchrotron Booster) [52]. Protons are then accelerated in the PS (Proton Synchrotron) to 25 GeV, followed by the SPS (Super Proton Synchrotron) to 450 GeV, at which stage they are injected into the LHC machine in bunches of up to $\mathcal{O}(10^{11})$ protons [52]. They then circulate around the 27 km ring for approximately 12 hours (which is called a fill). The proton beams are bent by dipole magnets and focused by quadrupole magnets and boosted to their final energies by RF (radiofrequency) cavities [52]. During a fill, beams travelling in opposite directions collide at a frequency of 40 MHz [52] at four points along the ring where experiments are located. These are the ATLAS, CMS, ALICE, and LHCb experiments. During 2011 and 2012 (collectively called Run 1), LHCb collected data at centre-of-mass collision energies of 7 and 8 TeV, respectively, and during

2015–2018 (Run 2) at 13 TeV.

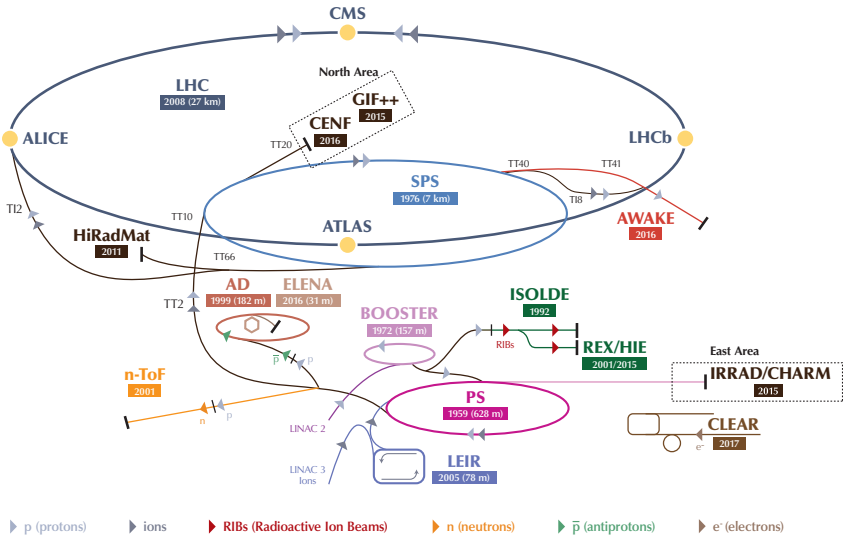

Figure 4.1: The CERN accelerator complex, as presented in Ref. [53]. The parts relevant to pp collisions at LHCb are the LINAC 2, BOOSTER, PS, SPS, and the LHC machine.

4.1 | The LHCb detector

The LHCb detector is shown in Fig. 4.2 in a right-handed coordinate system where the origin is at the interaction point, the beam line is along the z-axis, the x-axis points into the page, and the y-axis points upwards. The detector is a single-arm forward spectrometer with pseudorapidity coverage $1.6 < \eta < 4.9$ [54], where $\eta = -\ln(\tan(\theta/2))$. The parameter θ is the angle with respect to the beam line in the x and y directions. The detector acceptance covers 15–300 mrad in the x direction and 15–250 mrad in the y direction. This geometry facilitates the study of b and c quarks since, as shown in Fig. 4.3, the $b\bar{b}$ production cross-section

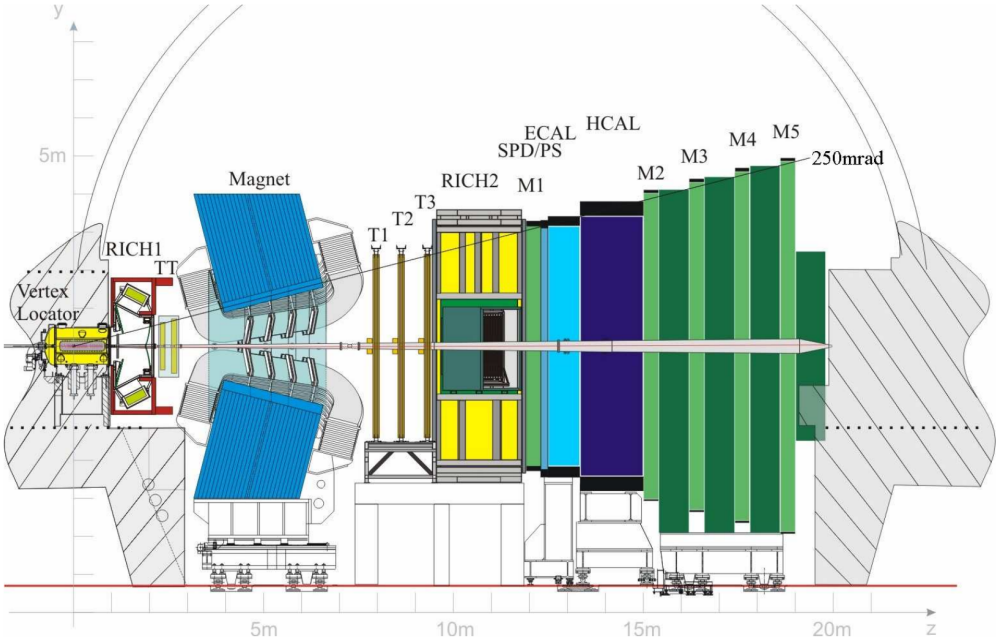

Figure 4.2: Side-view of the LHCb detector, as found in Ref. [54], in a right-handed coordinate system where the origin is at the interaction point and the beam line is along the z-axis. Sub-detectors are labelled.

peaks in the forward (and backward) region which is enclosed by the detector acceptance.

As a heavy flavour physics experiment, good vertex resolution is necessary because displaced vertices are a signature of b and c-hadron decays. To ensure this, luminosity-levelling is used. This is when the transverse overlap of colliding beams is adjusted to ensure roughly constant luminosity [56], as shown in Fig. 4.4. It leads to a relatively lower luminosity than other LHC experiments, with only 1 pp collision per bunch-crossing, and therefore smaller data samples. For example, the Run 1 and Run 2 combined dataset collected by LHCb has a total integrated luminosity of $9\,\text{fb}^{-1}$, whereas that collected by ATLAS in Run 2 alone was $140\,\text{fb}^{-1}$. Using luminosity-levelling, the datasets at LHCb are smaller

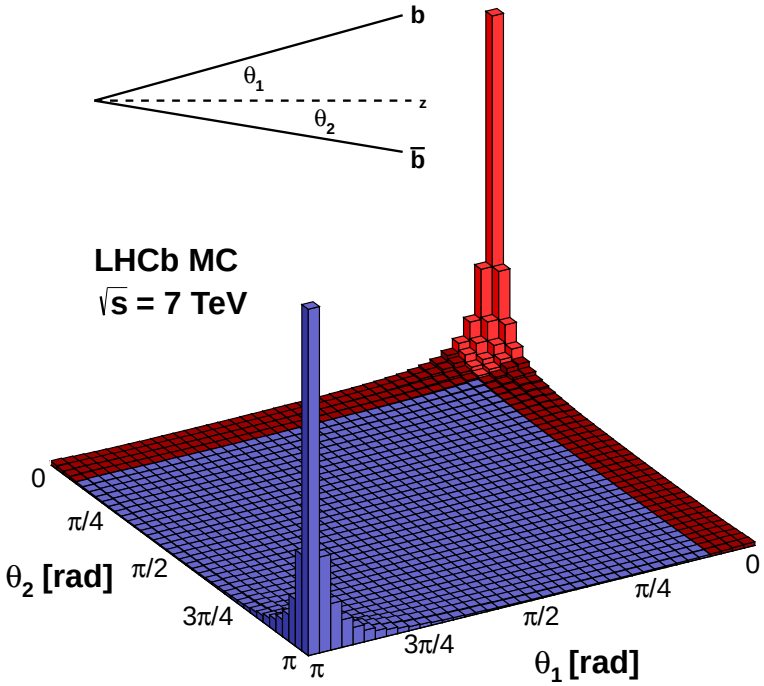

Figure 4.3: The $b\bar{b}$ production cross-section and detector acceptance at LHCb (highlighted in red) as found in Ref. [55].

but include less pile-up. These are soft pp collisions and reducing them leads to a cleaner environment for reconstructing events.

The following sections describe the different sub-detectors at LHCb with a focus on reliable tracking and particle identification since these are vital to the measurement in this thesis.

4.1.1 | Tracking

The tracking system measures tracks formed by the path of charged particles from which the charges and momenta of these particles are deduced. There are four parts of the LHCb detector needed for this; the vertex locator (VELO), the

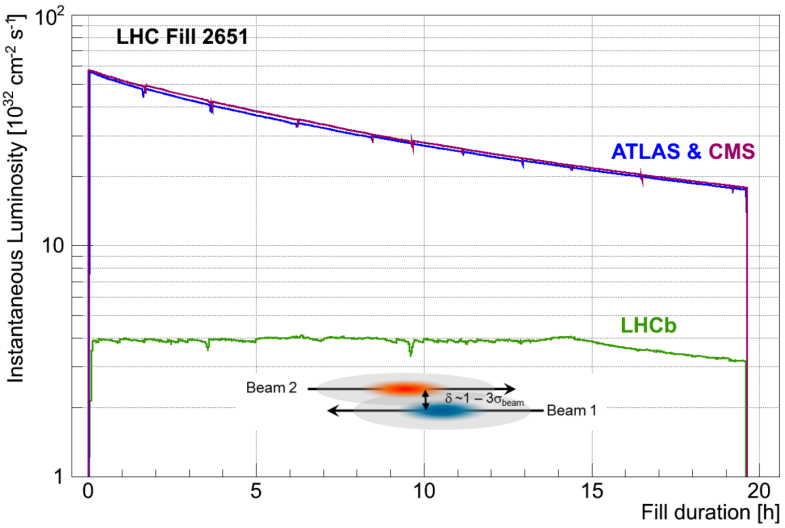

Figure 4.4: Roughly constant instantaneous luminosity as a function of fill duration at LHCb, compared to ATLAS and CMS, achieved using luminosity-levelling, as presented in Ref. [56].

tracker turicensis (TT), the magnet, and three downstream tracking stations (T1–T3).

4.1.1.1 | Vertex Locator

The VELO is the closest part of the detector to the interaction region, as shown in the leftmost part of Fig. 4.2. A cross-section of the VELO stations is shown at the top of Fig. 4.5 from Ref. [54]. Each station consists of a left and right detector module on either side of the beam axis. This, in turn, consists of R and ϕ sensors to measure the radial distance and azimuthal angle of a vertex from the beam line, as shown on the bottom of Fig. 4.5. The R and ϕ sensors are composed of silicon strip detectors (semiconductor detectors) oriented as concentric semi-circular strips for resolution in R, or oriented radially outward for resolution in ϕ. This resolution is improved by reducing the pitch (width) of sensors closest

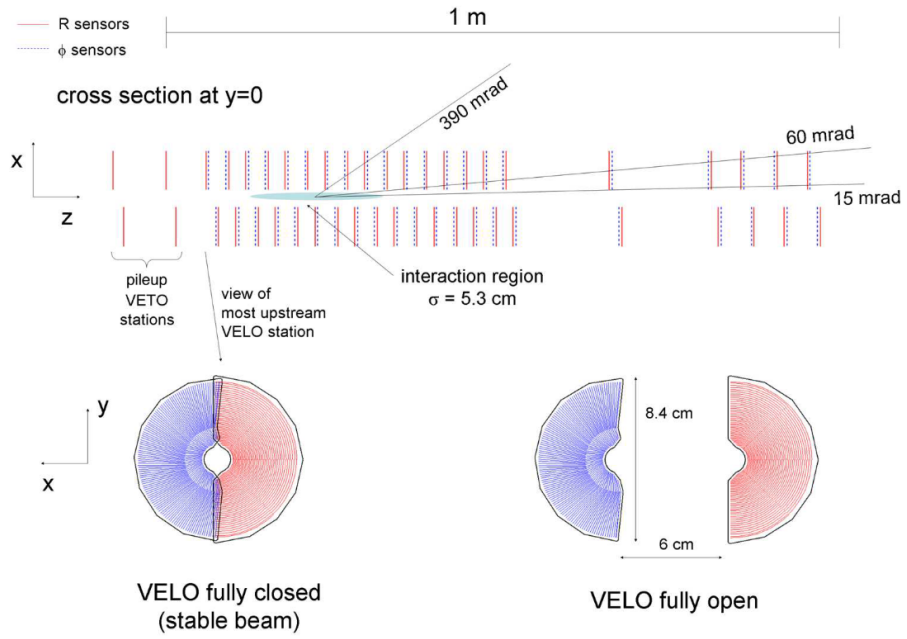

Figure 4.5: Figures from Ref. [54] of (top) a view from above of the VELO stations with left and right modules on either side of the beam line along the z-axis, with alternating R sensors (in red) and ϕ sensors (in blue), and (bottom) a view along the beam pipe of the R and ϕ sensors when the VELO is (left) closed and (right) open.

to the beam. To achieve good flight distance measurements, the left and right modules must be located as close as possible to the beam. They are held 8 mm from the beam during physics running, but for safety they are retracted to 3 cm during beam injection [57]. This is illustrated at the bottom of Fig. 4.5.

This detector design enables excellent vertex resolution with a typical primary vertex (PV) resolution in the transverse plane of 10 µm and 50 µm along the beam axis [58]. This facilitates measurements of impact parameter, defined as the distance of closest approach between a track and its PV. For a particle with transverse momentum greater than 1 GeV/c, the impact parameter can be measured with a resolution of 35 µm [58].

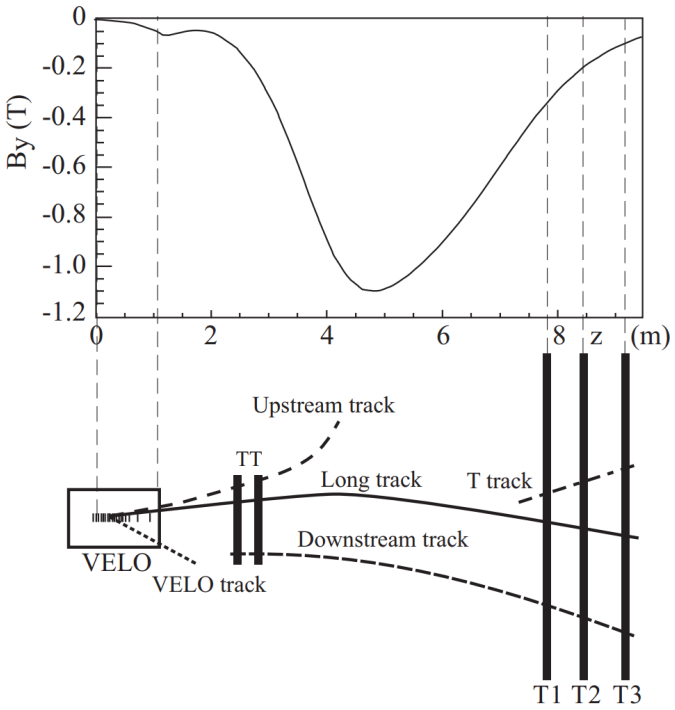

Figure 4.6: Variations of the magnetic field over the tracking system, as presented in Ref. [58], with a diagram of the different track types depending on their reconstruction.

4.1.1.2 | Magnet

To make momentum measurements, a non-superconducting dipole magnet with a maximum field strength of 1 T [58] in the y-direction provides a total bending power of around 4 T m in the $x - z$ plane [59]. The magnet consists of aluminium coils around an iron yoke, and is positioned between the TT and T1–T3. This results in a magnetic field over the tracking system as shown in Fig. 4.6.

Since the magnet deflects charged particles in the $x - z$ plane, if there are variations between the left and right halves of the detector, this will result in detection asymmetries. Therefore, the LHCb experiment collects data in one of two magnet configurations, 'up' or 'down', depending on the direction of the

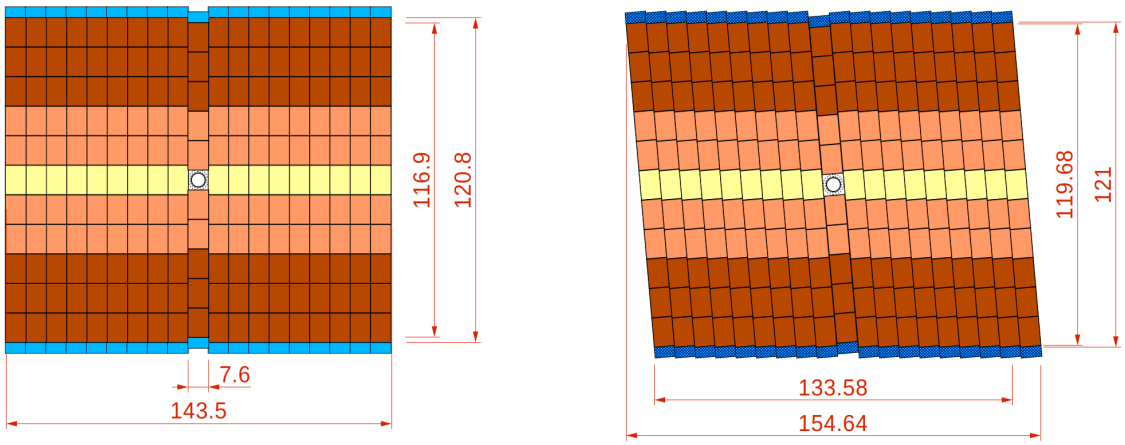

Figure 4.7: Cross-sections of (left) an x-layer and (right) a u-layer in the TT, as provided in Ref. [60].

magnetic field. This allows control over the detection asymmetries to a precision of 10^{-3} [58].

4.1.1.3 | Tracking Stations

The Tracker Turicensis (TT) is upstream of the magnet and consists of four layers of silicon micro-strip detectors in an $x - u - v - x$ geometry, where the x layers have vertical strips and strips in the second and third layers are rotated by a stereo angle $+5°$ and $-5°$ [60], as shown in Fig. 4.7. With a strip pitch of around 200 µm [60], the TT has a spatial resolution of approximately 50 µm [58].

The T1–T3 tracking stations are downstream of the magnet and consist of an Inner Tracker (IT) close to the beam, as shown in Fig. 4.8, and an Outer Tracker (OT) for the outer regions, as shown in Fig. 4.9. The IT uses the same silicon microstrip detectors as the TT, but the OT is a straw-tube detector. As shown in Fig. 4.9, each tracking station is made up of 4 modules in an $x - u - v - x$ geometry, where each module consists of two layers of straw tubes. Each straw

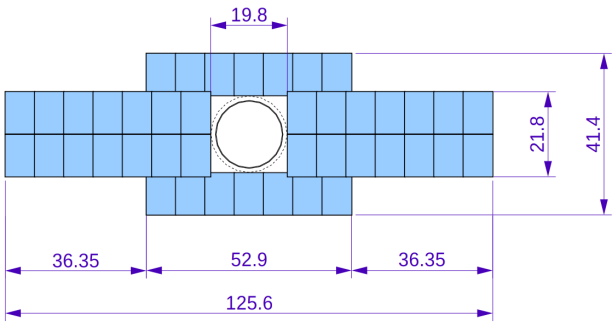

Figure 4.8: Example of an x-layer of the IT as shown in Ref. [63].

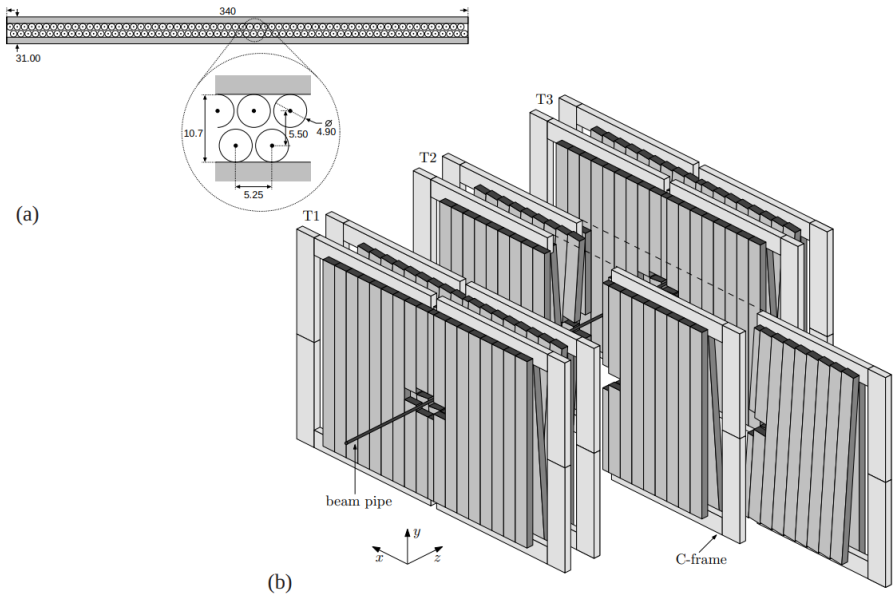

Figure 4.9: Schematics from Ref. [61] of (a) the cross-section of a layer of the OT and (b) the arrangement of modules in $x-u-v-x$ layers in each of the T1, T2, and T3 stations.

tube has dimensions as shown in Fig. 4.9 and is filled with a mixture of Ar, CO_2, and O_2 in relative amounts of 70%, 28.5%, and 1.5%, resulting in a drift time of less than 50 ns [61]. The spatial resolution was found to be 205 µm in Run 1 [62]. This improved to 171 µm in Run 2, when calibration of the time and spatial alignment of the OT was moved from offline to online (during data-taking) [62].

4.1.1.4 | Track Reconstruction

Figure 4.6 shows the different types of tracks and the sub-detectors they leave hits in. Of particular importance in this thesis are long and downstream tracks. Long tracks are reconstructed using an algorithm called 'forward tracking' where VELO tracks are extrapolated to associated T-tracks [64]. Hits in the TT are then added and checked for consistency. Downstream tracks are reconstructed using T-tracks which are extrapolated back to the TT to search for a compatible hit [65]. All reconstructed tracks are then processed using a Kalman filter [66] where measurements of a track from different sub-detectors are added individually and combined. This allows the full trajectory of the particle to be determined and removes noise from multiple scattering [67].

Tracking efficiency is defined as the probability of reconstructing the trajectory of a charged particle that has traversed the entirety of the tracking system [56]. This can be measured using $J/\psi \to \mu^+\mu^-$ decays where one muon is tagged and the other is probed. The efficiency is shown in Fig. 4.10 and varies with the momentum of a single track and the number of tracks in an event. There is a discrepancy in this efficiency between 2011 and 2012 data which is partially due to the difference in centre-of-mass energies leading to higher hit multiplicities in 2012 [56]. In Run 2, the efficiencies were similar [68] but a small decrease was observed due to the reduction in bunch-spacing (from 50 ns in Run 1 to 25 ns in Run 2), resulting in more spillover [69]. These are remnant events from previous and following bunch crossings [54].

The momentum resolution of the tracking system is shown in Fig. 4.11 and is also determined using $J/\psi \to \mu^+\mu^-$ decays. A relative uncertainty of 0.5% is

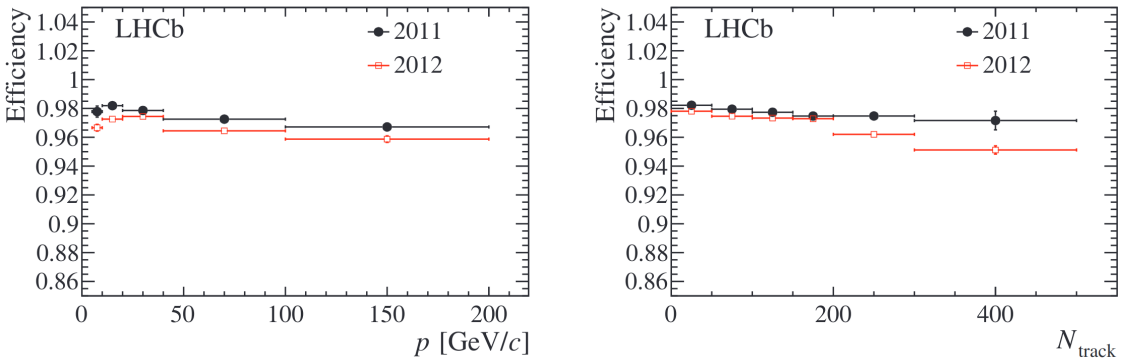

Figure 4.10: Tracking efficiency as a function of (left) momentum for a single track and (right) number of long tracks from $J/\psi \to \mu^+\mu^-$ decays in Run 1 data, as presented in Ref. [56].

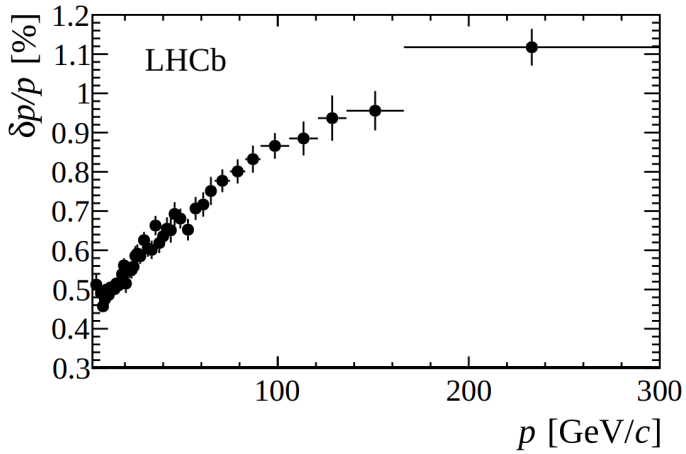

Figure 4.11: Relative momentum resolution as a function of momentum for long tracks from $J/\psi \to \mu^+\mu^-$ decays in Run 1 data, as found in Ref. [56].

found at low momentum and 1% at 200 GeV/c [56].

4.1.2 | Particle Identification

Particle identification (PID) is provided using the remaining parts of the LHCb detector. These are the two Ring-Imaging Cherenkov Detectors (RICH 1 and RICH 2), the calorimeters, and the muon detectors (M1–M5).

4.1.2.1 | RICH Detectors

The two RICH detectors provide PID using Cherenkov radiation. This is a cone of radiation emitted by charged particles when they travel faster than light in a medium. As shown in Fig. 4.12, spherical and flat mirrors reflect and focus this radiation out of LHCb acceptance and on to Hybrid Photon Detectors (HPDs) where they form Cherenkov rings [54]. The radius of these rings depends on the Cherenkov angle, θ_c, which is defined by,

$$\cos(\theta_c) = \frac{1}{n\beta}, \tag{4.1}$$

where n is the refractive index of the medium (or radiator) and $\beta = v/c$. Using the Cherenkov angle β can be measured, and in conjunction with track momentum measurements from the tracking system, the particle mass can be determined. This is illustrated in Fig. 4.13 where the Cherenkov angle varies with track momentum for isolated tracks (where Cherenkov rings do not overlap on the HPDs) in the RICH 1 detector. There is clear separation between the particle species, thus showing excellent PID.

As shown in Fig. 4.12, the two RICH detectors differ in their radiators and their positions along the beam pipe. This results in different angular acceptance and momentum coverage. The upstream RICH 1 detector has an angular acceptance of 25–300 mrad and uses C_4F_{10} gas leading to a momentum range of $p \in [1, 60]$ GeV/c [54]. The downstream RICH 2 detector has an angular acceptance of 15–120 mrad and uses CF_4 gas resulting in a momentum coverage of $p \in [15, 100]$ GeV/c [54]. During Run 1, RICH 1 additionally included an aerogel radiator, for particles below the threshold for C_4F_{10} gas. However, this was later removed in Run 2 as it did not reach performance requirements [71].

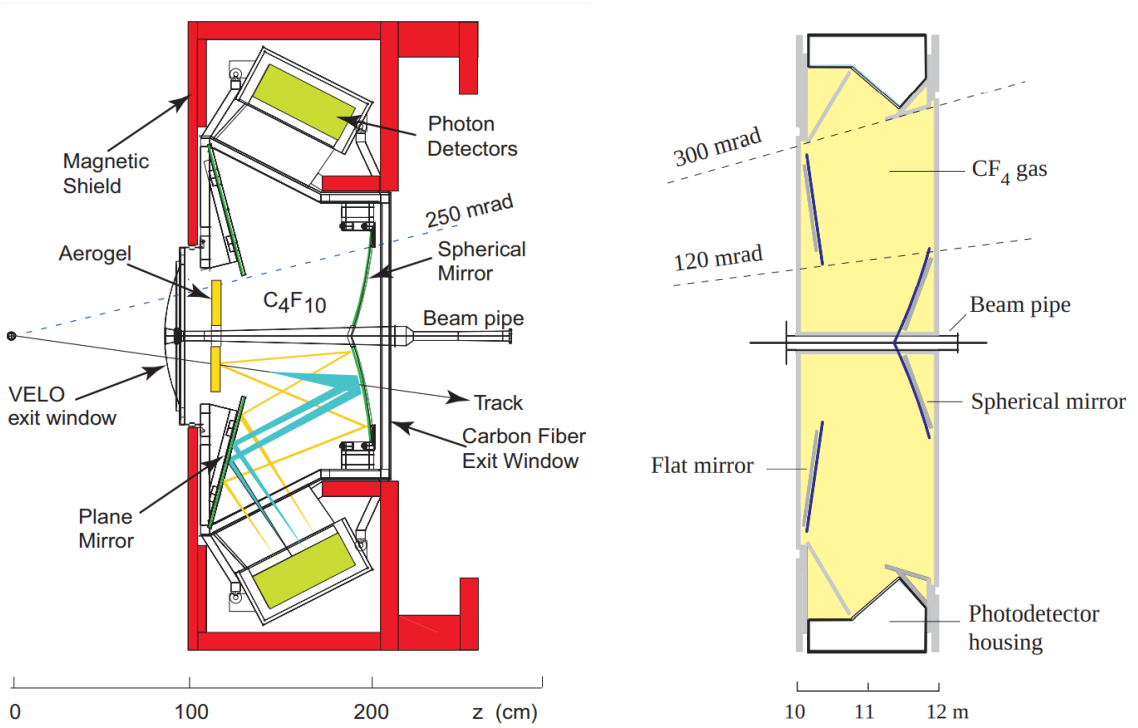

Figure 4.12: Schematics of (left) the RICH 1 detector from the side and (right) the RICH 2 detector from above with their z positions labelled, as found in Ref. [54].

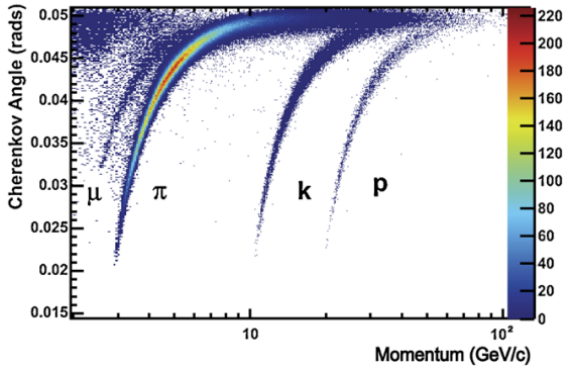

Figure 4.13: Distribution of Cherenkov angle as a function of momentum for isolated tracks in the RICH 1 detector, as found in Ref. [70].

4.1.2.2 | Charged Hadron Separation

Charged hadrons are primarily differentiated using information from the RICH detectors. To do this, the observed pattern of hits in the RICH detectors are com-

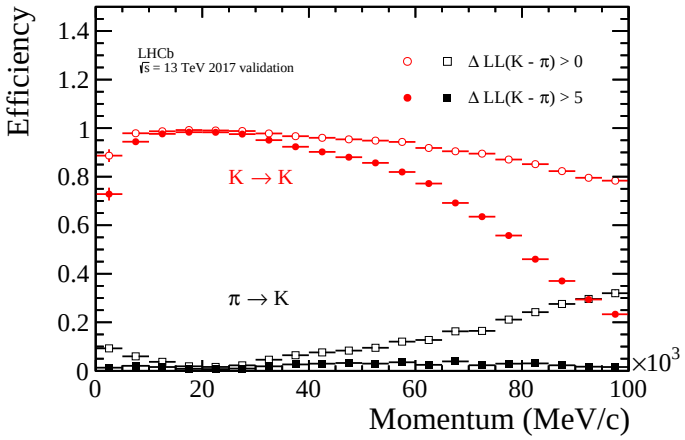

Figure 4.14: The RICH kaon identification efficiency (red) and pion misidentification rates (black) for $\Delta\text{LL}(K-\pi) > 0$ and $\Delta\text{LL}(K-\pi) > 5$ requirements using 2017 data, as found in Ref. [73].

pared to expected patterns given a particle mass hypothesis, forming a likelihood function, $\mathcal{L}(\text{hits}|K)$ [72]. To achieve separation between different charged particle species, all likelihoods are compared to a reference hypothesis, chosen to be a pion hypothesis. Therefore, for kaons this forms the $\Delta\text{LL}(K-\pi)$ variable[1] defined as,

$$\Delta\text{LL}(K-\pi) = \ln\mathcal{L}(\text{hits}|K) - \ln\mathcal{L}(\text{hits}|\pi). \tag{4.2}$$

The RICH kaon identification efficiency and pion misidentification rates are shown in Fig. 4.14 in red and black, respectively, and show excellent separation between kaons and pions. The plot was made using 2017 calibration data with the procedure outlined in Ch. 6.3.2.

In a similar fashion to the $\Delta\text{LL}(K-\pi)$ variable, a $\Delta\text{LL}(e-\pi)$ variable can be defined, though using observed and expected hits in the calorimeters.

[1] This variable is denoted `PIDK` in the measurement presented in this thesis.

4.1.2.3 | Calorimeters

The calorimeter system consists of 4 sub-detectors. From left to right in Fig. 4.2, they are the Scintillating Pad Detector (SPD), the Pre-Shower (PS), the Electromagnetic Calorimeter (ECAL), and finally the Hadronic Calorimeter (HCAL). Together, they measure energies and identify signatures of electrons, photons, and hadrons.

The SPD/PS are two layers of scintillating pads separated by a 15 mm thick lead wall, as shown in Fig. 4.15. When a charged particle passes through a scintillating pad it produces scintillation light on photomultiplier tubes (PMTs). This means that the presence or lack of scintillation light in the SPD informs whether the particle is charged or neutral. The lead wall varies the profile of the energy deposit for charged pions and electrons in the PS, thus enabling them to be distinguished.

The ECAL has a "shashlik" structure, consisting of alternating layers of 4 mm scintillator and 2 mm lead absorbers [74]. As shown in Fig. 4.15, similarly to the SPD and PS, the ECAL is divided into an inner (red), middle (blue), and outer (white) section, where the sizes of calorimeter cells increase with distance from the beam. The ECAL extends to 25 radiation lengths such that the entire electromagnetic shower can be contained, allowing accurate energy measurements [74]. The relative resolution of ECAL energy measurements is shown on the left of Fig. 4.16 and is proportional to $1/\sqrt{E}$.

The HCAL extends to 5.6 interaction lengths and consists of alternating layers of 1 cm iron absorbers and scintillator [74]. As shown in Fig. 4.15, it is divided into an inner section (green) and an outer section (red) with varying cell sizes.

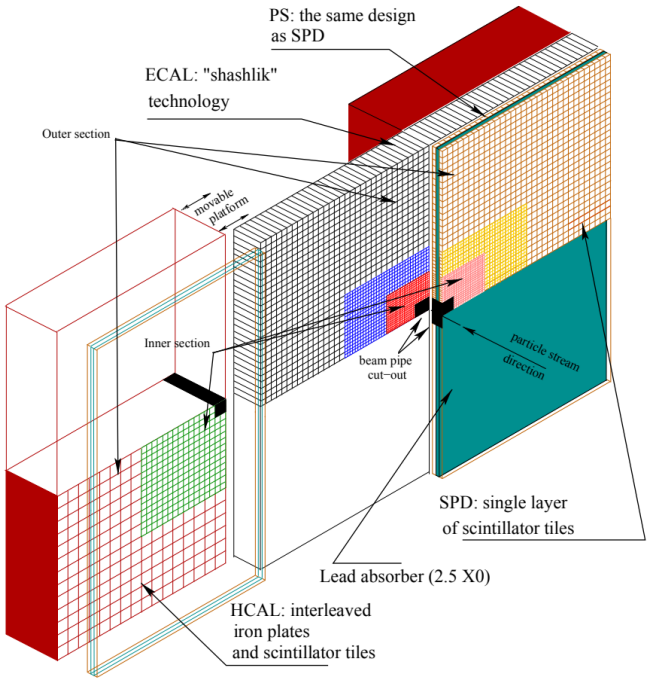

Figure 4.15: Layout of the LHCb calorimeter system, as found in Ref. [74].

The resolution of HCAL energy measurements is shown on the right of Fig. 4.16.

Using calorimeter information, photons and neutral pions can be reconstructed. Photons require clusters in the ECAL that are clearly separated from clusters extrapolated from charged tracks. Neutral pions are predominantly reconstructed from their decay to a pair of photons using two resolved ECAL clusters. The ECAL clusters are determined by grouping 3×3 cells around a local maximum in energy deposition [75]. The smaller the transverse energy of a photon, the more the ECAL cluster can overlap with other clusters, making it harder to resolve. Therefore, as shown in Fig. 4.17, low transverse energy clusters have worse reconstruction efficiency.

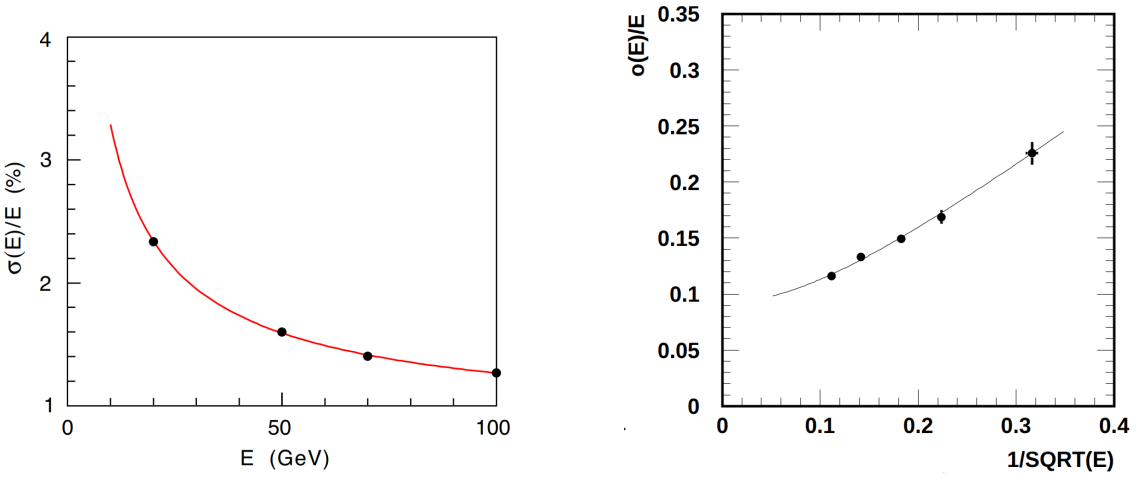

Figure 4.16: Relative resolutions of (left) ECAL energy measurements as a function of energy and (right) HCAL energy measurements as a function of $1/\sqrt{E}$ using electron and pion test-beam data. Reproduced from Ref. [54] and Ref. [76], respectively.

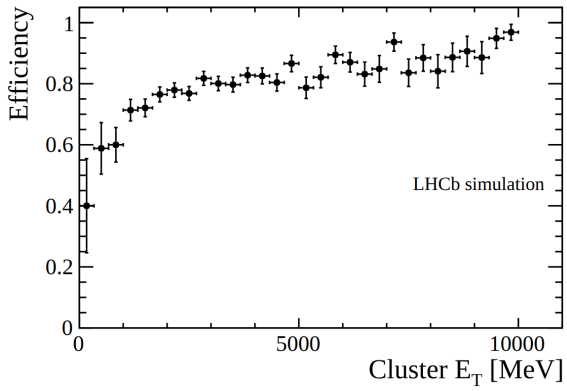

Figure 4.17: Reconstruction efficiency for an ECAL cluster as a function of the transverse energy in the cluster as determined using simulation for $B^0 \to K^{*0}\gamma$ decays, as shown in Ref. [77].

4.1.2.4 | Muon Detectors

The muon system is located at the end of the detector, as shown in Fig. 4.2, and consists of 5 stations. The first station, M1, is between RICH 2 and the calorimeters and is used in the first level trigger, as will be described in Ch. 4.2. The remaining stations, M2–M5, are downstream of the calorimeters with 80 cm thick

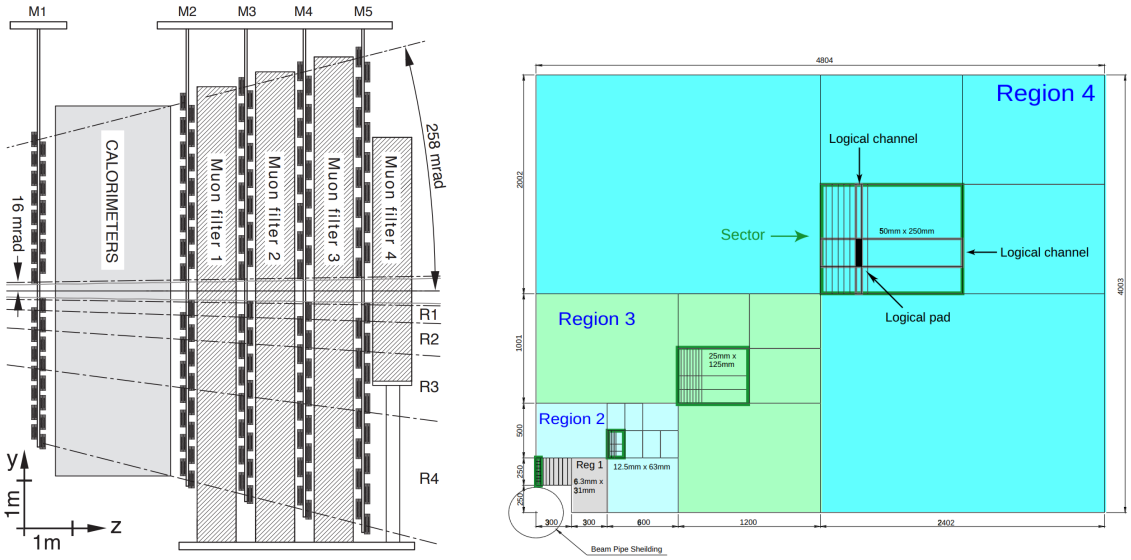

Figure 4.18: The arrangement of (left) the muon stations, M1–M5, with 80 cm thick iron absorbers labelled 'muon filters', as found in Ref. [78], and (right) regions in a quadrant of a station divided into logical pads, as found in Ref. [79].

iron absorbers between each station [78], as shown on the left of Fig. 4.18. Each muon station consists of four quadrants divided into regions, as shown on the right of Fig. 4.18, where each region then consists of a number of logical pads [79]. The muon detectors are made of multi-wire proportional chambers (MWPCs) organised onto these logical pads. These identify muon hits and the information is then encoded in a variable called `isMuon`.

4.2 | Trigger System

With an input bunch crossing rate of 40 MHz, it is not possible to retain all data collected by the LHCb detector. To manage this, a series of triggers are used to select and save only interesting data. The trigger system comprises of a hardware trigger followed by two software triggers, as shown in Fig. 4.19.

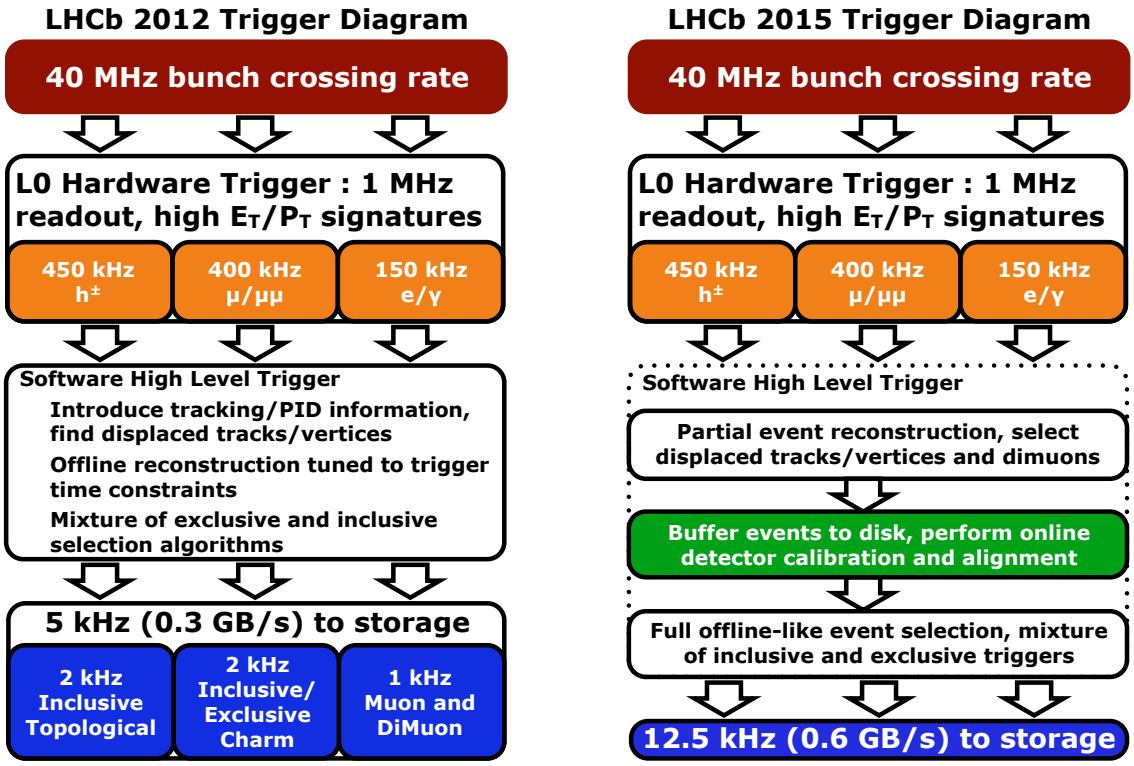

Figure 4.19: Flow diagrams of trigger schemes in (left) Run 1 and (right) Run 2 with associated rates, from Refs. [80] and [69], respectively.

The hardware trigger uses thresholds on transverse energy measurements from the ECAL and HCAL along with the information from the SPD and PS to distinguish hadrons, photons, and electrons. Muons are also identified in this stage using hits in the muon detectors with associated straight-line tracks. The transverse momentum of a muon is estimated using the track direction. If this is above a threshold, the event is retained [69].

There are two software triggers denoted HLT1 (High Level Trigger 1) and HLT2 (High Level Trigger 2). In HLT1, events are partially reconstructed. The positions of PVs are determined and long tracks are identified and retained if their transverse momentum is over a threshold [69]. In addition, fake tracks from ran-

dom combinations of hits are removed. During Run 1, this was achieved using a goodness-of-fit parameter from the Kalman Filter used to fit tracks, as explained in Ch. 4.1.1.4. During Run 2, a neural network was introduced [69].

During Run 1, events then move to a second stage software trigger called HLT2. However, for data collected in Run 2, events are buffered while they wait for updates to the detector calibration and alignment during data-taking [69]. Examples include alignments of the VELO and tracking stations, alignments of the mirrors in the RICH detectors, and calibration of the refractive indices of the gases in the RICH detectors [69]. During Run 1, these were performed offline, but having moved them online (during data-taking) for Run 2, a great improvement in trigger efficiency was seen [69].

At the HLT2 stage, the full event is reconstructed and further track and vertex quality requirements are placed on data. In addition, a multivariate classifier is used to remove fake events from random combinations of hits [81]. The events that are output from HLT2 then enter a 'stripping' stage. Here, candidates are reconstructed as a specific decay chain. The reconstruction specific to this thesis is described in Ch. 6.

4.3 | Simulation

In this thesis, simulation is used to determine selection efficiencies and model mass distributions of signal and background components. Different types of simulation are used for this, primarily centrally produced samples. For these, pp collisions are generated using Pythia8 [82] configured to LHCb [83]. The resulting $b\bar{b}$ pairs hadronise and decay, where this and the decay of subsequent unstable par-

ticles is described using EVTGEN [84] with final state radiation generated using PHOTOS [85]. The detector response to the resulting particles is modelled using a full LHCb detector description with the GEANT4 toolkit [86,87] as described in Ref. [88].

When generating simulation the implementation of the detector response is the most computationally intensive. In simulation, signal events are generated on top of underlying pp interactions. Therefore, to avoid repeating the detector response on underlying pp interactions, these interactions are reused multiple times with the REDECAY algorithm [89].

Fast simulation samples are also used in this thesis. These are generated using RAPIDSIM [90] or amplitude models fitted using LAURA^{++} [91]. Here, a decay is generated using EVTGEN then the detector response is modelled using Gaussian functions to estimate resolution effects.

5

Analysis Strategy

This thesis presents a measurement of γ using $B^{\pm} \to D^{*}K^{\pm}$ and $B^{\pm} \to D^{*}\pi^{\pm}$ decays where the D^{*} meson decays to either $D^{*} \to D\gamma$ or $D^{*} \to D\pi^{0}$, and the resulting D meson decays to the $K^{0}_{S}\pi^{+}\pi^{-}$ or $K^{0}_{S}K^{+}K^{-}$ final state. The measurement uses a data sample collected by the LHCb experiment from 2011–2012 and 2015–2018 in pp collisions at centre-of-mass energies of 7, 8, and 13 TeV, corresponding to a total integrated luminosity of approximately $9\,\text{fb}^{-1}$. These data are divided into bins according to the D-decay phase space using the 'optimal' binning scheme for $D \to K^{0}_{S}\pi^{+}\pi^{-}$ decays, and the '2-bins' binning scheme for $D \to K^{0}_{S}K^{+}K^{-}$ decays. The measurement is model-independent, and therefore combined strong-phase inputs from CLEO [41] and BESIII [42, 43] are used. As detailed in Ch. 3, the signal yield per Dalitz-bin for intermediate $D^{*} \to D\pi^{0}$ decays can be parameterised as,

$$N_{i}^{+} = h_{B}^{+}(K_{-i} + r_{B}^{2}K_{+i} + 2r_{B}\sqrt{K_{-i}K_{+i}}[c_{i}\cos(\delta_{B}+\gamma) - s_{i}\sin(\delta_{B}+\gamma)]), \quad (5.1a)$$

$$N_{i}^{-} = h_{B}^{-}(K_{+i} + r_{B}^{2}K_{-i} + 2r_{B}\sqrt{K_{+i}K_{-i}}[c_{i}\cos(\delta_{B}-\gamma) + s_{i}\sin(\delta_{B}-\gamma)]), \quad (5.1b)$$

and for intermediate $D^* \to D\gamma$ decays as,

$$N_i^+ = h_B^+(K_{-i} + r_B^2 K_{+i} - 2r_B\sqrt{K_{-i}K_{+i}}[c_i\cos(\delta_B+\gamma) - s_i\sin(\delta_B+\gamma)]), \quad (5.2a)$$

$$N_i^- = h_B^-(K_{+i} + r_B^2 K_{-i} - 2r_B\sqrt{K_{+i}K_{-i}}[c_i\cos(\delta_B-\gamma) + s_i\sin(\delta_B-\gamma)]), \quad (5.2b)$$

where the hadronic parameters, r_B and δ_B, are unique to each B decay. To apply these equations to an LHCb data set, a number of modifications must be made.

5.1 | Efficiency Modulation

In Eqs. 5.1 and 5.2, K_i is the probability of a flavour-tagged D^0 decay in a Dalitz bin i and, as shown in Ch. 2, is defined as

$$K_i \equiv \frac{\int_i \mathrm{d}s_-\mathrm{d}s_+ \, |\mathcal{A}_D|^2}{\int \mathrm{d}s_-\mathrm{d}s_+ \, |\mathcal{A}_D|^2}. \quad (5.3)$$

This assumes a uniform acceptance over the D-decay phase space, but this does not hold at LHCb. The LHCb detector is a forward-arm spectrometer, and thus, depending on their momenta, K^0_S mesons can escape the tracking region and decay outside of the acceptance. In addition, low-momentum pions from the K^0_S decay can escape the tracking region. This results in a non-uniform efficiency profile, as illustrated in Fig. 5.1. The figure shows the variation of the efficiency relative to the mean over the Dalitz plot for the $D \to K^0_S\pi^+\pi^-$ final state from intermediate $D^* \to D\gamma$ and $D^* \to D\pi^0$ decays. The relative efficiency is seen to decrease as $s_\pm$ increases, which corresponds to higher momentum K^0_S mesons. The same trend is seen for $D \to K^0_S K^+K^-$ decays. In this analysis, yields in a given Dalitz bin are measured as a proxy for decay rates. The K_i parameters could be measured if the reconstruction efficiency profile, $\eta(s_-, s_+)$, were known.

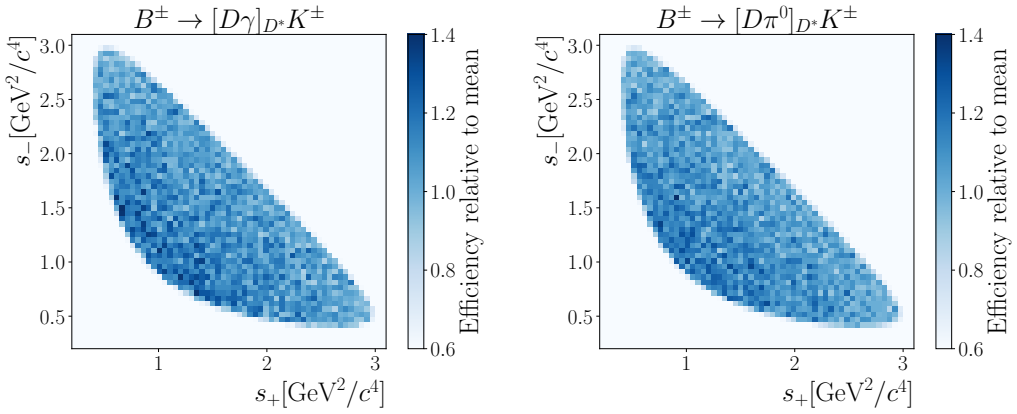

Figure 5.1: Efficiency relative to mean over the Dalitz plot for $D \to K^0_S\pi^+\pi^-$ decays from simulation for (left) $B^\pm \to [D\gamma]_{D^*}K^\pm$ decays and (right) $B^\pm \to [D\pi^0]_{D^*}K^\pm$ decays with downstream K^0_S candidates.

Since it is not, the measured values are efficiency-modulated. This defines a new quantity,

$$F_i \equiv \frac{\int_i \mathrm{d}s_-\mathrm{d}s_+\eta(s_-,s_+)\left|\mathcal{A}_D\right|^2}{\int \mathrm{d}s_-\mathrm{d}s_+\eta(s_-,s_+)\left|\mathcal{A}_D\right|^2}, \tag{5.4}$$

the *measured* fractional yield of a D^0 decay in a Dalitz bin.

The strong-phase inputs, c_i and s_i, could also be efficiency-modulated, leading to

$$c_i' \equiv \frac{\int_i \mathrm{d}s_-\mathrm{d}s_+\eta(s_-,s_+)\left|\mathcal{A}_D\right|\left|\mathcal{A}_{\overline{D}}\right|\cos(\Delta\delta_D)}{\sqrt{\int_i \mathrm{d}s_-\mathrm{d}s_+\eta(s_-,s_+)\left|\mathcal{A}_D\right|^2\int_i \mathrm{d}s_-\mathrm{d}s_+\eta(s_-,s_+)\left|\mathcal{A}_{\overline{D}}\right|^2}}, \tag{5.5}$$

and a similar equation for s_i'. However, previous analyses indicate that the impact on the strong-phase inputs is small [45]. Therefore, values from CLEO [41] and BESIII [42, 43] are used directly and an associated systematic uncertainty is assigned, as will be detailed in Ch. 9.

The F_i values vary depending on the D decay and the K^0_S candidate type, resulting in 40 values. It is possible to determine them using the signal $B^\pm \to D^*K^\pm$ decays alongside the determination of *CP*-violation in this mode, however this

results in 43 observables and significantly degrades the precision of the measurement. To reduce the number of observables, the F_i values can be measured using another decay mode.

In the most recent analysis of $B^\pm \to DK^\pm$ decays [45], the $B^\pm \to D\pi^\pm$ channel was used to determine the F_i values since this channel has similar kinematics to the $B^\pm \to DK^\pm$ mode. A similar approach is employed here with $B^\pm \to D^*\pi^\pm$ decays, which are topologically very similar to $B^\pm \to D^*K^\pm$ decays. Figure 5.2 shows that $s(K^0_S\pi^+)$, $s(K^0_S\pi^-)$ and $s(\pi^+\pi^-)$ distributions in phase-space simulation are very similar, as seen by the p-values from Kolmogorov-Smirnov tests [92, 93]. As the p-values are all above 5%, the distributions with kaon and pion companion hadrons are compatible.

This means that the F_i values can be shared between the $B^\pm \to D^*K^\pm$ and $B^\pm \to D^*\pi^\pm$ decays and are measured in both. Due to the relative branching fractions, there is an order of magnitude more $B^\pm \to D^*\pi^\pm$ decays than $B^\pm \to D^*K^\pm$. This means the F_i measurement is driven by the $B^\pm \to D^*\pi^\pm$ mode which greatly improves the precision of the F_i measurement compared to using $B^\pm \to D^*K^\pm$ decays alone. The $B^\pm \to D^*\pi^\pm$ mode also exhibits *CP*-violation, and therefore is also a signal mode. Compared to $B^\pm \to D^*K^\pm$ decays, the level of *CP*-violation in $B^\pm \to D^*\pi^\pm$ decays is expected to be much smaller. This is because $r_B^{D^*\pi}$ is expected to be around 0.009 [47], whereas $r_B^{D^*K}$ is expected to be around 0.1 [47]. This means that the interference, using which γ is measured, is smaller in $B^\pm \to D^*\pi^\pm$ decays. The γ measurement is therefore driven by the $B^\pm \to D^*K^\pm$ mode, and the primary role of the $B^\pm \to D^*\pi^\pm$ channel is to determine the F_i values.

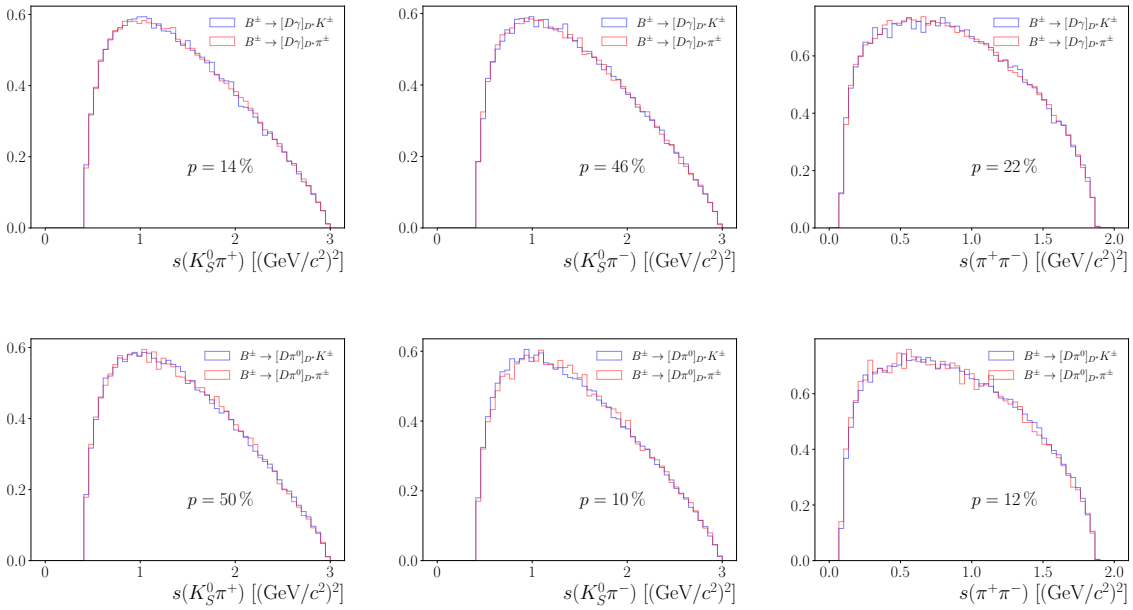

Figure 5.2: Normalised histograms (from left to right) of $s(K^0_S\pi^+)$, $s(K^0_S\pi^-)$, and $s(\pi^+\pi^-)$ for (top) $B^\pm \to [D\gamma]_{D^*}K^\pm$ and $B^\pm \to [D\gamma]_{D^*}\pi^\pm$ decays in blue and red respectively, and (bottom) $B^\pm \to [D\pi^0]_{D^*}K^\pm$ and $B^\pm \to [D\pi^0]_{D^*}\pi^\pm$ in blue and red respectively. The histograms are from simulation with $D \to K^0_S\pi^+\pi^-$ decays and downstream K^0_S candidates. The p-values from Kolmogorov-Smirnov tests [92, 93] are labelled.

5.2 | *CP* Observables

From Eqs. 5.1 and 5.2, one could fit the parameters r_B, δ_B, and γ. However, this poses a problem as the uncertainty on γ is inversely proportional to r_B, and r_B is bounded (must be greater than 0). This leads to a non-Gaussian uncertainty on γ which can lead to underestimated errors. Therefore, *CP* observables are defined for each B decay, which are unbounded and have reliable errors. For $B^\pm \to D^*K^\pm$ decays they are defined as,

$$x_\pm^{D^*K} = r_B^{D^*K}\cos(\delta_B^{D^*K} \pm \gamma) \tag{5.6a}$$

$$y_\pm^{D^*K} = r_B^{D^*K}\sin(\delta_B^{D^*K} \pm \gamma). \tag{5.6b}$$

A similar parameterisation is also applicable for $B^{\pm} \to D^{*}\pi^{\pm}$ decays, but leads to fit instabilities. This is because $r_B^{D^*\pi}$ is almost an order of magnitude smaller than $r_B^{D^*K}$ [47]. If r_B is small, the associated *CP* observables, when parameterised as shown in Eq. 5.6, become highly correlated with the F_i values, leading to fit instabilities. To avoid this, the cartesian parametrisation for the $B^{\pm} \to D^{*}\pi^{\pm}$ *CP* observables is replaced by an alternative parameterisation [94],

$$\xi^{D^*\pi} = \frac{r_B^{D^*\pi}}{r_B^{D^*K}} \exp[i(\delta_B^{D^*\pi} - \delta_B^{D^*K})]. \tag{5.7}$$

By taking the real and imaginary parts of $\xi^{D^*\pi}$, the cartesian *CP* observables can be recovered:

$$x_{\pm}^{D^*\pi} = \Re(\xi^{D^*\pi})x_{\pm}^{D^*K} - \Im(\xi^{D^*\pi})y_{\pm}^{D^*K} \tag{5.8a}$$

$$y_{\pm}^{D^*\pi} = \Re(\xi^{D^*\pi})y_{\pm}^{D^*K} + \Im(\xi^{D^*\pi})x_{\pm}^{D^*K}. \tag{5.8b}$$

This parameterisation does not depend on γ, and therefore all information regarding *CP*-violation in both the D^*K and $D^*\pi$ modes are measured via $x_{\pm}^{D^*K}$ and $y_{\pm}^{D^*K}$.

Using the *CP* observables and F_i values, the yields in Eqs. 5.1 and 5.2 can be re-written. For B^+ decays with intermediate $D^* \to D\pi^0$ decays, the yield per Dalitz bin is

$$N_i^+ = h_B^+(F_{-i} + [x_+^2 + y_+^2]F_{+i} + 2\sqrt{F_{-i}F_{+i}}[c_i x_+ - s_i y_+]), \tag{5.9}$$

and the yield for B^- mesons is

$$N_i^- = h_B^-(F_{+i} + [x_-^2 + y_-^2]F_{-i} + 2\sqrt{F_{+i}F_{-i}}[c_i x_- + s_i y_-]). \tag{5.10}$$

For B^+ decays with intermediate $D^* \to D\gamma$ decays, the yield per Dalitz bin is

$$N_i^+ = h_B^+(F_{-i} + [x_+^2 + y_+^2]F_{+i} - 2\sqrt{F_{-i}F_{+i}}[c_i x_+ - s_i y_+]). \tag{5.11}$$

and for B^- mesons, it is

$$N_i^- = h_B^-(F_{+i} + [x_-^2 + y_-^2]F_{-i} - 2\sqrt{F_{+i}F_{-i}}[c_i x_- + s_i y_-]). \tag{5.12}$$

Therefore, in this analysis, *CP* observables are obtained from fits to the Dalitz bin yields, and then interpreted in terms of the hadronic parameters and γ.

5.3 | Partial Reconstruction

To determine the *CP* observables, candidates are split into categories based on the B charge, the B decay, the D decay, long or downstream K_S^0 candidates and the Dalitz bin. Within these categories, extended maximum-likelihood fits are performed to the reconstructed mass spectra. Candidates are reconstructed as $B^\pm \to Dh^\pm$, where the light neutral particle from the D^* decay is missed. This is because, at LHCb, the reconstruction of low momentum neutral particles is complicated by overlapping clusters in the calorimeters. Reconstructing the π^0 or γ from the D^* decay can cause a 70–90% reduction of the signal yield depending on the identification criteria applied. To circumvent this, the neutral pion and photon are missed and the signal decays are partially reconstructed.

Although the π^0 or γ from the D^* decays are not reconstructed, the signal components from each intermediate D^* decay can be distinguished using their Dh mass spectra, $m(Dh)$, determined using the momentum and total energy of the Dh combination: $m(Dh) = \sqrt{E(Dh)^2 - p(Dh)^2}$. This is a result of the spin-parity (J^P) structure of the D^* decays: $0^- \to [0^-0^-]_{1^-}0^-$ for decays such as $B^\pm \to [D\pi^0]_{D^*}h^\pm$, and $0^- \to [0^-1^-]_{1^-}0^-$ for decays such as $B^\pm \to [D\gamma]_{D^*}h^\pm$. To conserve total angular momentum and parity in the D^* decay, the photon is

preferentially emitted perpendicular to the momentum of the D^* meson and the neutral pion is preferentially emitted parallel to the D^* momentum. To quantify this, the helicity angle, θ, is defined as the angle between the momentum of the light neutral particle in the D^* rest frame and the D^* momentum in the $B^\pm$ rest frame. The probability distribution of $\cos\theta$, $P(\cos\theta)$, is derived using spherical harmonics, Y_l^m, where to conserve parity in the D^* decay, the orbital angular momentum, l, must be 1. The photon is massless and has spin 1, therefore it has $m = \pm 1$, and the pion has spin 0, therefore it has $m = 0$. The probability distributions of the helicity angle have the following proportionalities,

$$D^* \to D\pi^0 : \qquad P(\cos\theta) \propto |Y_1^0|^2 \propto \cos^2\theta, \tag{5.13}$$

$$D^* \to D\gamma : \qquad P(\cos\theta) \propto |Y_1^{\pm 1}|^2 \propto 1 - \cos^2\theta, \tag{5.14}$$

To relate this dependence to the reconstructed mass, four-momentum conservation results in the mass of the Dh combination as,

$$m_{Dh}^2 = m_D^2 + m_h^2 + E_D E_h - p_D p_h \cos\theta, \tag{5.15}$$

where E is total energy and p is linear momentum. By taking $\cos\theta = -1$ and $\cos\theta = +1$, the kinematic limits of m_{Dh}^2 can be found, and are denoted A and B respectively. With these, the reconstructed mass can be re-written as

$$m_{Dh}^2 = \frac{1}{2}(A^2 + B^2 + (B^2 - A^2)\cos\theta). \tag{5.16}$$

A Taylor expansion of this then shows that m_{Dh} is proportional to $\cos\theta$. This means that, for $D^* \to D\pi^0$ decays, since $P(\cos\theta)$ is proportional to $\cos^2\theta$, the $m(Dh)$ spectrum is a parabola with a positive coefficient, as illustrated on the left of Fig. 5.3, and for $D^* \to D\gamma$ decays, $P(\cos\theta)$ is proportional to $1 - \cos^2\theta$, and

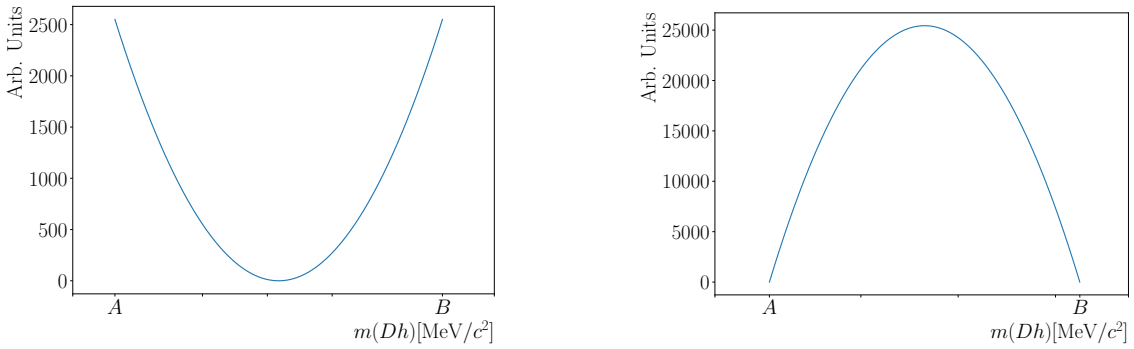

Figure 5.3: Illustrations of (left) a positive parabola in $m(Dh)$ distribution for signal decays with intermediate $D^* \to D\pi^0$ decays, and (right) a negative parabola for signal decays with intermediate $D^* \to D\gamma$ decays.

the $m(Dh)$ spectrum is a parabola with a negative coefficient, as illustrated on the right of Fig. 5.3. The $m(Dh)$ distribution for intermediate $D^* \to D\pi^0$ decays can be written as,

$$P(m_{Dh}) = \left(m_{Dh} - \frac{A+B}{2}\right)^2 \tag{5.17}$$

and for intermediate $D^* \to D\gamma$ decays it can be written as,

$$P(m_{Dh}) = -(m_{Dh} - A)(m_{Dh} - B). \tag{5.18}$$

Thus far, these $m(Dh)$ spectra have been derived in the absence of detector effects. To obtain realistic distributions, both reconstruction and resolution effects must be taken into account. Reconstruction efficiencies at LHCb are larger for higher momentum candidates, and therefore events at higher $m(Dh)$. This is parameterised using a linear term in the $m(Dh)$ distribution with the parameter ζ. When ζ is close to one, the variance due to reconstruction effects is small. Resolution effects also alter the $m(Dh)$ distribution and are accounted for by convolving it with a resolution function, $p_{\mathrm{Res}}(m|\vec{\theta})$, such as a Gaussian function. The exact functional form is determined using the fully reconstructed $B^\pm \to Dh^\pm$ peak,

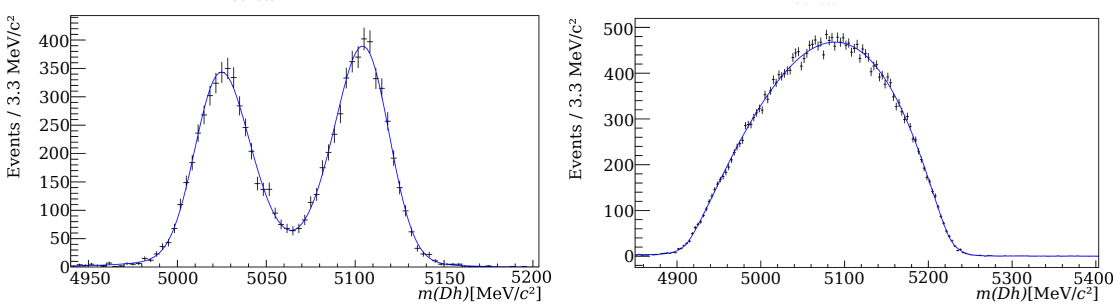

Figure 5.4: Mass distributions from simulation for (left) $B^{\pm} \to [D\pi^0]_{D^*}K^{\pm}$ signal decays and (right) $B^{\pm} \to [D\gamma]_{D^*}K^{\pm}$ signal decays with $D \to K^0_S\pi^+\pi^-$ decays and downstream K^0_S candidates. The fit projections are overlaid.

which in the absence of detector effects is a δ-function. Therefore, the $B^{\pm} \to Dh^{\pm}$ peak can be used to calibrate the resolution of the detector. These reconstruction and resolution effects result in a double-peaked structure for intermediate $D^* \to D\pi^0$ decays, with the probability density function (PDF)

$$p(m) = \int_A^B \mathrm{d}\mu \left(\mu - \frac{A+B}{2}\right)^2 p_{\mathrm{Res}}(m|\vec{\theta}) \left(\frac{1-\zeta}{B-A}\mu + \frac{B\zeta - A}{B-A}\right), \tag{5.19}$$

and a single wide peak for intermediate $D^* \to D\gamma$ decays, where the PDF is

$$p(m) = -\int_A^B \mathrm{d}\mu(\mu - A)(\mu - B)p_{\mathrm{Res}}(m|\vec{\theta}) \left(\frac{1-\zeta}{B-A}\mu + \frac{B\zeta - A}{B-A}\right). \tag{5.20}$$

These distributions are shown using fits to simulation samples in Fig. 5.4.

5.4 | Preliminary Sensitivity Study

Given that this is the first analysis of its kind studying this signal mode, a preliminary sensitivity study is useful to determine the optimal fit configuration and the expected sensitivity to γ to assess the viability of this analysis. Since $B^{\pm} \to D^*K^{\pm}$ decays drive the sensitivity to γ, for simplicity only this mode is included in this

sensitivity study. It is performed in a signal-only set-up to determine the maximum sensitivity obtainable. Since there are two types of intermediate D^* decays, the interplay between these is assessed by considering various fit configurations. The intuitive configuration is where the two D^* modes are fitted simultaneously, but a hypothetical configuration can also be explored where each D^* mode is fitted separately and then statistically combined by taking the weighted average.

The sensitivity study is performed by generating pseudodata for both D^* decay modes. The *CP* observables are then fitted while the F_i values are fixed to those from Ref. [45]. For each fit configuration 1000 pseudodatasets are generated and fitted using the same model. The mean statistical uncertainty on each *CP* observable is then compared between the fit configurations. The fit configurations in question are referred to as:

1. $D^* \to D\gamma$ signal;
2. $D^* \to D\pi^0$ signal;
3. Both D^* decays as signal,

and these are illustrated in Fig. 5.5. The first configuration, shown in blue in Fig. 5.5, refers to the scenario where only the $D^* \to D\gamma$ mode is used to determine the *CP* observables. Dalitz-bin yields for both the $D^* \to D\gamma$ and $D^* \to D\pi^0$ modes are generated using central values for the *CP* observables [47], then only yields for the $D^* \to D\gamma$ mode are fitted to determine the *CP* observables. Those for the $D^* \to D\pi^0$ mode are fixed from their generation, since this mode is not treated as a signal decay. The second scenario, shown in red in Fig. 5.5, considers the opposite case where only the Dalitz-bin yields of the $D^* \to D\pi^0$ mode are used to

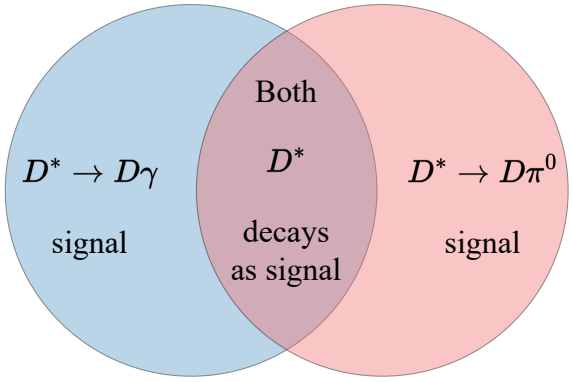

Figure 5.5: Illustration of fit configurations tested in the sensitivity study where the blue sector represents the configuration where only events from the $D^* \to D\gamma$ mode are used as signal, the red sector represents the configuration where only events from the $D^* \to D\pi^0$ mode are used as signal, and finally the intersection where both D^* decays are used as signal.

Table 5.1: Statistical uncertainties on the *CP* observables for different fit configurations, as calculated using pseudodata. The last column corresponds to a simultaneous fit to both D^* modes.

CP Observable	$D^* \to D\pi^0$ signal	$D^* \to D\gamma$ signal	Combining $D^* \to D\pi^0$ and $D^* \to D\gamma$ signals	Both D^* decays as signal
$x_-^{D^*K}$	0.018	0.048	0.017	0.022
$y_-^{D^*K}$	0.025	0.053	0.023	0.027
$x_+^{D^*K}$	0.016	0.048	0.015	0.019
$y_+^{D^*K}$	0.019	0.061	0.018	0.025

determine the *CP* observables and those of the $D^* \to D\gamma$ mode are fixed from generation. Finally, the third configuration is the intersection in Fig. 5.5 where the Dalitz-bin yields of both D^* decay modes are fitted simultaneously to determine the *CP* observables. The mean statistical uncertainties on the *CP* observables for each of these configurations are shown in Tab. 5.1, where the uncertainties in the "$D^* \to D\pi^0$ signal" and "$D^* \to D\gamma$ signal" columns are additionally statistically combined by taking the weighted average. These results are given in the "Combining $D^* \to D\pi^0$ and $D^* \to D\gamma$ signals" column.

Table 5.2: Fit errors on the *CP* observables for toys where events are generated and fitted exclusively for one D^* decay and there are no events for the other D^* decay.

CP Observable	$D\pi^0$	$D\gamma$
$x_-^{D^*K}$	0.013	0.017
$y_-^{D^*K}$	0.017	0.020
$x_+^{D^*K}$	0.012	0.018
$y_+^{D^*K}$	0.016	0.023

The branching ratio for $D^* \to D\pi^0$ decays is approximately twice that of $D^* \to D\gamma$ decays [18], and therefore, in the generated sample, the yield for the $D^* \to D\pi^0$ mode is twice that of the $D^* \to D\gamma$ mode. However, comparing the uncertainties in the "$D^* \to D\pi^0$ signal" and "$D^* \to D\gamma$ signal" columns of Tab. 5.1, those in the "$D^* \to D\gamma$ signal" column are more than a factor of $\sqrt{2}$ times greater than those in the "$D^* \to D\pi^0$ signal" column. This is because when the *CP* observables are determined using only the $D^* \to D\pi^0$ mode, the $D^* \to D\gamma$ mode is treated as a background. This means that the "$D^* \to D\pi^0$ signal" configuration has a purity of 67%, and the "$D^* \to D\gamma$ signal" configuration has a purity of 33%. Thus, the per-event sensitivity of the $D^* \to D\gamma$ mode is lower due to the presence of the $D^* \to D\pi^0$ mode. If both D^* decay modes had the same per-event sensitivity, the uncertainties in the "$D^* \to D\gamma$ signal" column would be $\sqrt{2}$ times larger than those in the "$D^* \to D\pi^0$ signal" column. This is observed when generating and fitting events exclusively for each D^* decay with no events for the other D^* decay mode. The results of this are shown in Tab. 5.2.

The maximum sensitivity possible from the $B^\pm \to D^*K^\pm$ signal mode is found using the *hypothetical* scenario where the "$D^* \to D\gamma$ signal" and "$D^* \to D\pi^0$ signal" configurations are statistically combined. This is compared to the configura-

tion which is used in this analysis ("Both D^* decays as signal") and demonstrates that since the $D^* \to D\gamma$ and $D^* \to D\pi^0$ modes are each a background with respect to the other, they dilute each other's sensitivities when fitted simultaneously. Since these are signal-only sensitivity studies with only the $D^* \to D\pi^0$ and $D^* \to D\gamma$ modes, their yields are anti-correlated. If the yield of one mode fluctuates up, the yield of the other must fluctuate down. These fluctuations result in uncertainties on the yields and further enhance the dilution of the sensitivity of these modes. The maximum sensitivity of this analysis is as shown in the "Both D^* decays as signal" column of Tab. 5.1. This corresponds to a sensitivity to γ of around 9°. This is a promising result for the $B^\pm \to D^* h^\pm$ decay mode since the uncertainty in the latest LHCb γ combination is around 4° [47].

This analysis will also measure hadronic parameters, such as $\delta_B^{D^*K}$ and $\delta_B^{D^*\pi}$ which are not well-constrained by other measurements of the same B mode [46] due to trigonometric ambiguities. The present work can remove these ambiguities and in doing so improve the weight of other analyses in future γ combinations.

5.5 | Analysis Overview

The CP observables and F_i values are determined using extended maximum-likelihood fits to the $m(Dh)$ spectra. A two-step fit procedure is used. First data are fitted in the global D-decay phase-space without splitting by B-charge or Dalitz bin. This fit is used to determine the mass distributions of the signal and background contributions. These distributions are subsequently fixed in each Dalitz bin for the second fit where data are also split by B-charge. In this second

fit, the *CP* observables and F_i values are determined. The overall analysis strategy can be summarised as follows.

First, data collected by the LHCb experiment are reconstructed as $B^{\pm} \to Dh^{\pm}$ candidates in the $D \to K^0_S h'^+ h'^-$ final states. A set of selection requirements are applied to these candidates to reduce background levels and increase the purity of the data sample, while maintaining a high efficiency on the signal processes. The resulting dataset is then split into eight categories: every combination of the two B decays, the two D decays, and the two K^0_S candidate types. Within each of these categories the $m(Dh)$ spectrum is fitted, parameterising the signal and background components. This fit considers events from the entire Dalitz phase space inclusively, and is therefore called the 'global fit'. Following the global fit, candidates are further split by B charge and their assigned Dalitz bin. The mass shape parameterisations from the global fit are fixed in each Dalitz bin, and the yield per Dalitz bin is fitted to determine the *CP* observables and F_i values. This is the '*CP* fit'. The resulting *CP* observables are then interpreted in terms of the physical parameters, including γ.

6

Selection and Efficiencies

Candidates are reconstructed as $B^{\pm} \to [K^0_S h^+ h^-]_D h'^{\pm}$ decays by combining tracks of decay products. At each step of this combination, conditions on momentum, track and vertex quality, and loose PID requirements reduce backgrounds from random track combinations and ensure data is collected at a manageable rate. These conditions are later superseded by tighter candidate selections which improve the purity of the data sample.

There are three stages to the candidate selection: a base selection, a multivariate classifier in the form of a boosted decision tree (BDT), and particle identification of the companion hadron. The selection and BDT developed for Ref. [45] are used again here since the candidate reconstruction is identical. However, some working points are re-optimised due to kinematic differences between the signal decays in this work and in Ref. [45].

Table 6.1: Summary of the candidate selection split by their application before and after the BDT.

Variable	Cut	Comment
Base selection requirements before BDT		
DTF convergence	True	
$m(D)$	$\lvert m(D) - m_{\text{PDG}}(D)\rvert < 25\,\text{MeV}/c^2$	
$m(K^0_S)$	$\lvert m(K^0_S) - m_{\text{PDG}}(K^0_S)\rvert < 15\,\text{MeV}/c^2$	
$p(h^\pm)$	$< 100\,\text{GeV}/c$	Companion hadron
$h^\pm$ has RICH	True	Companion hadron
$p(K^\pm_D)$	$< 100\,\text{GeV}/c$	In $D \to K^0_S K^+ K^-$
$K^\pm_D$ has RICH	True	In $D \to K^0_S K^+ K^-$
K^0_S flight distance χ^2	> 49	Long K^0_S
$\Delta z^{DB}_{\text{sig}}$	> 0.5	All candidates
Selection requirements after BDT		
$h^\pm$ is muon	False	In $B^\pm \to D^* h^\pm$
$h'^\pm_D$ is muon	False	In $D \to K^0_S h'^+ h'^-$
$\pi^\pm_D$ `PIDe`	< 0	In $D \to K^0_S \pi^+ \pi^-$
$K^\pm_D$ `PIDK`	> -5	In $D \to K^0_S K^+ K^-$
Companion hadron particle identification		
$K^\pm$ `PIDK`	> 12	Companion hadron
$\pi^\pm$ `PIDK`	< 12	Companion hadron

6.1 | Base Selection

Reconstructed events must first fulfill hardware trigger requirements. These are related to transverse energy measurements in the HCAL and ECAL for candidates associated with the signal, and additionally in the muon chambers for candidates that are not associated with the signal. This is followed by software trigger requirements which vary depending on when data samples were collected. For Run 1 data, the `HLT1TrackAllL0` trigger is followed by one of the `HLT2Topo{2,3,4}BodyBBDT` triggers. Whereas, for Run 2 data, one of the `HLT1{Track,TwoTrack}` triggers is followed by one of the `HLT2Topo{2,3,4}Body` triggers. These were discussed in Ch. 4.2.

The resulting candidates are then subject to the base selection which was developed for the work in Ref. [45] and is shown in the first 9 rows of Tab. 6.1. The DTF convergence refers to a kinematic fit [95] where the masses of the D and K^0_S mesons are constrained to their known values [18] to improve the mass resolution of the final B meson candidate. The unconstrained D and K^0_S meson masses are then also required to be within $25\,\mathrm{MeV}/c^2$ and $15\,\mathrm{MeV}/c^2$ of their PDG values, respectively, to suppress backgrounds from random track combinations. Then, the momentum of the companion hadron is required to be less than $100\,\mathrm{GeV}/c$ with activity in the RICH detectors, to ensure good particle identification. This is also a requirement on the charged kaon from the $D \to K^0_S K^+ K^-$ decay.

These selections are followed by specific background-suppressing requirements. First, background contributions from $D \to h^+h^-\pi^+\pi^-$ final states are reduced using a flight distance (FD) requirement, χ^2_{FD}, on the K^0_S meson,

$$\chi^2_{\mathrm{FD}} = \left(\frac{\mathrm{FD}}{\sigma(\mathrm{FD})}\right)^2, \tag{6.1}$$

where $\sigma(\mathrm{FD})$ denotes the error associated with the flight distance measurement (FD). This requirement is only necessary for long K^0_S candidates since downstream K^0_S candidates decay further into the detector, and therefore must have longer flight distances.

There are also background contributions from B decays which reach the final state without an intermediate D meson. This is called the charmless background and it is reduced by ensuring well-separated D and B decay vertices in the z-axis. This is essentially a requirement on the flight distance of the D meson in the

Table 6.2: Signal efficiency in the $B^{\pm} \to D^{*}K^{\pm}$ sample for different $\Delta z_{\text{sig}}^{DB}$ requirements.

	$\Delta z_{\text{sig}}^{DB}$ **requirement**			
	0.5	**1**	**2**	**4**
Efficiency (%)	84	77	64	44

z-direction, and it is constructed as,

$$\Delta z_{\text{sig}}^{DB} = \frac{z_{\text{DV}}^{D} - z_{\text{DV}}^{B}}{\sqrt{\sigma^2(z_{\text{DV}}^{D}) + \sigma^2(z_{\text{DV}}^{B})}}, \tag{6.2}$$

where z_{DV}^{X} refers to the z position of the X particle at its decay vertex, and $\sigma(z_{\text{DV}}^{X})$ is the uncertainty associated with this measurement. The z-axis is specifically chosen as B-meson candidates, and therefore also D-meson candidates, are boosted in this direction. This means that the magnitude of the flight distance is similar to its projection in the z-direction, but the associated uncertainty is much larger than that in the z-direction. Therefore, the $\Delta z_{\text{sig}}^{DB}$ distribution is wider than the χ^2_{FD} distribution, and the selection requirement can be considered more carefully.

The requirement chosen on the $\Delta z_{\text{sig}}^{DB}$ parameter in Ref. [45] is 0.5. By tightening this, the presence of any residual charmless background can be probed using the $m(Dh)$ distribution from data in the D-mass sidebands. This is shown in Fig. 6.1. Regardless of the requirement, the mass spectrum is seen to be very similar to that of the combinatorial background (an exponential function), such that any residual charmless background could be accounted for by it. Furthermore, as shown in Tab. 6.2, tightening the $\Delta z_{\text{sig}}^{DB}$ requirement significantly impacts the efficiency. Therefore, to maximise the statistical sensitivity of the analysis, the selection is not tightened.

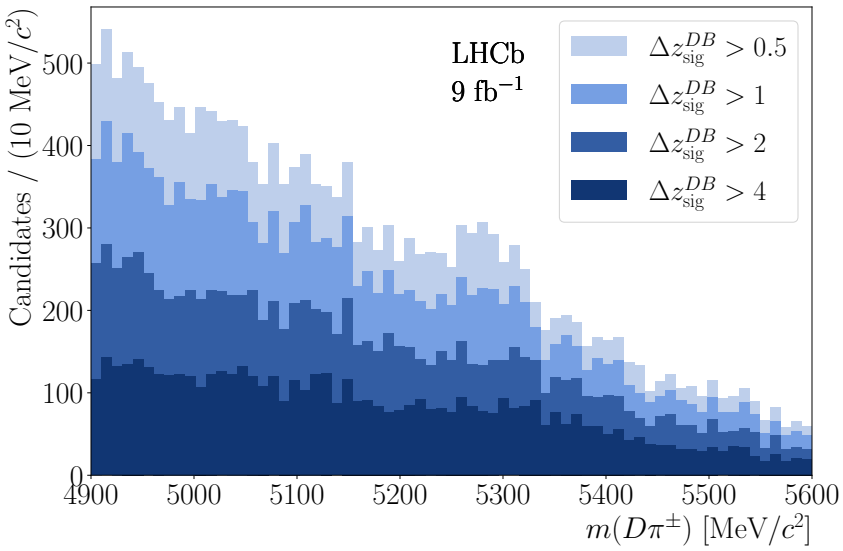

Figure 6.1: Distributions of $m(D\pi^{\pm})$ in data for different $\Delta z_{\text{sig}}^{DB}$ requirements using candidates in the upper D-mass sideband reconstructed as $B^{\pm} \to [K_S^0\pi^+\pi^-]_D\pi^{\pm}$ with downstream K_S^0 mesons.

6.1.1 | Signal Efficiencies

The selection described thus far can be applied to simulation to determine the associated efficiencies. These are evaluated using samples generated with the $D \to K_S^0\pi^+\pi^-$ final state. They are then shared with the $D \to K_S^0K^+K^-$ mode in the global and *CP* fits since they are input as efficiency ratios relative to the $B^{\pm} \to D\pi^{\pm}$ background component.

The efficiencies for the trigger and base selection are shown in Fig. 6.2 with separate plots for Run 1 and Run 2, as well as each K_S^0 candidate type. There is little variation between these plots, showing that the selection does not bias between these categories. The figure shows efficiencies for the signal decays but also, for reference, the background from $B^{\pm} \to D\pi^{\pm}$ decays. The selection was originally developed for the analysis in Ref. [45], where the signal was $B^{\pm} \to D\pi^{\pm}$

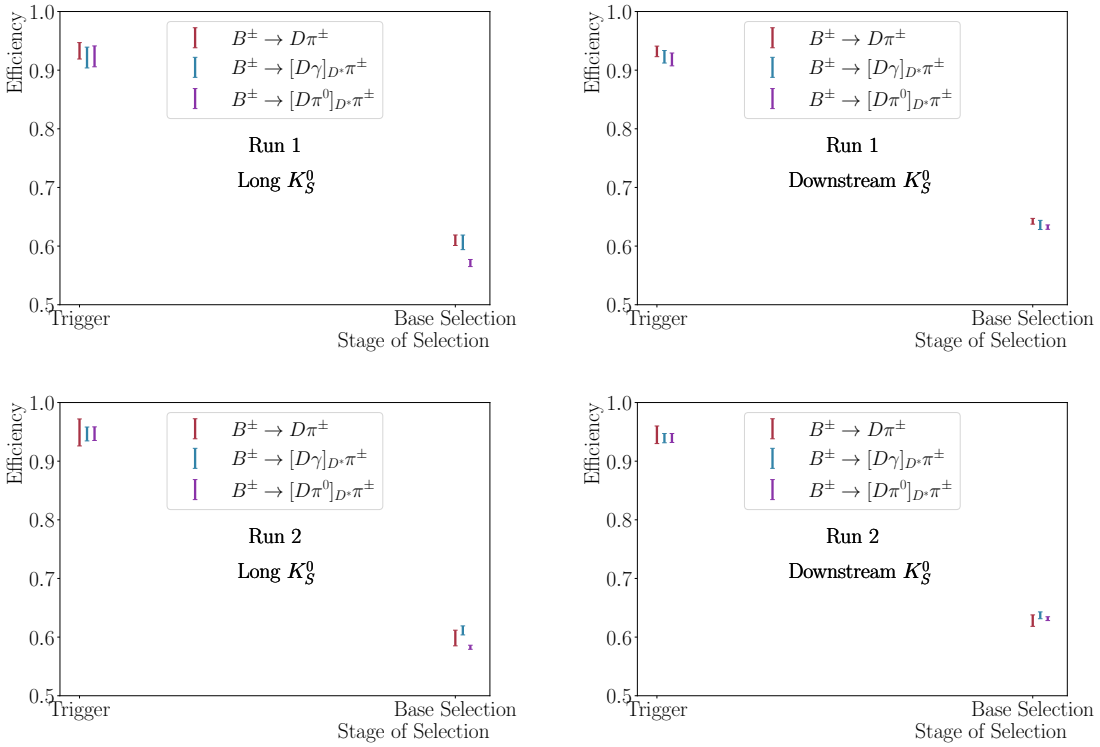

Figure 6.2: Selection efficiencies at the trigger and base selection stages for (left) long K^0_S candidates, (right) downstream K^0_S candidates, (top) Run 1, and (bottom) Run 2.

decays. The reuse of the selection here is validated as the efficiencies do not vary significantly between the signal decays and the background from $B^\pm \to D\pi^\pm$ decays.

6.2 | Boosted Decision Tree

The cut-based initial selection removes background components efficiently if the signal and background distribution in the selection variables are well-separated. There are a number of variables for which these distributions differ in shape but overlap. A BDT is a machine learning algorithm which uses correlations between

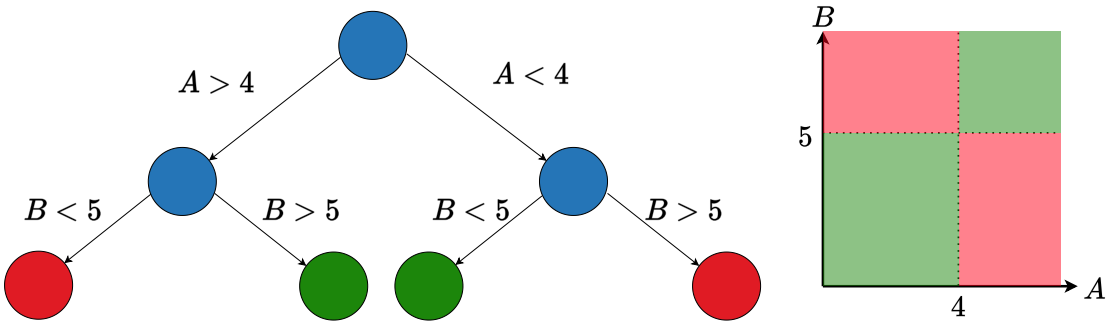

Figure 6.3: Illustration of (left) a decision tree for arbitrary cuts on variables, A and B, leading to the classification of events as signal or background indicated in green and red, respectively, as well as their (right) in the two-dimensional space for A and B.

input variables to discriminate between signal and background [96]. Using signal and background training samples, a decision tree, as illustrated in Fig. 6.3, can be used to classify events as signal or background using a sequence of selection requirements based on the input variables. This produces an N-dimensional space (for N input variables), as shown in Fig. 6.3, of labelled signal and background events which are used to assess the discriminating power of the decision tree. Multiple decision trees can be used sequentially (thus producing a boosted decision tree) where at each step events that were incorrectly classified have increased weights [97]. Once the BDT has been trained, it is applied to a test sample to check for overtraining. This may occur when there are too many input variables and the training sample is too small, such that the BDT uses statistical fluctuations to classify events.

In this analysis, the BDT is implemented using the TMVA toolkit [98] and re-used from the analysis in Ref. [45]. It is trained using $B^{\pm} \to [K^0_S\pi^+\pi^-]_D\pi^{\pm}$ decays, separately for long and downstream K^0_S candidates since input distributions are expected to differ. The signal sample is taken from simulation for

$B^{\pm} \to [K^0_S \pi^+ \pi^-]_D \pi^{\pm}$ decays for Run 1 and Run 2. The background sample consists of candidates from the high $m(Dh)$ sideband (5800–7000 MeV/c^2), which is predominantly combinatorial background. Candidates in each of these samples are evenly split by `eventNumber` to separate odd events, used for training, and even events for testing. The input variables for the BDT are summarised in Tab. 6.3, as determined for the work in Ref. [45], and are ranked by importance for long K^0_S candidates. The importance of a variable can differ between long and downstream K^0_S candidates. In particular, the largest differences are for variables associated with the K^0_S meson where the presence or lack of VELO tracks can alter the distribution of the variable. In Tab. 6.3, the BDT variables which have not yet been defined are:

- θ_{DIRA}: the angle between the flight distance and momentum vectors of a particle,
- p_T asymmetry for the $B^{\pm}$ meson defined as $(p_T^B - p_T^{\text{cone}})/(p_T^B + p_T^{\text{cone}})$ where p_T^{cone} is the the sum of the p_T of all other tracks in a cone of radius 1.5 units around the $B^{\pm}$ candidate,
- χ^2_{IP}: the difference in χ^2 of the PV fit with and without a particle,
- 'Distance of closest approach' between pairwise combinations of particles from a decay vertex.

As mentioned, the same BDT trained for the analysis in Ref. [45] (which is detailed in Ref. [99]) is used here. This is because candidates are reconstructed in the same way and the BDT is used to reduce combinatorial background. To

ensure this is valid for the signals in this analysis, distributions of the most important variables for long K^0_S mesons can be compared between simulation for $B^\pm \to D\pi^\pm$, $B^\pm \to [D\gamma]_{D^*}\pi^\pm$, and $B^\pm \to [D\pi^0]_{D^*}\pi^\pm$ decays, as well as data in the high $m(Dh)$ sideband (5800–7000 MeV/c^2) representing a background-enriched sample. This is shown in Fig. 6.4, for $\log(\rho)$ of the B meson which uses the radial distance of the B vertex to the beam line, $\log(p_T)$ of the companion hadron, and $\log_{10}(1-\cos(\theta_{\mathrm{DIRA}}))$ of the K^0_S and D meson. The plots show that the distributions in simulation are very similar regardless of whether or not there is a D^* meson in the decay. These distributions are also very different to that of the background-enriched sample. Therefore, $B^\pm \to D\pi^\pm$ decays can be used as a proxy for the signal in this analysis and the same BDT trained for the analysis in Ref. [45] is applicable here.

The BDT response is shown in Fig. 6.5 and was determined in Ref. [99]. There is good separation between signal and combinatorial background and the similarity of the BDT output distributions between the training and test samples suggest little overtraining. In Fig. 6.5, the logarithmic y-scale plot for the downstream K^0_S candidates shows some signal at a BDT output of -1. The analysis in Ref. [45] found this was due to random track combinations in the simulation sample which could not be removed, and this had a negligible impact on performance in the analysis.

Table 6.3: BDT input parameters ranked by importance for long K^0_S candidates from the analysis in Ref. [45] as given in Ref. [99].

Parameter	**Importance for long/downstream K^0_S candidates (Rank for downstream K^0_S candidates)**	**Description**
log10(1-Ks_DIRA_BPV)	7.2 % / 3.5 % (16)	$\log(1-\cos(\theta_{\mathrm{DIRA}}))$ of the K^0_S meson
log(Bu_RHO_BPV)	5.7 % / 5.5 % (5)	Radial distance from B vertex to beam line
log(Bach_PT)	5.2 % / 6.9 % (1)	Transverse momentum of the companion hadron
log10(1-D0_DIRA_BPV)	4.9 % / 5.8 % (4)	$\log(1-\cos(\theta_{\mathrm{DIRA}}))$ of the D meson
log10(1-Bu_DIRA_BPV)	4.9 % / 6.4 % (3)	$\log(1-\cos(\theta_{\mathrm{DIRA}}))$ of the $B^\pm$ meson
log(D0_RHO_BPV)	4.8 % / 5.3 % (6)	Radial distance from D vertex to beam line
Bu_PTASY_1.5	4.7 % / 4.9 % (7)	p_T asymmetry for the $B^\pm$ meson
log(D0_PT)	4.7 % / 6.6 % (2)	Transverse momentum of the D meson
log(Bu_constD0KSPV_CHI2NDOF)	4.2 % / 4.5 % (9)	χ^2/d.o.f of the DTF
log(Bu_FDCHI2_OWNPV)	3.9 % / 4.1 % (11)	χ^2_{FD} of the $B^\pm$ meson
log(max_Ksh1h2_IPCHI2_OWNPV)	3.9 % / 3.0 % (20)	Maximum χ^2_{IP} of the K^0_S decay products
log(D0_IPCHI2_OWNPV)	3.8 % / 3.3 % (17)	χ^2_{IP} of the D meson
log(min_Ksh1h2_IPCHI2_OWNPV)	3.7 % / 0.9 % (26)	Minimum χ^2_{IP} of the K^0_S decay products
log(Bu_P)	3.7 % / 3.9 % (12)	Momentum of the $B^\pm$ meson
log(Bu_IPCHI2_OWNPV)	3.6 % / 4.6 % (8)	χ^2_{IP} of the $B^\pm$ meson
Bu_MAXDOCA	3.6 % / 3.3 % (18)	'Distance of closest approach' for $B^\pm$ vertex
log(Bach_IPCHI2_OWNPV)	3.3 % / 4.3 % (10)	χ^2_{IP} of the companion hadron
log(Bu_PT)	3.3 % / 3.7 % (14)	Transverse momentum of the $B^\pm$ meson
log(max_h1h2_IPCHI2_OWNPV)	3.1 % / 3.8 % (13)	Maximum χ^2_{IP} of the D decay products
log(min_h1h2_IPCHI2_OWNPV)	3.0 % / 3.4 % (19)	Minimum χ^2_{IP} of D decay products
log(Ks_VTXCHI2DOF)	2.9 % / 2.3 % (21)	χ^2 of the vertex fit for the K^0_S meson
D0_MAXDOCA	2.9 % / 1.0 % (25)	'Distance of closest approach' for the D vertex
log(D0_VTXCHI2DOF)	2.7 % / 1.6 % (24)	χ^2 of the vertex fit for D meson
log(D0_P)	2.7 % / 1.8 % (22)	Momentum of the D meson
log(Bach_P)	2.2 % / 3.6 % (15)	Momentum of the companion hadron
log(Bu_VTXCHI2DOF)	1.8 % / 1.7 % (23)	χ^2 of the vertex fit for the $B^\pm$ meson

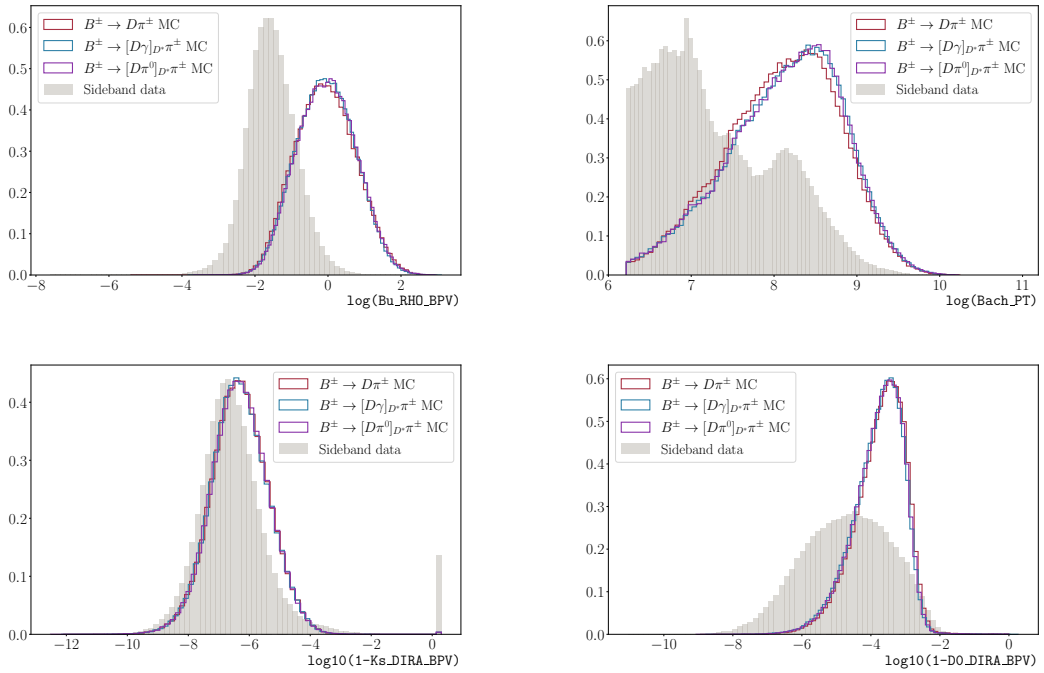

Figure 6.4: Normalised distributions from simulation for $B^\pm \to D\pi^\pm$ (in red), $B^\pm \to [D\gamma]_{D^*}\pi^\pm$ (in blue), $B^\pm \to [D\pi^0]_{D^*}\pi^\pm$ (in purple), and in high $m(Dh)$ sideband data (in grey) for the most important input variables for long K^0_S mesons: (top, left) the logarithm of the radial distance between the B meson vertex and the beam line, and (top, right) $\log(p_T)$ of the companion hadron, as well as the $\log_{10}(1-\cos(\theta_{\text{DIRA}}))$ of (bottom, left) the K^0_S meson and (bottom, right) the D meson.

6.2.1 | BDT Working Point

The working point of the BDT is re-optimised because the signal from partially reconstructed $B^\pm \to D^*h^\pm$ decays is at a lower $m(Dh)$ range compared to the signal in Ref. [45]. This means that the signal in the present work is more susceptible to the combinatorial background. Only working points tighter than those in Ref. [45] are tested because loosening the BDT requirement was shown not

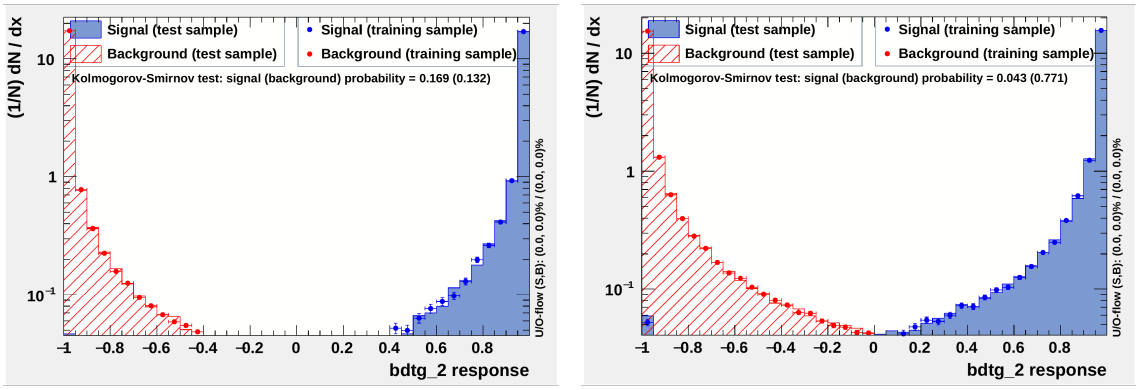

Figure 6.5: Reproductions of the BDT response from Ref. [99] with training and testing samples in logarithmic y-scale for (left) long and (right) downstream K^0_S candidates.

to significantly improve the signal efficiency [45]. The optimal working point is determined using a pseudodata study with the aim to maximise sensitivity to γ.

This pseudodata study requires a full description of all signal and background contributions, which are discussed in Ch. 7. The optimisation was therefore repeated as the analysis evolved. The procedure is as follows. First, the full data sample is split by Run 1 or Run 2 and K^0_S candidate type, and the BDT requirement under testing is applied. Then, the global fit is performed to each data sample to determine the signal and background yields. Using these yields, pseudodata are generated and fitted in the *CP* fit. At generation, inputs for the *CP* observables are taken from the latest LHCb γ combination [47]. The fitted *CP* observables are then interpreted to determine γ and the corresponding statistical uncertainty. The statistical uncertainties are averaged over 100 pseudodatasets, and are shown in Fig. 6.6 for each BDT requirement tested.

Figure 6.6 shows that there is a small improvement to the sensitivity of the analysis when tightening the BDT requirement, and therefore the tightest work-

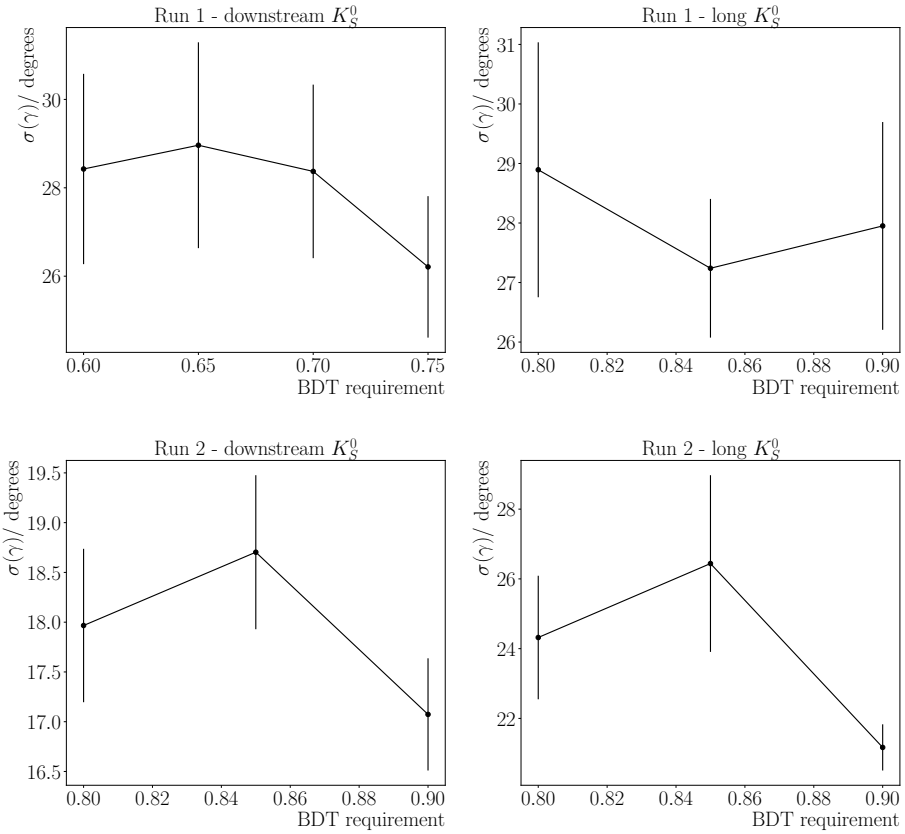

Figure 6.6: Variation in mean uncertainty on γ at different BDT requirements determined using pseudodata for separate data-taking runs and K^0_S candidate types.

ing points are used in this analysis, as shown in Tab. 6.4. A different working point is necessary for data with downstream K^0_S candidates collected in Run 1 to ensure similar signal-to-background ratios between all data sets. This ratio differs between long and downstream K^0_S candidates because a different BDT is trained for each and it differs between Run 1 and Run 2 due to differences in trigger selections when candidates are reconstructed.

Table 6.4: BDT working points for Run 1, Run 2, and different K^0_S candidate types.

	Run 1	**Run 2**
Long K^0_S	0.9	0.9
Downstream K^0_S	0.75	0.9

6.2.2 | BDT Efficiency

The BDT efficiencies on the signal components are shown in Fig. 6.7 with the $B^\pm \to D\pi^\pm$ component, on which the BDT was trained, for comparison. The efficiencies do not vary significantly between the data categories, indicating that different working points are necessary to ensure similar BDT performance. The efficiencies on the signal components are around 85–90%. Therefore 10–15% could be gained, at most, by retraining the BDT on the partially reconstructed signal if the performance of BDT were perfect. However, this is not true as the efficiency on the $B^\pm \to D\pi^\pm$ component suggests. The difference in efficiency for the signal and $B^\pm \to D\pi^\pm$ component is 3%, and therefore only a 3% efficiency gain would be achievable. This validates the re-use of the BDT from Ref. [45] in the present work.

6.3 | Particle Identification

Following the BDT, the remainder of the selection requirements in Tab. 6.1 refer to particle identification. The `IsMuon` cuts refer to activity in the muon chambers, and together with the `PIDe` selection, suppress semi-leptonic background contributions. The PID requirement on the charged kaon from the D decay is used to increase signal purity and reduces contributions from mis-identified $D \to K^0_S\pi^\pm h^\mp$ decays.

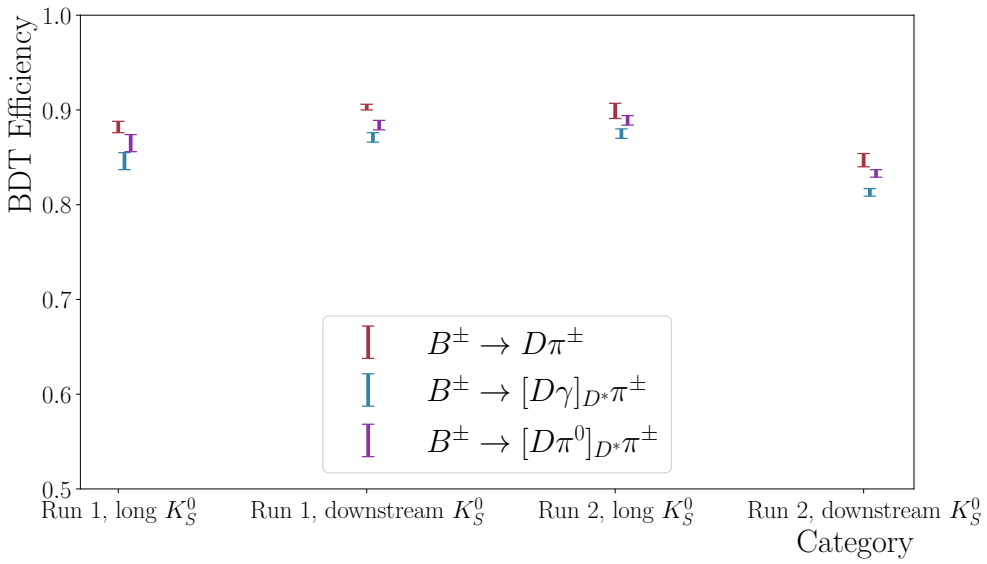

Figure 6.7: BDT efficiencies on signal components, and for reference the fully reconstructed $B^\pm \to D\pi^\pm$ background, split by Run 1, Run 2 and K^0_S candidate type.

The final part of Tab. 6.1 refers to PID requirements on the companion hadrons. These requirements do not remove events from the analysis, but instead separate the data into the $D\pi$ and DK modes. Therefore, this varies the size of the crossfeed component from mis-identified companion hadrons. The working point of this PID requirement is tightened for this analysis compared to Ref. [45] where a requirement at 4 was used. When studying a partially reconstructed $B^\pm \to D^*h^\pm$ signal, the $m(Dh)$ distribution is broader, therefore the associated crossfeed is also broader, and a tighter PID requirement is necessary. The plots in Fig. 6.8 show the variations in the signal and crossfeed components when the PID requirement is varied. The plot labelled $D\pi \to DK$ is the crossfeed from true pions misidentified as kaons. When the PID requirement for a kaon is tightened, the crossfeed component in the DK mode is reduced, resulting in a purer

$B^{\pm} \to D^{*}K^{\pm}$ sample. The plot labelled $DK \to DK$ shows the signal in the DK sample, that is true kaons identified as kaons. Tightening the PID requirement for a kaon lowers the efficiency for kaons to be correctly identified. Overall, tightening the `PIDK` requirement moves events from the DK to the $D\pi$ mode. Therefore, as shown in the plots labelled $D\pi \to D\pi$ and $DK \to D\pi$, the efficiency for correctly identifying pions increases and the crossfeed component in the $B^{\pm} \to D^{*}\pi^{\pm}$ sample increases. This means there is a compromise between purity and efficiency to be made, as shown in Tab. 6.5.

6.3.1 | PID Working Point

Similarly to the optimisation of the BDT working point, a pseudodata study is used and this requires a full description of all signal and background components. For this study, PID efficiencies are determined using PIDCALIB2 [100], an LHCb software package which uses calibration samples to determine PID efficiencies as a function of momentum and pseudorapidity, as will be discussed in Ch. 6.3.2. Simulation events in similar kinematic regions are weighted by these efficiencies and used to determine the $m(Dh)$ distributions of signal and background components, as well as their associated crossfeed components. The combinatorial background is modelled separately by an exponential function where the slope is measured in the high $m(Dh)$ sideband in data and extrapolated to the fit region (4900–5600 MeV/c^2). Pseudodata are then generated for the *CP* fit using these mass distributions and fitted. When doing so, the yields of the crossfeed components are parameterised in terms of those for the correctly identified components and scaled for PID efficiencies and the removal of events from the $m(Dh)$

Table 6.5: Signal efficiency and purity in the $B^{\pm} \to D^{*}K^{\pm}$ sample for different PID requirements.

	PID requirement			
	6	**8**	**10**	**12**
Efficiency (%)	81	76	72	67
Purity (%)	78	87	92	95

Table 6.6: Average statistical uncertainty on γ for different PID requirements from the pseudodata study.

	PID requirement			
	6	**8**	**10**	**12**
Fit Error on γ (°)	9.83	9.69	9.63	9.46

fit range due to the PID requirement. The yield for the combinatorial background is taken from those found in Ref. [45] and scaled between PID requirements using data in the high $m(Dh)$ sideband. The fitted *CP* observables are then interpreted in terms of γ and the average statistical uncertainty on γ over 100 pseudodatasets is calculated, as shown in Tab. 6.6.

In Tab. 6.6, the uncertainty on the fit error on γ is around 10%. Therefore, although there is no significant improvement in sensitivity by tightening the PID requirement, there is a clear trend indicating the tightest reasonable kaon PID requirement on the $B^{\pm} \to D^{*}K^{\pm}$ signal maximises sensitivity to γ. This is because the $B^{\pm} \to D^{*}\pi^{\pm}$ sample has an order of magnitude higher yield. Therefore, any increase of $B^{\pm} \to D^{*}K^{\pm}$ crossfeed events in the $B^{\pm} \to D^{*}\pi^{\pm}$ sample has a negligible effect on the $B^{\pm} \to D^{*}\pi^{\pm}$ purity. In contrast, reducing $B^{\pm} \to D^{*}\pi^{\pm}$ crossfeed in the $B^{\pm} \to D^{*}K^{\pm}$ sample improves its purity and sensitivity to γ.

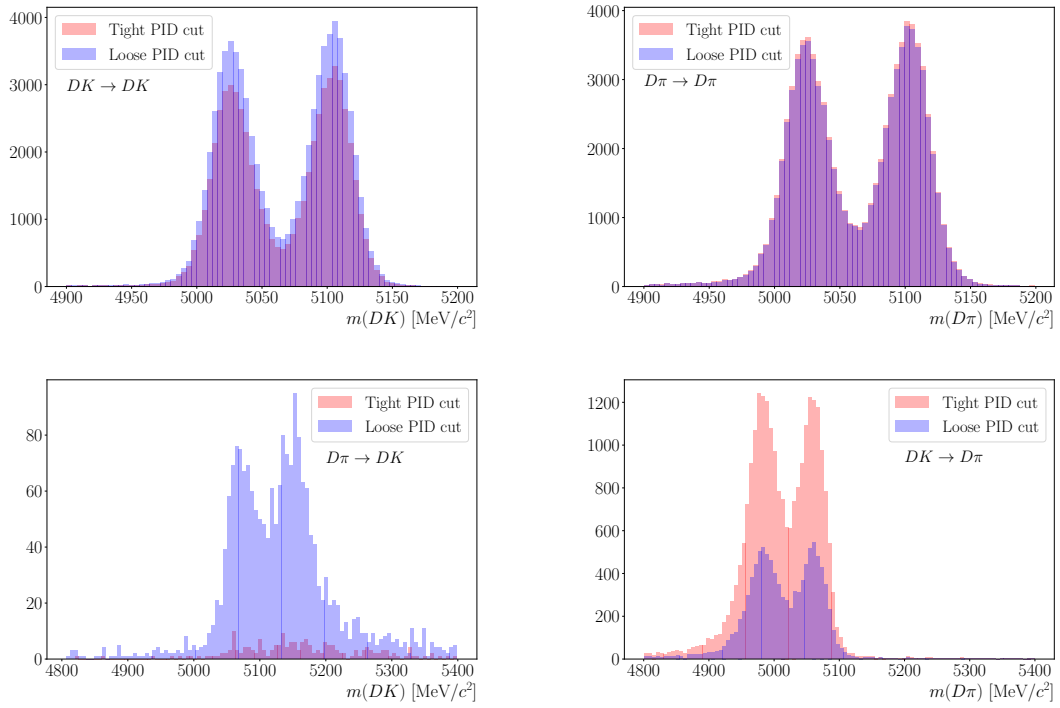

Figure 6.8: Changes in $m(Dh)$ distributions for loose and tight PID requirements in $B^{\pm} \to D^*(\to D\pi^0)h^{\pm}$ decays for (top, left) the DK signal in the DK channel, (top, right) the $D\pi$ signal in the $D\pi$ channel, (bottom, left) the $D\pi$ crossfeed in the DK channel, and (bottom, right) the DK crossfeed in the $D\pi$ channel.

6.3.2 | PID Efficiencies

The PID efficiencies are estimated using the PIDCALIB2 software package [100] instead of applying the selection to simulation samples. It is non-trivial to model PID variables in simulation as they depend on not only kinematics, detector occupancy, and alignment, but also temperature, gas pressure, and beam conditions [100]. Therefore, a data-driven method is used with calibration samples.

The calibration sample for kaon-pion identification uses $D^{*+} \to [K^-\pi^+]_{D^0}\pi^+$ decays, where the charge on the pion from the D^* decay tags the flavour of the D meson, and the kaon and pion from the D meson are distinguished using their

charges. A two-dimensional mass fit is performed to the calibration sample using the $m(D)$ and $m(D^* - D)$ distributions to extract signal sWeights [101]. The PID efficiency is then calculated using the ratio of the sum of the signal sWeights before and after applying a PID selection. These efficiencies are determined for a number of kinematic bins in momentum and pseudorapidity.

The PID efficiency for a specific simulation sample is then found by weighting the calibration sample in each momentum and pseudorapidity bin [100],

$$w_i = \frac{R_i}{C_i} \times \frac{R}{C}, \tag{6.3}$$

where $R_i(C_i)$ is the number of tracks in the simulation (calibration) sample in the i^{th} kinematic bin, and $R(C)$ is the total number of tracks in the simulation (calibration) sample. The PID efficiency in each kinematic bin for the simulation sample is calculated as the efficiency for the calibration sample multiplied by the weights, w_i.

In this analysis, simulation samples are generated using signal $B^\pm \to D^* h^\pm$ decays and have the full selection and BDT applied. Separate samples are used for each companion hadron and each K^0_S candidate type. However, all samples are generated in the $D \to K^0_S \pi^+ \pi^-$ final state and the resulting efficiencies are shared with the $D \to K^0_S K^+ K^-$ mode. This is because, as found in studies for the analysis in Ref. [45], the PID efficiencies are similar regardless of the D-decay mode. Figure 6.9 shows these PID efficiencies per kinematic bin in the (p, η) phase space of the kaon for $B^\pm \to [D\pi^0]_{D^*} K^\pm$ simulation samples for a PID requirement of `PIDK` > 12.

These PID efficiencies are used to weight simulation events in order to parameterise the mass distributions of the signal and misidentified crossfeed com-

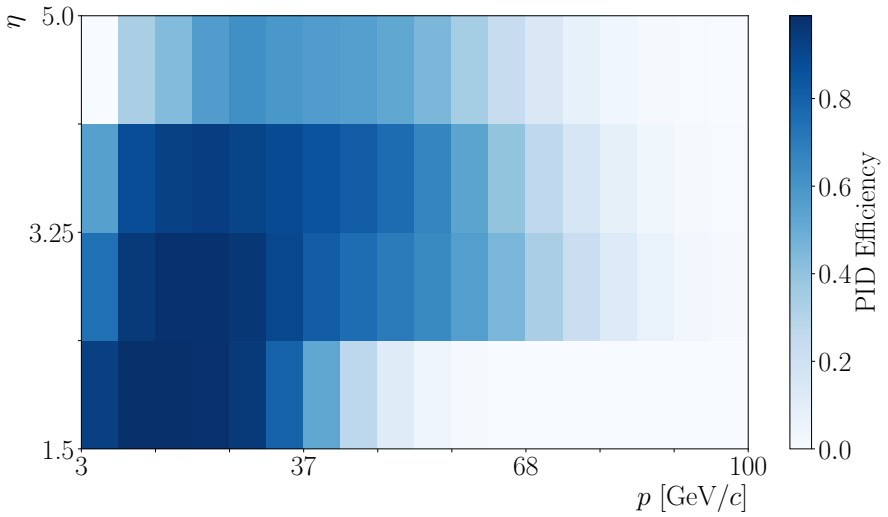

Figure 6.9: Variation in PID efficiency across the (p, η) phase space for $B^{\pm} \to [D\pi^0]_{D^*} K^{\pm}$ signal for a PID requirement at 12.

ponents. The efficiencies are then averaged over the kinematic phase space as well as over Run 1 and Run 2 and used to parameterise yields in the global fit. The resulting efficiencies are shown in Tab. 6.7.

In Tab. 6.7, there are 3 sources of uncertainty on the PID efficiencies which are added in quadrature. The uncertainty due to the choice of the (p, η) binning is assessed using 4 alternative binning schemes and the standard deviation of these is the associated uncertainty. The systematic uncertainty due to the use of the sWeights procedure is estimated to be an absolute value of 0.1% [100]. Finally, the statistical uncertainty due to the finite size of the simulation sample is assessed by bootstrapping [102] the efficiency calculation 500 times.

Table 6.7: Signal PID efficiencies averaged over Run 1 and Run 2 and given as percentages.

Decay Mode	ϵ_{PID} (%)	
	Downstream K^0_S	Long K^0_S
$B^\pm \to [D\gamma]_{D^*}\pi^\pm$	99.7 ± 0.1	99.7 ± 0.1
$B^\pm \to [D\pi^0]_{D^*}\pi^\pm$	99.7 ± 0.1	99.7 ± 0.1
$B^\pm \to [D\gamma]_{D^*}K^\pm$	68.2 ± 0.6	67.6 ± 0.4
$B^\pm \to [D\pi^0]_{D^*}K^\pm$	67.3 ± 0.6	65.9 ± 0.4

6.4 | Final Sample

In the final sample there are instances where more than one candidate is reconstructed per event and may share tracks. To remove such candidates, they are identified by finding candidates with the same `eventNumber` and `runNumber` for each combination of the B decay, D decay, K^0_S candidate type, and magnet polarity in the fit region, 4900–5600 MeV/c^2. Then, one of these candidates is randomly chosen to be retained.

The resulting number of candidates reconstructed as $B^\pm \to DK^\pm$ is approximately 40,000 and as $B^\pm \to D\pi^\pm$ is around 700,000. The $B^\pm \to DK^\pm$ candidates reconstructed in the $D \to K^0_S\pi^+\pi^-$ final state with downstream K^0_S mesons is shown in Fig. 6.10 for the fit region. The fully reconstructed $B^\pm \to DK^\pm$ peak can be seen clearly at around 5270 MeV/c^2, and the double peak structure of the signal from partially reconstructed $B^\pm \to [D\pi^0]_{D^*}K^\pm$ decays is seen in the region 4950–5150 MeV/c^2. However, the purity in this region is not comparable to that near the fully reconstructed peak. This is evident by the large presence of events around 4900 MeV/c^2, for which simulation (shown in Fig. 5.4) indicates very few signal events. Candidates in the signal region (4900–5250 MeV/c^2) can be plotted

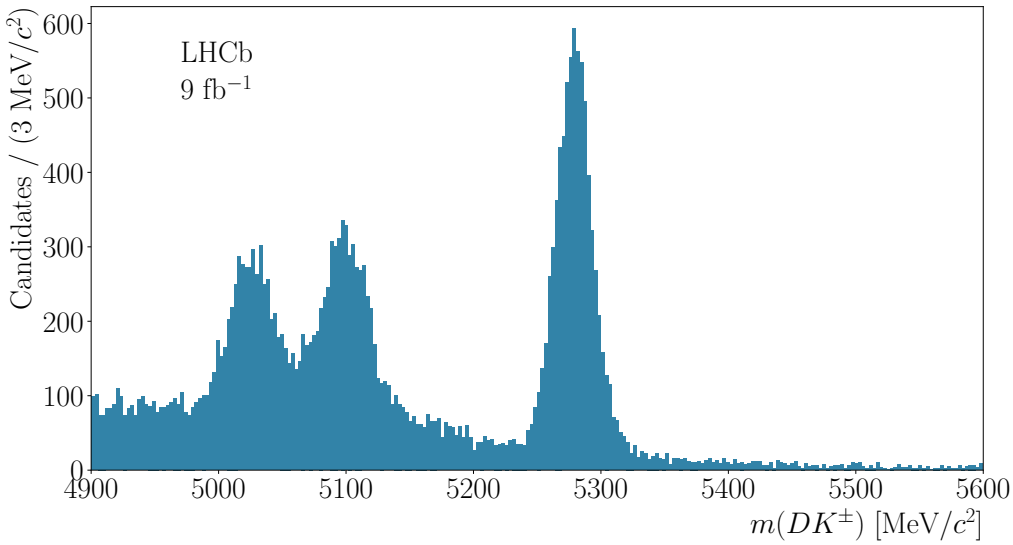

Figure 6.10: Distribution of $m(DK^{\pm})$ for candidates in the fit region (4900–5600 MeV/c^2) reconstructed as $B^{\pm} \to DK^{\pm}$ in the $D \to K^0_S\pi^+\pi^-$ final state with downstream K^0_S mesons.

in the Dalitz phase space, as shown in Fig. 6.11, where large contamination from partially reconstructed backgrounds means *CP*-violation is not directly visible by comparing plots for B^+ and B^- mesons. This also means that especially careful parameterisation is required to differentiate components when performing the global fit.

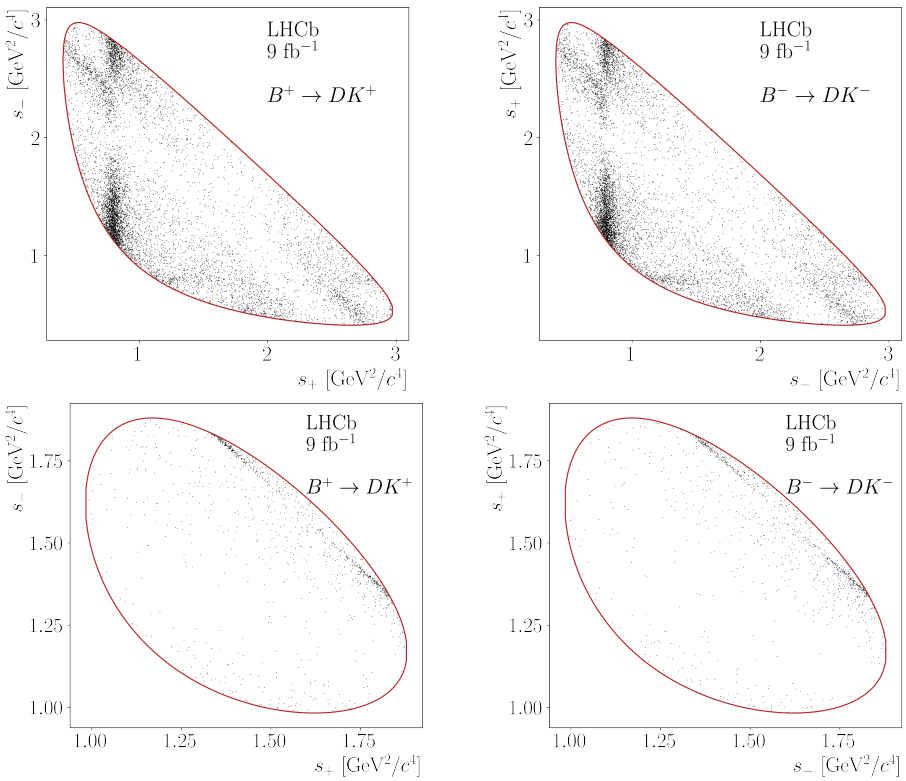

Figure 6.11: Dalitz plot distributions for candidates in the signal region (4900–5250 MeV/c^2) reconstructed as (left) $B^+ \to DK^+$ or (right) $B^- \to DK^-$, in (top) the $D \to K^0_S\pi^+\pi^-$ or (bottom) the $D \to K^0_S K^+ K^-$ final states with downstream K^0_S mesons.

7

Global Fit

In this analysis, *CP*-violation is measured by examining yield variations over D-decay Dalitz phase spaces for $B^{\pm}$ meson decays. This is determined by fitting the $m(Dh)$ spectrum in every Dalitz plot bin separately for B^{+} and B^{-} decays. As the mass distribution can also vary depending on the B decay, D decay, and K^0_S candidate type, data are additionally split into these categories. However, this results in 160 categories, in which fitting every mass shape parameter and yield would not be reliable. Therefore, a two-step fit procedure is employed.

First is the global fit. Data are split into 8 categories depending on the B decay, D decay, and K^0_S candidate type, and the $m(Dh)$ spectrum is fitted. All shape parameters and global yields, that is yields over the entire D-decay phase space, are fitted inclusively for $B^{\pm}$ decays. This is followed by the *CP* fit, where data are now additionally split by $B^{\pm}$ charge and Dalitz plot bin. The shape parameters are fixed from the global fit and the global yields are used as normalisation factors. Therefore, only variations of the yields over the Dalitz phase space are fitted, hence determining the *CP* observables. The following chapter describes the parameterisation of the first step, the global fit.

7.1 | Fit Set-Up

The Run 1 and Run 2 data samples for both magnet polarities are combined and split into 8 categories as outlined above. The fit is performed simultaneously across these categories to the $m(Dh)$ range, [4900, 5600] MeV/c^2. This encapsulates all of the partially reconstructed signal candidates, while including a sufficient amount of the combinatorial background above the $B^{\pm}$ meson mass in order to constrain it.

An extended maximum likelihood fit [103] is applied to the resulting data to determine mass shape parameters and global yields. In each category, the $m(Dh)$ spectrum is divided into 250 uniform mass bins to make the fit faster. In a standard maximum likelihood fit, the likelihood is the product of the normalised PDFs at each data point given a set of estimators [103]. Therefore, locating the maximum of this likelihood, determines the most likely estimators, and the shape of the distribution that best describes the data. An extended maximum likelihood fit is similar, except the PDF is not normalised [103]. This means that both the shape and size of the distribution are fitted. In the global fit, these are fitted simultaneously in each of the 8 categories. The total $m(Dh)$ distribution for each category is,

$$P_{\text{tot}}(m|\vec{\theta}) = N_{\text{s}} p_{\text{s}}(m|\vec{\theta}) + \sum_{\text{b}} N_{\text{b}} p_{\text{b}}(m|\vec{\theta}), \tag{7.1}$$

where $p_{\text{s(b)}}(m|\vec{\theta})$ denotes the normalised signal (background) PDF in $m(Dh)$ given a set of parameters, $\vec{\theta}$, and $N_{\text{s(b)}}$ is the associated yield. The total expected yield is found by adding all N_{s} and N_{b} yields and is denoted, $N_{\text{tot}}^{\text{exp}}$. This means that the

total normalised PDF is,

$$p_{\text{tot}}(m|\vec{\theta}) = \frac{1}{N_{\text{tot}}} P_{\text{tot}}(m|\vec{\theta}). \tag{7.2}$$

The data are a set of observed, binned masses, m_i, with an observed yield, N_i^{obs}, in mass bin i. The resulting likelihood function for each category in a mass bin is therefore,

$$\mathcal{L}(m_i|\vec{\theta}) = \left[\prod_i p_i(m_i|\vec{\theta})\right] \left[\prod_i \text{Poisson}(N_i^{\text{obs}}|N_i^{\text{exp}})\right], \tag{7.3}$$

where $p_i(m_i|\vec{\theta})$ is the normalised PDF in bin i. In practice, rather than maximise this likelihood, the negative log-likelihood is minimised,

$$-\ln \mathcal{L}(m_i|\vec{\theta}) = -\left[\sum_i p_i(m_i|\vec{\theta})\right] - \left[\sum_i \text{Poisson}(N_i^{\text{obs}}|N_i^{\text{exp}})\right], \tag{7.4}$$

and this is implemented using RooFit [104].

7.2 | Mass Shape Parameterisation

For each signal and background component, except the combinatorial background, the parameterisation of the $m(Dh)$ distribution is determined using simulation, of which there are 3 types. Simulation produced by LHCb with complete detector description is used to model dominant two-body B decays, including the signals, as well as their associated crossfeed components. Samples for the latter are determined by swapping the mass hypothesis of the companion hadron when reconstructing candidates. When this simulation is used, samples corresponding to Run 1 and Run 2 are combined and weighted by luminosity and beam energy using Ref. [105]. This weighting is used to account for different B-hadron

production cross-sections. The tracks are then additionally weighted by the PID efficiency on the companion hadron in their (p, η) phase-space.

Simulation samples are also generated using RAPIDSIM [90]. This is a fast simulation package and is used to model multi-body decays or less common two-body decays, and their associated crossfeed components. Instead of a full detector description with GEANT4, generated momenta are smeared by Gaussian functions to estimate resolution effects. In general, the backgrounds chosen to be modelled using RAPIDSIM are broad in the $m(Dh)$ spectrum, with widths of the order $100\,\text{MeV}/c^2$ compared to $10\,\text{MeV}/c^2$ for $B^\pm \to Dh^\pm$ decays, one of the narrowest background components modelled using centrally produced LHCb simulation. This means that the resolution difference between simulation and data is negligible for background components modelled using RAPIDSIM.

Finally, simulation samples are also generated using amplitude models fitted using LAURA^{++} [91], a Dalitz plot fitting package. Pseudodatasets are generated from amplitude models to model 3-body B decays, namely $B^0_s \to DK^\pm\pi^\mp$ decays using the amplitude model in Ref. [106], $B^0 \to DK^\pm\pi^\mp$ decays using Ref. [107], and $B^0 \to D\pi^\pm\pi^\mp$ decays using Ref. [108]. The generated four-momenta are then smeared to account for resolution effects. These background components are also very broad in the $m(Dh)$ spectrum, and resolution differences between simulation and data are negligible.

Where RAPIDSIM was used, I generated the simulation samples myself, but samples from LAURA^{++} had already been produced. Simulation samples produced by LHCb were centrally generated but I wrote some of the decay files which specify how the decay proceeds using EVTGEN [109]. The crossfeed components associated with multi-body B decays were modelled using centrally pro-

duced LHCb simulation using the dominant resonances for each background. The contribution from these crossfeed components is very small, therefore it is sufficient to only consider these resonances.

7.2.1 | Mass Shapes

The mass shapes of the signal components and most background contributions can be described using two parameterisations. These are the *HORNSdini* and *HILLdini* mass shapes which parameterise components where either a pion or a photon is not reconstructed. They arise due to the spin-parity of the D^* decay, as detailed in Ch. 5.3, and their functional forms are,

$$p(m) = \int_A^B \mathrm{d}\mu \left(\mu - \frac{A+B}{2}\right)^2 p_{\mathrm{Res}}(m|\vec{\theta}) \left(\frac{1-\zeta}{B-A}\mu + \frac{B\zeta - A}{B-A}\right), \tag{7.5}$$

for the HORNSdini distribution and,

$$p(m) = -\int_A^B \mathrm{d}\mu(\mu - A)(\mu - B) p_{\mathrm{Res}}(m|\vec{\theta}) \left(\frac{1-\zeta}{B-A}\mu + \frac{B\zeta - A}{B-A}\right), \tag{7.6}$$

for the HILLdini distribution. The parameters A and B refer to the kinematic end-points of the decay and ζ describes the variance in the shapes due to reconstruction effects. The resolution function, $p_{\mathrm{Res}}(m|\vec{\theta})$, is described by a set of parameters, $\vec{\theta}$, and the form of this function can differ depending on the shape and size of the component in the fit range. Generally, a single or double Gaussian function is sufficient for broad backgrounds where only tails enter the fit range. However, for components such as the signals, a more complex shape is required and is discussed next.

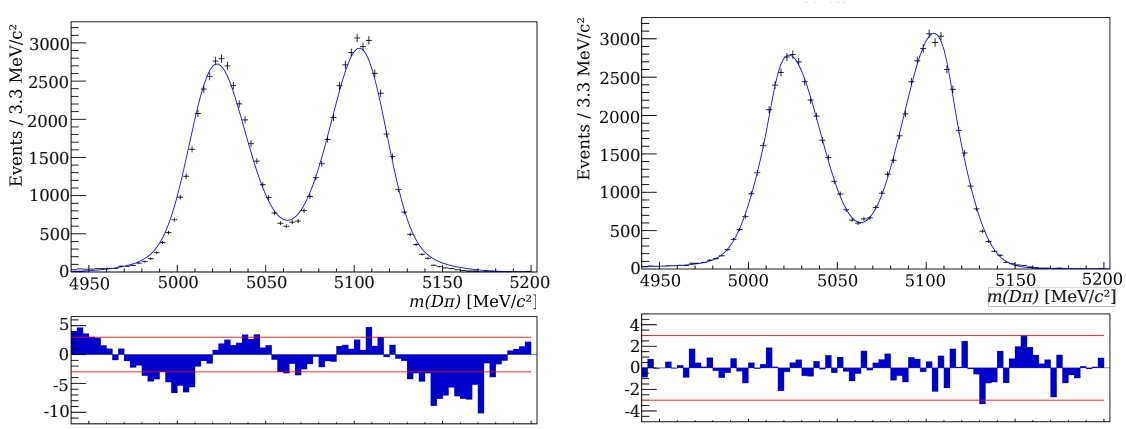

Figure 7.1: Simulated mass distributions of $B^{\pm} \to [D\pi^0]_{D^*}\pi^{\pm}$ decays with long K^0_S mesons. This is fitted with (left) a double Gaussian resolution function and (right) using the mass shape of the fully reconstructed $B^{\pm} \to D\pi^{\pm}$ component as the resolution function.

7.2.2 | Signal Components

7.2.2.1 | $B^{\pm} \to [D\pi^0]_{D^*}h^{\pm}$

The mass shape of the signal component from $B^{\pm} \to [D\pi^0]_{D^*}h^{\pm}$ decays is modelled using the sum of two HORNSdini functions. The choice of resolution function is a key factor for obtaining an accurate fit to simulation. In previous analyses, such as Ref. [46], a double Gaussian function was used. This was not sufficient in this analysis, as shown on the left of Fig. 7.1 as evidenced by the large pull distribution. The pulls are worst at the tails indicating that it is the resolution function which is incorrect and must be re-evaluated.

The work presented in this thesis is one of the first instances where the resolution function is determined by fitting the $m(Dh)$ distribution of the fully reconstructed $B^{\pm} \to Dh^{\pm}$ background, which will be detailed in Ch. 7.2.3.1. In the absence of resolution effects, the mass distribution of this background would be

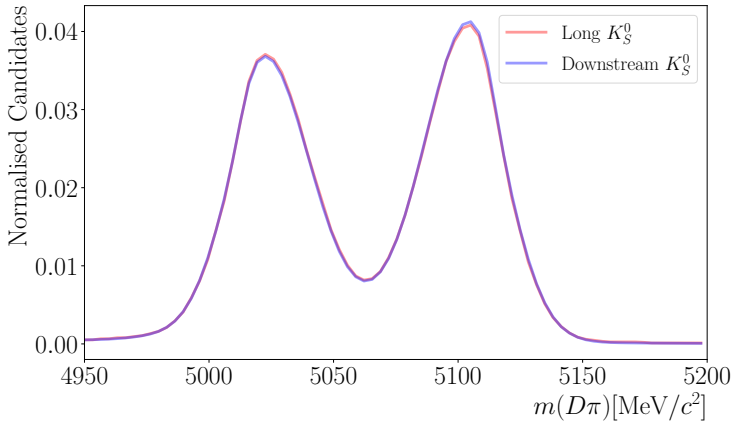

Figure 7.2: Comparison of fit projections for mass distributions of $B^{\pm} \to [D\pi^0]_{D^*}\pi^{\pm}$ decays with downstream (in blue) and long (in red) K^0_S mesons. The fit projections have been normalised and show that the models for downstream and long K^0_S mesons are very similar.

close to a δ-function. Therefore, by fitting the mass peak, resolution effects are calibrated. The resolution is dependent on momentum and therefore varies over the mass fit range. This means that a secondary HORNSdini function is required to allow sufficient freedom in the fit to correctly model the tails of the distribution. This parameterisation significantly improves the fits to simulation, as shown on the right of Fig. 7.1 where pulls are predominantly contained within $\pm 3\sigma$ and do not deviate out of this range for the tails of the distributions. The parameterisations are very similar between the two K^0_S candidate types, as shown in Fig. 7.2. Therefore, only fits for downstream K^0_S mesons are shown, and where possible only fits to the DK sample are included in this chapter. Fits to the $D\pi$ sample are shown in App. A.

The majority of the shape parameters from this simulation fit are subsequently fixed in the fit to data, however, a few vary freely to account for data-simulation resolution differences. These are the ζ parameter, the width of the resolution

function for the core HORNSdini function, and the shift between the two HORNSdini functions. The ζ parameter is shared between all B decays, D decays, and K^0_S candidate types, but there is a separate width parameter for each B decay. This is because, candidates reconstructed as $B^\pm \to DK^\pm$ have a larger companion hadron mass compared $B^\pm \to D\pi^\pm$ candidates, therefore the momentum distribution of the decay products is smaller. This leads to improved resolution and a smaller width parameter. The shift between the HORNSdini functions accounts for resolution differences between simulation and data and is separate for each K^0_S candidate type. This is because long K^0_S candidates have better resolution compared to downstream K^0_S candidates since they are reconstructed with additional information from the VELO.

7.2.2.2 | $B^\pm \to [D\gamma]_{D^*}h^\pm$

The mass shape of the signal component from $B^\pm \to [D\gamma]_{D^*}h^\pm$ is parameterised using a HILLdini function where resolution effects are accounted for using the mass distribution of the fully reconstructed $B^\pm \to Dh^\pm$ background. One of the resulting fits to simulation is shown in Fig. 7.3.

In the fit to data, since the shape of this signal component is broad, the ζ parameter can account for resolution differences between simulation and data and varies separately for each B decay and D decay. However, to ensure a stable fit, these parameters must be fixed. To determine what the new parameters are, an iterative fitting procedure is used until the ζ parameters converge.

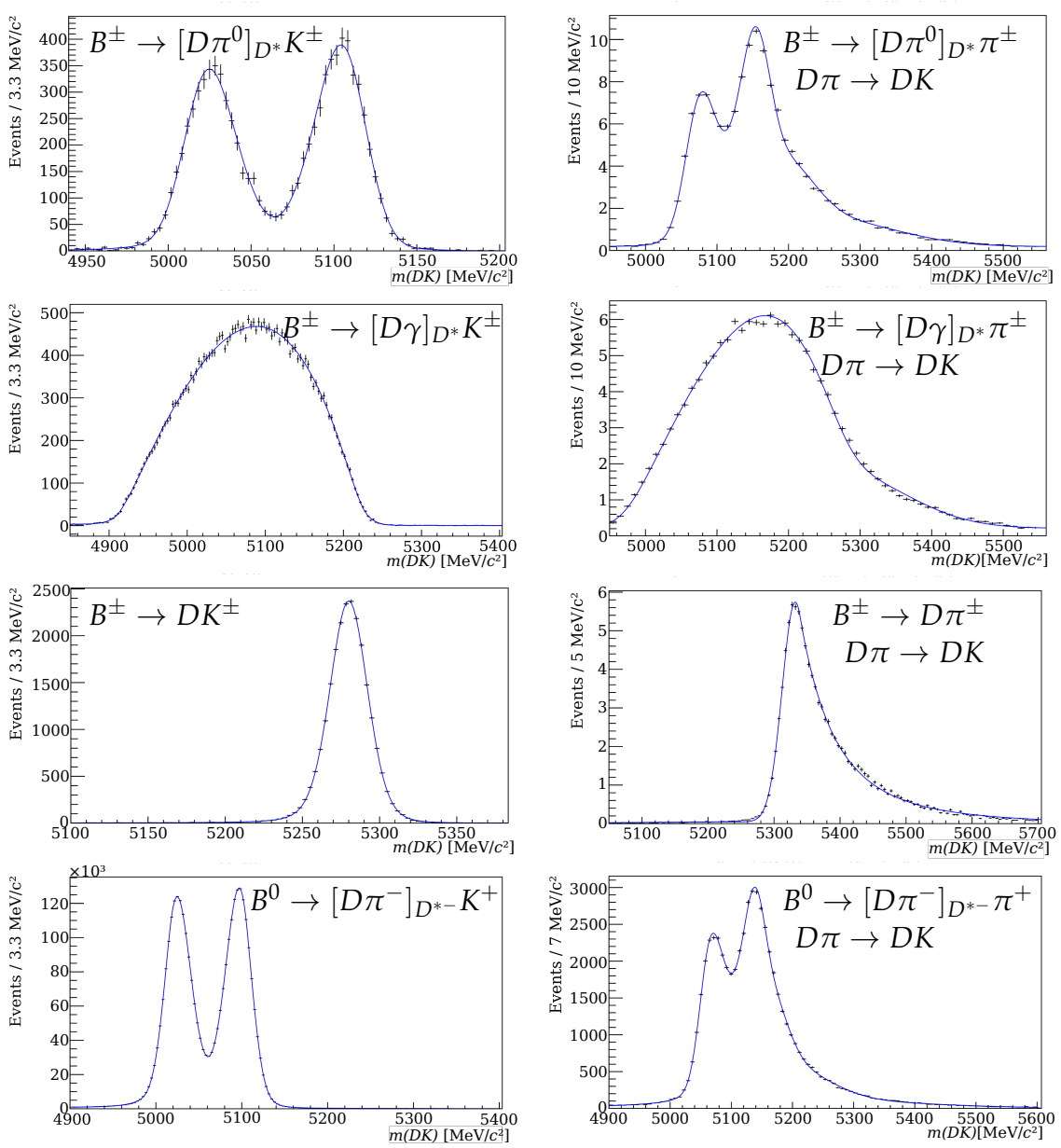

Figure 7.3: Simulated mass distributions of (left) $B^\pm \to [D\pi^0]_{D^*} K^\pm$, $B^\pm \to [D\gamma]_{D^*} K^\pm$, $B^\pm \to DK^\pm$, and $B^0 \to [D\pi^-]_{D^{*-}} K^+$ decays where the companion hadron is correctly identified and (right) the associated $D\pi \to DK$ crossfeed components, with downstream K^0_S candidates. The projections of the fit results are overlaid.

7.2.2.3 | $B^{\pm} \to [D\pi^0/\gamma]_{D^*}h^{\pm}$ Crossfeed

Crossfeed components from signal decays with misidentified companion hadrons also contribute to the measurement of γ. These are modelled using simulation samples where the mass hypothesis of the companion hadron is swapped and events are weighted by PID misidentification rates. The mass distributions of the crossfeed components associated with $B^{\pm} \to [D\pi^0]_{D^*}h^{\pm}$ decays are described using a HORNSdini function with a quadruple Gaussian resolution function. The crossfeed components associated with $B^{\pm} \to [D\gamma]_{D^*}h^{\pm}$ decays, are modelled using a HILLdini function with a triple Gaussian resolution function. In both cases, these shapes were determined empirically by adding Gaussian functions to model the resolution until a sufficient fit to simulation was obtained. Examples of these fits are shown in Fig. 7.3. These crossfeed components are relatively small with negligible resolution differences between simulation and data. Thus, in the fit to data, all shape parameters are fixed from the fit to simulation.

7.2.3 | Background Components

The following section provides the mass shape parameterisations for each of the backgrounds. First, the background component from fully reconstructed $B^{\pm} \to Dh^{\pm}$ is discussed, which is one of the largest background components. There is also a discussion of the numerous partially reconstructed backgrounds. These are grouped by similar families of decay and how they are modelled. Backgrounds from $B_s^0 \to \overline{D}^0 K^- \pi^+$, $B^0 \to \overline{D}^0 K^- \pi^+$, and $B^0 \to \overline{D}^0 \pi^- \pi^+$ are discussed together, and are modelled using LAURA++. This is followed by backgrounds from $B^{\pm} \to Dh^{\pm}\pi^0$, $B^{\pm} \to D\pi^{\pm}\pi^{\mp}\pi^{\pm}$, and $\Lambda_b^0 \to Dp\pi^-$ decays, which are mod-

elled using RapidSim. This is also used for backgrounds from $B \to D^* h\pi$ and $B_s^0 \to D^* K^\mp \pi^\pm$ decays, which are explained next. Then, the parameterisation of the crossfeed components for these backgrounds is explained. Finally, the combinatorial background is discussed.

7.2.3.1 | $B^\pm \to Dh^\pm$

The mass shape of the fully reconstructed $B^\pm \to Dh^\pm$ background is modelled using the sum of a modified Gaussian function [45] and a single Gaussian function. The shape is parameterised as,

$$p(m) = \begin{cases} f \exp\left(\frac{-(\Delta m)^2(1+\beta(\Delta m)^2)}{2\sigma^2+\alpha_L(\Delta m)^2}\right) + (1-f)p_G(m|\mu,\sigma), & \text{if } \Delta m < 0 \\ f \exp\left(\frac{-(\Delta m)^2(1+\beta(\Delta m)^2)}{2\sigma^2+\alpha_R(\Delta m)^2}\right) + (1-f)p_G(m|\mu,\sigma), & \text{if } \Delta m > 0, \end{cases} \tag{7.7}$$

where $p_G(m|\mu,\sigma)$ is a Gaussian function, α_L, α_R, and β model the tails, and f corresponds to the fraction of the modified Gaussian function in the total mass shape. The parameter Δm is defined as $m - m_B$, where m_B is the B-meson mass. This shape was first used in Ref. [45], and found to be a more accurate fit for the $B^\pm \to Dh^\pm$ mass distribution compared to a double Crystal Ball function or a number of Gaussian functions. An example of the fit to simulation is shown in Fig. 7.3. In the subsequent fit to data, the width parameters vary separately for different B decays and K_S^0 candidate types due to expected resolution differences similar to the signal components.

7.2.3.2 | Partially Reconstructed Backgrounds

One of the most prominent background contributions is from $B^0 \to [\overline{D}^0 \pi^-]_{D^{*-}} h^+$ decays (and the charge-conjugate) where the pion from the D^* decay is not re-

constructed. This means that the mass shape for this background decay is very similar to that of the signal component, $B^{\pm} \to [D\pi^0]_{D^*}h^{\pm}$ decays and is parameterised identically. An example of fit to simulation is shown in Fig. 7.3. In the subsequent fit to data, resolution parameters between this background and the signal $B^{\pm} \to [D\pi^0]_{D^*}h^{\pm}$ decays are shared.

For all remaining partially reconstructed backgrounds, the mass distributions are considerably wider than the components described thus far. This means they are parameterised using either a HORNSdini or HILLdini function where a single or double Gaussian function is sufficient for the resolution function. For these broad distributions, resolution differences between simulation and data are small and all shape parameters from simulation fits are fixed in the fit to data.

There are a number of background contributions with complex resonant structures which are modelled using simulation samples generated with LAURA^{++} and appropriate amplitude analyses. Namely, background components from $B^0_s \to \overline{D}^0 K^- \pi^+$ decays with the amplitude analysis in Ref. [106], $B^0 \to \overline{D}^0 K^- \pi^+$ decays with Ref. [107], and $B^0 \to \overline{D}^0 \pi^- \pi^+$ decays with Ref. [108], where charge-conjugates are implied. The mass distributions of these components are modelled using a HORNSdini function with a single Gaussian resolution function. In contrast to other components described thus far, this relatively simple resolution function provides a sufficient fit to the simulation sample. This is because the sample is generated using LAURA^{++}, where generated momenta are smeared to model resolution effects. The resulting simulation fits are shown in Fig. 7.4. Of note are the simulation fits for the $B^0 \to \overline{D}^0 \pi^- \pi^+$ decays, where there are two fits, one to the $m(\overline{D}^0 \pi^-)$ sample and the other to $m(\overline{D}^0 \pi^+)$, which are subsequently combined in equal proportions for the fit to data. The simula-

tion generated by LAURA^{++} is flavour-specific, and therefore to account for the charge-conjugates of all resonances in the amplitude analysis, the $m(\overline{D}^0\pi^-)$ and $m(\overline{D}^0\pi^+)$ samples are fitted separately and combined.

There are also background components with multiple resonances but no existing amplitude analyses, meaning LAURA^{++} cannot be used. Instead, these are modelled by estimating the largest expected resonance structures using amplitude analyses for similar decays. There is no amplitude analysis for $B^\pm \to DK^\pm\pi^0$ decays. However, a sample can be generated by estimating the leading contributions to the $B^\pm \to DK^\pm\pi^0$ component. To do this, the fit fractions for resonant and non-resonant structures in the amplitude analysis of $B^0 \to \overline{D}^0K^-\pi^+$ decays [107] are scaled by the ratios of branching fractions [18] for the corresponding B^0 and $B^\pm$ decays. From this, a RAPIDSIM simulation sample is generated consisting of 99% $B^\pm \to DK^{*\pm}(892)$ decays and 1% $B^\pm \to D^*(2400)K^\pm$ decays. It is subsequently fitted using a HORNSdini function with a Gaussian resolution function, as shown in Fig. 7.4.

Similarly, the background contribution from $B^\pm \to D\pi^\pm\pi^0$ decays is modelled using simulation generated using RAPIDSIM for $B^\pm \to D\rho^\pm$ decays and a non-resonant component. These are fitted using a HORNSdini and HILLdini function, respectively, each with a Gaussian resolution function, as shown in Fig. 7.4. Here, each of the contributions are shown separately, since this is a large background component and the fit to data is sensitive to the relative amounts of these contributions which therefore varies freely.

There is also a background component from $B^\pm \to D\pi^\pm\pi^\pm\pi^\mp$ decays where two pions are not reconstructed. Here, only the contribution where two *like-sign* pions are missed is considered. This is because in the B^+ sample the favoured

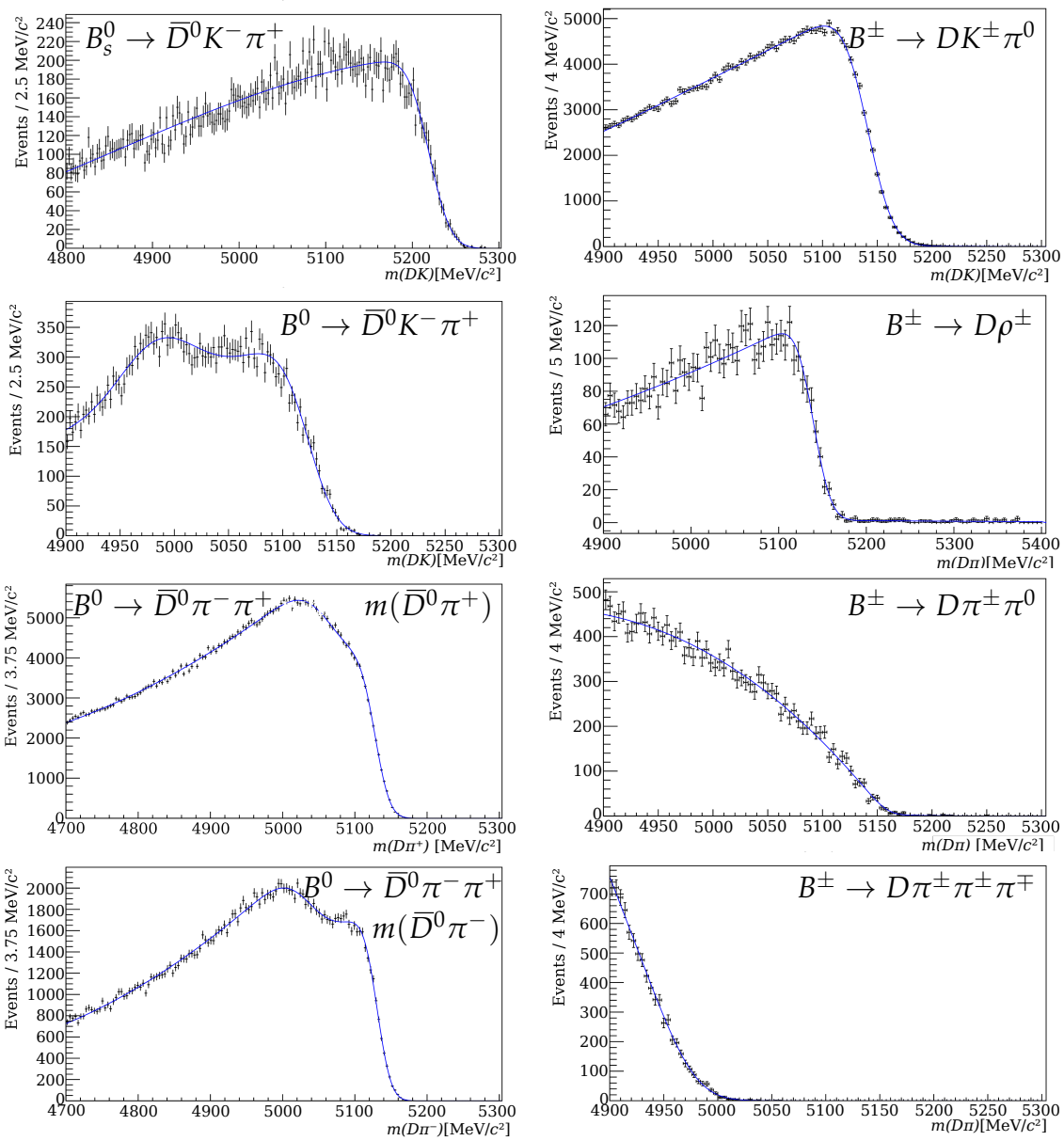

Figure 7.4: Simulated mass distributions of (left) $B_s^0 \to \overline{D}^0 K^- \pi^+$, $B^0 \to \overline{D}^0 K^- \pi^+$, and $B^0 \to \overline{D}^0 \pi^- \pi^+$ decays. Distributions for (right) $B^\pm \to DK^\pm \pi^0$ decays, $B^\pm \to D\pi^\pm \pi^0$ decays from the $B^\pm \to D\rho^\pm$ resonance, $B^\pm \to D\pi^\pm \pi^0$ decays from non-resonant contributions, and $B^\pm \to D\pi^\pm \pi^\pm \pi^\mp$ decays from the $B^\pm \to Da_1^\pm$ resonance. The projections of the fit results overlaid.

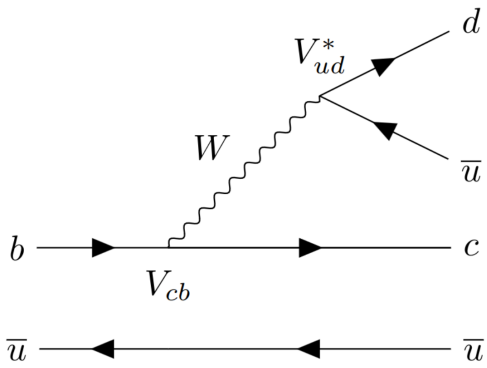

Figure 7.5: Feynman diagram of Cabibbo-favoured $B^- \to D^0[\pi^-[\pi^+\pi^-]_{\rho^0}]_{a_1^-}$ decays.

decay is via $\overline{D}^0$ mesons. The dominant contribution to the $B^\pm \to D\pi^\pm\pi^\pm\pi^\mp$ component is from $B^\pm \to Da_1^\pm$ decays where, as shown in Fig. 7.5, favoured $B^- \to D\pi^-\pi^+\pi^-$ decays result in D^0 mesons. Here, when the like-sign pions are not reconstructed, these events are reconstructed in the B^+ sample. Hence, this background results in D^0 decays in a sample where the predominant decay is to $\overline{D}^0$. The background where the oppositely charged pions are missed leads to $\overline{D}^0$ decays in the B^+ sample and is therefore a small contribution that can be accounted for by other larger backgrounds with similar mass shapes. The PDF for the $B^\pm \to D\pi^\pm\pi^\pm\pi^\mp$ background is modelled using RapidSim simulation generated using resonant $B^\pm \to D[[\pi^\pm\pi^\mp]_{\rho^0}\pi^\pm]_{a_1^\pm}$ decays. Since only the tail of this background enters the mass fit range, this resonance alone is sufficient to model the background. It is fitted with a HILLdini function as shown in Fig. 7.4.

There is a small background contribution from $\Lambda_b^0 \to Dp\pi^-$ decays where the pion is missed and the proton is misidentified as a kaon and here, only the tail enters the $m(Dh)$ fit region. This background was also included in the measurement of γ using partially reconstructed $B^\pm \to D^*h^\pm$ decays with 2-body D-decays [46],

and since the background is very small the same Gaussian parameterisation is used.

The background contributions from $B \to D^* h\pi$ decays (with either charged or neutral B mesons) are modelled using simulation samples for charged B decays, $B^\pm \to D^*[\pi^\pm\pi^0]_{\rho^\pm}$ and $B^\pm \to D^*[K^\pm\pi^0]_{K^{*\pm}(892)}$. This is because only the tails of the $m(Dh)$ distributions enter the fit range, therefore the shapes are very similar for decays from charged and neutral B mesons. For the DK sample, the mass distributions with a missing photon or pion from the D^* decay are similar and thus the shape for $B^\pm \to [D\gamma]_{D^*}[K^\pm\pi^0]_{K^{*\pm}(892)}$ decays represents all contributions to the $B \to D^*K\pi$ background. For the $D\pi$ sample, as the companion hadron mass is smaller, more of the mass shape is enclosed by the fit range, and the difference in the parameterisation with a missing photon or pion is not negligible. These samples are fitted using HORNSdini and HILLdini functions and are shown in Fig. 7.6.

For $B_s^0 \to [D\gamma/\pi^0]_{D^*}K^\pm\pi^\mp$ decays, the $m(Dh)$ distributions are parameterised using simulation samples for $B_s^0 \to [D\gamma/\pi^0]_{D^*}[K^\pm\pi^\mp]_{K^{*0}}$ decays. Here, a pseudoscalar particle decays to two vector particles, therefore for each D^* decay there is a longitudinal and transverse polarisation to consider. This leads to different mass distributions, as shown in Fig. 7.6, which are fitted using HORNSdini or HILLdini functions. In the fit to data, for each D^* decay, the distributions of the polarisations are combined using $f_L = 0.9 \pm 0.06 \pm 0.03$ [110], the fraction of the longitudinal component.

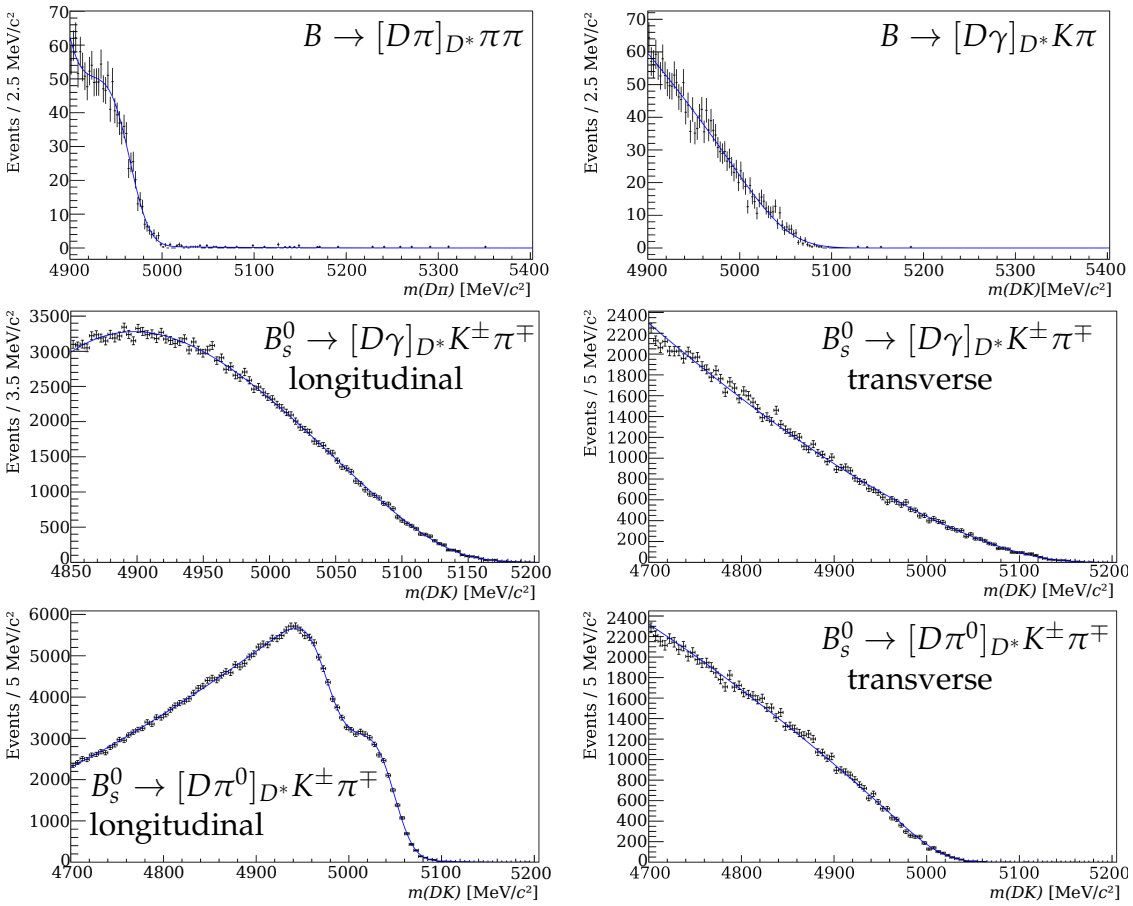

Figure 7.6: Simulated mass distributions of $B \to [D\pi/\gamma]_{D^*}h\pi$ and $B_s^0 \to D^*K^{\pm}\pi^{\mp}$ decays where either a photon or pion is missed for longitudinal and transverse polarisations. The projections of the fit results overlaid.

7.2.3.3 | Crossfeed Components

The crossfeed components associated with partially reconstructed backgrounds are very small. Therefore, for backgrounds with complex resonant structure, simulation generated using only the dominant resonance is sufficient. For some of these components, only the tails of their $m(Dh)$ distribution enter the fit range and a Gaussian function is sufficient to model this. However, in other cases where the fit range covers more of the mass shape, the mass distributions are

determined empirically using either a HORNSdini or HILLdini function with an appropriate number of Gaussian functions to model the resolution. The crossfeed due to the partially reconstructed $B^0 \to [\overline{D}^0\pi^-]_{D^{*-}}h^+$ background decay is modelled using a HORNSdini function with a quadruple Gaussian function for the resolution and is shown in Fig. 7.3. Also shown in this figure is the crossfeed component associated with the fully reconstructed $B^\pm \to Dh^\pm$ background. This is modelled using the sum of two Crystal Ball functions.

All crossfeed components are much smaller than components with correctly identified hadrons. This means that the difference in resolution between simulation and data for the crossfeed components can be neglected without significant impact on the quality of the global fit. Therefore, in the fit to data all shape parameters are fixed using the fits to simulation.

7.2.3.4 | Combinatorial Background

There are a number of different decays and combinations of random tracks which contribute to the combinatorial background. Therefore, in the global fit, it is modelled using an exponential function with a slope and yield which vary separately for each B decay, D decay, and K^0_S candidate type.

7.2.3.5 | Backgrounds that are not included

A number of other backgrounds were considered but not included in the final fit configuration. In some cases, this is because they do not enter the fit range, for example, $B^0_s \to DK^\pm\pi^\mp$ and $B^0 \to DK^\pm\pi^\mp$ decays where the kaon is not reconstructed. In other cases, they are very small backgrounds at the very low end

of the $m(Dh)$ fit region and have mass distributions similar to other components which can account for them. This is true for the crossfeed component associated with $B^{\pm} \to D\pi^{\pm}\pi^{\pm}\pi^{\mp}$ decays and the background from $B^{\pm} \to DK^{\pm}\pi^{\pm}\pi^{\mp}$ where the kaon is not reconstructed. These are omitted from the fit model and are accounted for by the combinatorial background since it is modelled with a freely varying yield.

7.3 | Yield Parameterisation

The yield parameterisation of the signal and background components vary depending on the size of the component and how accurately branching fractions are known. The fully reconstructed $B^{\pm} \to D\pi^{\pm}$ background is a prominent component with a peaking shape in the $m(Dh)$ spectrum. It lies in a region where there are few other components, and as a result, the yield for this component is allowed to vary freely in every category since it can be fitted accurately. For other components, except the combinatorial background which also varies freely in every category, there are three types of yield parameterisation.

If the branching fractions [18] of the decays are known with relatively small uncertainty, then the yield is parameterised in terms of the $B^{\pm} \to D\pi^{\pm}$ yield, $N_{D\pi^{\pm}}$. For example, the yield of the $B^{\pm} \to [D\pi^0]_{D^*}K^{\pm}$ signal component is parameterised as,

$$N_{[D\pi^0]_{D^*}K^{\pm}} = N_{D\pi^{\pm}} \times R^{\mathcal{B}}_{D^*K^{\pm}} \times \mathcal{B}(D^* \to D\pi^0) \times \frac{\epsilon_{[D\pi^0]_{D^*}K^{\pm}}}{\epsilon_{D\pi^{\pm}}}, \tag{7.8}$$

where $R^{\mathcal{B}}_{D^*K^{\pm}}$ is the ratio $\mathcal{B}(B^{\pm} \to [D\pi^0]_{D^*}K^{\pm})/\mathcal{B}(B^{\pm} \to D\pi^{\pm})$ and ϵ encapsulates all efficiencies. This parameterisation is applied for all signal components

and the fully reconstructed background from $B^{\pm} \to DK^{\pm}$ decays. In each of these cases, the ratio of the branching fractions is fixed to their values from the PDG [18]. The yield for the background from $B^0 \to D^{*\mp}h^{\pm}$ decays is parameterised similarly but the ratio of the branching fractions is Gaussian-constrained rather than fixed. This ensures fit stability and is necessary since this background contribution has a very similar shape to the $B^{\pm} \to [D\pi^0]_{D^*}h^{\pm}$ signal. Furthermore, the ratio of the branching fractions can be cross-checked against values from the PDG [18].

There are a number of backgrounds for which branching fractions carry large uncertainties and the parameterisation in Eq. 7.8 would be unreliable. In this case, yields from Ref. [46] are used, which studied $B^{\pm} \to D^*h^{\pm}$ decays with 2-body D-decays, leading to a larger dataset with similar backgrounds to this analysis. The larger dataset enabled more freedom in the yield parameterisations of these background contributions, and therefore can provide a reliable parameterisation here. For example, the yield for the $B_s^0 \to \overline{D}^0 K^-\pi^+$ background can be parameterised as,

$$N(B_s^0 \to \overline{D}^0 K^-\pi^+)_{K_S^0hh} = \frac{N(B_s^0 \to \overline{D}^0 K^-\pi^+)_{\pi K}}{N(B^- \to D^0\pi^-)_{K\pi}} \times N(B^- \to D^0\pi^-)_{K_S^0hh} \quad (7.9)$$

where $N(B^- \to D^0\pi^-)$ refers to the yield of the fully reconstructed $B^- \to D^0\pi^-$ background, and charge conjugates are implied. The subscripts refer to the modes the decays belong to in this analysis and in Ref. [46]:

- K_S^0hh denotes yields in this analysis;
- πK denotes yields in the $D(\to \pi^{\pm}K^{\mp})K^{\pm}$ modes in Ref. [46];
- $K\pi$ denotes yields in the $D(\to K^{\pm}\pi^{\mp})\pi^{\pm}$ modes in Ref. [46].

The yields can be deconstructed into branching ratios and efficiencies. Equation 7.9 is written with explicit D flavours to highlight where the branching ratios with different D flavours cancel; $\mathcal{B}(\overline{D}^0 \to K^+\pi^-) = \mathcal{B}(D^0 \to K^-\pi^+)$ and $\mathcal{B}(\overline{D}^0 \to K^0_S\pi^+\pi^-) = \mathcal{B}(D^0 \to K^0_S\pi^+\pi^-)$. This analysis and Ref. [46] have the same lower limit in the $m(Dh)$ fit range, and the same PID requirements, therefore the following assumption of the ratio of the efficiencies can be assumed to hold;

$$\frac{\epsilon(B^0_s \to [K^0_S hh]_{\overline{D}^0} K^+\pi^-)}{\epsilon(B^- \to [K^0_S hh]_{D^0}\pi^-)} = \frac{\epsilon(B^0_s \to [\pi K]_{\overline{D}^0} K^+\pi^-)}{\epsilon(B^- \to [K\pi]_{D^0}\pi^-)}. \tag{7.10}$$

This assumption was tested using simulation samples for the B^0_s background, as well as other low-mass backgrounds by calculating the ratio of the two sides of the equality. It was found to be consistent with unity within 1–3%, indicating that the assumption is valid.

The parameterisation in Eq. 7.9 uses explicit D flavours and thus is only applicable to decays with negligible global CP asymmetry. There are two decays for which this is not the case, $B^0 \to DK^\pm\pi^\mp$ and $B^0 \to D^*K^\pm\pi^\mp$. For these the yield of the $B^0_s \to \overline{D}^0 K^-\pi^+$ and $B^0_s \to \overline{D}^{*0} K^-\pi^+$ decays are used. For example,

$$\begin{aligned} N(B^0 \to DK^\pm\pi^\mp) = N(B^0_s \to DK^\pm\pi^\mp) \\ \times \frac{\mathcal{B}(B^0 \to DK^\pm\pi^\mp)}{\mathcal{B}(B^0_s \to DK^\pm\pi^\mp)} \times \frac{f_d}{f_s} \times \frac{\epsilon(B^0 \to DK^\pm\pi^\mp)}{\epsilon(B^0_s \to DK^\pm\pi^\mp)}), \end{aligned} \tag{7.11}$$

where $f_{d(s)}$ are fragmentation fractions, the probability that a b-quark is bound to a $d(s)$-quark.

The yields of the crossfeed components, $N_{\text{crossfeed}}$, are fixed to the yield of the correctly identified components, $N_{\text{correct PID}}$, scaled to the misidentification rate,

$$N_{\text{crossfeed}} = N_{\text{correct PID}} \times \frac{1-\epsilon^{\text{PID}}}{\epsilon^{\text{PID}}} \times \frac{\epsilon^{\text{mass}}_{\text{crossfeed}}}{\epsilon^{\text{mass}}_{\text{correct PID}}}. \tag{7.12}$$

In this equation, ϵ^{PID} denotes the PID efficiency, and $\epsilon^{\text{mass}}_{\text{correct PID (crossfeed)}}$ is the efficiency due to the mass fit range for the correctly identified (crossfeed) component. The latter accounts for the fact that when the mass hypothesis of the companion hadron is swapped, the mass shapes skew, shifting events into or out of the mass fit range.

7.4 | Summary

In the global fit, the $m(Dh)$ spectrum is fitted to determine all shape parameters and global yields. The parameters which are allowed to vary in this fit are:

- The width of the resolution function associated with the core HORNSdini functions for the $B^{\pm} \to [D\pi^0]_{D^*}h^{\pm}$ and $B^0 \to [D\pi^{\mp}]_{D^{*\mp}}h^{\pm}$ components.
- The shift between the two HORNSdini functions for the $B^{\pm} \to [D\pi^0]_{D^*}h^{\pm}$ and $B^0 \to [D\pi^{\mp}]_{D^{*\mp}}h^{\pm}$ components.
- The ζ parameter for the $B^{\pm} \to [D\pi^0]_{D^*}h^{\pm}$ and $B^0 \to [D\pi^{\mp}]_{D^{*\mp}}h^{\pm}$ shapes which describes reconstruction effects.
- The width parameters for the $B^{\pm} \to Dh^{\pm}$ shapes.
- The Δm parameter, related to the mean of the $B^{\pm} \to Dh^{\pm}$ shapes.
- The yield of the $B^{\pm} \to D\pi^{\pm}$ component for every D decay and K^0_S candidate type.
- The Gaussian-constrained ratio of branching fractions for $B^0 \to [D\pi^{\mp}]_{D^{*\mp}}\pi^{\pm}$ and $B^{\pm} \to D\pi^{\pm}$ decays.

- The Gaussian-constrained ratio of branching fractions for $B^0 \to [D\pi^\mp]_{D^{*\mp}} K^\pm$ and $B^\pm \to D\pi^\pm$ decays.

- The fraction of the resonant contribution from $B^\pm \to D\rho^\pm$ decays in the $B^\pm \to D\pi^\pm\pi^0$ component.

- The combinatorial yield and shape parameters in all 8 categories.

7.5 | Validation

Pseudoexperiments are used to assess the stability and performance of the global fit and determine if there are any biases due to the parameterisation. To do this, pseudodata are generated using the fit model described above and fitted to the same model. Then pull distributions,

$$\mathcal{P} = \frac{\mathcal{O}_{\text{fit}} - \mathcal{O}_{\text{gen}}}{\sigma_{\text{fit}}}, \tag{7.13}$$

are determined using the generated and fitted values, $\mathcal{O}_{\text{gen(fit)}}$, and the error on the fitted values, σ_{fit}. From 1000 pseudodata sets, 99% converge successfully, indicating very good fit stability. The means and widths of the pull distributions are calculated and if the fit is unbiased, pull means are consistent with 0, and if the associated statistical uncertainty is correctly estimated the pull width is consistent with 1. This is true for all parameters, and one example is shown in Fig. 7.7. However, there are two combinatorial slope parameters which show small biases, as shown in Fig. 7.8. This is taken into account when determining the systematic uncertainty due to the mass shape parameterisation in Ch. 8.

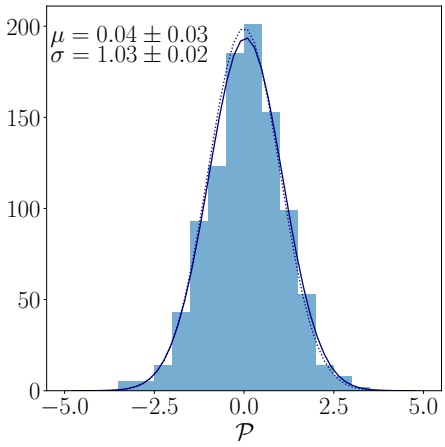

Figure 7.7: Pull distribution for the yield of $B^{\pm} \to D\pi^{\pm}$ decays in the $D \to K^0_S\pi^+\pi^-$ final state with downstream K^0_S candidates. The solid line shows a Gaussian function with the mean (μ) and width (σ) of the pull distribution, and the dashed line indicates a normal Gaussian function corresponding to a correctly estimated parameter with no fit biases.

7.6 | Results

The $m(Dh)$ distribution and projections of the fit results are shown in Figs. 7.9–7.12, where the residuals indicate a good fit to data. The signal and background yields over the fit region are quoted in Tab. 7.1. In general, the yields of most components are determined with smaller uncertainties than their Poisson error. This is because these yields are parameterised in terms of ratios of other yields which have been fixed from external measurements [18, 46] or simulation. The yields of the fully reconstructed $B^{\pm} \to Dh^{\pm}$ background can be cross-checked using the results of Ref. [45] where they were treated as signal, and are consistent given selection differences between the two analyses. The Gaussian-constrained yield parameters for the $B^0 \to [\overline{D}^0\pi^-]_{D^{*-}}h^+$ background can be cross-checked and are found to be consistent with PDG values [18] for the ratio of the branching

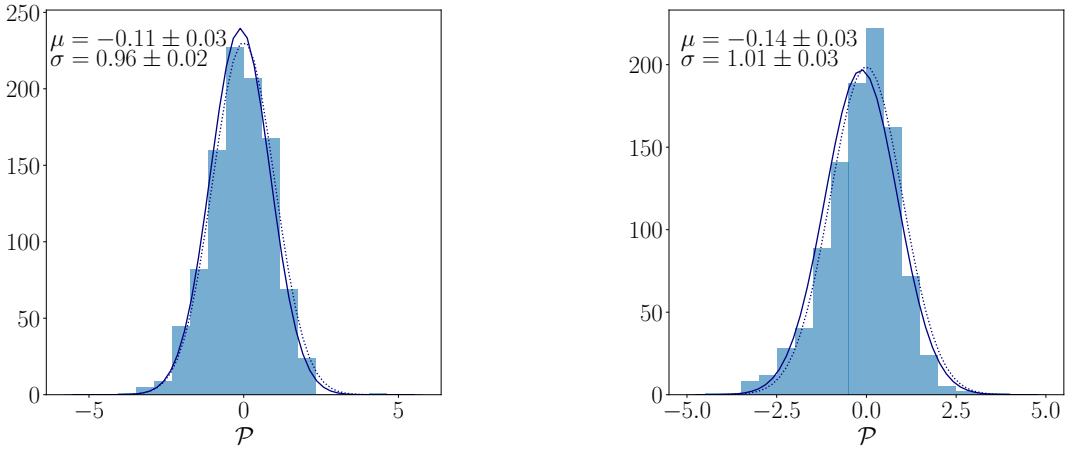

Figure 7.8: Pull distributions for combinatorial slope parameters in the DK sample with (left) $D \to K^0_S\pi^+\pi^-$ decays and downstream K^0_S candidates and (right) $D \to K^0_S K^+ K^-$ decays and long K^0_S candidates. The solid line shows a Gaussian function with the mean (μ) and width (σ) of each pull distribution, and the dashed line indicates a normal Gaussian function corresponding to a correctly estimated parameter with no fit biases.

fractions in the yield parameterisation.

Using the results of the global fit, shape parameters are fixed in each Dalitz plot bin for the *CP* fit, and the global yields are used as normalisation factors in order to determine how each component is distributed over the Dalitz phase space, thus measuring *CP*-violation.

Table 7.1: Signal and background yields from the global fit over the full mass range, 4900–5600 MeV/c^2. All yields and uncertainties are rounded to the nearest integer and uncertainties of 1 mean one or fewer. Backgrounds that are not written explicitly in this table are included in the 'Other Backgrounds' component.

		Reconstructed as:	
D decay	Component	$B^\pm \to DK^\pm$	$B^\pm \to D\pi^\pm$
$D \to K^0_S\pi^+\pi^-$	$B^\pm \to D^*[D\pi^0]K^\pm$	6244 ± 12	2716 ± 5
	$B^\pm \to D^*[D\pi^0]\pi^\pm$	340 ± 1	113 170 ± 229
	$B^\pm \to D^*[D\gamma]K^\pm$	3144 ± 6	1247 ± 2
	$B^\pm \to D^*[D\gamma]\pi^\pm$	166 ± 1	60 285 ± 121
	$B^\pm \to DK^\pm$	10 398 ± 21	4726 ± 9
	$B^\pm \to D\pi^\pm$	590 ± 1	196 804 ± 398
	Other backgrounds	10 402 ± 105	206 664 ± 592
	Combinatorial background	1343 ± 147	15 177 ± 706
$D \to K^0_S K^+K^-$	$B^\pm \to D^*[D\pi^0]K^\pm$	790 ± 3	344 ± 1
	$B^\pm \to D^*[D\pi^0]\pi^\pm$	43 ± 1	14 327 ± 65
	$B^\pm \to D^*[D\gamma]K^\pm$	397 ± 1	157 ± 1
	$B^\pm \to D^*[D\gamma]\pi^\pm$	21 ± 1	7636 ± 34
	$B^\pm \to DK^\pm$	1527 ± 6	694 ± 2
	$B^\pm \to D\pi^\pm$	88 ± 1	29 786 ± 135
	Other backgrounds	1573 ± 15	31 278 ± 115
	Combinatorial background	263 ± 46	4413 ± 261

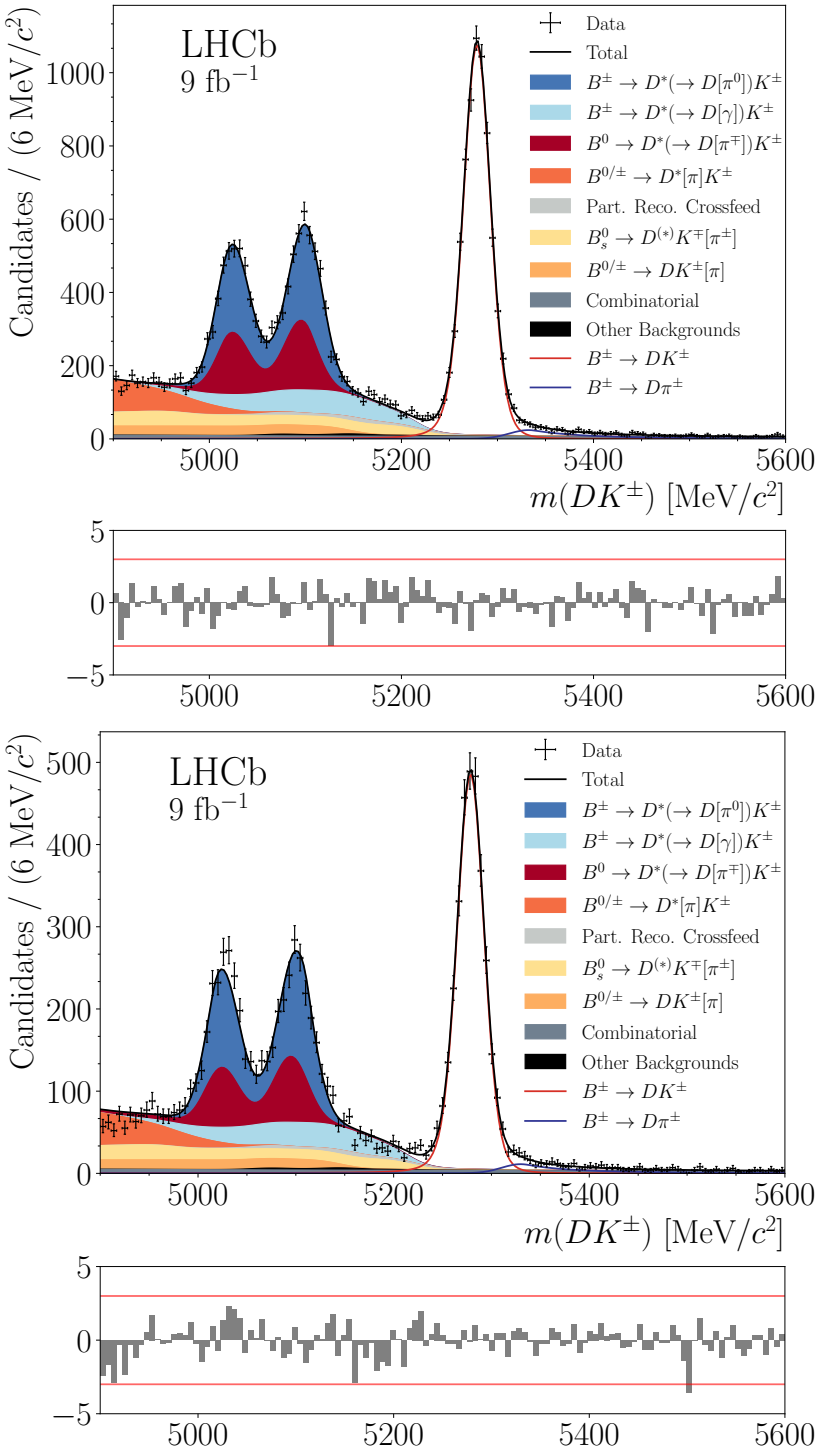

Figure 7.9: Mass distributions for DK samples with $D \to K^0_S\pi^+\pi^-$ decays reconstructed with (top) downstream K^0_S candidates and (bottom) long K^0_S candidates. The projections of the fit results are overlaid. In the legend, particles in square brackets are not reconstructed.

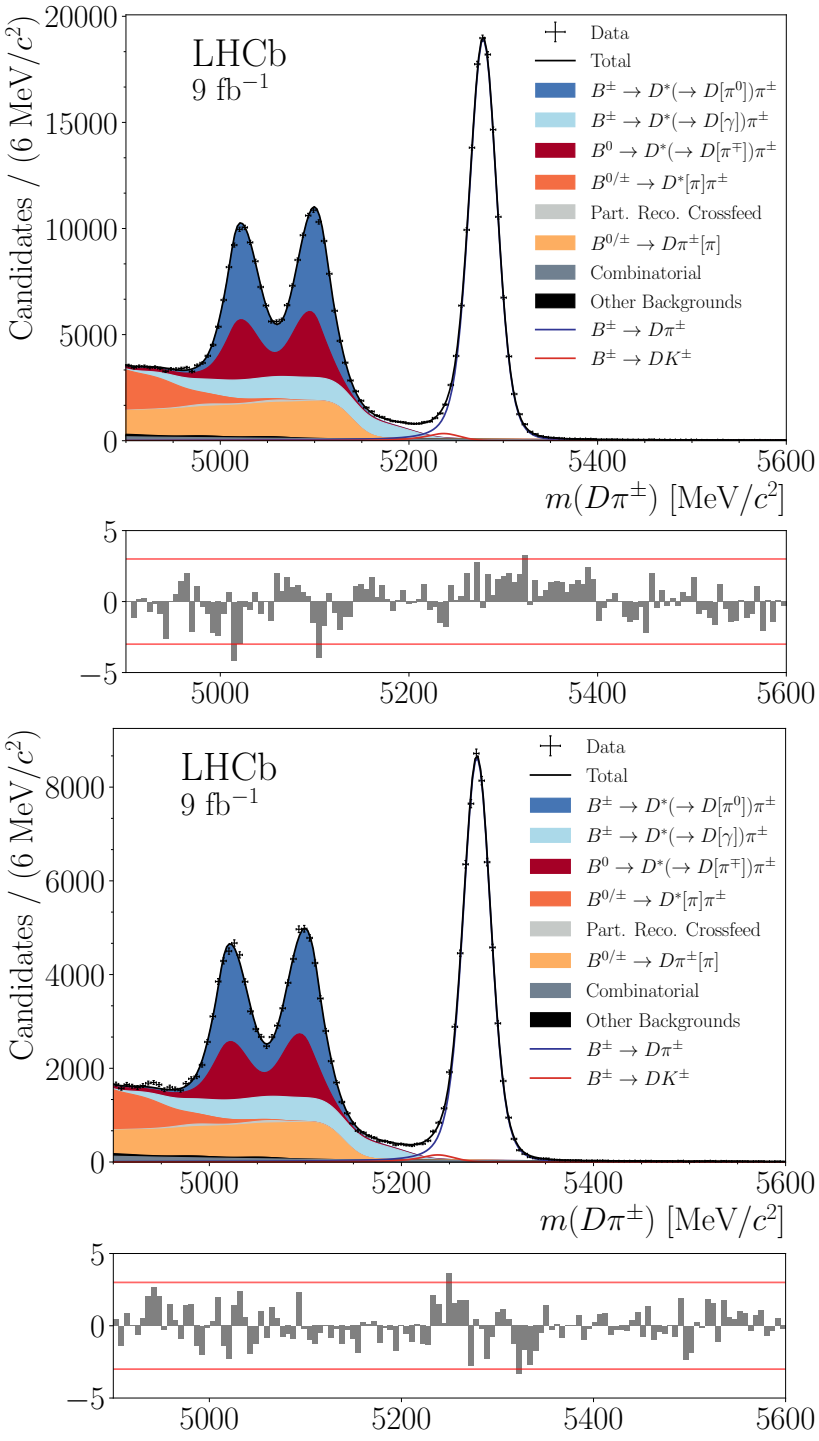

Figure 7.10: Mass distributions for $D\pi$ samples with $D \to K^0_S\pi^+\pi^-$ decays reconstructed with (top) downstream K^0_S candidates and (bottom) long K^0_S candidates. The projections of the fit results are overlaid. In the legend, particles in square brackets are not reconstructed.

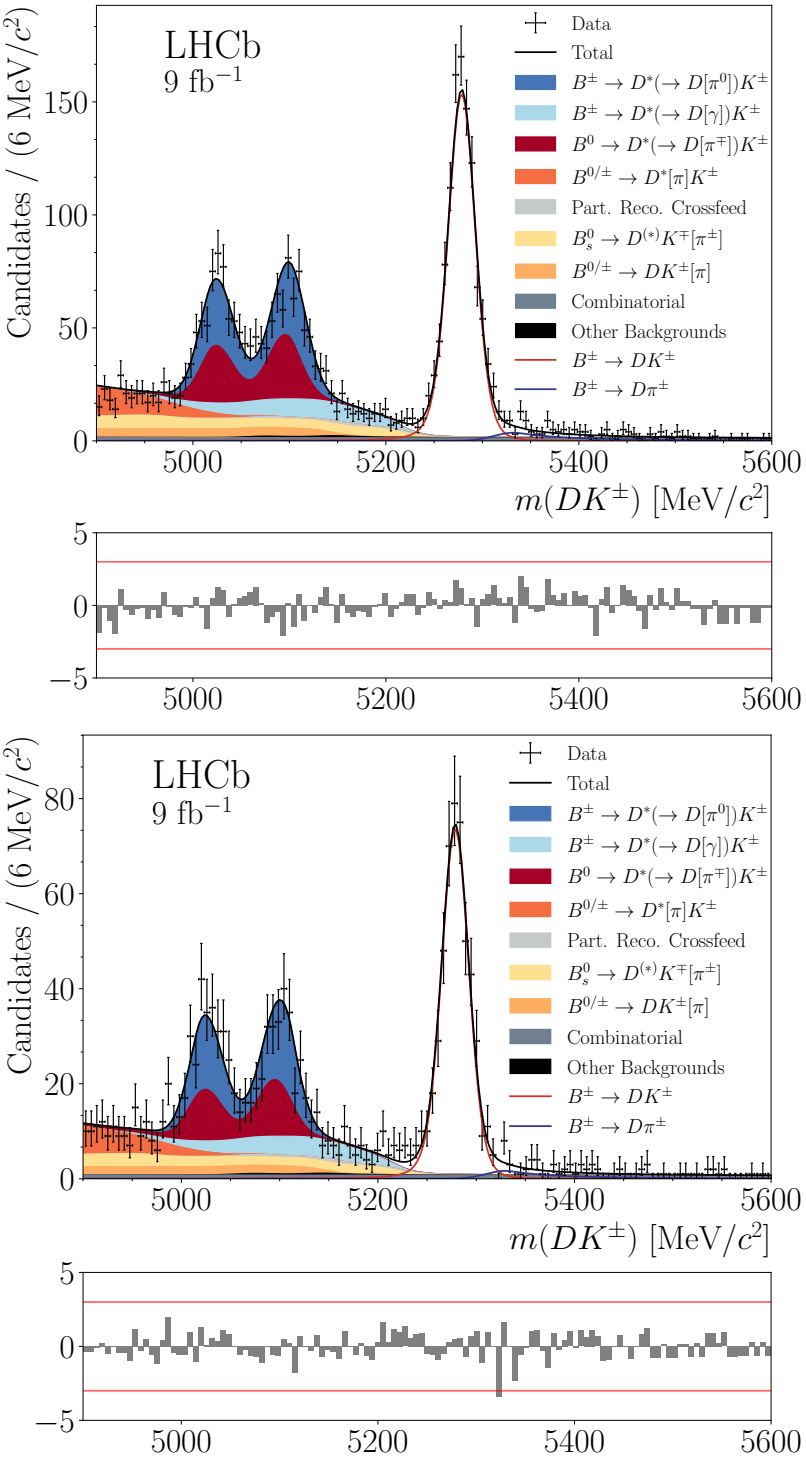

Figure 7.11: Mass distributions for DK samples with $D \to K^0_S K^+ K^-$ decays reconstructed with (top) downstream K^0_S candidates and (bottom) long K^0_S candidates. The projections of the fit results are overlaid. In the legend, particles in square brackets are not reconstructed.

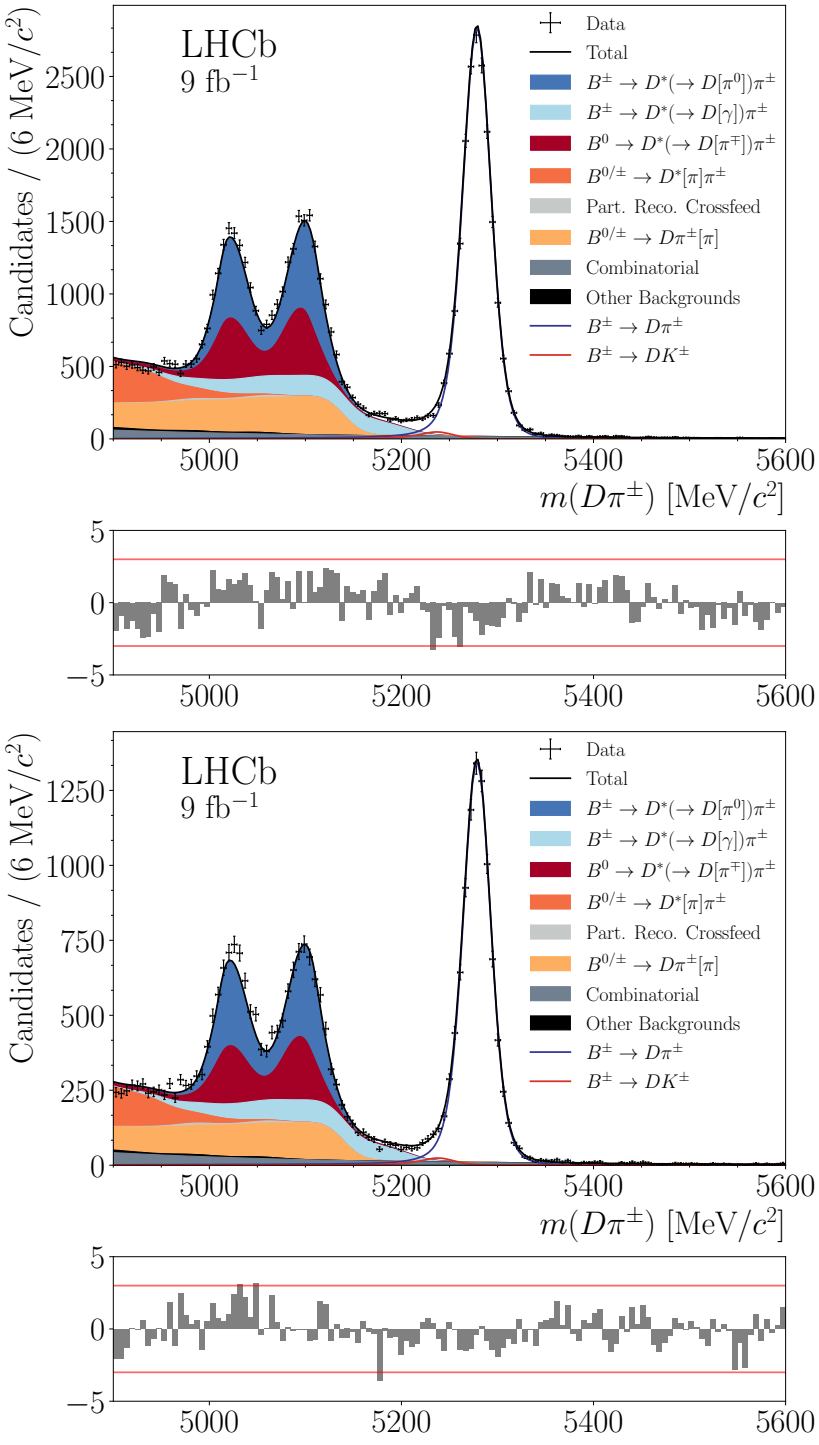

Figure 7.12: Mass distributions for $D\pi$ samples with $D \to K^0_S K^+ K^-$ decays reconstructed with (top) downstream K^0_S candidates and (bottom) long K^0_S candidates. The projections of the fit results are overlaid. In the legend, particles in square brackets are not reconstructed.

8

Measurement of CP-Violation

The second part of the two-step fit procedure is the CP fit. Here, data from the 8 categories depending on B decay, D decay, and K^0_S candidate types, are additionally split by the charge of the reconstructed B meson and their Dalitz plot bin assignment. There are 16 possible Dalitz plot bins for candidates reconstructed in the $D \to K^0_S\pi^+\pi^-$ final state, and 4 for the $D \to K^0_S K^+ K^-$ final state.

Similarly to the global fit, a simultaneous, binned extended maximum likelihood fit is performed to the $m(Dh)$ spectrum in the fit range, 4900-5600 MeV/c^2. The mass distributions for all components are fixed from the global fit. The yield per Dalitz plot bin is determined differently depending on the component, as discussed in Ch. 8.1-8.3. In these parameterisations, the normalisations are also composed differently depending on the component. Some components use global yields as normalisations. For the signal and fully reconstructed $B^\pm \to Dh^\pm$ components, these global B^+ and B^- yields are allowed to vary freely, to account for production and detector asymmetries. For most backgrounds, these global yields are fixed to their values from the global fit. For the combinatorial background, the yield per Dalitz plot bin is allowed to vary freely.

8.1 | Signal Parameterisation

As detailed in Ch. 5, and presented in Eqs. 5.9-5.12, the signal yield per Dalitz plot bin, i, is parameterised as,

$$N_i^+ = h_B^+(F_{-i} + [(x_+^{D^*K})^2 + (y_+^{D^*K})^2]F_{+i} + 2\sqrt{F_{-i}F_{+i}}[c_i x_+^{D^*K} - s_i y_+^{D^*K}]) \quad (8.1)$$

for $B^+ \to [D\pi^0]_{D^*}K^+$ signal decays,

$$N_i^- = h_B^-(F_{+i} + [(x_-^{D^*K})^2 + (y_-^{D^*K})^2]F_{-i} + 2\sqrt{F_{+i}F_{-i}}[c_i x_-^{D^*K} + s_i y_-^{D^*K}]) \quad (8.2)$$

for $B^- \to [D\pi^0]_{D^*}K^-$ signal decays,

$$N_i^+ = h_B^+(F_{-i} + [(x_+^{D^*K})^2 + (y_+^{D^*K})^2]F_{+i} - 2\sqrt{F_{-i}F_{+i}}[c_i x_+^{D^*K} - s_i y_+^{D^*K}]) \quad (8.3)$$

for $B^+ \to [D\gamma]_{D^*}K^+$ signal decays, and

$$N_i^- = h_B^-(F_{+i} + [(x_-^{D^*K})^2 + (y_-^{D^*K})^2]F_{-i} - 2\sqrt{F_{+i}F_{-i}}[c_i x_-^{D^*K} + s_i y_-^{D^*K}]) \quad (8.4)$$

for $B^- \to [D\gamma]_{D^*}K^-$ signal decays. In these equations, the normalisation constants, $h_B^\pm$, are modified using charge-separated global yields, N_{total}^+ and N_{total}^-, which are allowed to vary in the *CP* fit to account for production and detector asymmetries. Therefore, the yield per Dalitz plot bin is,

$$N_i^\pm = \frac{Y_i^\pm}{\sum_j Y_j^\pm} \times N_{\text{total}}^\pm, \quad (8.5)$$

where, for example for $B^+ \to [D\pi^0]_{D^*}K^+$ signal decays, Y_i^+ is defined as,

$$Y_i^+ = F_{-i} + [(x_+^{D^*K})^2 + (y_+^{D^*K})^2]F_{+i} + 2\sqrt{F_{-i}F_{+i}}[c_i x_+^{D^*K} - s_i y_+^{D^*K}], \quad (8.6)$$

where the F_i parameters and the cartesian *CP* observables are determined in the *CP* fit.

In the case of the $B^{\pm} \to D^{*}K^{\pm}$ signal component, there are 4 *CP* observables; $x_{\pm}^{D^{*}K}$ and $y_{\pm}^{D^{*}K}$. For the signal from $B^{\pm} \to D^{*}\pi^{\pm}$ decays an alternative parameterisation is used to ensure stability, as discussed in Ch. 5. This results in 2 additional observables; $\Re(\xi^{D^{*}\pi})$ and $\Im(\xi^{D^{*}\pi})$.

For the parameterisation in Eqs. 8.1-8.4, external strong-phase inputs, c_i and s_i, are used [42, 43]. The F_i parameters refer to the measured fractional yields of D^0 decays in a Dalitz plot bin and these are determined in the *CP* fit. As discussed in Ch. 5, they are shared between the $B^{\pm} \to D^{*}K^{\pm}$ and $B^{\pm} \to D^{*}\pi^{\pm}$ signal components, but their measurement is driven by $B^{\pm} \to D^{*}\pi^{\pm}$ decays due to their larger yield. In Ch. 8.4, the exact configuration of the F_i parameters is detailed.

The form of the parameterisation for the fully reconstructed $B^{\pm} \to Dh^{\pm}$ background component is similar to the signal parameterisation, with the exception of separate *CP* observables, F_i parameters, and normalisations. The *CP* observables for this background have been measured previously [45] and serve as an important cross-check. This is especially true given that candidates are reconstructed identically in the present work and in Ref. [45], with only small variations in selection. Therefore, the datasets in both measurements are highly correlated and one can expect very similar results.

8.2 | Crossfeed Component Parameterisation

The crossfeed components from misidentified companion hadrons are distributed over the Dalitz phase space in the same way as their correctly identified counterparts, but with additional scale factors. These account for the PID efficiency and the fact that events can be shifted into or out of the mass fit range when the mass

Table 8.1: Dalitz plot distribution for every background component, except the combinatorial background.

Component	Dalitz Distribution
$B^0 \to D^{*-}h^+$	D^0-like
$B^0 \to D^{(*)}\pi\pi$	50/50
$B^0 \to D^{(*)}K\pi$	*CP*-violating
$B^+ \to D^{(*)}h^+\pi^0$	*CP*-violating
$B \to D\pi\pi\pi$	$\overline{D}^0$-like
$B_s \to D^{(*)}K\pi$	$\overline{D}^0$-like
$B^0 \to D^{*-}K^+\pi^0$	D^0-like
$\Lambda_b^0 \to D^0 p\pi^-$	$\overline{D}^0$-like

hypothesis of the companion hadron is swapped. The yield parameterisation per Dalitz plot bin is

$$N_{\text{crossfeed},\,i} = N_{\text{correct PID},\,i} \times \frac{1-\epsilon^{\text{PID}}}{\epsilon^{\text{PID}}} \times \frac{\epsilon^{\text{mass}}_{\text{crossfeed}}}{\epsilon^{\text{mass}}_{\text{correct PID}}}. \tag{8.7}$$

8.3 | Background Parameterisation

In general, background components can be split into one of four types of distributions over the Dalitz plot: D^0-like, $\overline{D}^0$-like, 50/50, and *CP*-violating. The categorisation depends on the underlying physics process causing the background and how the background is reconstructed. Table 8.1 shows the distribution for each background component. The only background which does not fall into any of these categories is the combinatorial background. Since this is due to random track combinations, the yield in each Dalitz plot bin is allowed to vary freely. The following sections describe the four main types of background and how they are parameterised in the *CP* fit.

8.3.1 | D^0-like Backgrounds

Backgrounds which are not *CP*-violating are labelled D^0-like if they decay via D^0 mesons and are reconstructed as B^- mesons, or conversely decay via $\overline{D}^0$ mesons and are reconstructed as B^+ mesons. For example, the background from $B^0 \to [\overline{D}^0\pi^-]_{D^{*-}}h^+$ decays is in this category. A background such as this would exhibit distributions over the Dalitz plot similar to those shown in Fig. 8.1, where the change of axes between the two plots should be noted. Since these backgrounds occur via $D^0(\overline{D}^0)$ mesons for $B^-(B^+)$ meson candidates, and $F_{+(-)i}$ is the fractional yield of a D^0 ($\overline{D}^0$) decay in a Dalitz plot bin, i, the yield per Dalitz plot bin, $N_i^{-(+)}$ is proportional to $F_{+(-)i}$. The constant of proportionality is fixed using the total yield determined in the global fit which is then halved to obtain charge-separated global yields. Thus, the yield per Dalitz plot bin is,

$$N_i^{-(+)} = N_{\text{total}}^{-(+)} \times F_{+(-)i}. \tag{8.8}$$

8.3.2 | $\overline{D}^0$-like Backgrounds

The $\overline{D}^0$-like backgrounds also do not violate *CP* and occur in the opposite way to D^0-like backgrounds. They decay via $\overline{D}^0$ mesons and are reconstructed as B^- mesons, or via D^0 mesons and are reconstructed as B^+ mesons. One example is from $\Lambda_b^0 \to D^0 p\pi^-$ decays, where the pion is not reconstructed and the proton is misidentified as a kaon. These decays occur via D^0 and are reconstructed as B^+ mesons. Therefore, the resonances in the Dalitz plots, shown in Fig. 8.2, are flipped compared to those in Fig. 8.1. Thus, yield per Dalitz plot bin is

$$N_i^{-(+)} = N_{\text{total}}^{-(+)} \times F_{-(+)i}. \tag{8.9}$$

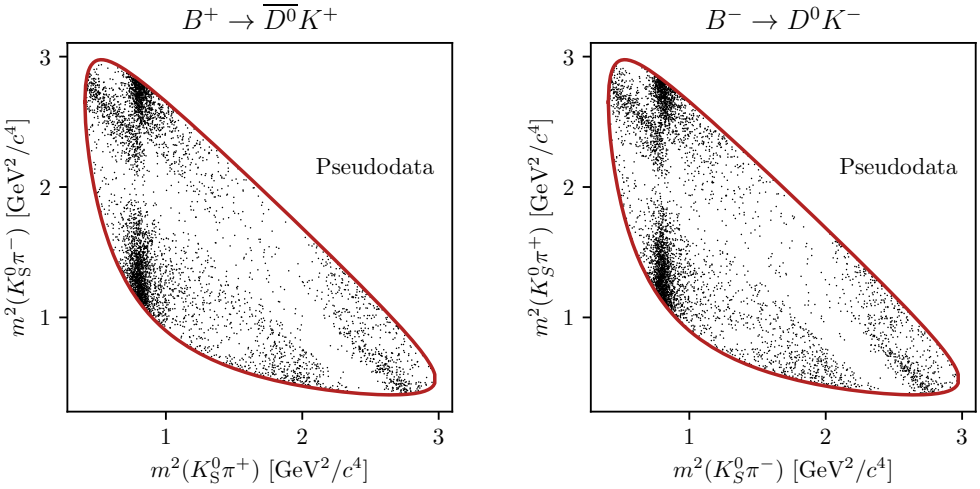

Figure 8.1: Dalitz plot distributions for (left) $B^+ \to \overline{D}^0 K^+$ samples and (right) $B^- \to D^0 K^-$ samples from pseudodata for D^0-like backgrounds. Note the change of axes between the two plots.

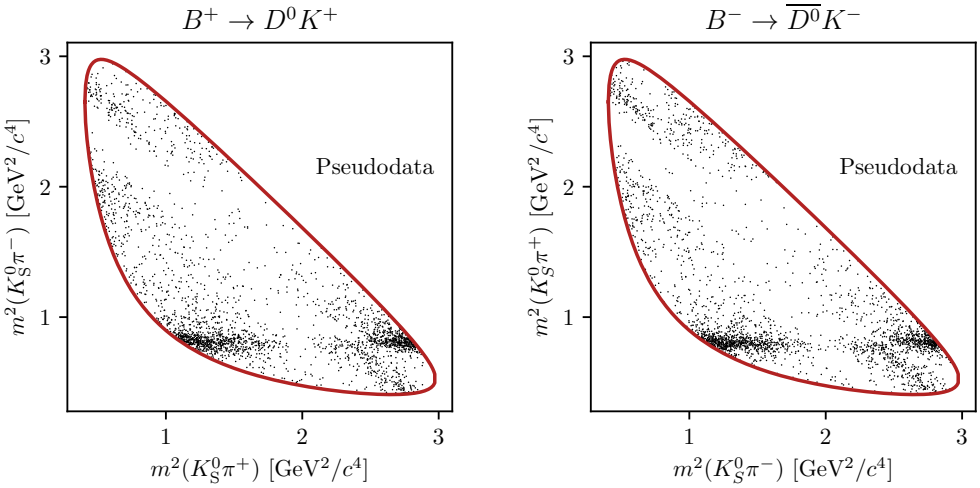

Figure 8.2: Dalitz plot distributions for (left) $B^+ \to D^0 K^+$ samples and (right) $B^- \to \overline{D}^0 K^-$ samples from pseudodata for $\overline{D}^0$-like backgrounds. Note the change of axes between the two plots.

8.3.3 | 50/50 Backgrounds

The third type of background arises from decays with either D^0 or $\overline{D}^0$ mesons in equal measure, such as $B^0 \to \overline{D}^0 \pi^+ \pi^-$ decays. This decay occurs via a $\overline{D}^0$ meson,

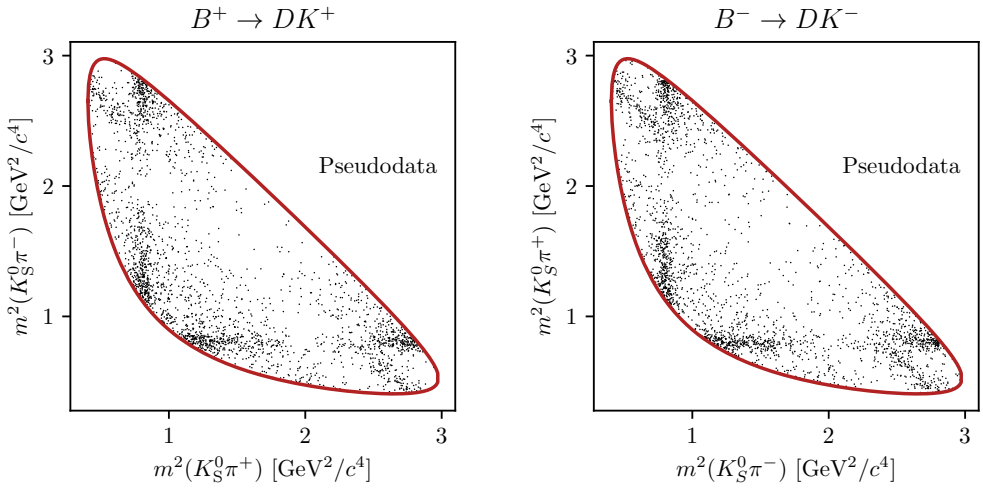

Figure 8.3: Dalitz plot distributions for (left) $B^+ \to DK^+$ samples and (right) $B^- \to DK^-$ samples from pseudodata for 50/50 backgrounds. Note the change of axes between the two plots.

but either of the pions could be missed, hence the decay could be reconstructed as either B^+ or B^- with equal probability. This means that the observed distribution over the Dalitz plot will be a sum of those in Figs. 8.1 and 8.2, as shown in Fig. 8.3. Therefore, the yield per Dalitz plot bin is proportional to the average of the F_i parameters, and is parameterised as

$$N_i^{+(-)} = N_{\text{total}}^{+(-)} \times \frac{F_{+i} + F_{-i}}{2}. \tag{8.10}$$

8.3.4 | *CP*-violating Backgrounds

The backgrounds described above are *CP*-conserving backgrounds where decays occur via either a D^0 meson or a $\overline{D}^0$ meson. There are also *CP*-violating backgrounds, such as $B^\pm \to DK^\pm\pi^0$, with decays to both D^0 and $\overline{D}^0$ mesons. This results in interference between the two possible decay amplitudes, and therefore, these backgrounds are parameterised over the Dalitz phase space in a similar

fashion to the signal components. The yield per Dalitz plot bin for a candidate reconstructed as a B^+ meson is

$$N_i^+ \propto F_{-i} + [x_+^2 + y_+^2]F_{+i} + 2\kappa\sqrt{F_{-i}F_{+i}}[c_i x_+ - s_i y_+], \tag{8.11}$$

where the cartesian *CP* observables correspond to the decay in question and κ is the coherence factor. Unlike the signal decays, contributions from *CP*-violating backgrounds can include multiple resonances. However, as the *CP* observables used to parameterise these backgrounds only correspond to a single resonance, the interference term is diluted, and this is accounted for by κ. If a background consists of predominantly one large resonance, then κ is close to unity, otherwise it is smaller than 1. For these backgrounds, it is not possible to determine the *CP* observables in the *CP* fit as the mass spectrum does not include the entirety of these components. As a result, the *CP* observables must be fixed. To do this, they are calculated using a value for γ from the latest LHCb γ combination [47] (63.8°) and hadronic parameters, for which the inputs are summarised in Tab. 8.2.

In Tab. 8.2, numerical values are generally taken from the latest LHCb γ combination [47] for relevant resonances. The backgrounds from $B^0 \to DK^+\pi^-$ and $B^0 \to D^*K^+\pi^-$ decays are parameterised using the r_B value for the $B^0 \to DK^{*0}$ resonance. The same resonance is used to fix the δ_B value for $B^0 \to DK^+\pi^-$ decays, whereas auxiliary studies for the analysis in Ref. [111] are used to fix the δ_B value for $B^0 \to D^*K^+\pi^-$ decays. The backgrounds from $B^+ \to DK^+\pi^0$ and $B^+ \to D^*K^+\pi^0$ decays are parameterised using the r_B and δ_B values for the $B^+ \to DK^{*+}$ resonance. The $B^+ \to D\pi^+\pi^0$ and $B^+ \to D^*\pi^+\pi^0$ decays are parameterised using the r_B value for $B^+ \to D\pi^+$ decays, since, as yet, there are no *CP*-violation measurements for $B^+ \to D\rho^+$ decays. This also means that the δ_B

Table 8.2: Hadronic inputs for *CP*-violating backgrounds. Numerical values are taken from Ref. [47] for relevant resonances, or using auxiliary studies in Ref. [111] unless stated otherwise.

Component	r_B	$\delta_B(^\circ)$	**Resonance**	κ
$B^0 \to DK^+\pi^-$	0.250	197	$B^0 \to DK^{*0}$	0.5
$B^0 \to [D\pi^0]_{D^*}K^+\pi^-$	0.250	70	Ref. [111]	0.5
$B^0 \to [D\gamma]_{D^*}K^+\pi^-$	0.250	70	Ref. [111]	0.5
$B^+ \to DK^+\pi^0$	0.106	35	$B^+ \to DK^{*+}$	0.5
$B^+ \to D^*K^+\pi^0$	0.106	35	$B^+ \to DK^{*+}$	0.5
$B^+ \to D\pi^+\pi^0$	0.0048	100	$B^+ \to D\pi^+$	1.0
$B^+ \to D^*\pi^+\pi^0$	0.0048	200	$B^+ \to D\pi^+$	0.5

values for these backgrounds are arbitrarily chosen to be 100° and 200°, respectively. An arbitrary choice can be made since the accuracy of the parameterisation of these backgrounds is driven the choice of the coherence factor, rather than the strong phases.

For all *CP*-violating backgrounds, except $B^+ \to D\pi^+\pi^0$ decays, the coherence factor is 0.5. This was estimated by calculating the fraction of the $B^0 \to DK^{*0}$ decay in the $B^0 \to DK^+\pi^-$ background component using branching fractions and efficiencies. This is then applied to all *CP*-violating backgrounds where it is likely that there are contributions from multiple resonances. The exception here is the background from $B^+ \to D\pi^+\pi^0$ decays. In the global fit, the fraction of the $B^+ \to D\rho^+$ contribution compared to the non-resonant component was determined. The fit to data found that $B^+ \to D\rho^+$ decays constitutes 99% of the background. Therefore, the coherence factor for this background is set to unity. The systematic uncertainty due to the choices of all hadronic parameter inputs is assessed by considering the full range of their possible values, and is determined in Ch. 9.6.

8.4 | F_i Parameterisation

As detailed in Ch. 5, there are separate F_i values for each D decay and K^0_S candidate type, but they are shared between the $B^\pm \to DK^\pm$ and $B^\pm \to D\pi^\pm$ candidates, since they have similar kinematic distributions. As explained in the preceding sections of this chapter, the F_i values are included in the parameterisation of all signal and background components. Therefore, one could consider sharing them or having two sets of F_i parameters; one for signals and one for backgrounds. To determine the optimal configuration, pseudodata studies are used to assess the corresponding change in the sensitivity to the *CP* observables.

The set of F_i values used to parameterise the $B^\pm \to D^*h^\pm$ signal components is labelled, $F_{\text{sig},\,i}$, and the set used to parameterise the background components is labelled, $F_{\text{bkg},\,i}$. There are 3 configurations which are tested:

- Configuration A: Both sets of F_i values, $F_{\text{sig},\,i}$ and $F_{\text{bkg},\,i}$, are allowed to vary in the *CP* fit.
- Configuration B: The F_i values are shared, that is $F_{\text{sig},\,i} = F_{\text{bkg},\,i}$, and these are allowed to vary in the *CP* fit.
- Configuration C: Since the $B^\pm \to D\pi^\pm$ component will dominate the measurement of the $F_{\text{bkg},\,i}$ values, these are fixed to the results from the $B^\pm \to Dh^\pm$ measurement [45], and only the $F_{\text{sig},\,i}$ values are allowed to vary in the *CP* fit.

The procedure for the study is as follows. In total, 100 pseudodatasets are generated for each of these configurations. The *CP* fit is run on these pseudodatasets and the mean and standard deviations of the statistical uncertainty on

the resulting $B^{\pm} \to D^{*}h^{\pm}$ *CP* observables are calculated and compared. Figure 8.4 shows this comparison and it is evident that all 3 configurations result in similar statistical sensitivities to the *CP* observables. However, Fig. 8.4 does not include systematic uncertainties, specifically in configuration C due to the fixed $F_{\text{bkg},i}$ values. This means that configuration C should not be used. Furthermore, in configuration B, when sharing the F_i values between the signal and background components, if there are inaccuracies in the background modelling, this could lead to a contamination of the signal measurements. Therefore to avoid this, configuration *A* is used where there are two separate sets of F_i values, $F_{\text{sig},i}$ and $F_{\text{bkg},i}$, and each is allowed to vary in the *CP* fit.

As the F_i values are measured fractional yields, they should sum to unity. Naïvely imposing this condition leads to fit instabilities [45], therefore in practice, the F_i values are reparameterised in terms of recursive fractions, $\mathcal{R}_i$. For $2\mathcal{N}$ Dalitz plot bins this is defined as,

$$F_i = \begin{cases} \mathcal{R}_i & , i = -\mathcal{N} \\ \mathcal{R}_i \prod_{j<i}(1-\mathcal{R}_j) & , -\mathcal{N} < i < +\mathcal{N} \\ \prod_{j<i}(1-\mathcal{R}_j) & , i = \mathcal{N}. \end{cases} \tag{8.12}$$

8.5 | Validation

Pseudoexperiments are used to assess the stability and performance of the *CP* fit and to determine if there are any biases due to the parameterisation. Similarly to the global fit, pseudodata are generated using the model described above with *CP* observables and F_i parameters that are approximately equal to those found from

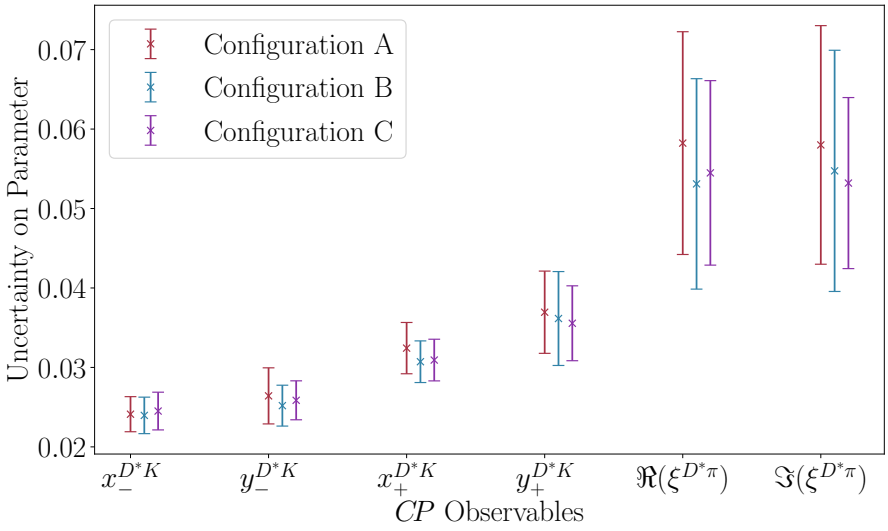

Figure 8.4: Similar mean and standard deviation of the statistical uncertainties on *CP* observables from 100 pseudodatasets in three possible configurations of the F_i values.

the fit to data, given in Ch. 8.6. This is with the exception of the combinatorial background which is due to a combination of random tracks. This is modelled by splitting the background into contributions from real and fake D mesons. When a real D meson is paired with a random companion hadron, the Dalitz distribution is 50/50 since the companion hadron could have either positive or negative charge. When there is a fake D meson, the background is assumed to be evenly distributed over the Dalitz phase space. Figure 8.5 shows the distribution over the Dalitz plots for events in the B mass sideband ($m_B \in [5600, 6000]\,\text{MeV}/c^2$ for $D \to K^0_S\pi^+\pi^-$ events and $m_B \in [5600, 7000]\,\text{MeV}/c^2$ for $D \to K^0_S K^+ K^-$ events) and outside the D mass sideband ($m_D \ni [1750, 1950]\,\text{MeV}/c^2$). Since only events from the high B mass sideband are selected for this figure, there are more events in the high s_+ and high s_- range. However, except for this feature, all events

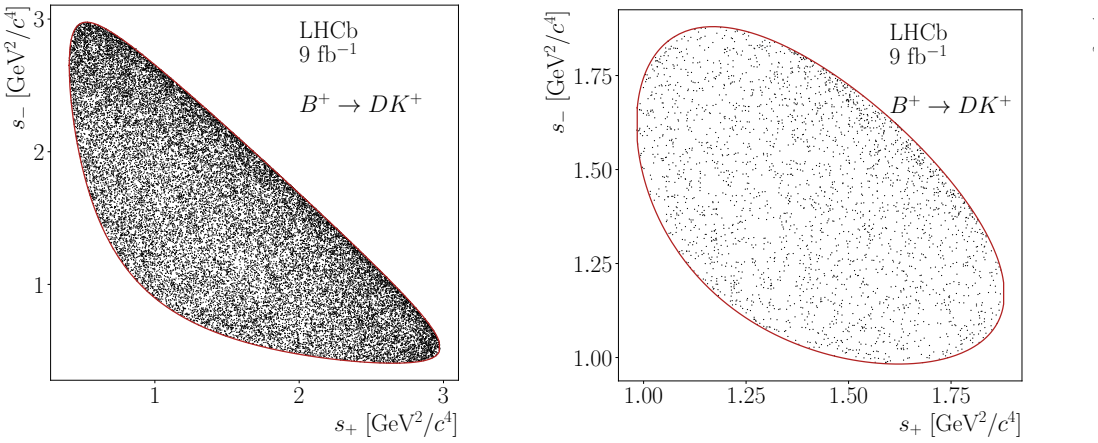

Figure 8.5: Distributions over the Dalitz plot for events in the B mass sideband ($m_B \in [5600, 6000]\,\text{MeV}/c^2$ for $D \to K^0_S\pi^+\pi^-$ events and $m_B \in [5600, 7000]\,\text{MeV}/c^2$ for $D \to K^0_S K^+K^-$ events) and outside the D mass sideband ($m_D \ni [1750, 1950]\,\text{MeV}/c^2$) in data, which are reconstructed as $B^+ \to DK^+$ with (left) $D \to K^0_S\pi^+\pi^-$ or (right) $D \to K^0_S K^+K^-$ and downstream K^0_S candidates.

are evenly distributed over the Dalitz plot, and the assumption is valid. This means that the yield per Dalitz plot bin for the combinatorial background from fake D mesons is proportional to the area of that Dalitz plot bin. The fraction of real and fake D mesons was determined in the $B^\pm \to Dh^\pm$ analysis [45], by fitting the D mass spectrum for candidates with $m(Dh)$ greater than $5600\,\text{MeV}/c^2$. This assumption and model for phase space distribution of the combinatorial background is only necessary for pseudoexperiments. In the fit to data, no such assumption is made.

A total of 1000 pseudoexperiments are performed using the model described in the preceding sections and all pseudodatasets converge successfully, indicating very good fit stability. The means and widths of the pull distributions, defined in Eq. 7.13, are calculated and shown in Tab. 8.3. In general, all pull means are consistent with 0 within 2σ, except for the $\Re(\xi^{D^*\pi})$ observable. This param-

Table 8.3: Means and widths of pull distributions for the $B^{\pm} \to D^{*}h^{\pm}$ *CP* observables from 1000 pseudodatasets with yields similar to those in data.

***CP* Observable**	**Pull Mean**	**Pull Width**
$x_{-}^{D^{*}K}$	0.07 ± 0.03	1.02 ± 0.02
$y_{-}^{D^{*}K}$	0.05 ± 0.03	1.05 ± 0.03
$x_{+}^{D^{*}K}$	-0.06 ± 0.03	0.99 ± 0.02
$y_{+}^{D^{*}K}$	0.03 ± 0.03	1.06 ± 0.03
$\Re(\xi^{D^{*}\pi})$	0.15 ± 0.03	0.95 ± 0.02
$\Im(\xi^{D^{*}\pi})$	0.03 ± 0.03	0.99 ± 0.02

eter also has a pull width which deviates significantly from unity. To be certain that this is not due to incorrect parameterisation, the pseudoexperiments are repeated with yields that are 100 times larger than those expected in data. The results of this are shown in Tab. 8.4. Here, all parameters are determined without biases and their uncertainties are estimated correctly since the pull widths are consistent with unity. Therefore, the bias seen in the $\Re(\xi^{D^{*}\pi})$ observable in Tab. 8.3 is a statistical effect. A correction is applied due to this, where the fitted value of the $\Re(\xi^{D^{*}\pi})$ observable is corrected using

$$\Delta\Re(\xi^{D^{*}\pi}) = \Re(\xi^{D^{*}\pi})_{\text{gen}} - < \Re(\xi^{D^{*}\pi})_{\text{fit}} >, \tag{8.13}$$

which is 0.02, and the overestimated uncertainty is corrected for by multiplying the statistical uncertainty by the pull width.

8.6 | Results

The $m(Dh)$ distributions and the fit projections are shown in App. B, but one set of results is shown in Fig. 8.6. The plot on the left corresponds to the $+2$ Dalitz plot bin in the $B^{-} \to DK^{-}$ sample and on the right is the corresponding

Table 8.4: Means and widths of pull distributions for the $B^{\pm} \to D^{*}h^{\pm}$ *CP* observables from 1000 pseudodatasets with 100 times the yield in data.

***CP* Observable**	**Pull Mean**	**Pull Width**
$x_{-}^{D^{*}K}$	-0.02 $\pm$ 0.04	0.99 $\pm$ 0.03
$y_{-}^{D^{*}K}$	0.04 $\pm$ 0.04	1.03 $\pm$ 0.03
$x_{+}^{D^{*}K}$	-0.05 $\pm$ 0.04	0.99 $\pm$ 0.03
$y_{+}^{D^{*}K}$	0.03 $\pm$ 0.04	1.00 $\pm$ 0.03
$\Re(\xi^{D^{*}\pi})$	0.05 $\pm$ 0.04	1.00 $\pm$ 0.03
$\Im(\xi^{D^{*}\pi})$	0.01 $\pm$ 0.04	1.03 $\pm$ 0.03

Dalitz plot bin, -2, for the $B^{+} \to DK^{+}$ sample. The asymmetry between the $B^{\pm} \to [D\pi^{0}]_{D^{*}}K^{\pm}$ signal components (shown in dark blue) in the B^{-} and B^{+} samples suggests that there is *CP*-violation in this mode. However, due to the comparatively smaller yields in the $B^{\pm} \to [D\gamma]_{D^{*}}K^{\pm}$ signal components (shown in light blue), the asymmetry here is less obvious.

Another feature of Fig. 8.6 is that the asymmetry in the $B^{\pm} \to DK^{\pm}$ background between the B^{-} and B^{+} samples is in the opposite direction compared to that for the $B^{\pm} \to [D\pi^{0}]_{D^{*}}K^{\pm}$ signal. This is because the strong phases, δ_{B}^{DK} and $\delta_{B}^{D^{*}K}$, are expected to differ by 180°. This leads to a sign change on the *CP* observables, which changes the sign on the interference term in the Dalitz plot bin yield parameterisation, resulting in a reversed asymmetry.

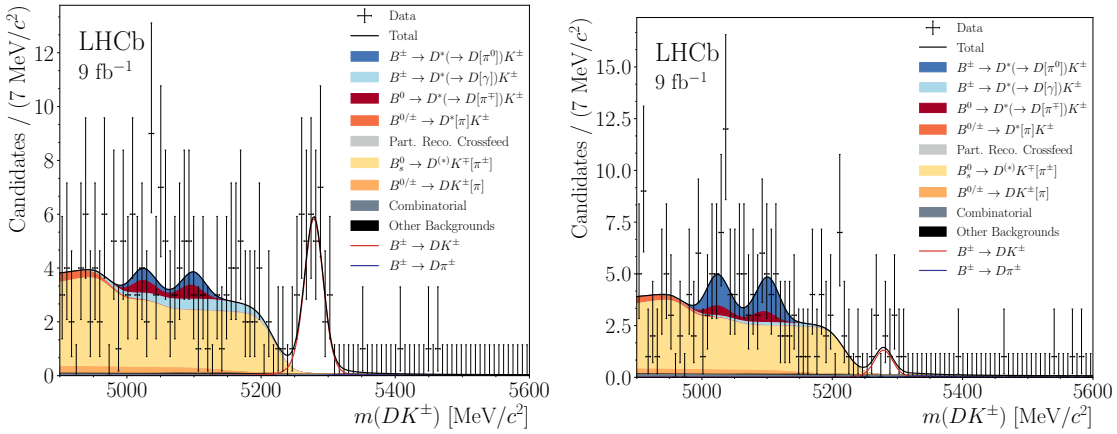

Figure 8.6: Mass distributions for DK samples with $D \to K^0_S\pi^+\pi^-$ decays reconstructed with downstream K^0_S candidates in (left) the B^- sample in Dalitz plot bin $+2$ and (right) the B^+ sample in Dalitz plot bin -2. The projections of the fit results are overlaid.

From the *CP* fit, the $B^\pm \to D^*h^\pm$ *CP* observables are determined to be:

$$
\begin{aligned}
x_-^{D^*K} &= (-6.3 \pm 2.9) \times 10^{-2}, \\
y_-^{D^*K} &= (-4.8 \pm 5.7) \times 10^{-2}, \\
x_+^{D^*K} &= (\ \ 6.0 \pm 2.6) \times 10^{-2}, \\
y_+^{D^*K} &= (\ \ 5.4 \pm 2.9) \times 10^{-2}, \\
\Re(\xi^{D^*\pi}) &= (\ 11.5 \pm 9.4) \times 10^{-2}, \\
\Im(\xi^{D^*\pi}) &= (-0.9 \pm 9.7) \times 10^{-2},
\end{aligned}
$$

with their associated statistical uncertainties. The uncertainty on the $y_-^{D^*K}$ parameter is larger than that of the other D^*K *CP* observables. This is because, as shown in Eqs. 8.2 and 8.4, the $y_-^{D^*K}$ parameter and s_i appear in the same term, and are therefore highly correlated. This means that the Dalitz plot bins where the magnitude of s_i is largest is where there should be the most sensitivity to $y_-^{D^*K}$, and for the $D \to K^0_S\pi^+\pi^-$ mode this is in bins ±5 and ±6. As shown in Fig. 8.7, these

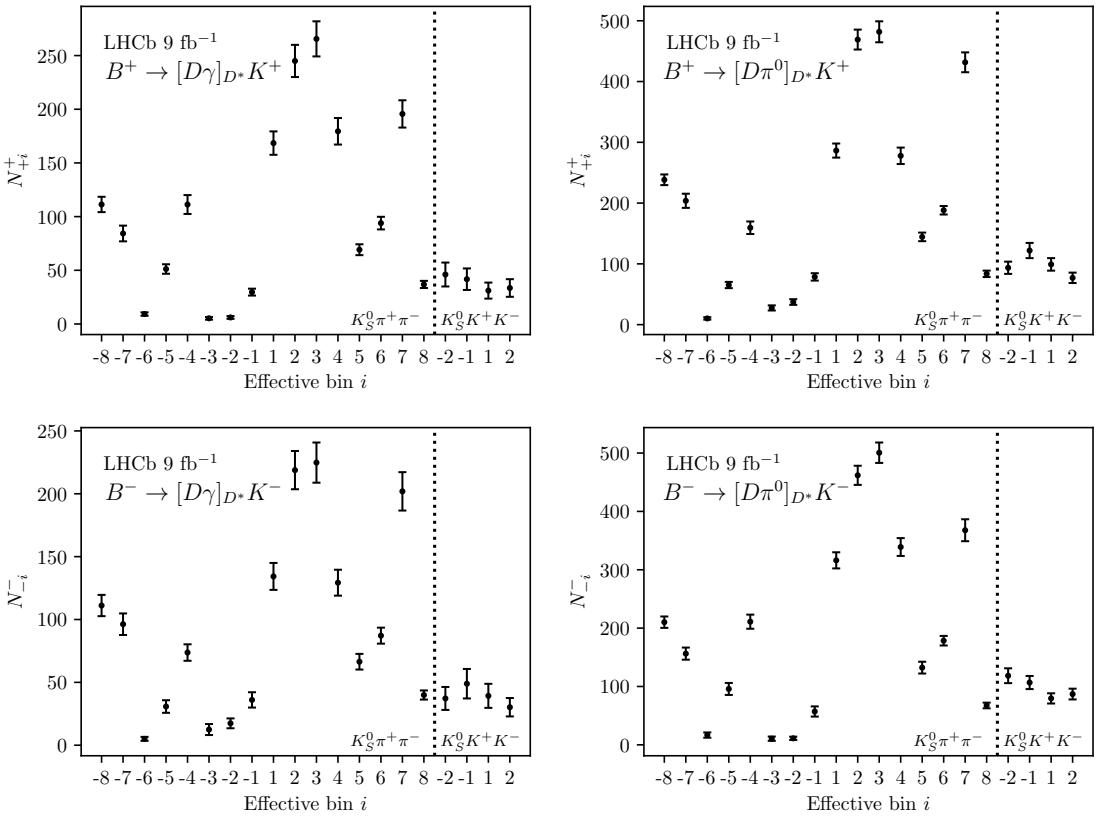

Figure 8.7: Dalitz plot bin yields determined using the fitted *CP* observables from the *CP* fit for (top) B^+ decays, (bottom) B^- decays, (left) with $D^* \to D\gamma$ decays and (right) $D^* \to D\pi^0$ decays.

are also the Dalitz plot bins which are among the smallest yields, and therefore there is low sensitivity to $y_-^{D^*K}$.

The statistical uncertainty is also much larger for the $\xi^{D^*\pi}$ than the D^*K *CP* observables. This is because in the $B^\pm \to D\pi^\pm$ mode there are much larger backgrounds, such as $B^\pm \to D\rho^\pm$, which severely contaminate this sample and reduce its purity.

The correlation matrix associated with these statistical uncertainties is shown in Tab. 8.5. Here, there is a large variation in the correlations from 10–77%. Similar correlations were also observed using pseudodata with all signal and back-

ground components. To determine the cause of the size of the correlations, pseudodata was also generated with only the signal components. When doing so, the size of the correlations dropped to 35%. Furthermore, generating signal-only pseudodata with only the $D^* \to D\gamma$ mode produced correlations of up to 40%, and pseudodata with only the $D^* \to D\pi^0$ mode produced correlations of up to 30%. This means that there are two sources driving the sizes of the statistical correlations in Tab. 8.5. First, the contamination due to the large background sources which severely impacts the purity of this measurement. Second, the presence of two signal modes, $D^* \to D\gamma$ and $D^* \to D\pi^0$, which, as discussed in Ch. 5.4, dilutes the sensitivity of this measurement. Both of these are due to the partially reconstructed nature of this analysis and cannot be avoided.

The results for these *CP* observables can be plotted, as shown in Fig. 8.8, where a likelihood scan is performed to determine the 68.3% and 95.5% confidence regions. Since the contours are close to ellipses, this suggests that the uncertainties are modelled well using a Gaussian function and therefore those obtained in the fit are accurate. From the definitions of the $B^\pm \to D^* K^\pm$ *CP* observables, it can be deduced that the length of the red and blue lines from the origin are each $r_B^{D^*K}$, and the angle between them is 2γ. Similarly, using the definition of the $\xi^{D^*\pi}$ parameter, the distance from the black point in the right-hand plot of Fig. 8.8 to the origin is the ratio $r_B^{D^*\pi}/r_B^{D^*K}$. The value of $r_B^{D^*K}$ and $r_B^{D^*\pi}/r_B^{D^*K}$ are each expected to be around 0.1 [47], therefore these appear to be consistent with the results in Fig. 8.8. The CKM angle γ is expected to be around 63.8° [47], but the result in Fig. 8.8 appears to be larger than this. Figure 8.8 does not give a clear indication of the uncertainty on γ, and therefore the consistency of this result with Ref. [47] cannot be judged without a complete interpretation of the results. This

Table 8.5: Statistical correlation matrix for the *CP* observables.

	$x_-^{D^*K}$	$y_-^{D^*K}$	$x_+^{D^*K}$	$y_+^{D^*K}$	$\Re(\xi^{D^*\pi})$	$\Im(\xi^{D^*\pi})$
$x_-^{D^*K}$	1.000	0.420	0.158	0.105	0.445	0.422
$y_-^{D^*K}$		1.000	0.115	0.232	0.765	0.631
$x_+^{D^*K}$			1.000	−0.095	0.012	0.409
$y_+^{D^*K}$				1.000	0.263	0.112
$\Re(\xi^{D^*\pi})$					1.000	0.597
$\Im(\xi^{D^*\pi})$						1.000

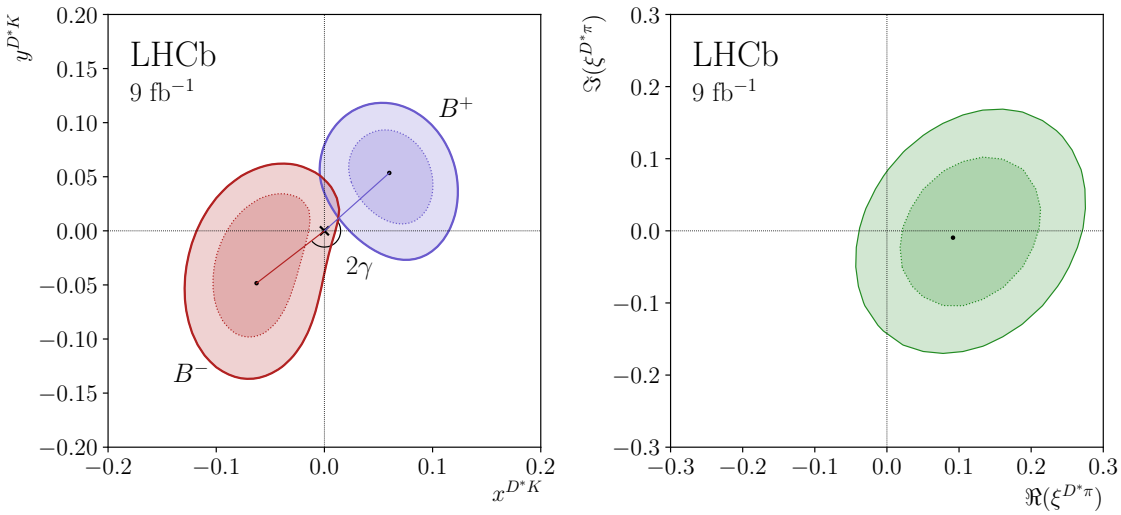

Figure 8.8: Contours at the 68.3% and 95.5% confidence levels indicated by the darker and lighter regions, respectively, for (left, red) $(x_-^{D^*K}, y_-^{D^*K})$ which is labelled B^- and (left, blue) $(x_+^{D^*K}, y_+^{D^*K})$ which is labelled B^+, and (right) $(\Re(\xi^{D^*\pi}), \Im(\xi^{D^*\pi}))$, including only statistical uncertainty. The black points indicate the central values.

is discussed in Ch. 10.

8.7 | Cross-Check

In this analysis, the *CP* observables for the fully reconstructed $B^\pm \to Dh^\pm$ modes are used as cross-checks. They do not supersede results from Ref. [45], since the

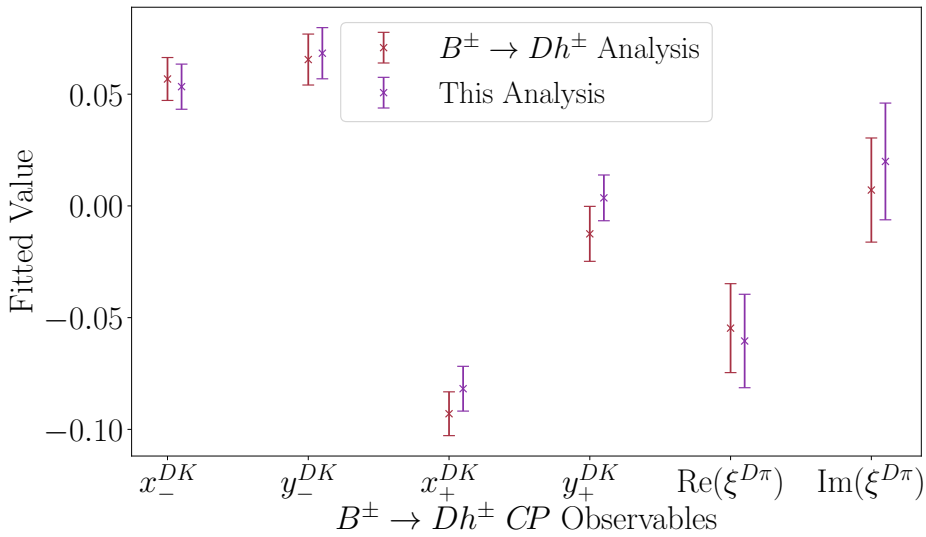

Figure 8.9: The $B^\pm \to Dh^\pm$ *CP* observables in this analysis (purple) and Ref. [45] (red), with statistical uncertainties only.

selections used here have been optimised for the partially reconstructed $B^\pm \to D^*h^\pm$ modes.

A comparison of the $B^\pm \to Dh^\pm$ *CP* observables in this analysis and in Ref. [45] is shown in Fig. 8.9 where the error is only the statistical uncertainty. Given that there is a large overlap between the datasets in this analysis and in Ref. [45], a strong agreement is expected and is seen, with consistency across all *CP* observables. Furthermore, there is a mix of both upward and downward fluctuations showing that there is no systematic effect between this analysis and Ref. [45] causing a skew of the results.

9

Systematic Uncertainties

Throughout this analysis, there are a number of assumptions that have been made. These result in systematic uncertainties which are evaluated here and summarised in Tab. 9.4. First, the systematic uncertainty due to the external strong-phase inputs is discussed in Ch. 9.1. This is followed by discussions of all LHCb-related experimental systematic uncertainties. In Ch. 9.8 a justification for those which are ignored and not evaluated is provided. The leading sources of systematic uncertainty are then discussed in Ch. 9.9, with commentary on their further reduction.

9.1 | Strong-Phase Inputs

In the *CP* fit, the c_i and s_i values are fixed to the combination [42,43] of the CLEO and BESIII measurements and these carry uncertainties. The systematic uncertainty due to ignoring these uncertainties is estimated by generating alternative strong-phase inputs by varying the central value of the c_i and s_i inputs according to the statistical uncertainty on their measurement while taking into account the

Table 9.1: Systematic uncertainty (σ) expressed in units of 10^{-2} associated with the external strong-phase inputs.

	$x_-^{D^*K}$	$y_-^{D^*K}$	$x_+^{D^*K}$	$y_+^{D^*K}$	$\Re(\xi^{D^*\pi})$	$\Im(\xi^{D^*\pi})$
σ	0.57	1.54	0.18	0.41	2.33	2.13

correlations between them. Then the *CP* fit is performed to data 1000 times, each time with a different set of c_i and s_i inputs. The standard deviation for each *CP* observable from these 1000 fits is taken to be its systematic uncertainty, this is shown in Tab. 9.1.

9.2 | Efficiency Correction of (c_i, s_i)

The strong-phase inputs used in this analysis are defined as,

$$c_i = \frac{\int_i \mathrm{d}s^2 \, |\mathcal{A}_D| \, |\mathcal{A}_{\overline{D}}| \cos(\Delta\delta_D)}{\sqrt{\int_i \mathrm{d}s^2 \, |\mathcal{A}_D|^2 \int_i \mathrm{d}s^2 \, |\mathcal{A}_{\overline{D}}|^2}}, \tag{9.1a}$$

$$s_i = \frac{\int_i \mathrm{d}s^2 \, |\mathcal{A}_D| \, |\mathcal{A}_{\overline{D}}| \sin(\Delta\delta_D)}{\sqrt{\int_i \mathrm{d}s^2 \, |\mathcal{A}_D|^2 \int_i \mathrm{d}s^2 \, |\mathcal{A}_{\overline{D}}|^2}}, \tag{9.1b}$$

and their inputs have been corrected for efficiency effects at these experiments. As mentioned in Ch. 5.1, the non-uniform acceptance at LHCb over the D-decay phase space means that the c_i and s_i values should be efficiency-corrected with the reconstruction efficiency profile, $\eta(s_-, s_+)$. This would result in strong-phase inputs that are defined as,

$$c_i' \equiv \frac{\int_i \mathrm{d}s_- \mathrm{d}s_+ \eta(s_-, s_+) \, |\mathcal{A}_D| \, |\mathcal{A}_{\overline{D}}| \cos(\Delta\delta_D)}{\sqrt{\int_i \mathrm{d}s_- \mathrm{d}s_+ \eta(s_-, s_+) \, |\mathcal{A}_D|^2 \int_i \mathrm{d}s_- \mathrm{d}s_+ \eta(s_-, s_+) \, |\mathcal{A}_{\overline{D}}|^2}}, \tag{9.2a}$$

$$s_i' \equiv \frac{\int_i \mathrm{d}s_- \mathrm{d}s_+ \eta(s_-, s_+) \, |\mathcal{A}_D| \, |\mathcal{A}_{\overline{D}}| \sin(\Delta\delta_D)}{\sqrt{\int_i \mathrm{d}s_- \mathrm{d}s_+ \eta(s_-, s_+) \, |\mathcal{A}_D|^2 \int_i \mathrm{d}s_- \mathrm{d}s_+ \eta(s_-, s_+) \, |\mathcal{A}_{\overline{D}}|^2}}. \tag{9.2b}$$

To assess the systematic uncertainty due to ignoring this efficiency-correction, amplitude models for $D \to K^0_S\pi^+\pi^-$ decays [112] and $D \to K^0_S K^+K^-$ decays [49], are used to provide a set of inputs, $\{c_i^{\text{model}}, s_i^{\text{model}}\}$, and their efficiency-corrected values, $\{c_i^{\text{eff}}, s_i^{\text{eff}}\}$. This efficiency correction is performed by estimating the reconstruction efficiency profile using simulation. By generating simulation with a uniform phase-space distribution, the reconstruction efficiency at a phase-space point is proportional to the yield at that point.

Pseudodata are generated with signal yields parameterised in terms of efficiency-corrected strong-phase inputs, $\{c_i^{\text{eff}}, s_i^{\text{eff}}\}$. Then the *CP* fit is performed where the strong-phase inputs in the fit model are not efficiency-corrected, $\{c_i^{\text{model}}, s_i^{\text{model}}\}$. The mean bias in the *CP* observables is assigned as the systematic uncertainty.

9.3 | Mass Shape Parameterisation

In the mass shape parameterisation described in Ch. 7, there are a number of parameters that are obtained in fits to simulation and subsequently fixed in the fit to data. These carry uncertainties which need to be propagated. Therefore, the associated systematic uncertainty due to ignoring them is evaluated using bootstrapping [102], as follows:

- The simulation samples are re-sampled with replacement such that each candidate is sampled with the same probability. The fits are then repeated 100 times for every signal and background component.
- The data are also re-sampled with replacement and the global fit is repeated

100 times, each time using a different set of results from the fits to simulation in the previous step.

- Without further re-sampling of the data, to avoid a statistical spread in the results, the *CP* fit is repeated 100 times, each time using a different result from the global fits in the previous step.

From the 100 *CP* fits, the standard deviations of the resulting *CP* observables are evaluated and taken to be the systematic uncertainties. This bootstrapping method benefits from ensuring that correlations between shape parameters are accounted for in the error propagation. It also implicitly accounts for the small fit biases identified when validating the global fit in Ch. 7.5.

9.4 | Fixed Ratios

The yield parameterisations in both the global fit and *CP* fit include a number of fixed branching ratios, efficiencies, and yield ratios. Each of the fixed values are taken from the PDG [18], simulation, or another analysis [46], respectively, and carry uncertainties. The associated systematic uncertainty due to ignoring them is evaluated as follows:

- Each fixed quantity is varied by sampling a shift using a Gaussian function with a mean of 0 and a width which is the uncertainty on the fixed quantity.
- The global and *CP* fits are repeated with the new fixed value.
- This is repeated 100 times.

The standard deviation of each *CP* observable from the 100 fits is taken to be its systematic uncertainties. The systematic uncertainties associated with the fixed branching ratios, efficiencies, and yield ratios are evaluated separately and summarised in Tab. 9.4.

In the global fit, the fixed yield ratios are determined using yields from the partially reconstructed $B^{\pm} \to D^{*}h^{\pm}$ analysis with 2-body D-decay final states [46]. These are employed in yield parameterisations similarly to the example shown in Eq. 7.9. For this parameterisation to be correct, the efficiencies in this analysis and Ref. [46] are assumed to be the same. This assumption was tested in simulation, as detailed in Ch. 7.3, and found to be correct within 1–3%. The systematic uncertainty due to this 1–3% variation is included in the procedure outlined above by multiplying the yield ratio by a factor sampled from a Gaussian function with a mean of 1 and a width of 0.03.

9.5 | Dalitz Plot Bin Migration

Dalitz plot bins are assigned using measurements of a candidate's momentum. The resolution of these measurements can lead to incorrect bin assignment and migration of events between neighbouring bins. The F_i values are measured in the *CP* fit, therefore any migration between bins is largely accounted for. However, the measurement of the F_i values for the signal decays are dominated by the $B^{\pm} \to D^{*}\pi^{\pm}$ components. Therefore, differing levels of bin migration between $B^{\pm} \to D^{*}\pi^{\pm}$ and $B^{\pm} \to D^{*}K^{\pm}$ decays will impact the *CP*-violation measurement. This is expected to be a small effect and the systematic uncertainty associated with ignoring this is accounted for as follows. A signal-only pseudodata

study is performed where data are generated assuming the physical observables $(r_B^{D^*K}, r_B^{D^*\pi}, \delta_B^{D^*K}, \delta_B^{D^*\pi}, \gamma)$ are at their current LHCb γ combination values [47] and using the amplitude model for $D \to K^0_S\pi^+\pi^-$ decays [112]. Then, the phase-space coordinates of each generated decay are smeared, to mimic resolution effects and the Dalitz plot bins are reassigned. The *CP* fit is then performed on this pseudodataset. After this, the signal-only pseudodata study is repeated without smearing the phase-space coordinates of each generated decay, thus isolating the effect of the momentum resolution. By comparing the resulting *CP* observables between the two pseudodata studies, the mean bias in them is determined and assigned as the systematic uncertainty.

In order to perform this study, first the experimental resolution is measured in simulation by comparing reconstructed phase-space coordinates to those calculated from truth-matched momentum measurements. As the sensitivity of this analysis is driven by candidates with $D \to K^0_S\pi^+\pi^-$ decays, the experimental resolution is measured using only these. Furthermore, to evaluate the resolution the rectangular Dalitz plot binning scheme, shown at the top of Fig. 9.1, is used, because it better describes continuous trends over the Dalitz phase space. The distribution of the resolution is shown at the bottom of Fig. 9.1 for $B^\pm \to [D\pi^0]_{D^*}\pi^\pm$ candidates.

Signal-only pseudodata are generated and the phase-space coordinates of each generated decay are smeared. To do this, first a shift is sampled from the $\Delta(m^2)$ distributions in Fig 9.1 for a simulated event in the same Dalitz plot bin as the generated decay. Then, this shift is multiplied by 120% to account for data-simulation resolution differences, and applied to the generated event. Once these shifts are sampled and applied to all pseudodata, the data are assigned new

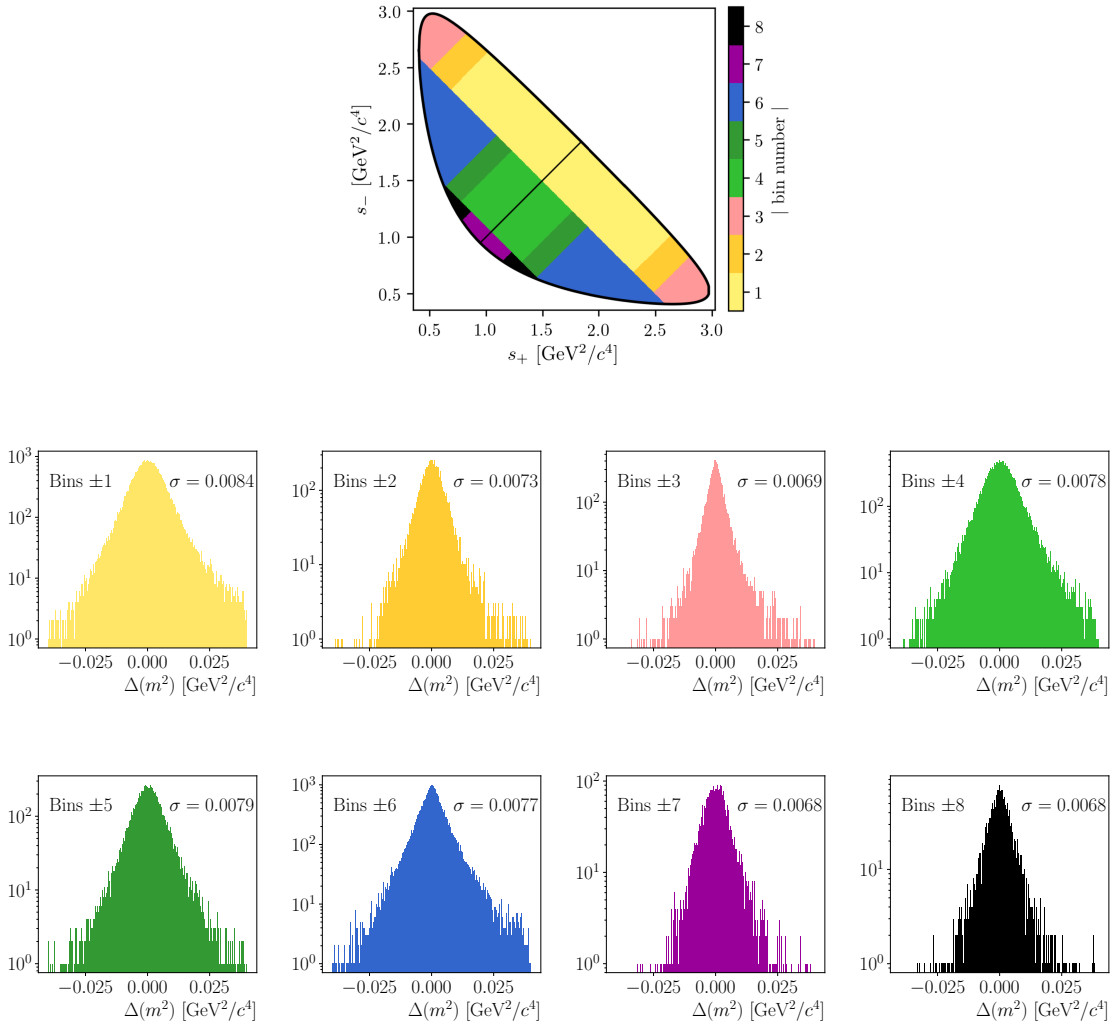

Figure 9.1: Shifts in simulation between true and reconstructed $m^2(K^0_S\pi^+)$ for (bottom) $B^\pm \to [D\pi^0]_{D^*}\pi^\pm$ decays in Dalitz plot bins of the (top) rectangular Dalitz plot binning scheme for $D \to K^0_S\pi^+\pi^-$ decays. The widths (σ) of the shifts in simulation are shown in units of GeV$^2/c^4$.

Dalitz plot bins and the *CP* fit is performed with the nominal fit model.

Then, by repeating this procedure without smearing the phase-space coordinates, the *CP* observables in both cases are compared. Since both sets of pseudodata studies generate data with the same input *CP* observables, the systematic

uncertainty is calculated using the mean biases between the resulting *CP* observables. For example, the systematic uncertainty (σ_{syst}) is

$$\sigma_{\text{syst}}(x) = \mu(x)_{\text{smear}} - \mu(x)_{\text{no smear}}, \tag{9.3}$$

for a *CP* observable, x, and the mean of its fitted values, $\mu(x)_{\text{(no) smear}}$, when pseudodata are generated with(out) phase-space coordinate smearing.

9.6 | Inputs for *CP*-Violating Backgrounds

In the *CP* fit, the *CP*-violating backgrounds are parameterised with corresponding *CP* observables which are fixed. The hadronic parameters used to calculate these *CP* observables carry uncertainties, and therefore there is an associated systematic uncertainty. This is evaluated by generating 1000 pseudodatasets with alternative hadronic parameter inputs and performing the *CP* fit with the nominal fit model. The systematic uncertainty for a *CP* observable, x, is then calculated as

$$\sigma_{\text{syst}}(x) = [\mu(x)_{\text{gen} \neq \text{fit}} - I(x)] - [\mu(x)_{\text{gen = fit}} - I(x)], \tag{9.4}$$

where:

- $\mu(x)_{\text{gen} \neq \text{fit}}$ is the mean of the fitted values of the *CP* observable when the model at generation and fitting are different, *i.e.* where alternative inputs are used for the *CP*-violating backgrounds during generation.
- $\mu(x)_{\text{gen = fit}}$ is the mean of the fitted values of the *CP* observable when the model at generation and fitting are the same, *i.e.* the mean of the fitted values from the pseudodata study in Ch. 8.5.

- $I(x)$ is the input value for the *CP* observable in each pseudodataset. The same value is used when generating pseudodata with alternative inputs for the *CP*-violating backgrounds and in Ch. 8.5.

To determine the systematic uncertainty, the coherence factors, κ, for all *CP*-violating backgrounds are varied from 0.5 to unity, except for the background contributions from $B^0 \to DK^\pm\pi^\mp$ and $B^\pm \to D\pi^\pm\pi^0$ decays. For $B^0 \to DK^\pm\pi^\mp$ decays, the coherence factor is varied to 0.958 instead. This is because this was the coherence factor measured for the $B^0 \to DK^{*0}(892)$ signal component in an amplitude measurement of $B^0 \to DK^\pm\pi^\mp$ decays [107]. In this thesis, $B^0 \to DK^{*0}(892)$ decays form a background component and therefore, 0.958 represents a maximum coherence factor for the $B^0 \to DK^\pm\pi^\mp$ background. For $B^\pm \to D\pi^\pm\pi^0$ decays, the coherence factor is nominally set to unity, and an associated systematic uncertainty is not evaluated. This is because the global fit showed with very good precision that the background from $B^\pm \to D\pi^\pm\pi^0$ decays consists of almost entirely $B^\pm \to D\rho^\pm$ decays. Therefore, the coherence factor for $B^\pm \to D\pi^\pm\pi^0$ decays is not varied in these pseudodata studies.

The strong phases for the $B^0 \to [D\pi^0]_{D^*}K^\pm\pi^\mp$ and $B^0 \to [D\gamma]_{D^*}K^\pm\pi^\mp$ decays are assumed to be equal in the *CP* fit, but this may not be true. The systematic uncertainty associated with this is assessed by introducing a phase shift between these δ_B parameters. Since the *CP*-violation parameters for these backgrounds have not been measured, the effect due to a maximal phase difference of 180° is assessed.

The systematic uncertainty due to the remaining r_B and δ_B hadronic parameters is assessed by shifting their nominal values to the upper and lower limits

of the 68.3% confidence level quoted in Ref. [47]. This results in two sets of inputs which are tested and shown in Tab. 9.2. Set A denotes the shift to the upper limits, and set B the shift to the lower limits. There are two cases where a lack of information on CP-violation, specifically in $B^{\pm} \to D^{(*)}\pi^{\pm}\pi^{0}$ decays, means that the strong-phase inputs were chosen arbitrarily. To assess the systematic uncertainty due to this, the strong phases are rotated by 180° in both set A and set B. Pseudodata studies were also carried out where they were rotated by 90° and 270° to assess the full spectrum of possible values, and it was found that all three rotations led to very similar systematic uncertainties.

For each CP observable, the systematic uncertainty is determined by taking the largest uncertainty from sets A and B. Large backgrounds for which there is little knowledge about their CP-violation dominate these uncertainties. The $B^{\pm} \to DK^{\pm}\pi^{0}$ decays have the largest impact on the $D^{*}K$ CP observables, and the $B^{\pm} \to D^{(*)}\pi^{\pm}\pi^{0}$ decays impact the $D^{*}\pi$ CP observables the most.

9.7 | Bias Correction

The validation of the CP fit in Ch. 8.5 found that a bias correction was necessary for the $\Re(\xi^{D^{*}\pi})$ observable. The size of this bias can differ depending on the input parameters for the pseudoexperiments. Therefore, alternative pseudoexperiment inputs are tested to determine the range of possible biases. Three sets of alternative inputs were chosen, shown in Tab. 9.3, from the 68.3% confidence level for the physical observables in the latest LHCb γ combination [47]. The pseudoexperiments are performed with these alternative inputs and the range of biases on the CP observables is taken as the systematic uncertainty.

Table 9.2: Variations in hadronic input parameters for *CP*-violating backgrounds to assess their associated systematic uncertainty.

Component	r_B	$\delta_B(^\circ)$	κ
Set A			
$B^0 \to DK^\pm\pi^\mp$	0.271	208	0.958
$B^\pm \to DK^\pm\pi^0$	0.124	54	1.0
$B^0 \to [D\gamma]_{D^*}K^\pm\pi^\mp$	0.271	111	1.0
$B^0 \to [D\pi^0]_{D^*}K^\pm\pi^\mp$	0.271	291	1.0
$B^\pm \to D^*K^\pm\pi^0$	0.124	54	1.0
$B^\pm \to D\pi^\pm\pi^0$	0.0055	280	1.0
$B^\pm \to D^*\pi^\pm\pi^0$	0.0055	20	1.0
Set B			
$B^0 \to DK^\pm\pi^\mp$	0.224	188	0.958
$B^\pm \to DK^\pm\pi^0$	0.089	19	1.0
$B^0 \to [D\gamma]_{D^*}K^\pm\pi^\mp$	0.224	29	1.0
$B^0 \to [D\pi^0]_{D^*}K^\pm\pi^\mp$	0.224	209	1.0
$B^\pm \to D^*K^\pm\pi^0$	0.089	19	1.0
$B^\pm \to D\pi^\pm\pi^0$	0.0044	280	1.0
$B^\pm \to D^*\pi^\pm\pi^0$	0.0044	20	1.0

Table 9.3: Nominal (top row) and alternative inputs for physical observables to determine the systematic uncertainty due to the bias correction.

γ	$r_B^{D^*K^\pm}$	$\delta_B^{D^*K^\pm}$	$r_B^{D^*\pi^\pm}$	$\delta_B^{D^*\pi^\pm}$
63.8°	0.098	308°	0.0091	137°
64°	0.100	315°	0.010	150°
60°	0.079	283°	0.0035	54°
67°	0.115	320°	0.0172	159°

9.8 | Negligible Systematic Uncertainties

There are some sources of systematic uncertainty which are ignored as their effects are negligible compared to the statistical precision of this result. These are discussed here.

9.8.1 | Bin-Dependent Mass Shapes

The mass shape parameterisations from the global fit are fixed in every Dalitz plot bin in the *CP* fit. It is possible that these shapes could vary over the D-decay phase space due to variations in particle kinematics over the Dalitz plot. This is predominantly minimised by the constraints on the D and K^0_S meson masses during candidate reconstruction, as explained in Ch. 6.1. To determine how large any remaining effect is, Kolmogorov-Smirnov tests [92, 93] are used to compare mass distributions in simulation for the signal decays and the fully reconstructed $B^\pm \to Dh^\pm$ backgrounds. Comparisons are made of these distributions between the global D-decay phase space and in each Dalitz plot bin of the rectangular binning scheme for the $D \to K^0_S\pi^+\pi^-$ final state. For this test, candidates from the $B^\pm \to D\pi^\pm$ mode with downstream K^0_S mesons are used as this category has the largest yield, making differences between the mass shapes more evident. In Fig. 9.2, the mass shapes in simulation for the global D-decay phase space are shown by the grey filled regions and the mass shapes in each Dalitz plot bin are shown by the coloured lines. The legend includes p-values from the Kolmogorov-Smirnov tests. This is an indication of how similar two histograms are, and if the p-value is greater than 5%, the histograms can be assumed to be similar. This is the case for all components and Dalitz plots bins, with most p-values at approximately 50%.

The slope of the combinatorial background can also vary between Dalitz plot bins. To investigate this, the high $m(Dh)$ sideband, (5600–6500 MeV/c^2) in data is fitted with an exponential for each Dalitz plot bin. Figure 9.3 shows very little variation between the exponential slope for each Dalitz plot bin and that for the

global D-decay phase space. Therefore, any associated systematic uncertainty would be very small, and negligible compared to the statistical precision of this measurement.

9.8.2 | Other CP-Violation Effects

The presence of D and K^0_S mesons in this analysis means that effects due to ignoring CP-violation, regeneration in K^0_S interactions with matter, and charm-mixing could affect the CP-violation measurement. The systematic uncertainty due to ignoring these effects was evaluated in the measurement of γ in $B^\pm \to Dh^\pm$ decays with the $D \to K^0_S h^+ h^-$ final state [45]. It was found to be an order of magnitude smaller than the statistical precision in that measurement. Given that there are larger statistical uncertainties here compared to Ref. [45], the systematic uncertainty due to ignoring these effects is expected to have a minimal effect on the final result and is ignored.

9.9 | Summary

All systematic uncertainties are summarised in Tab. 9.4. The total LHCb-related systematic uncertainty is shown, and once including the systematic uncertainty due to the external strong-phase inputs, the total systematic uncertainty is also given. For comparison, the statistical uncertainties are included at the bottom of the table, where it is evident that the result is statistically limited.

The correlation matrix related to the systematic uncertainty due to the external strong-phase inputs is shown in Tab. 9.5. In addition, the correlation matrix

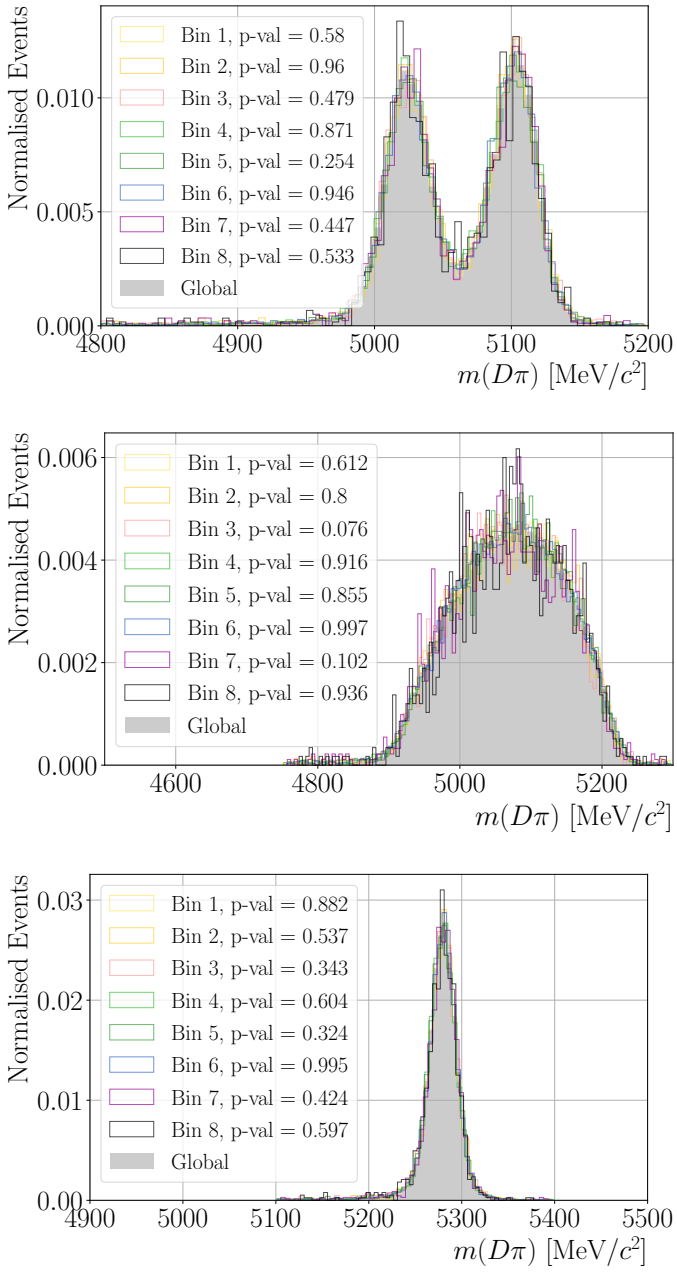

Figure 9.2: Mass distributions in simulation for (top) $B^{\pm} \to [D\pi^0]_{D^*}\pi^{\pm}$, (center) $B^{\pm} \to [D\gamma]_{D^*}\pi^{\pm}$, and (bottom) $B^{\pm} \to D\pi^{\pm}$ with downstream K^0_S mesons split by Dalitz bin in the rectangular binning scheme indicated by the coloured lines and the global D-decay phase space indicated by the shaded grey histograms. The p-values from Kolmogorov-Smirnov tests are shown in the legend.

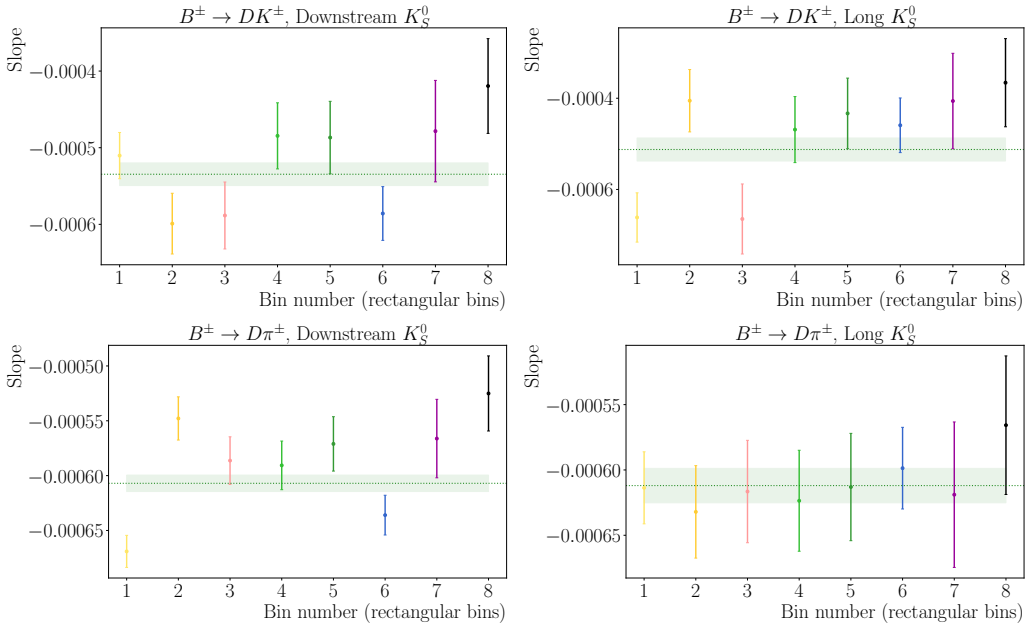

Figure 9.3: Exponential slopes fitted to the high mass sideband in data for (top) $B^\pm \to DK^\pm$ and (bottom) $B^\pm \to D\pi^\pm$ candidates with (left) downstream K^0_S candidates and (right) long K^0_S candidates. The coloured points indicate the slopes when fitting in each Dalitz plot bin in the rectangular binning scheme, and the green shaded lines indicate the fitted slope to the global D-decay phase space.

associated with the LHCb-related systematic uncertainties is shown in Tab. 9.6. For systematic uncertainties determined using repeated fits to data, the correlations are taken from those of the fitted central values. For systematic uncertainties assessed using pseudodata studies, if the average bias between a pair of *CP* observables is in the same direction a correlation of $+100\%$ is used, otherwise a correlation of -100% is used.

The leading sources of systematic uncertainty (mass shape parametrisation, fixed branching ratios, fixed yield ratios, and inputs for *CP*-violating backgrounds) are driven by the parameterisation of two background components; $B^\pm \to DK^\pm\pi^0$ and $B^\pm \to D\pi^\pm\pi^0$ decays. These are large *CP*-violating backgrounds for which there are currently no amplitude analyses or *CP*-violation measurements. The

Table 9.4: Summary of the systematic uncertainties, and for comparison, the statistical uncertainties. Values are expressed in units of 10^{-2}.

Source	$x_-^{D^*K}$	$y_-^{D^*K}$	$x_+^{D^*K}$	$y_+^{D^*K}$	$\Re(\xi^{D^*\pi})$	$\Im(\xi^{D^*\pi})$
Strong-phase inputs	0.57	1.54	0.18	0.41	2.33	2.13
Efficiency correction of (c_i, s_i)	0.23	0.29	0.21	0.20	0.47	0.31
Mass shape parameterisation	0.38	0.61	0.41	0.34	1.19	0.96
Fixed branching ratios	0.58	0.44	0.33	0.50	1.09	0.54
Fixed efficiencies	0.23	0.48	0.18	0.27	0.70	0.38
Fixed yield ratios	0.66	0.85	0.46	0.43	1.45	0.77
Dalitz-bin migration	0.00	0.02	0.04	0.10	0.03	0.11
Inputs for CPV backgrounds	0.35	0.33	0.38	0.21	2.22	1.93
Bias Correction	0.29	0.35	0.12	0.16	0.62	0.51
Total LHCb systematic uncertainties	1.11	1.36	0.85	0.87	3.28	2.46
Total systematic uncertainty	1.25	2.05	0.87	0.95	4.02	3.26
Statistical uncertainty	2.93	5.69	2.58	2.87	9.37	9.67

lack of amplitude analyses means that the $m(Dh)$ distribution has been modelled by estimating the largest contributions to these decays. The lack of *CP*-violation measurements for these backgrounds results in hadronic parameter inputs which carry large uncertainties or are unknown and therefore the full spectrum of possible values must be considered. Both of these result in large systematic uncertainties. Therefore, to avoid limiting a future version of this measurement, further work must include amplitude analyses and *CP*-violation measurements of these backgrounds.

Table 9.5: Correlation matrix associated with the systematic uncertainty due to the external strong-phase inputs.

	$x_-^{D^*K}$	$y_-^{D^*K}$	$x_+^{D^*K}$	$y_+^{D^*K}$	$\Re(\xi^{D^*\pi})$	$\Im(\xi^{D^*\pi})$
$x_-^{D^*K}$	1.000	0.886	−0.117	−0.063	0.916	0.904
$y_-^{D^*K}$		1.000	−0.124	−0.115	0.935	0.889
$x_+^{D^*K}$			1.000	−0.280	−0.130	0.063
$y_+^{D^*K}$				1.000	0.085	−0.077
$\Re(\xi^{D^*\pi})$					1.000	0.941
$\Im(\xi^{D^*\pi})$						1.000

Table 9.6: Correlation matrix associated with the LHCb-related experimental systematic uncertainties.

	$x_-^{D^*K}$	$y_-^{D^*K}$	$x_+^{D^*K}$	$y_+^{D^*K}$	$\Re(\xi^{D^*\pi})$	$\Im(\xi^{D^*\pi})$
$x_-^{D^*K}$	1.000	0.630	−0.241	−0.016	0.602	0.083
$y_-^{D^*K}$		1.000	0.008	0.154	0.735	0.230
$x_+^{D^*K}$			1.000	0.515	0.232	0.618
$y_+^{D^*K}$				1.000	0.237	0.112
$\Re(\xi^{D^*\pi})$					1.000	−0.201
$\Im(\xi^{D^*\pi})$						1.000

10

CKM Angle γ Result

The *CP* observables for $B^{\pm} \to D^{*}h^{\pm}$ decays are measured to be:

$$
\begin{aligned}
x_{-}^{D^{*}K} &= (-6.3 \pm 2.9 \pm 1.1 \pm 0.6) \times 10^{-2}, \\
y_{-}^{D^{*}K} &= (-4.8 \pm 5.7 \pm 1.4 \pm 1.5) \times 10^{-2}, \\
x_{+}^{D^{*}K} &= (\ \ 6.0 \pm 2.6 \pm 0.9 \pm 0.2) \times 10^{-2}, \\
y_{+}^{D^{*}K} &= (\ \ 5.4 \pm 2.9 \pm 0.9 \pm 0.4) \times 10^{-2}, \\
\Re(\xi^{D^{*}\pi}) &= (\ 11.5 \pm 9.4 \pm 3.3 \pm 2.3) \times 10^{-2}, \\
\Im(\xi^{D^{*}\pi}) &= (-0.9 \pm 9.7 \pm 2.5 \pm 2.1) \times 10^{-2},
\end{aligned}
$$

where the first uncertainty is statistical, the second is systematic, and the third is due to external strong-phase inputs. The following chapter explains how these *CP* observables are interpreted in terms of the physical observables, $r_B^{D^{*}K}$, $\delta_B^{D^{*}K}$, $r_B^{D^{*}\pi}$, $\delta_B^{D^{*}\pi}$, and the CKM angle γ. To do this, a maximum-likelihood fit is performed using the LHCb GAMMACOMBO package [113].

10.1 | Method

The statistical methods by which the GAMMACOMBO package combines multiple *CP*-violation measurements to determine underlying physical observables are detailed in Ref. [113]. The same software package can be used to interpret a single measurement and this is outlined here.

The observables from the measurement in this thesis can be denoted,

$$\vec{A^{\text{obs}}} = (x_-^{D^*K}, y_-^{D^*K}, x_+^{D^*K}, y_+^{D^*K}, \Re(\xi^{D^*\pi}), \Im(\xi^{D^*\pi})), \tag{10.1}$$

where the underlying physics parameters are,

$$\vec{\alpha} = (r_B^{D^*K}, \delta_B^{D^*K}, r_B^{D^*\pi}, \delta_B^{D^*\pi}, \gamma). \tag{10.2}$$

The PDF associated with the measurement, $f(\vec{A^{\text{obs}}}|\vec{\alpha})$, is assumed to be a multi-dimensional Gaussian distribution,

$$f(\vec{A^{\text{obs}}}|\vec{\alpha}) \propto \exp\left[-\frac{1}{2}(\vec{A}(\vec{\alpha}) - \vec{A^{\text{obs}}})^T V^{-1} (\vec{A}(\vec{\alpha}) - \vec{A^{\text{obs}}})\right], \tag{10.3}$$

where V is the covariance matrix, including both statistical and systematic uncertainties and their correlations. In the case of interpreting a single measurement, the likelihood function is equal to the PDF, $\mathcal{L}(\vec{\alpha}) = f(\vec{A^{\text{obs}}}|\vec{\alpha})$. Using this, a χ^2-function, defined as $\chi^2(\vec{\alpha}) = -2\ln\mathcal{L}(\vec{\alpha})$, is minimised to determine the best-fit physics parameters at the global minimum, $\chi^2(\vec{\alpha}_{\text{min}})$.

The confidence level (CL) where, for example, γ is γ_0, is determined as follows:

1. With $\gamma = \gamma_0$, a new χ^2-function is defined and minimised, resulting in a new minimum, $\chi^2(\vec{\alpha'}_{\text{min}})$.

2. The deviation from the global minimum is calculated
   $\Delta\chi^2 = \chi^2(\vec{\alpha}'_{\text{min}}) - \chi^2(\vec{\alpha}_{\text{min}})$.

3. Pseudodatasets, $\vec{A}^{\text{MC}}$, are generated according to the PDF, $f(\vec{A^{\text{obs}}}|\vec{\alpha}'_{\text{min}})$.

4. Each pseudodataset is minimised. Once where γ allowed to vary, and once where it is fixed to γ_0.

5. The difference between these minima is computed, $(\Delta\chi^2)^{\text{MC}}$.

6. The value of $1-\text{CL}$ is the fraction of pseudodatasets with $\Delta\chi^2 < (\Delta\chi^2)^{\text{MC}}$.

Within the GAMMACOMBO package, this is called the PLUGIN method. There is also an alternative procedure called the PROB method. In this case, the deviation, $\Delta\chi^2$, from the global minimum is calculated, and assumed to follow a χ^2-distribution. The CL is then determined using the cumulative distribution function for a χ^2-function. For example, for one degree of freedom, the 68.3% CL corresponds to a $\Delta\chi^2$ value of 1. This approach relies on the assumption that the $\Delta\chi^2$ deviation follows a χ^2-distribution, and therefore that the parameter estimates follow Gaussian distributions. This is true for asymptotically large samples [114], and is a good assumption given the elliptical contours for the *CP*-observables, shown in Fig. 8.8. However, there are small deviations in the contours in Fig. 8.8 from an ellipse. Therefore, the PLUGIN method is more suitable as the generation of sufficient pseudodatasets ensures reliable coverage.

10.2 | Interpretation

The parameterisation of the *CP* observables allows for a two-fold symmetry with solutions where $\gamma \to \gamma + 180^\circ$ and $\delta_B \to \delta_B + 180^\circ$. By convention, $0 < \gamma < 180^\circ$ is chosen, and therefore the physics parameters are interpreted to be,

$$\begin{aligned}
\gamma &= (92^{+21}_{-17})^\circ, \\
r_B^{D^*K} &= 0.080^{+0.022}_{-0.023}, \\
\delta_B^{D^*K} &= (310^{+15}_{-20})^\circ, \\
r_B^{D^*\pi} &= 0.009^{+0.005}_{-0.007}, \\
\delta_B^{D^*\pi} &= (304^{+37}_{-38})^\circ.
\end{aligned}$$

The solution for γ is consistent with the current LHCb γ combination, where $\gamma = (63.8^{+3.5}_{-3.7})^\circ$ [47]. These solutions are depicted in Fig. 10.1 where the confidence intervals for γ are shown, and in Fig. 10.2 where the two-dimensional confidence regions between the hadronic parameters are shown.

The solutions listed above were determined using the PLUGIN method described in the preceding section. The confidence intervals for γ are shown in Fig. 10.1, where the PLUGIN (points) and PROB (purple shaded region) methods are compared. There is reasonable agreement between the two methods, with a small deviation in the right-hand tail of the $1-$CL distribution. This is because the uncertainty on γ is inversely proportional to the central value of r_B, which is bounded to be greater than 0. This is taken into account when generating pseudodata for the PLUGIN method and results in a slightly higher right-hand tail in the $1-$CL distribution for γ.

Taking, as an example, the lower limit of the uncertainty on γ, 17°, this is

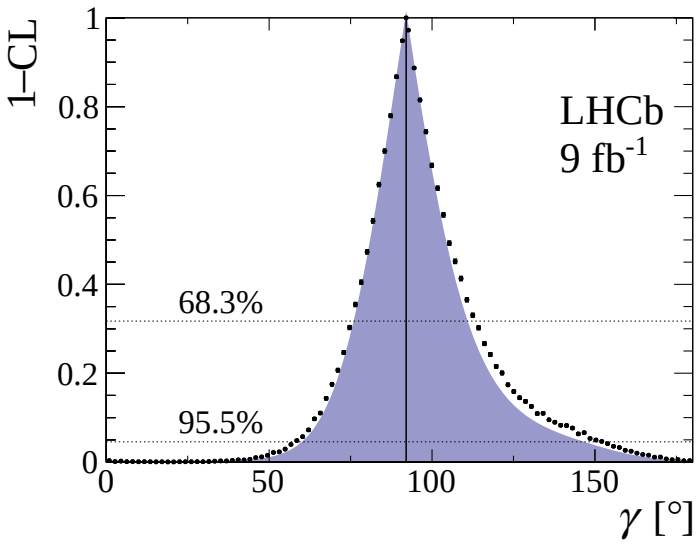

Figure 10.1: Confidence intervals at 68.3% and 95.5% for the CKM angle γ determined using the PLUGIN (black points) and PROB (purple shaded region) methods.

composed of a large statistical component, 16°, an LHCb-related systematic uncertainty of 4°, and a strong-phase-related uncertainty of 4°. A sensitivity study with all signal and background components estimated a statistical sensitivity of 15°. Therefore, the result found here is slightly larger, but within expectation. The sensitivity study was performed using current LHCb averages for inputs for the physical observables. Here, the input for $r_B^{D^*K} = 0.098$, is larger than, though still consistent with, the central value measured in this analysis. Since the uncertainty on γ is inversely proportional to the central value of r_B, the smaller central value of $r_B^{D^*K}$ leads to a larger statistical uncertainty on γ.

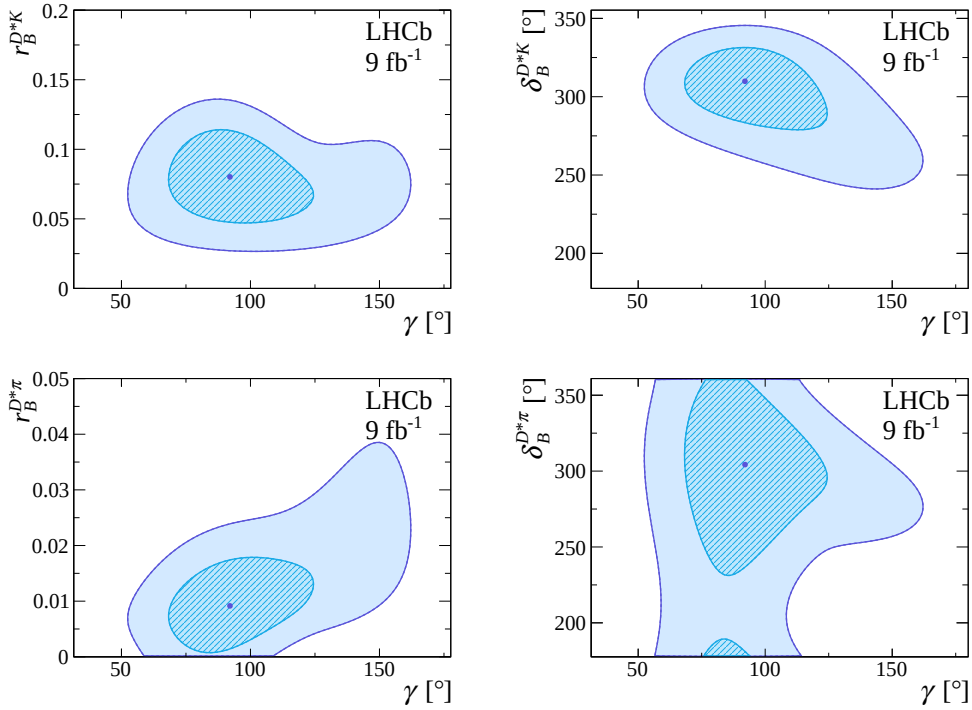

Figure 10.2: Two-dimensional confidence regions at 68.3% and 95.5% indicated by the lighter and darker shades respectively, for (top, left) γ vs. $r_B^{D^*K}$, (top, right) γ vs. $\delta_B^{D^*K}$, (bottom left) γ vs. $r_B^{D^*\pi}$, and (bottom, right) γ vs. $\delta_B^{D^*\pi}$.

10.3 | Comparison with Other Measurements

The results of this measurement can be compared to a number of similar LHCb measurements [46,51]. These are considered below and a combination of γ, $r_B^{D^*K}$, and $\delta_B^{D^*K}$ using these measurements for $B^\pm \to D^*K^\pm$ decays is given in Ch. 10.3.3. This is subsequently compared to γ measurements from Belle [48] and BaBar [49] for the same B decay in Ch. 10.3.4.

10.3.1 | Fully Reconstructed $B^{\pm} \to D^{*}h^{\pm}$, $D \to K^{0}_{S}h^{+}h^{-}$ at LHCb

A description of this measurement [51] is given in Ch. 3.5.3. Similarly to the work in this thesis, $B^{\pm} \to D^{*}h^{\pm}$ decays with $D \to K^{0}_{S}h^{+}h^{-}$ final states are studied, but candidates are fully reconstructed. As there is an overlap in selection, the correlation between Ref. [51] and the measurement in this thesis must be determined.

10.3.1.1 | Correlation

All events in Ref. [51] also appear in this analysis. Therefore, one may naïvely expect that there is a strong correlation between the two analyses. In fact, the correlation can be dismissed as negligible due to a number of differences between the two analyses that result in common events carrying different weights.

By comparing signal yields in each analysis, it is found that Ref. [51] contains 45% of the $B^{\pm} \to [D\gamma]_{D^{*}}K^{\pm}$ signal yield and 18% of the $B^{\pm} \to [D\pi^{0}]_{D^{*}}K^{\pm}$ signal yield in the present work. It is not viable to remove these overlapping events from the measurement in this thesis. An example of the $m(Dh)$ spectrum of events in Ref. [51] and the present work is shown in Fig. 10.3, and below this spectrum is the efficiency of remaining events if overlapping events are removed from the present work. This efficiency drops significantly in the signal region, 4950–5200 MeV/c^{2}, indicating that removing fully reconstructed events would result in a large signal loss. Furthermore, the trend in the efficiency is not simple, rising from low to high $m(Dh)$ values since reconstruction efficiency is dependent on momentum. Therefore, if fully reconstructed events are removed

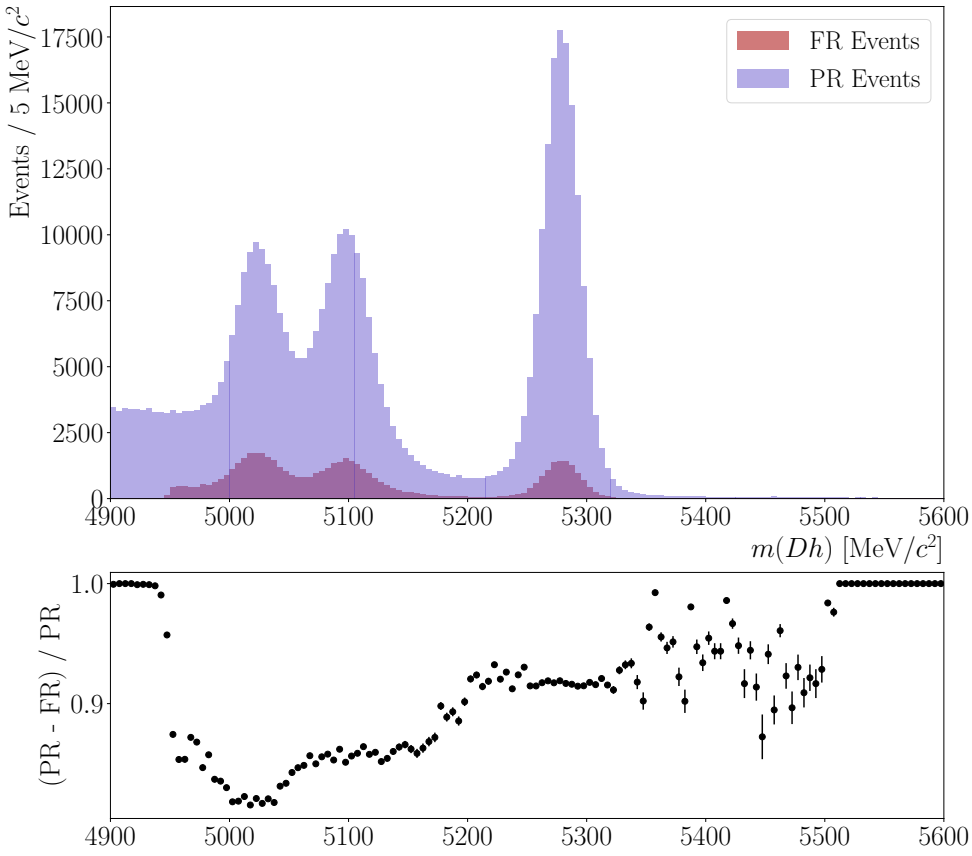

Figure 10.3: The $m(Dh)$ spectrum of events in the fully reconstructed analysis [51] (labelled 'FR') and the present work with partial reconstruction (labelled 'PR), indicating their overlap and below this, the efficiency associated with the remaining events if fully reconstructed events are removed from the present work.

from the present work, it would complicate the parameterisation of the signal and background components in the 4950–5500 MeV/c^2 mass range. Instead, the correlation between Ref. [51] and the present work is determined.

First, the sensitivity in each analysis is driven by different D^* decays. In Ref. [51], the reconstruction efficiency for a single photon in a $D^* \to D\gamma$ candidate is higher than that for two low-momentum photons forming a $D^* \to D\pi^0$

candidate. This results in a larger yield for candidates with $D^* \to D\gamma$ decays compared to $D^* \to D\pi^0$ decays, and thus the sensitivity is driven by the $D^* \to D\gamma$ mode. In contrast, the present work does not reconstruct photons or neutral pions, therefore the reconstruction efficiency does not differ between the two D^* decays. Instead, the yield for the $D^* \to D\pi^0$ mode is larger that of the $D^* \to D\gamma$ mode because $\mathcal{B}(D^* \to D\pi^0)$ is twice $\mathcal{B}(D^* \to D\gamma)$. Therefore, here, the sensitivity is driven by the $D^* \to D\pi^0$ mode. Furthermore, in Ref. [51], the reconstruction of photons and neutral pions means that the two D^* decay modes are well-separated. Whereas, in the present work, they overlap and occupy the same $m(Dh)$ region. The correlation between the two analyses due to these differences and the overlap in the signal yield is assessed using pseudodata studies.

The *CP* fit model is modified to separate the $D^* \to D\gamma$ and $D^* \to D\pi^0$ modes. Then, 1000 signal-only pseudodata are generated using signal yields measured in Ref. [51], and the *CP* fit is performed. Then, a second pseudodata study is performed using the nominal signal-only *CP* fit model, where the two D^* decay modes are not separated. For this study, pseudodata must include the overlap between the signal yields in the two analyses. Therefore, pseudodata from the previous toy study are reused and only excess events are generated to total the signal yields in this analysis. The nominal signal-only *CP* fit is then performed. The correlations between the fitted *CP* observables for each set of pseudodata studies are calculated and shown in Tab. 10.1. The average of the diagonal components shows there is an average correlation of 17% due to the overlap and treatment of the signal components in the two analyses.

This 17% correlation is then diluted due to the different background environments in each analysis. The impact of this in the present work is determined as

Table 10.1: Correlation matrix for the fitted $B^{\pm} \to D^{*}h^{\pm}$ *CP* observables in signal-only pseudodata for this analysis (labelled 'PR') and the fully reconstructed analysis (labelled 'FR').

	$x^{D^*K}_{-,\mathrm{PR}}$	$y^{D^*K}_{-,\mathrm{PR}}$	$x^{D^*K}_{+,\mathrm{PR}}$	$y^{D^*K}_{+,\mathrm{PR}}$	$\Re(\xi^{D^*\pi}_{\mathrm{PR}})$	$\Im(\xi^{D^*\pi}_{\mathrm{PR}})$
$x^{D^*K}_{-,\mathrm{FR}}$	0.18	0.01	0.04	−0.01	−0.01	0.04
$y^{D^*K}_{-,\mathrm{FR}}$	0.02	0.20	−0.03	0.03	0.08	−0.01
$x^{D^*K}_{+,\mathrm{FR}}$	0.01	−0.04	0.24	0.01	0.00	−0.02
$y^{D^*K}_{+,\mathrm{FR}}$	0.02	0.01	−0.01	0.19	−0.00	0.07
$\Re(\xi^{D^*\pi}_{\mathrm{FR}})$	−0.00	−0.04	0.02	−0.02	0.10	−0.02
$\Im(\xi^{D^*\pi}_{\mathrm{FR}})$	0.01	−0.06	−0.03	0.05	−0.04	0.10

follows. First, 1000 signal-only pseudodata are generated and the *CP* fit is performed. Then, 1000 pseudodata with signal and background components are generated and the *CP* fit is performed. The signal components in both sets of pseudodata studies must be identical to avoid a statistical spread in the correlation. The correlations between the resulting *CP* observables are calculated, and are shown in Tab. 10.2. From the diagonal elements, an average correlation of 53% is found due to the background environment in the present work. The same study was repeated by the proponents of Ref. [51], and an average correlation of 42% was found.

Overall, the correlation due to the overlap and treatment of the signal components, and the background environment in each analysis can be calculated as, at most, 3%, since

$$17\% \times 53\% \times 42\% = 3\%. \tag{10.4}$$

This is an upper limit since there are further differences between the two analyses which have not been assessed here, such as the looser PID requirement in Ref. [51]. The correlations due to these differences cannot be determined trivially

Table 10.2: Correlation matrix for the fitted $B^{\pm} \to D^{*}h^{\pm}$ *CP* observables in signal-only pseudodata (labelled 'sig') and in pseudodata with all signal and background components (labelled 'sig+bkg').

	$x_{-,\,\mathrm{sig}}^{D^*K}$	$y_{-,\,\mathrm{sig}}^{D^*K}$	$x_{+,\,\mathrm{sig}}^{D^*K}$	$y_{+,\,\mathrm{sig}}^{D^*K}$	$\Re(\xi_{\,\mathrm{sig}}^{D^*\pi})$	$\Im(\xi_{\,\mathrm{sig}}^{D^*\pi})$
$x_{-,\,\mathrm{sig+bkg}}^{D^*K}$	0.61	−0.01	−0.08	0.01	−0.15	0.12
$y_{-,\,\mathrm{sig+bkg}}^{D^*K}$	0.01	0.42	0.01	0.01	−0.06	−0.12
$x_{+,\,\mathrm{sig+bkg}}^{D^*K}$	−0.03	0.06	0.58	−0.15	0.09	−0.06
$y_{+,\,\mathrm{sig+bkg}}^{D^*K}$	−0.04	−0.03	−0.19	0.48	−0.02	0.12
$\Re(\xi_{\,\mathrm{sig+bkg}}^{D^*\pi})$	−0.13	−0.07	0.01	−0.04	0.56	−0.01
$\Im(\xi_{\,\mathrm{sig+bkg}}^{D^*\pi})$	0.12	−0.12	−0.03	0.15	0.04	0.54

and would further reduce the 3% correlation found. The effect of this 3% statistical correlation on a combined value of γ is estimated using pseudodata. The inclusion of a 3% statistical correlation shifts the uncertainty on γ by 1%. Therefore, the correlation can be dismissed as negligible, and the two analyses can be treated as statistically independent.

The experimental systematic uncertainties are uncorrelated since the global and *CP* fits are parameterised differently in the two analyses due to the difference in reconstruction. Therefore, any fixed quantities and the systematic uncertainty associated with ignoring the uncertainties on the fixed quantities are uncorrelated. This is not the case for the systematic uncertainty due to use of external strong phase inputs, since the same inputs are used. The correlation between the two analyses due to this is evaluated by repeating the *CP* fit to data for each analysis 1000 times with the same randomly sampled strong-phase inputs. The correlations between the resulting *CP* observables are shown in Tab. 10.3.

Table 10.3: Correlation matrix between this analysis (labelled 'PR') and the fully reconstructed analysis (labelled 'FR') due to the use of the same external strong-phase inputs.

	$x_{-,\mathrm{PR}}^{D^*K}$	$y_{-,\mathrm{PR}}^{D^*K}$	$x_{+,\mathrm{PR}}^{D^*K}$	$y_{+,\mathrm{PR}}^{D^*K}$	$\Re(\xi_{\mathrm{PR}}^{D^*\pi})$	$\Im(\xi_{\mathrm{PR}}^{D^*\pi})$
$x_{-,\mathrm{FR}}^{D^*K}$	-0.02	-0.03	-0.04	0.10	-0.02	-0.04
$y_{-,\mathrm{FR}}^{D^*K}$	0.04	0.05	0.05	0.10	0.06	0.03
$x_{+,\mathrm{FR}}^{D^*K}$	0.03	0.01	0.11	0.16	0.07	0.04
$y_{+,\mathrm{FR}}^{D^*K}$	0.19	0.26	-0.20	0.14	0.26	0.17
$\Re(\xi_{\mathrm{FR}}^{D^*\pi})$	0.04	0.02	0.01	-0.16	-0.00	0.05
$\Im(\xi_{\mathrm{FR}}^{D^*\pi})$	0.01	0.01	0.07	-0.04	0.02	0.06

10.3.1.2 | Comparison

The results for the *CP* observables in this analysis and in Ref. [51] are compared in Tab. 10.4. The uncertainties on the $\xi^{D^*\pi}$ parameter are twice as large in this analysis as in Ref. [51]. This is due to the dominant presence of the $B^\pm \to D\pi^\pm\pi^0$ background in this analysis which is suppressed in Ref. [51] due to the extra discrimination power from the neutral reconstruction.

The results for the D^*K *CP* observables are depicted in Fig. 10.4 with their corresponding 68.3% and 95.5% confidence regions due to statistical uncertainties. The central values are consistent, and in general, the results from this analysis have smaller statistical uncertainties, indicating that they will carry more weight when the two results are combined. Furthermore, Fig. 10.4 shows that the central value for $r_B^{D^*K}$ is larger in Ref. [51], and therefore the fully reconstructed analysis has smaller statistical uncertainties on γ. The value of γ from Ref. [51] is $\gamma = (69^{+13}_{-14})^\circ$ indicating this. Nevertheless, the central values in both analyses are consistent.

Table 10.4: Comparison of $B^{\pm} \to D^{*}h^{\pm}$ *CP* observables in this analysis and in Ref. [51] with implicit $\times 10^{-2}$.

CP Observable	This Analysis	Ref. [51]
$x_{-}^{D^{*}K}$	-6.3 $\pm$ 2.9 $\pm$ 1.1 $\pm$ 0.6	-8.9 $\pm$ 3.6 $\pm$ 2.1 $\pm$ 0.4
$y_{-}^{D^{*}K}$	-4.8 $\pm$ 5.7 $\pm$ 1.4 $\pm$ 1.5	-16.8 $\pm$ 4.0 $\pm$ 1.5 $\pm$ 0.4
$x_{+}^{D^{*}K}$	6.0 $\pm$ 2.6 $\pm$ 0.9 $\pm$ 0.2	11.4 $\pm$ 3.2 $\pm$ 1.3 $\pm$ 0.3
$y_{+}^{D^{*}K}$	5.4 $\pm$ 2.9 $\pm$ 0.9 $\pm$ 0.4	3.6 $\pm$ 4.4 $\pm$ 2.2 $\pm$ 0.7
$\Re(\xi^{D^{*}\pi})$	11.5 $\pm$ 9.4 $\pm$ 3.3 $\pm$ 2.3	0.5 $\pm$ 5.0 $\pm$ 2.8 $\pm$ 0.8
$\Im(\xi^{D^{*}\pi})$	-0.9 $\pm$ 9.7 $\pm$ 2.5 $\pm$ 2.1	7.9 $\pm$ 5.0 $\pm$ 4.1 $\pm$ 1.5

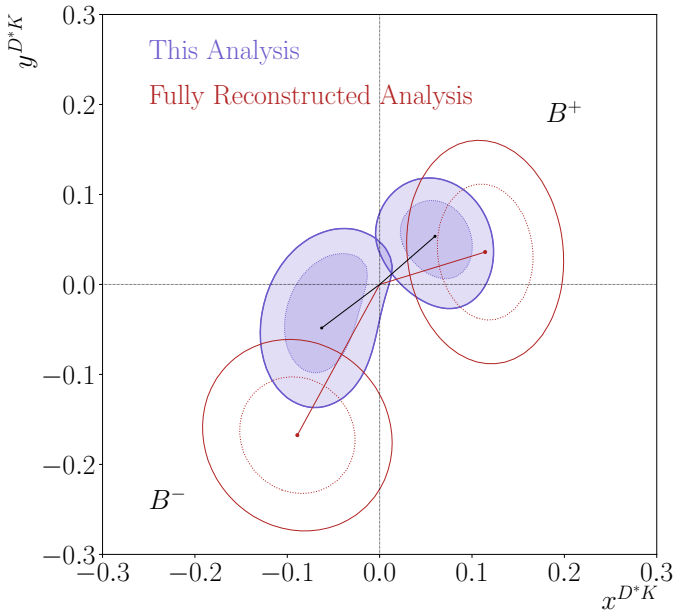

Figure 10.4: Comparison of $D^{*}K$ *CP* observables in this analysis (purple) and Ref. [51] (red) with their 68.3% and 95.5% confidence regions due to statistical uncertainties.

10.3.2 | $B^{\pm} \to D^{*}h^{\pm}$, $D \to h^{+}h^{-}$ at LHCb

A description of the measurement of *CP*-violation in $B^{\pm} \to D^{*}h^{\pm}$ with 2-body D-decay final states at LHCb [46] is given in Ch. 3.5.2. In this analysis, partially reconstructed $B^{\pm} \to D^{*}h^{\pm}$ decays are signal but with 2-body D-decay final states. This means that the observables are *CP* asymmetries and ratios, as opposed to the

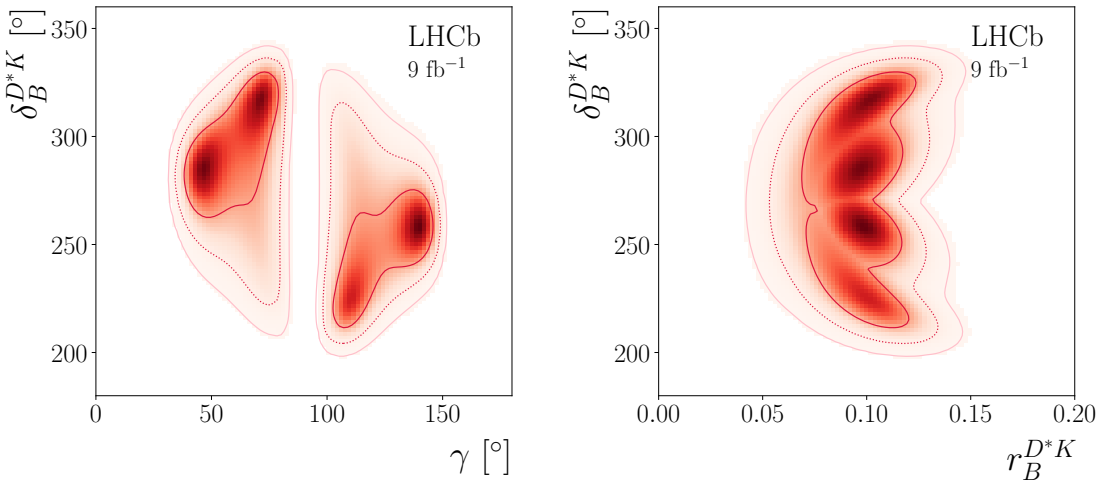

Figure 10.5: Results from Ref. [46], which studied $B^{\pm} \to D^* h^{\pm}$ decays with 2-body D-decay final states, depicting the four-fold symmetry in solutions for γ in two-dimensional confidence regions in (left) $\delta_B^{D^*K}$ and γ, and (right) $\delta_B^{D^*K}$ and $r_B^{D^*K}$.

cartesian *CP* observables. The trigonometric relation between these asymmetries and ratios and the physical observables leads to a four-fold degeneracy in the solution for γ, as shown in Fig. 10.5.

The analysis in this thesis and Ref. [51] consider the self-conjugate $D \to K^0_S h^+ h^-$ final state, and therefore in each case a single solution for γ is found, breaking the degeneracy in Ref. [46]. Also, as is evident by comparing results for the hadronic parameters in Fig. 10.5 and those in this thesis, the present work places very strong constraints on these parameters.

10.3.3 | Combination of $B^{\pm} \to D^{*}K^{\pm}$ Decays at LHCb

The combined value of γ and the $D^{*}K$ hadronic parameters from this analysis, Ref. [46], and Ref. [51] using the PROB method are

$$\begin{aligned} \gamma &= (74 \pm 8)^{\circ}, \\ r_B^{D^{*}K} &= 0.096 \pm 0.013, \\ \delta_B^{D^{*}K} &= (315 \pm 8)^{\circ}, \end{aligned}$$

and Fig. 10.6 shows the γ result with its 68.3% and 95.5% confidence levels. It is evident from the comparison of these combinations to results from Ref. [46] that the inclusion of this analysis and Ref. [51] significantly improve constraints on the hadronic parameters.

The uncertainty on γ using $B^{\pm} \to D^{*}K^{\pm}$ decays is around twice that from a combination using only $B^{\pm} \to DK^{\pm}$ decays (4°) [45,46]. This can be attributed to the difference in purity for $B^{\pm} \to D^{*}K^{\pm}$ and $B^{\pm} \to DK^{\pm}$ decays. As shown in the global fit results in Ch. 7.6, the region for $B^{\pm} \to DK^{\pm}$ decays contains very little background. In comparison, the region for $B^{\pm} \to D^{*}K^{\pm}$ decays is contaminated by many different backgrounds, leading to *CP*-violation measurements with comparatively worse statistical sensitivity per signal decay.

The CKM angle γ and the $D^{*}K$ hadronic parameters have also been measured by the Belle [48] and BaBar [49] collaborations. Therefore, the combination of the LHCb $B^{\pm} \to D^{*}K^{\pm}$ results can be compared to these.

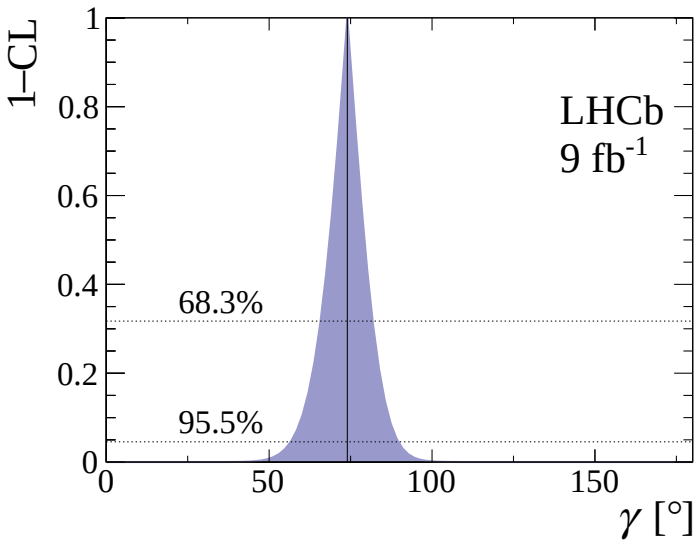

Figure 10.6: Confidence intervals at 68.3% and 95.5% for the CKM angle γ from a combination of this analysis, Ref. [51], and Ref. [46].

10.3.4 | Belle and BaBar Results

The Belle and BaBar collaborations have also performed measurements [48,49] of γ using $B^{\pm} \to D^{*}h^{\pm}$ decays in the $D \to K^{0}_{S}h^{+}h^{-}$ final states with full reconstruction. As discussed in Ch. 3.5.1, the Belle and BaBar measurements [48,49] use a model-dependent approach, whereby instead of using external strong-phase inputs, c_i and s_i, an amplitude model is used to determine r_D and δ_D. This method leads to model-related uncertainties. Therefore, no global combination is made between the LHCb, Belle, and BaBar results.

A comparison of the results for the hadronic parameters and γ from Belle, BaBar, and LHCb is shown in Fig. 10.7 using black error bars. The results are consistent between all experiments. The comparison shows that the larger data samples at LHCb lead to greater statistical sensitivity.

10.4 | Future Work

If this analysis is repeated with Run 3 data without further consideration, it will be systematically limited. To prevent this, a number of extra studies and measurements must first be performed. The largest systematic uncertainties arise from the mass shape parameterisation, fixed branching ratios, fixed yield ratios, and the inputs for the *CP*-violating backgrounds. In all cases these are driven by backgrounds from $B^{\pm} \to Dh^{\pm}\pi^0$ decays which are not well-understood, both in terms of their $m(Dh)$ spectra and their hadronic parameters.

To improve the modelling of the $m(Dh)$ distributions, amplitude analyses for $B^{\pm} \to D\pi^{\pm}\pi^0$ and $B^{\pm} \to DK^{\pm}\pi^0$ decays are needed. Using these, simulation could be generated using LAURA^{++} in order to better model these backgrounds. Furthermore, with a larger dataset, one can expect to allow more freedom in the $m(Dh)$ shape and yield parameterisation. This will additionally serve to reduce the systematic uncertainty associated with the fixed branching ratios and yield ratios.

To reduce the systematic uncertainty due to the inputs for the hadronic parameters in $B^{\pm} \to Dh^{\pm}\pi^0$ decays, *CP*-violation measurements are needed whereby r_B, δ_B, and κ are measured directly. Currently, a lack of prior knowledge of these values means systematic uncertainties are evaluated by considering a wide spectrum of values. By having measurements of these parameters, a smaller set of variations would be tested, reducing the associated systematic uncertainties.

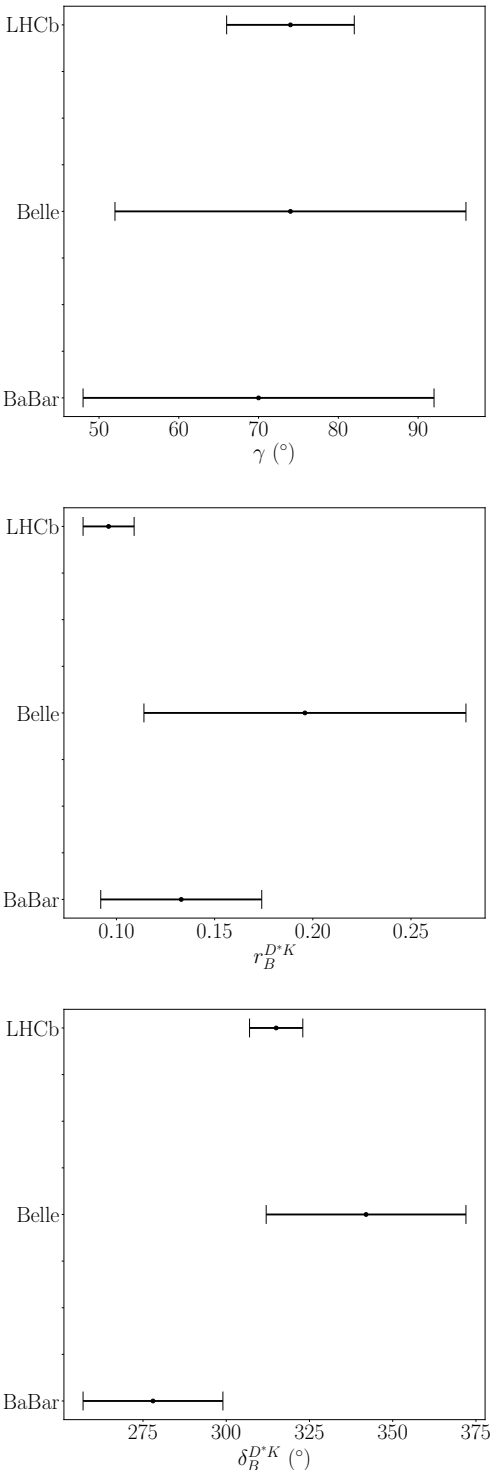

Figure 10.7: Results (with statistical and systematic uncertainties) for (top) γ, (center) $r_B^{D^*K}$, and (bottom) $\delta_B^{D^*K}$, from a combination of $B^\pm \to D^*K^\pm$ results from LHCb [46,51] and this thesis (labelled 'LHCb'), Belle [48], BaBar [49].

11

Summary

A *CP*-violation measurement of CKM angle γ is presented using $B^{\pm} \to D^{*}h^{\pm}$ decays in the $D \to K^{0}_{S}h^{+}h^{-}$ final state. The measurement uses $9\,\text{fb}^{-1}$ of pp collision data collected by LHCb at centre-of-mass energies of 7, 8, and 13 TeV. The candidates are partially reconstructed, meaning photons and neutral pions from the D^{*} meson decays are not reconstructed, thereby avoiding a signal efficiency reduction of 75% due to the reconstruction of low momentum neutral particles at LHCb. The *CP*-violation measurement is performed by parameterising the physical observables, γ, $r_B^{D^*K}$, $\delta_B^{D^*K}$, $r_B^{D^*\pi}$ and $\delta_B^{D^*\pi}$, in terms of *CP* observables, $x_{\pm}^{D^*K}$, $y_{\pm}^{D^*K}$, and $\xi^{D^*\pi}$. These are measured to be

$$
\begin{aligned}
x_{-}^{D^*K} &= (-6.3 \pm 2.9 \pm 1.1 \pm 0.6) \times 10^{-2}, \\
y_{-}^{D^*K} &= (-4.8 \pm 5.7 \pm 1.4 \pm 1.5) \times 10^{-2}, \\
x_{+}^{D^*K} &= (\ \ 6.0 \pm 2.6 \pm 0.9 \pm 0.2) \times 10^{-2}, \\
y_{+}^{D^*K} &= (\ \ 5.4 \pm 2.9 \pm 0.9 \pm 0.4) \times 10^{-2}, \\
\Re(\xi^{D^*\pi}) &= (\ 11.5 \pm 9.4 \pm 3.3 \pm 2.3) \times 10^{-2}, \\
\Im(\xi^{D^*\pi}) &= (-0.9 \pm 9.7 \pm 2.5 \pm 2.1) \times 10^{-2},
\end{aligned}
$$

where the first uncertainty is statistical, the second is systematic, and the third is due to external strong-phase inputs from a combination of CLEO [41] and BESIII [42, 43] measurements.

From this the physical observables are found to be

$$\begin{aligned}
\gamma &= (92^{+21}_{-17})^\circ, \\
r_B^{D^*K} &= 0.080^{+0.022}_{-0.023}, \\
\delta_B^{D^*K} &= (310^{+15}_{-20})^\circ, \\
r_B^{D^*\pi} &= 0.009^{+0.005}_{-0.007}, \\
\delta_B^{D^*\pi} &= (304^{+37}_{-38})^\circ.
\end{aligned}$$

Excellent consistency is found between these results, the latest LHCb γ combination [47], and another LHCb analysis [51] which measures the same decay chain with the inclusion of neutral particles in the reconstruction.

Given that this is a partially reconstructed analysis, an increased background level is seen compared to Ref. [51], therefore requiring a careful parameterisation of the $m(Dh^\pm)$ spectrum. This also results in one of the far-reaching outcomes of this analysis. The mass shape parameterisation developed for this measurement will be useful in future partially reconstructed γ measurements at LHCb. The work presented here measures γ in one of the best channels, given the negligible theoretical uncertainties, the high branching fraction for $B^\pm \to D^*K^\pm$ decays, and their high sensitivity to γ. Furthermore, since the self-conjugate $D \to K^0_S h^+ h^-$ final state is studied, this results in a single value for γ. Therefore, the results of this analysis also serve to remove degeneracies in existing analyses, such as Ref. [46], and therefore increases their weight in future combinations. This not only improves the combined measurement of γ, but also of the hadronic parameters,

$r_B^{D^*K}$ and $\delta_B^{D^*K}$. This is seen in the combination of LHCb $B^\pm \to D^*K^\pm$ measurements presented.

11.1 | Outlook

Looking forward, if this analysis is repeated with Run 3 and Run 4 ($50\,\text{fb}^{-1}$) data, and later with Run 5 and Run 6 data ($300\,\text{fb}^{-1}$), the statistical uncertainty on γ will greatly improve, not only due to the higher luminosities but also due to Upgrade I [115] and Upgrade II [116] developments. However, if the measurement is repeated without further consideration, it will be systematically limited. To prevent this, amplitude analyses and *CP*-violation measurements are needed to improve the parameterisation of some of the largest backgrounds.

Currently, comparisons of γ between direct and indirect determinations are limited by the experimental uncertainties on direct γ measurements. With future measurements, the experimental uncertainty on the combination of γ measurements is expected to reduce. The inclusion of Run 3 and Run 4 data is expected to result in an uncertainty on γ of 1° [117], which is on par with theoretical uncertainties on indirect measurements. The field is, therefore, entering an exciting and pivotal stage.

Appendices

A | Mass Fits to Simulation

Figure A.1 shows fits to simulation in the $D\pi$ sample for the signals and two prominent backgrounds, as well as their crossfeed components.

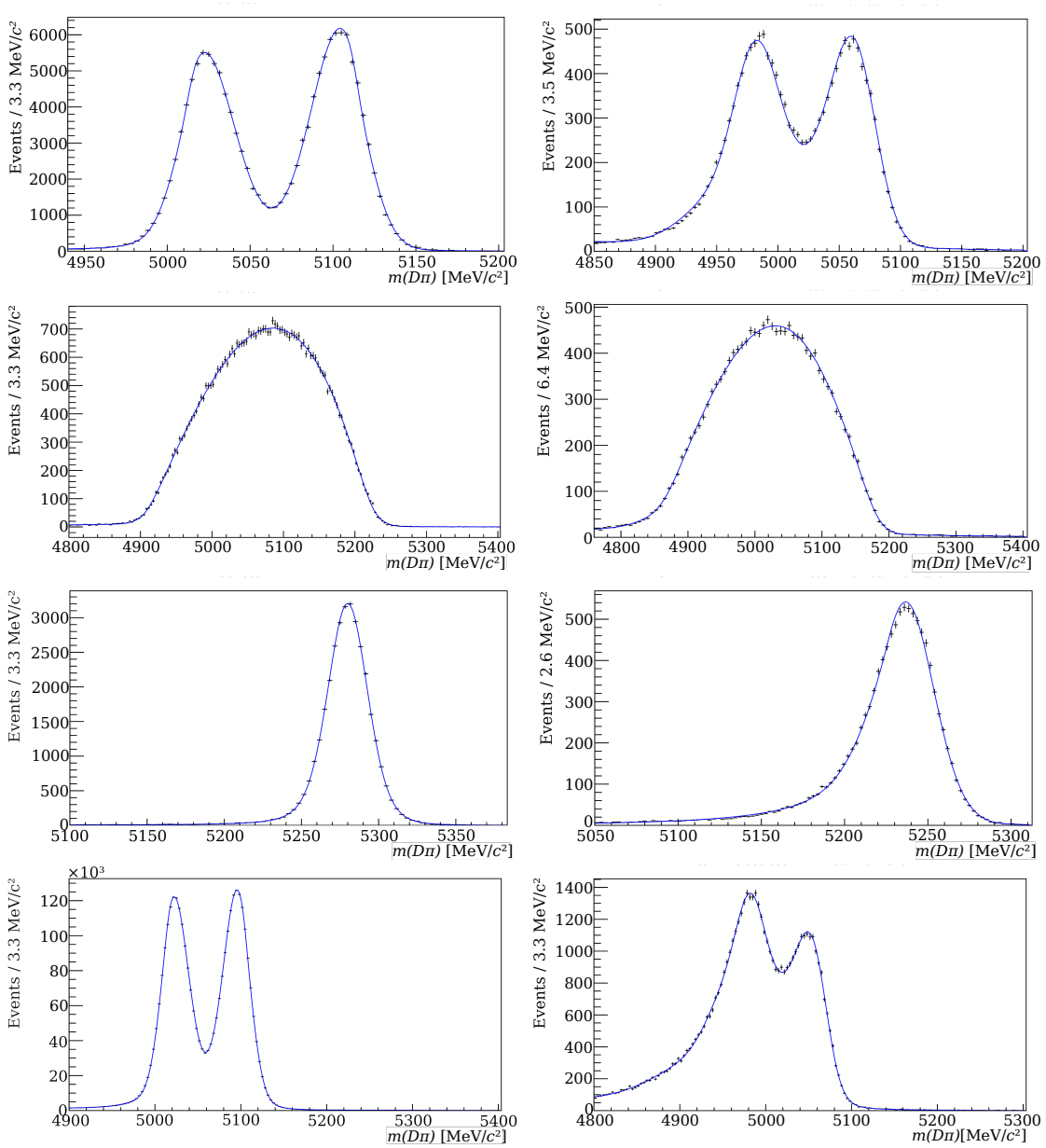

Figure A.1: Simulated mass distributions of (left, from top to bottom) $B^{\pm} \to [D\pi^0]_{D^*}\pi^{\pm}$, $B^{\pm} \to [D\gamma]_{D^*}\pi^{\pm}$, $B^{\pm} \to D\pi^{\pm}$, and $B^0 \to [D\pi^-]_{D^{*-}}\pi^+$ decays and (right) their associated $DK \to D\pi$ crossfeed components, with downstream K^0_S candidates. The projections of the fit results are overlaid.

B | *CP* Fit Projections

Figures B.3–B.7 shows with mass distributions from the *CP* fit with fit projections overlaid. The legends are not included, but are identical to those in Fig. 8.6.

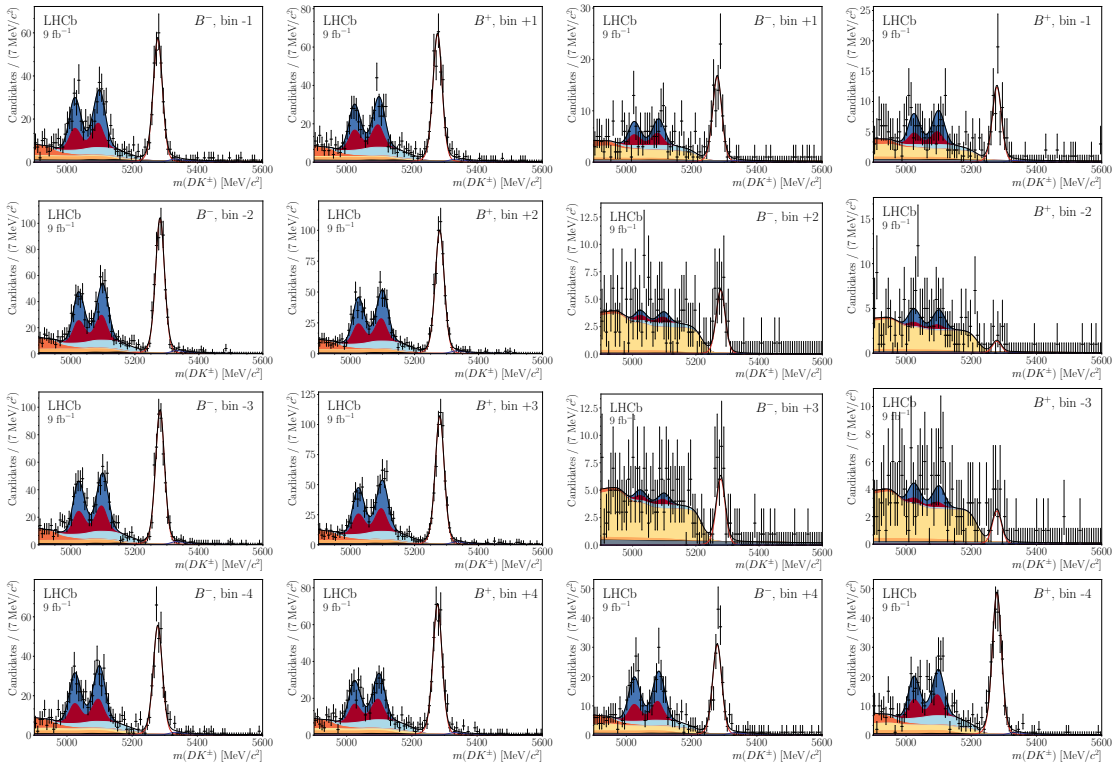

Figure B.2: Mass distributions for DK samples with $D \to K^0_S\pi^+\pi^-$ decays reconstructed with downstream K^0_S candidates for Dalitz bins 1-4. The projections of the fit results are overlaid, and the Dalitz bin number and B meson charge are labelled. The legend is not included, but is identical to that in Fig. 8.6

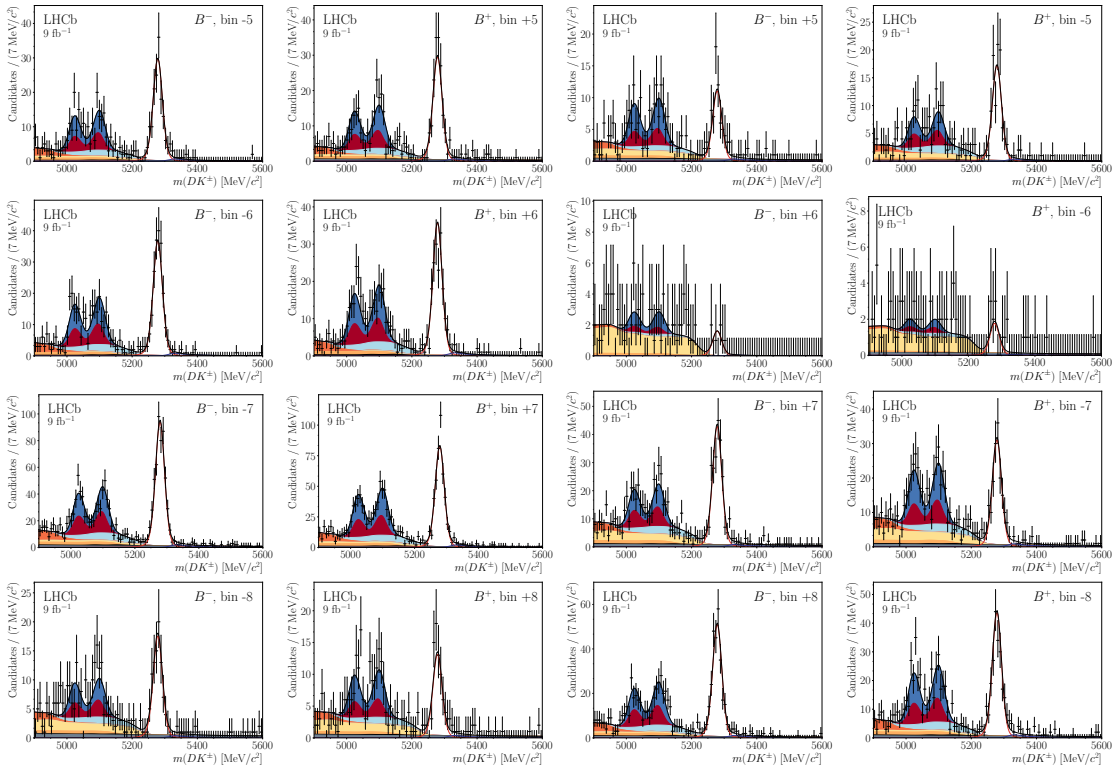

Figure B.3: Mass distributions for DK samples with $D \to K^0_S\pi^+\pi^-$ decays reconstructed with downstream K^0_S candidates for Dalitz bins 5-8. The projections of the fit results are overlaid, and the Dalitz bin number and B meson charge are labelled. The legend is not included, but is identical to that in Fig. 8.6

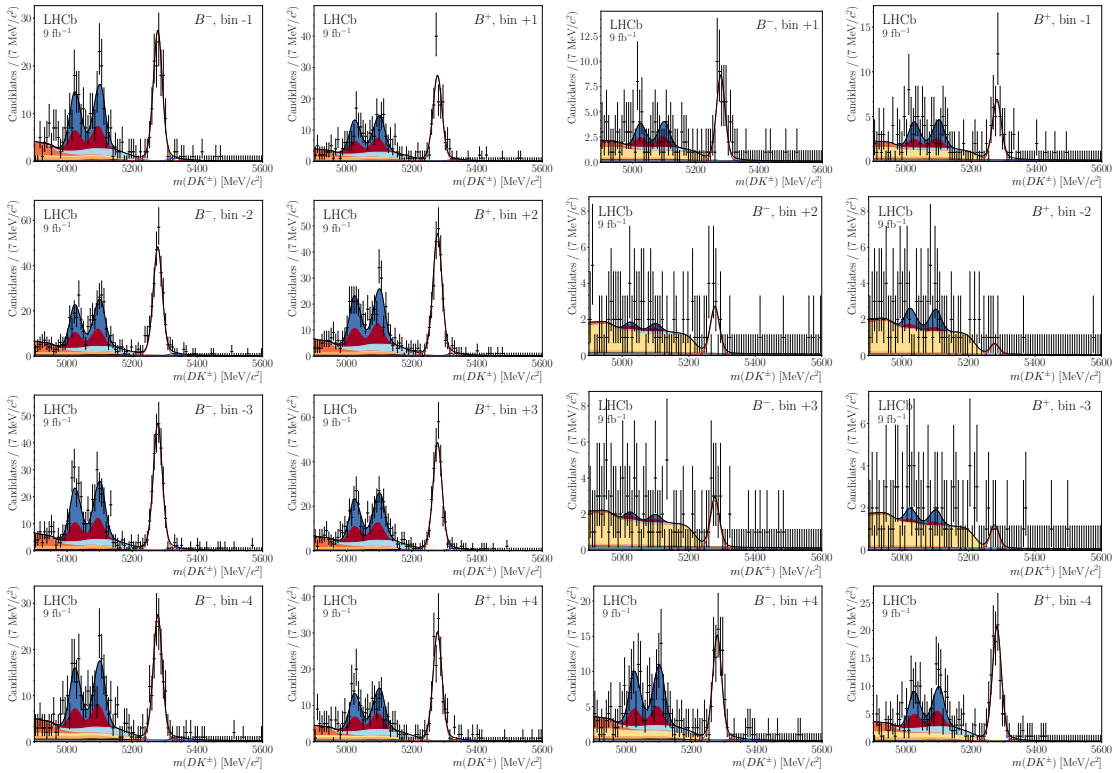

Figure B.4: Mass distributions for DK samples with $D \to K^0_S\pi^+\pi^-$ decays reconstructed with long K^0_S candidates for Dalitz bins 1-4. The projections of the fit results are overlaid, and the Dalitz bin number and B meson charge are labelled. The legend is not included, but is identical to that in Fig. 8.6

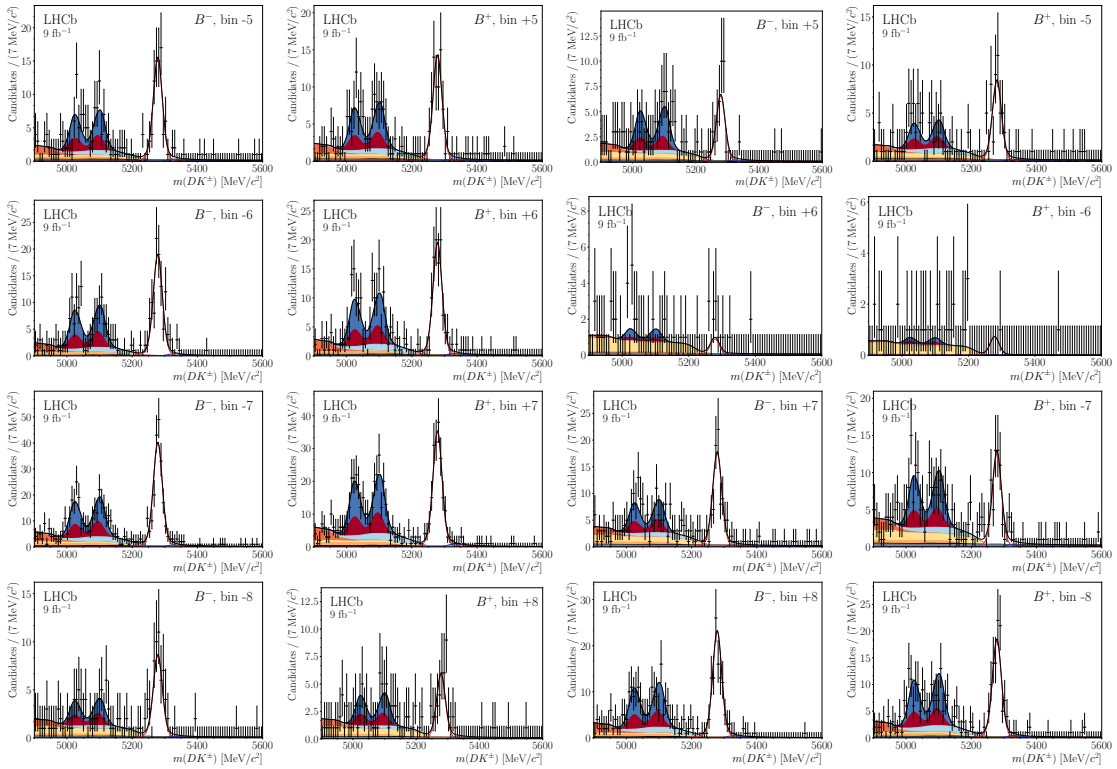

Figure B.5: Mass distributions for DK samples with $D \to K^0_S\pi^+\pi^-$ decays reconstructed with long K^0_S candidates for Dalitz bins 5-8. The projections of the fit results are overlaid, and the Dalitz bin number and B meson charge are labelled. The legend is not included, but is identical to that in Fig. 8.6

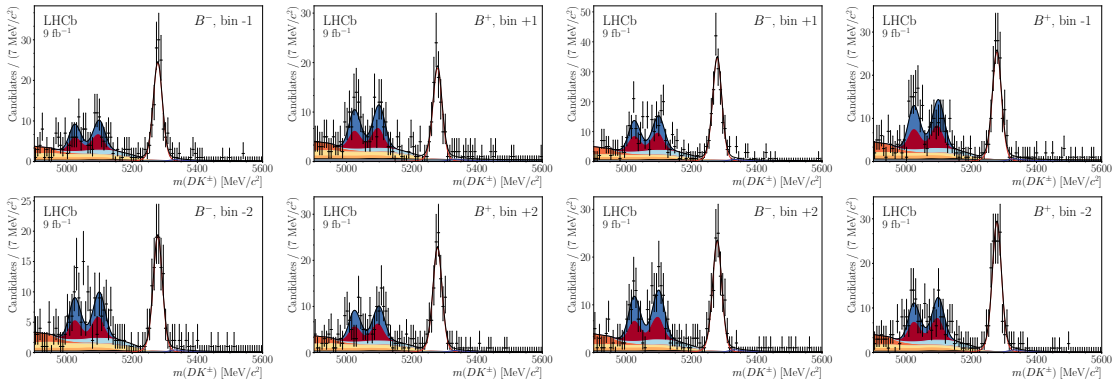

Figure B.6: Mass distributions for DK samples with $D \to K^0_S K^+ K^+$ decays reconstructed with downstream K^0_S candidates. The projections of the fit results are overlaid, and the Dalitz bin number and B meson charge are labelled. The legend is not included, but is identical to that in Fig. 8.6

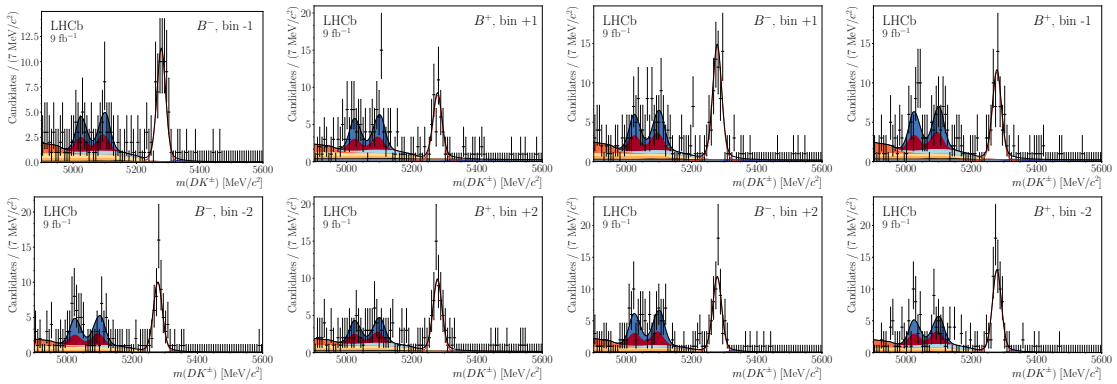

Figure B.7: Mass distributions for DK samples with $D \to K^0_S K^+ K^+$ decays reconstructed with long K^0_S candidates. The projections of the fit results are overlaid, and the Dalitz bin number and B meson charge are labelled. The legend is not included, but is identical to that in Fig. 8.6

References

[1] LHCb Collaboration, R. Aaij *et al.*, *A model-independent measurement of the CKM angle γ in partially reconstructed $B^{\pm} \to D^{*}h^{\pm}$ decays with $D \to K^{0}_{S}h^{+}h^{-}$ ($h = \pi, K$)*, JHEP **02** (2024) 118, arXiv:2311.10434.

[2] A. D. Sakharov, *Violation of CP invariance, C asymmetry, and baryon asymmetry of the universe*, Sov. Phys. Usp. **34** (1991) 392.

[3] J. H. Christenson, J. W. Cronin, V. L. Fitch, and R. Turlay, *Evidence for the 2π Decay of the K^{0}_{2} Meson*, Phys. Rev. Lett. **13** (1964) 138.

[4] NA48 Collaboration, V. Fanti *et al.*, *A new measurement of direct CP violation in two pion decays of the neutral kaon*, Phys. Lett. B **465** (1999) 335.

[5] BABAR Collaboration, B. Aubert *et al.*, *Observation of CP Violation in the B^{0} Meson System*, Phys. Rev. Lett. **87** (2001) 091801.

[6] Belle Collaboration, K. Abe *et al.*, *Observation of Large CP Violation in the Neutral B Meson System*, Phys. Rev. Lett. **87** (2001) 091802.

[7] LHCb Collaboration, R. Aaij *et al.*, *Observation of CP violation in $B^{\pm} \to DK^{\pm}$ decays*, Phys. Lett. B **712** (2012) 203.

[8] LHCb Collaboration, R. Aaij *et al.*, *Observation of CP Violation in Charm Decays*, Phys. Rev. Lett. **122** (2019) 211803.

[9] J. Brod and J. Zupan, *The ultimate theoretical error on γ from $B \to DK$ decays*, JHEP **2014** (2014) .

[10] M. Blanke and A. J. Buras, *Emerging ΔM_d-anomaly from tree-level determinations of $|V_{cb}|$ and the angle γ*, Eur. Phys. J. C **79** (2019) 1.

[11] P. W. Higgs, *Broken symmetries and the masses of gauge bosons*, Phys. Rev. Lett. **13** (1964) 508.

[12] E. Noether, *Invariante variationsprobleme*, Nachrichten von der Gesellschaft der Wissenschaften zu Göttingen, Mathematisch-Physikalische Klasse **1918** (1918) 235.

[13] M. Thomson, *Modern Particle Physics*, Cambridge University Press, 2013.

[14] G. Luders, *On the Equivalence of Invariance under Time Reversal and under Particle-Antiparticle Conjugation for Relativistic Field Theories*, Kong. Dan. Vid. Sel. Mat. Fys. Med. **28N5** (1954) 1.

[15] NOvA Collaboration, M. A. Acero *et al.*, *First measurement of neutrino oscillation parameters using neutrinos and antineutrinos by NOvA*, Phys. Rev. Lett. **123** (2019) 151803.

[16] N. Cabibbo, *Unitary symmetry and leptonic decays*, Phys. Rev. Lett. **10** (1963) 531.

[17] M. Kobayashi and T. Maskawa, *CP-violation in the renormalizable theory of weak interaction*, Prog. Theor. Phys. **49** (1973) 652.

[18] Particle Data Group, R. L. Workman *et al.*, *Review of particle physics*, Prog. Theor. Exp. Phys. **2022** (2022) 083C01.

[19] P. A. M. Dirac, *The quantum theory of the electron*, Proceedings of the Royal Society of London. Series A, Containing Papers of a Mathematical and Physical Character **117** (1928) 610.

[20] L.-L. Chau and W.-Y. Keung, *Comments on the Parametrization of the Kobayashi-Maskawa Matrix*, Phys. Rev. Lett. **53** (1984) 1802.

[21] L. Wolfenstein, *Parametrization of the Kobayashi-Maskawa matrix*, Phys. Rev. Lett. **51** (1983) 1945.

[22] J. Brod, A. Lenz, G. Tetlalmatzi-Xolocotzi, and M. Wiebusch, *New physics effects in tree-level decays and the precision in the determination of the quark mixing angle γ*, Phys. Rev. D **92** (2015) .

[23] A. Lenz and G. Tetlalmatzi-Xolocotzi, *Model-independent bounds on new physics effects in non-leptonic tree-level decays of B-mesons*, JHEP **07** (2020) 177, arXiv:1912.07621.

[24] CKMfitter group, J. Charles *et al.*, *CP violation and the CKM matrix: Assessing the impact of the asymmetric B factories*, Eur. Phys. J. **C41** (2005) 1, arXiv:hep-ph/0406184, updated results and plots available at http://ckmfitter.in2p3.fr/.

[25] Y. Grossman and M. Savastio, *Effects of $K^0 - \overline{K^0}$ mixing on determining γ from $B^\pm \to DK^\pm$*, JHEP **2014** (2014) 8.

[26] A. Bondar, A. Poluektov, and V. Vorobiev, *Charm mixing in a model-independent analysis of correlated $D^0\overline{D^0}$ decays*, Phys. Rev. D **82** (2010) 034033, arXiv:1004.2350.

[27] M. Gronau and D. Wyler, *On determining a weak phase from charged B decay asymmetries*, Phys. Lett. B **265** (1991) 172.

[28] M. Gronau and D. London, *How to determine all the angles of the unitarity triangle from $B^0 \to DK^0_S$ and $B^0_s \to D\phi$*, Phys. Lett. B **253** (1991) 483.

[29] D. Atwood, I. Dunietz, and A. Soni, *Enhanced CP Violation with $B \to KD^0(\overline{D}^0)$ Modes and Extraction of the Cabibbo-Kobayashi-Maskawa Angle γ*, Phys. Rev. Lett. **78** (1997) 3257.

[30] D. Atwood, I. Dunietz, and A. Soni, *Improved methods for observing CP violation in $B^\pm \to K^\pm D$ and measuring the CKM phase γ*, Phys. Rev. D **63** (2001) 036005.

[31] CLEO Collaboration, D. M. Asner *et al.*, *Updated measurement of the strong phase in $D^0 \to K^+\pi^-$ decay using quantum correlations in $e^+e^- \to D^0\overline{D}^0$ at cleo*, Phys. Rev. D **86** (2012) 112001.

[32] BESIII Collaboration, M. Ablikim *et al.*, *Improved measurement of the strong-phase difference $\delta_D^{k\pi}$ in quantum-correlated $D^0\overline{D}^0$ decays*, Eur. Phys. J. C **82** (2022) .

[33] R. H. Dalitz, *Cxii. on the analysis of τ-meson data and the nature of the τ-meson*, The London, Edinburgh, and Dublin Philosophical Magazine and Journal of Science **44** (1953) 1068, arXiv:https://doi.org/10.1080/14786441008520365.

[34] A. Bondar, *Proceedings of BINP Special Analysis Meeting on Dalitz Analysis*, (unpublished) (2002).

[35] A. Bondar and A. Poluektov, *Feasibility study of model-independent approach to ϕ_3 measurement using Dalitz plot analysis*, Eur. Phys. J. C **47** (2006) 347.

[36] A. Bondar and A. Poluektov, *The use of quantum-correlated D^0 decays for ϕ_3 measurement*, Eur. Phys. J. C **55** (2008) 51.

[37] A. Giri, Y. Grossman, A. Soffer, and J. Zupan, *Determining γ using $B^{\pm} \to DK^{\pm}$ with multibody D decays*, Phys. Rev. D **68** (2003) .

[38] S. Chung *et al.*, *Partial wave analysis in K-matrix formalism*, Annalen der Physik **507** (1995) 404.

[39] A. Poluektov, *Unbinned model-independent measurements with coherent admixtures of multibody neutral D meson decays*, Eur. Phys. J. C **78** (2018) .

[40] CLEO Collaboration, J. Libby *et al.*, *Model-independent determination of the strong-phase difference between D^0 and $\bar{D}^0 \to K^0_{S,L} h^+ h^-$ ($h = \pi, K$) and its impact on the measurement of the CKM angle γ/ϕ_3*, Phys. Rev. D **82** (2010) 112006.

[41] CLEO Collaboration, J. Libby *et al.*, *Model-independent determination of the strong-phase difference between D^0 and $\overline{D^0} \to K^0_{S,L} h^+ h^- (h = K, \pi)$ and its impact on the measurement of the CKM angle γ/ϕ_3*, Phys. Rev. D **82** (2010) .

[42] BESIII Collaboration, M. Ablikim *et al.*, *Improved model-independent determination of the strong-phase difference between D^0 and $\overline{D^0} \to K^0_{S,L} K^+ K^-$ decays*, Phys. Rev. D **102** (2020) .

[43] BESIII Collaboration, M. Ablikim *et al.*, *Model-independent determination of the relative strong-phase difference between D^0 and $\overline{D^0} \to K^0_{S,L}\pi^+\pi^-$ and its impact on the measurement of the CKM angle γ/ϕ_3*, Phys. Rev. D **101** (2020) .

[44] A. Bondar and T. Gershon, *On ϕ_3 measurements using $B^- \to D^*K^-$ decays*, Phys. Rev. D **70** (2004) 091503.

[45] LHCb Collaboration, R. Aaij *et al.*, *Measurement of the CKM angle γ in $B^\pm \to DK^\pm$ and $B^\pm \to D\pi^\pm$ decays with $D \to K^0_S h^+h^-$*, JHEP **02** (2021) 0169, arXiv:2010.08483.

[46] LHCb Collaboration, R. Aaij *et al.*, *Measurement of CP observables in $B^\pm \to D^{(*)}K^\pm$ and $B^\pm \to D^{(*)}\pi^\pm$ decays using two-body D final states*, JHEP **04** (2021) 081, arXiv:2012.09903.

[47] LHCb Collaboration, *Simultaneous determination of the CKM angle γ and parameters related to mixing and CP violation in the charm sector*, LHCb-CONF-2022-003, 2022.

[48] Belle Collaboration, A. Poluektov *et al.*, *Evidence for direct CP violation in the decay $B \to D^{(*)}K$, $D \to K^0_S\pi^+\pi^-$ and measurement of the CKM phase ϕ_3*, Phys. Rev. D **81** (2010) 112002.

[49] BABAR Collaboration, P. del Amo Sanchez *et al.*, *Evidence for Direct CP Violation in the Measurement of the Cabbibo-Kobayashi-Maskawa Angle γ with $B^\mp \to D^{(*)}K^{(*)\mp}$ Decays*, Phys. Rev. Lett. **105** (2010) 121801.

[50] BABAR Collaboration, P. del Amo Sanchez *et al.*, *Measurement of $D^0 - \overline{D^0}$ Mixing Parameters Using $D^0 \to K^0_S\pi^+\pi^-$ and $D^0 \to K^0_S K^+K^-$ Decays*, Phys. Rev. Lett. **105** (2010) 081803.

[51] LHCb Collaboration, R. Aaij *et al.*, *Measurement of the CKM angle γ using the $B^{\pm} \to D^{*}h^{\pm}$ channels*, JHEP **12** (2023) 013, arXiv:2310.04277.

[52] L. Evans and P. Bryant, *LHC Machine*, JINST **3** (2008) S08001.

[53] E. Mobs, *The CERN accelerator complex - August 2018. Complexe des accélérateurs du CERN - Août 2018*, , General Photo.

[54] LHCb Collaboration, R. Aaij *et al.*, *The LHCb Detector At The LHC*, JINST **3** (2008) S08005.

[55] LHCb Collaboration, C. Elsasser, *$\bar{b}b$ production angle plots*, https://lhcb.web.cern.ch/lhcb/speakersbureau/html/bb_ProductionAngles.html.

[56] LHCb Collaboration, R. Aaij *et al.*, *LHCb detector performance*, Int. J. Mod. Phys. A **30** (2015) 1530022.

[57] LHCb Collaboration, P. R. Barbosa-Marinho *et al.*, *LHCb VELO (VErtex LOcator): Technical Design Report*, Technical design report. LHCb, CERN, Geneva, 2001.

[58] R. Aaij *et al.*, *Performance of the LHCb Vertex Locator*, JINST **9** (2014) P09007.

[59] LHCb Collaboration, S. Amato *et al.*, *LHCb magnet: Technical Design Report*, Technical design report. LHCb, CERN, Geneva, 2000.

[60] O. Steinkamp, *Layout and R&D for an All-Silicon TT Station* , CERN, Geneva, 2003.

[61] LHCb Outer Tracker Group, *Performance of the LHCb Outer Tracker*, JINST **9** (2014) P01002.

[62] P. d'Argent *et al.*, *Improved performance of the LHCb Outer Tracker in LHC Run 2*, JINST **12** (2017) P11016.

[63] LHCb Collaboration, P. R. Barbosa-Marinho *et al.*, *LHCb inner tracker: Technical Design Report*, Technical design report. LHCb, CERN, Geneva, 2002. revised version number 1 submitted on 2002-11-13 14:14:34.

[64] O. Callot and S. Hansmann-Menzemer, *The Forward Tracking: Algorithm and Performance Studies* , CERN, Geneva, 2007.

[65] O. Callot, *Downstream Pattern Recognition* , CERN, Geneva, 2007.

[66] R. Frühwirth, *Application of Kalman filtering to track and vertex fitting*, Nucl. Instr. and Meth. **262** (1987) 444.

[67] J. Van Tilburg, *Track simulation and reconstruction in LHCb*, 2005. Presented on 01 Sep 2005.

[68] LHCb Collaboration, *Muon track reconstruction efficiency at LHCb*, LHCB-FIGURE-2020-010, 2020.

[69] R. Aaij *et al.*, *Design and performance of the LHCb trigger and full real-time reconstruction in Run 2 of the LHC*, JINST **14** (2019) P04013.

[70] LHCb RICH Collaboration, M. Adinolfi *et al.*, *Performance of the LHCb RICH detector at the LHC*, Eur. Phys. J. C **73** (2013) .

[71] A. Papanestis and C. D'Ambrosio, *Performance of the LHCb RICH detectors during the LHC Run II*, Nucl. Instr. and Meth. **876** (2017) 221, The 9th international workshop on Ring Imaging Cherenkov Detectors (RICH2016).

[72] R. W. Forty and O. Schneider, *RICH pattern recognition* , CERN, Geneva, 1998.

[73] LHCb Collaboration, *PID performance plots*, https://twiki.cern.ch/twiki/bin/view/LHCb/PIDConferencePlots, 2020.

[74] LHCb Calorimeter Group, C. A. Beteta *et al.*, *Calibration and performance of the LHCb calorimeters in Run 1 and 2 at the LHC*, CERN-LHCb-DP-2020-001, 2020.

[75] O. Deschamps *et al.*, *Photon and neutral pion reconstruction*, LHCb-2003-091, 2003.

[76] C. Coca *et al.*, *The hadron calorimeter prototype beam-test results*, LHCb-2000-036, 2000.

[77] LHCb Collaboration, *Selected HLT2 reconstruction performance for the LHCb upgrade*, LHCb-FIGURE-2021-003, 2021.

[78] A. A. Alves Jr *et al.*, *Performance of the LHCb muon system*, JINST **8** (2013) P02022.

[79] LHCb Collaboration, P. R. Barbosa-Marinho *et al.*, *LHCb muon system: Technical Design Report*, Technical design report. LHCb, CERN, Geneva, 2001.

[80] R. Aaij *et al.*, *The LHCb trigger and its performance in 2011*, JINST **8** (2013) P04022.

[81] V. V. Gligorov and M. Williams, *Efficient, reliable and fast high-level triggering using a bonsai boosted decision tree*, JINST **8** (2013) P02013.

[82] T. Sjöstrand, S. Mrenna, and P. Skands, *A brief introduction to PYTHIA 8.1*, Comp. Phys. Comm. **178** (2008) 852, arXiv:0710.3820.

[83] I. Belyaev *et al.*, *Handling of the generation of primary events in Gauss, the LHCb simulation framework*, J. Phys. Conf. Ser. **331** (2011) 032047.

[84] D. J. Lange, *The EvtGen particle decay simulation package*, Nucl. Instrum. Meth. **A462** (2001) 152.

[85] N. Davidson, T. Przedzinski, and Z. Was, *PHOTOS interface in C++: Technical and physics documentation*, Comp. Phys. Comm. **199** (2016) 86, arXiv:1011.0937.

[86] Geant4 collaboration, J. Allison *et al.*, *Geant4 developments and applications*, IEEE Trans. Nucl. Sci. **53** (2006) 270.

[87] Geant4 collaboration, S. Agostinelli *et al.*, *Geant4: A simulation toolkit*, Nucl. Instrum. Meth. **A506** (2003) 250.

[88] M. Clemencic *et al.*, *The LHCb simulation application, Gauss: Design, evolution and experience*, J. Phys. Conf. Ser. **331** (2011) 032023.

[89] D. Müller, M. Clemencic, G. Corti, and M. Gersabeck, *ReDecay: A novel approach to speed up the simulation at LHCb*, Eur. Phys. J. **C78** (2018) 1009, arXiv:1810.10362.

[90] G. A. Cowan, D. C. Craik, and M. D. Needham, *RapidSim: an application for the fast simulation of heavy-quark hadron decays*, Comp. Phys. Comm. **214** (2017) 239, arXiv:1612.07489.

[91] J. Back *et al.*, *Laura^{++}: A Dalitz plot fitter*, Comp. Phys. Comm. **231** (2018) 198, arXiv:1711.09854.

[92] A. N. Kolmogorov, *Sulla Determinazione Empirica di Una Legge di Distribuzione*, Giornale dell'Istitutio Italiano degli Attuari **4** (1933) 83.

[93] N. Smirnov, *Table for Estimating the Goodness of Fit of Empirical Distributions*, Ann. Math. Statist. **19** (1948) 279 .

[94] J. Garra Ticó *et al.*, *Study of the sensitivity to CKM angle γ under simultaneous determination from multiple B meson decay modes*, Phys. Rev. D **102** (2020) 053003, arXiv:1909.00600.

[95] W. D. Hulsbergen, *Decay chain fitting with a Kalman filter*, Nucl. Instrum. Meth. **A552** (2005) 566, arXiv:physics/0503191.

[96] L. Breiman, J. H. Friedman, R. A. Olshen, and C. J. Stone, *Classification and regression trees*, Wadsworth international group, Belmont, California, USA, 1984.

[97] Y. Freund and R. E. Schapire, *A decision-theoretic generalization of on-line learning and an application to boosting*, J. Comput. Syst. Sci. **55** (1997) 119.

[98] H. Voss, A. Hoecker, J. Stelzer, and F. Tegenfeldt, *TMVA - Toolkit for Multivariate Data Analysis with ROOT*, PoS **ACAT** (2007) 040.

[99] M. Bjorn and S. S. Malde, *Measurement of the CKM angle γ in $B^{\pm} \to \left[K^0_S h^+ h^-\right]_D h'^{\pm}$ decays using the full Run 1 and 2 dataset* , 2020. LHCb-ANA-2020-001 linked to LHCb-PAPER-2020-19.

[100] L. Anderlini *et al.*, *The PIDCalib package*, LHCb-PUB-2016-021, 2016.

[101] M. Pivk and F. R. Le Diberder, *sPlot: A statistical tool to unfold data distributions*, Nucl. Instrum. Meth. **A555** (2005) 356, arXiv:physics/0402083.

[102] B. Efron, *Bootstrap Methods: Another Look at the Jackknife*, Ann. Statist. **7** (1979) 1.

[103] R. Barlow, *Extended maximum likelihood*, Nucl. Instrum. Meth. A **297** (1990) 496.

[104] W. Verkerke and D. Kirkby, *The RooFit toolkit for data modeling*, eConf **C0303241** (2003).

[105] LHCb Collaboration, R. Aaij *et al.*, *Measurement of the b-Quark Production Cross Section in 7 and 13 TeV pp Collisions*, Phys. Rev. Lett. **118** (2017) 052002.

[106] LHCb Collaboration, R. Aaij *et al.*, *Dalitz plot analysis of $B_s^0 \to \overline{D}^0 K^- \pi^+$ decays*, Phys. Rev. **D90** (2014) 072003, arXiv:1407.7712.

[107] LHCb Collaboration, R. Aaij *et al.*, *Constraints on the unitarity triangle angle γ from Dalitz plot analysis of $B^0 \to DK^+\pi^-$ decays*, Phys. Rev. D **93** (2016) 112018.

[108] LHCb Collaboration, R. Aaij *et al.*, *Dalitz plot analysis of $B^0 \to \overline{D^0}\pi^+\pi^-$ decays*, Phys. Rev. D **92** (2015) .

[109] P. Golonka and Z. Was, *PHOTOS Monte Carlo: A precision tool for QED corrections in Z and W decays*, Eur. Phys. J. **C45** (2006) 97, arXiv:hep-ph/0506026.

[110] BABAR Collaboration, B. Aubert *et al.*, *Measurement of the Branching Fraction and Polarization for the Decay $B^- \to D^{*0}K^{*-}$*, Phys. Rev. Lett. **92** (2004) .

[111] LHCb Collaboration, R. Aaij *et al.*, *Study of CP violation in $B^0 \to DK^*(892)^0$ decays with $D \to K\pi(\pi\pi)$, $\pi\pi(\pi\pi)$, and KK final states*, arXiv:2401.17934, submitted to JHEP.

[112] BaBar Collaboration and Belle Collaboration, I. Adachi *et al.*, *Measurement of $\cos 2\beta$ in $B^0 \to D^{(*)}h^0$ with $D \to K^0_S\pi^+\pi^-$ decays by a combined time-*

dependent Dalitz plot analysis of BaBar and Belle data, Phys. Rev. D **98** (2018) 112012.

[113] LHCb Collaboration, R. Aaij *et al.*, *Measurement of the CKM angle γ from a combination of LHCb results*, JHEP **12** (2016) 087, arXiv:1611.03076.

[114] E. Lehmann, *Elements of Large-sample Theory*, Springer, 1998.

[115] LHCb collaboration, R. Aaij *et al.*, *The LHCb Upgrade I*, arXiv:2305.10515, submitted to JINST.

[116] LHCb collaboration, *Framework TDR for the LHCb Upgrade II: Opportunities in flavour physics, and beyond, in the HL-LHC era*, CERN-LHCC-2021-012, LHCB-TDR-023, CERN, Geneva, 2021.

[117] LHCb Collaboration, I. Bediaga *et al.*, *Physics case for an LHCb Upgrade II - Opportunities in flavour physics, and beyond, in the HL-LHC era*, LHCB-PUB-2018-009, 2019.